A MICROSTRUCTURAL EXAMINATION OF DUPLEX FERRITE-MARTENSITE CORROSION RESISTING STEELS

by

Robert Douglas Knutsen

A thesis submitted to the Faculty of Engineering, University of Cape Town in fulfilment of the degree of Doctor of Philosophy

Department of Materials Engineering
University of Cape Town

August 1989

ABSTRACT

This thesis reports a study of the microstructural evolution of chromium containing duplex ferrite-martensite steels and examines the effects of the microstructure on the mechanical properties. Emphasis has been placed on determining the microstructural factors responsible for the persistent occurrence of anisotropy in a modified 12 wt % Cr steel designated 3CR12. In addition an investigation has been carried out in order to refine the grain structure of a ferritic steel containing 16-17 wt % Cr by inducing a duplex ferrite-martensite phase structure.

The microstructural evolution of 3CR12 was studied during cooling from a solution heat treatment at 1380°C and the natures of the phase transformations evident were investigated. Energy dispersive X-ray spectroscopy (EDS), in association with a scanning electron microscope (SEM), was used to determine the composition of the phases arising from the solid state δ-ferrite to austenite transformation. It is shown that the high temperature δ-ferrite phase partially decomposes to austenite via a Widmanstätten growth mechanism and consequently a banded two phase structure is produced after hot rolling. The element partitioning which arises during the solid state δ-ferrite decomposition leads to compositional banding with an indelible nature. A model is proposed for the events leading to the generation of the banded phase structure and the formation of an elongated ferritic microstructure in 3CR12 after sub-critical annealing. The type and distribution of non-metallic inclusions occurring in 3CR12 has also been assessed.

Characteristic fracture modes developed during impact testing have been related to the grain morphology and the occurrence of non-metallic inclusions. It is shown that splits form parallel to the rolling plane when Charpy specimens are subjected to impact testing and that both impact energy and mode of fracture are dependent on the directional properties of the 3CR12 microstructure. Splitting is predominantly caused by the low energy crack path provided by long, undulating grain boundaries parallel to the rolling plane, and inclusions, particularly manganese sulphides (MnS), facilitate low energy modes of fracture associated with the splitting phenomenon. MnS inclusions are also found to affect the corrosion resistance of 3CR12 and careful control of the chemistry of the steel permits these inclusions to be restricted to levels at which acceptable impact and corrosion properties are maintained.

Refinement of the grain structure of ferritic steels containing 16-17 wt % Cr was carried out by modifying the ratio of ferritising elements to austenitising elements in the steel chemistry. Suitable nickel additions have been determined which provide alloys with sufficient austenitising ability to refine the high temperature δ-ferrite phase and consequently a duplex ferrite-martensite microstructure is produced. Tempering of these alloys at 700°C results in a lamellar ferrite-martensite structure which gives rise to an attractive combination of impact and tensile properties which may provide a stainless steel with superior cost effectiveness to austenitic grades.

ACKNOWLEDGEMENTS

I wish to express my appreciation to all those who assisted me during the course of this project, in particular:

Professor A Ball, my supervisor, for his advice and support.

Dr R Hutchings for his help and encouragement in the initial stages of the project.

Mrs H Böhm and Mrs Betz for their invaluable laboratory assistance and for their help in the preparation of the final manuscript.

Messrs J Hewitt and J P Hoffman of Middelburg Steel and Alloys for the numerous discussions.

Mr B Greeves and Mr J Petersen for the photographic work. Mr N Dreze and Mr G Newins for their technical assistance.

Mrs J Sharland and Mrs A Ball for their administrative support.

My wife, Colleen, for helping type the manuscript.

The Staff and my fellow students for their support and encouragement.

Finally, the CSIR, FRD and Middelburg Steel and Alloys are greatly acknowledged for the provision of financial support.

Dedicated to my parents

CONTENTS

CHAPTER THREE EXPERIMENTAL PROCEDURE AND MATERIALS

CHAPTER FOUR RESULTS

-ooOoo-

CHAPTER 1

INTRODUCTION

1.1 GENERAL INTRODUCTION

Strength, toughness and ductility are the most important properties specified for structural steels. On account of corrosion also being prevalent in a large number of engineering applications, a suitable structural steel would be one that combines these properties with good corrosion resistance. Sensible alloy selection requires the maintenance of a reasonable level of cost effectiveness within the system and in many instances protective coatings are applied to low cost mild steels and related alloys. However, these attempts to provide corrosion protection can often be very tedious and this has led a number of development organisations towards the consideration of ferritic grade stainless steels.

Ferritic stainless steels represent the cheapest family of chromium containing corrosion resisting steels, but what these steels gain in their resistance to corrosive attack, they generally lose in terms of ductility, toughness, and forming and welding properties. The introduction of commercial methods of obtaining low interstitial levels in ferritic stainless steels has improved the properties of these steels remarkably, but it is well known that grain-coarsening occurs readily in these steels due to the greater atomic mobility in body-centered cubic structures, and poor toughness is a consequence. Furthermore, ferritic stainless steels, like mild steels, show a ductile-brittle cleavage transition, but their impact transition temperature is considerably higher than that for mild steel due to the embrittling effect of chromium dissolved in ferrite. This impact transition temperature can be reduced, whilst also increasing the upper shelf energy, by decreasing the grain size, but, due to the non-transformable nature of ferritic grades, the coarse grain size is a major problem.

Owing to the fact that ferritic stainless steels are generally considered to have single phase microstructures, the ferrite formed during solidification (δ-ferrite) remains stable down to

room temperature. This means that any refinement of the large grains produced at elevated temperatures generally only occurs due to the rolling and subsequent recrystallisation processes. Additional grain refinement, however, could be achieved by transformation reactions induced as a result of steel chemistry modification. Transformation, or partial transformation, of the large grained δ-ferrite to austenite during cooling from the high temperature region may lead to either fully austenitic or duplex ferrite-austenite structures at intermediate temperatures. Further cooling to ambient can then result in either the regression of austenite to α-ferrite, the formation of martensite, or retention of stable austenite. These transformations will of course ultimately depend on the steel chemistry and the cooling rate. In this way the decomposition of the high temperature δ-ferrite, by suitable minor alloy addition, can modify the properties of the original ferritic stainless steel both in terms of a more refined microstructure after rolling, and improved weldability due to the presence of a duplex structure at elevated temperature.

The principle of transformation grain refining has been applied to the ferritic grade AISI 409 stainless steel and has resulted in the development of a transformable steel containing approximately 12 wt % chromium. The alloy, designated 3CR12 [Middelburg Steel and Alloys (Pty) Ltd, *S. Afr. Pat.* 78/4764, 1978], is titanium stablised, and produces a ferritic grain structure much finer than the parent AISI 409 after sub-critical annealing. Mechanical properties in this condition are comparable to mild steel, but obviously the corrosion resistance is far superior to that of conventional carbon steels. In addition, the ductile-brittle cleavage transition temperature is much reduced compared to AISI 409. Reheating this alloy above the lower critical temperature (A_{C1}) gives rise to a duplex ferrite-austenite microstructure which will transform to ferrite-martensite during air cooling to ambient. The improved weldability of 3CR12 compared to AISI 409 is attributed to the formation of the duplex structure at elevated temperature[1].

As a result of the excellent combination of mechanical and corrosion properties, the steel 3CR12 has found acceptance in numerous applications in the coal and gold mining industries, in particular where abrasion-corrosion conditions are prevalent[2]. Furthermore, the use of this material has been extended into the agricultural, fishing, transport, and liquor and wine industries and it is estimated that the current annual production of 3CR12 is of the order of 50 000 tonnes.

1.2 AIM OF RESEARCH

One of the problems with a microduplex steel such as 3CR12 is the development of a banded microstructure after hot rolling which can lead to marked directionality in the steel.

The banded structure has its origin due to hot rolling being carried out in the duplex ferrite-austenite region. Although a certain degree of anisotropy is not uncommon in many rolled products, the persistent directionality in 3CR12, even after heat treatment, gives rise to very characteristic fracture properties. This concerns, in particular, a delamination or "splitting" phenomenon which occurs during tensile and Charpy V-notch impact testing[3,4]. For instance, impact testing of specimens notched in the through-thickness direction, which results in extensive splitting, gives rise to impact energies approximately one quarter of specimens notched in the rolling plane. As well as the banded grain structure in 3CR12, numerous non-metallic inclusions of various shapes, sizes, and degrees of coherency occur stringered parallel to the rolling direction. Their occurrence is to some extent related to the complex chemistry of the 3CR12 steel. These inclusions will no doubt affect the fracture properties of the steel to a greater or lesser extent, depending on the exact nature of the inclusions and their distribution. In view of this, it is possible that finer control of the alloy chemistry could modify the inclusion composition in order to avoid the effects of the more deleterious inclusions and therefore reduce anisotropy.

The question which arises is whether the persistent occurrence of a marked directional microstructure after heat treatment is determined by (1) the mechanisms of microstructural evolution, or (2) the stringered non-metallic inclusion populations prominent in this steel, or perhaps (3) a combination of more than one principle effect? This investigation has involved a detailed study of both the evolution of the 3CR12 microstructure and of the chemistry, morphology, and dispersion of inclusions and precipitates occurring in the steel matrix. The effect of these basic microstructural characteristics and non-metallic particle distributions on the impact properties have been examined for a range of commercial run-of-the-mill 3CR12 heats, with a view to determining the factors responsible for the persistent directional properties of the steel.

In addition to the microstructural examination of 3CR12, an investigation concerning the development of a modified ferritic stainless steel containing approximately 16 wt % chromium has been conducted. Existing 16-18 wt % chromium containing ferritic stainless steels offer good corrosion resistance but suffer tremendous limitations in their application as a result of poor toughness and weldability. Austenitic stainless steels of the type AISI 304 and 316 provide superb corrosion resistance as well as good toughness and welding properties, although their application can sometimes be limited by their strength. Despite the attractive properties of the austenitic stainless steels, their high nickel content (6-10 wt %) limits their use for obvious economic reasons. On the other hand, ferritic stainless steels of the type AISI 430 are relatively cheap and a modified version of this alloy aimed at providing good welding and mechanical properties could offer a much cheaper substitute for austenitic stainless steels in many applications. The investigation has led to the analysis

of several alloy compositions possessing various ferrite-forming/austenite-forming element ratios, with the intention of deriving a suitable chemistry that will render transformation characteristics similar to 3CR12. In this way it is hoped that the advantages of the grain refinement provided by the duplex phase structure inherent in the 3CR12 chemistry can be similarly exploited by a duplex steel containing approximately 16 wt % chromium. An alloy of this type will help bridge the gap between conventional ferritic and austenitic stainless steels, whilst still being competitive in terms of cost effectiveness.

These investigations have contributed towards a better understanding of the circumstances surrounding the modification of single phase ferritic stainless steels. Both the advantages and limitations of promoting duplex ferrite-martensite phase structures are discussed in the context of developing improved engineering materials.

-ooOoo-

CHAPTER 2

LITERATURE REVIEW

2.1 GENERAL PRINCIPLES OF DUPLEX STEELS

Duplex or dual phase steels include a wide range of alloys possessing predominantly two-phase microstructures. Depending on the alloy type, these microstructures may be ferrite-martensite, ferrite-austenite, or martensite-austenite. The terms duplex and dual phase, however, are not always synonymous, and dual phase is often applied more specifically to two-phase ferrite-martensite steels satisfying certain strength-ductility criteria[5]. These alloys are characterised by a microstructure consisting of about 75-85 vol % ferrite with the remainder being a mixture of martensite, lower bainite, and retained austenite[5-9].

The range of alloys commonly referred to as dual phase steels are essentially low carbon, low alloy steels that are thermomechanically processed to have better formability than ferrite-pearlite steels of similar strength[5]. Typically martensite contents range from 15 to 20 vol %, thereby giving rise to a microstructure of discrete hard islands in a soft ferrite matrix. The stress-strain behaviour of dual phase steels is characteristically different from that of ferrite-pearlite steels such as plain carbon steel, or the microalloyed high strength low alloy (HSLA) steels. These differences have been summarised as follows[5]:

> *The* ferrite-pearlite steels *possess yield point elongation, a high ratio of yield strength to ultimate tensile strength (YS/UTS), and their strength and ductility (uniform elongation) are inversely related.*
>
> Dual phase steels *have a continuous stress-strain curve with no yield point elongation. They have better formability than the ferrite-pearlite steels of equivalent strength, and their strength-ductility data fall on a separate curve to that for ferrite-pearlite steels (fig 2.1).*

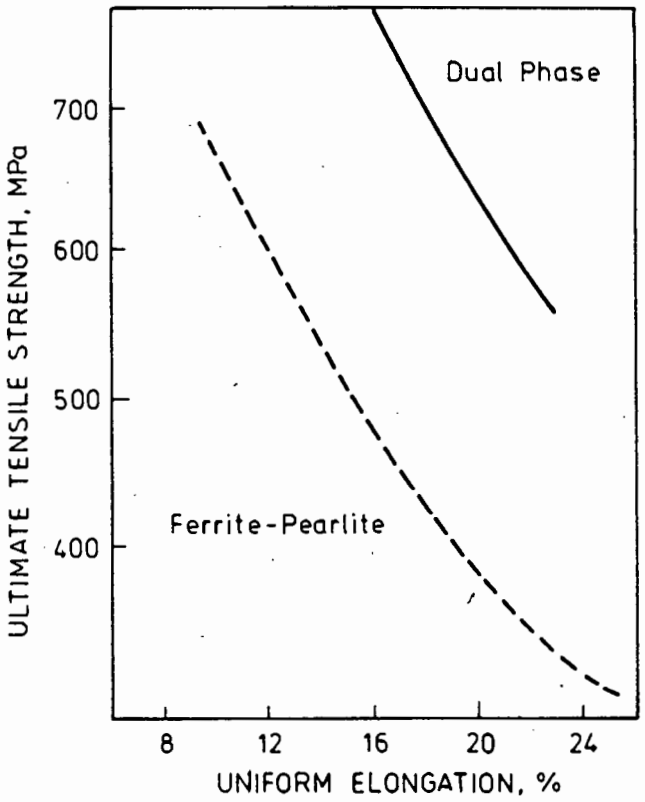

FIGURE 2.1 : Comparison of the strength-ductility relationships of ferrite-pearlite and dual phase steels (after Ref 5).

The stress-strain behaviour of dual phase steels has been correlated to the initial dislocation substructure present prior to deformation and the dislocation substructure which is developed during deformation[9]. Prior to deformation, the dislocation densities in the ferrite are highest immediately adjacent to the martensite and decrease away from the martensite. The high dislocation density near the martensite has been attributed to the martensite transformation shear and to the volume expansion of 2 or 3% associated with this transformation. Consequently, it is the unpinned dislocations and residual stresses produced by the martensite transformation that are generally considered responsible for the low yield stress in dual phase steels. The multi-stage work hardening behaviour which follows is controlled by the multiplication of these dislocations and the development of incipient dislocation cells within the ferrite[9]. The resultant high work hardening rate is what gives rise to the improved ductility/formability properties of dual phase steels.

More highly alloyed two phase steels may or may not benefit from a duplex microstructure in the same way as low alloy dual phase steels. Modified stainless steels generally rely on the formation of duplex structures to improve the strength and toughness properties of the single phase alloy without loss in corrosion resistance. For instance, the duplex ferrite-austenite stainless steels have improved strength and stress corrosion cracking resistance over fully austenitic steels[10]. In addition, it has been noted that the presence of the ferrite

causes a marked refinement of the grain size of both the ferrite and austenite, which in turn leads to an improvement in the resistance to intergranular corrosion and contributes to the increase in strength. The intrinsically fine grained structure of these alloys is also reported to give rise to superplastic behaviour at elevated temperatures[11,12]. Besides the more exotic applications of superplastic materials, this property provides much improved hot workability[13].

Duplex ferrite-martensite stainless steels are less common than the ferrite-austenite types and they have not been as well researched. Nevertheless, it has been shown that the presence of a strong, tough, low carbon martensite phase in microduplex ferrite-martensite stainless steels leads to improved strength and toughness over the level of properties of a completely ferritic alloy[14,15]. Once again the intrinsic fine grained structure of these alloys is largely responsible for the improvement in properties and the ductile-to-brittle transition temperatures are substantially lowered compared to the single phase materials. Alloys containing on the order of more than 40 vol % martensite show much reduced evidence of microcracking in the cleavage prone ferrite phase during deformation[14]. In addition, the similar restriction to grain growth found in the ferrite-austenite steels, due to the presence of a second phase, results in much improved weldability of the ferrite-martensite steels compared to the single phase ferritic steels[16]. Although the ferrite-martensite steels so far reported are much less alloyed than the ferrite-austenite steels in terms of chromium and nickel contents, and therefore their corrosion resistance is not as great, they do possess mechanical property and cost advantages. The strength and toughness of these alloys can be varied by heat treatment[16], which gives rise to more flexible application, and the lower alloy content, especially nickel, leads to the production of much cheaper steels.

2.2 EVOLUTION OF DUPLEX STEELS

The formation of duplex microstructures in steels is related to both the alloy composition and thermal history of the steel. For conventional dual phase steels, the low carbon content and relatively low alloy content (eg, Mn = 1-3 wt %, Si = 0.5-1 wt %) allows the phase equilibria to be represented on an Fe-C equilibrium phase diagram[5] (fig 2.2). The vertical composition line roughly corresponding to the carbon content of dual phase alloys, indicates a fully austenitic microstructure above about 870°C (A_3 temperature). Below this temperature, the austenite transforms to produce increasing amounts of ferrite as the steel is cooled through the intercritical region (between the A_1 and A_3 temperatures). The phase diagram in fig 2.2 indicates that a ferrite plus carbide microstructure is developed on equilibrium cooling below the A_1 temperature. This means that in order to obtain a dual phase ferrite-martensite microstructure at room temperature, the steel must be rapidly

cooled from some temperature within the intercritical region. However, small alloy additions retard transformation behaviour and dual phase microstructures may be developed during air cooling.

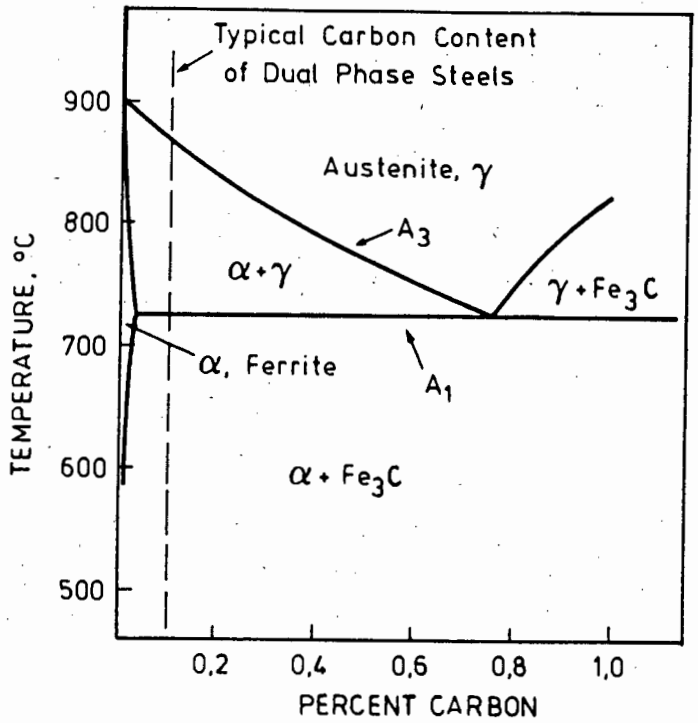

FIGURE 2.2 : Schematic Fe-C phase diagram for dual phase steels (after Ref 5).

The addition of larger amounts of alloying elements modifies the Fe-C phase diagram considerably. To illustrate this, the effect of carbon on the constitution of Fe-Cr-C alloys containing 12 wt % Cr[10] is shown in fig 2.3(a). Typically, alloys of this nature containing between 0.1 and 0.2 wt % C can undergo similar transformations to that illustrated for the dual phase steels in fig 2.2. That is, they are fully austenitic for a wide range in temperature above approximately 900°C, and transform to form a ferrite plus carbide structure below 800°C. An intercritical austenite plus ferrite region occurs between 800°C and appproximately 900°C. For Fe-Cr-C alloys containing much less than 0.1 wt % C, however, fully austenitic microstructures are not obtained at intermediate temperatures due to the incomplete decomposition of the high temperature δ-ferrite phase. A similar situation arises when considering Fe-Cr-C(0.1 wt %) alloys containing between 12 and 17 wt % Cr (fig 2.3(b)). Decomposition of the high temperature δ-ferrite is by no means complete and a duplex ferrite plus austenite structure can occur over a wide temperature range. For example, a duplex structure exists between approximately 850°C and 1200°C for an alloy containing 15 wt % Cr.

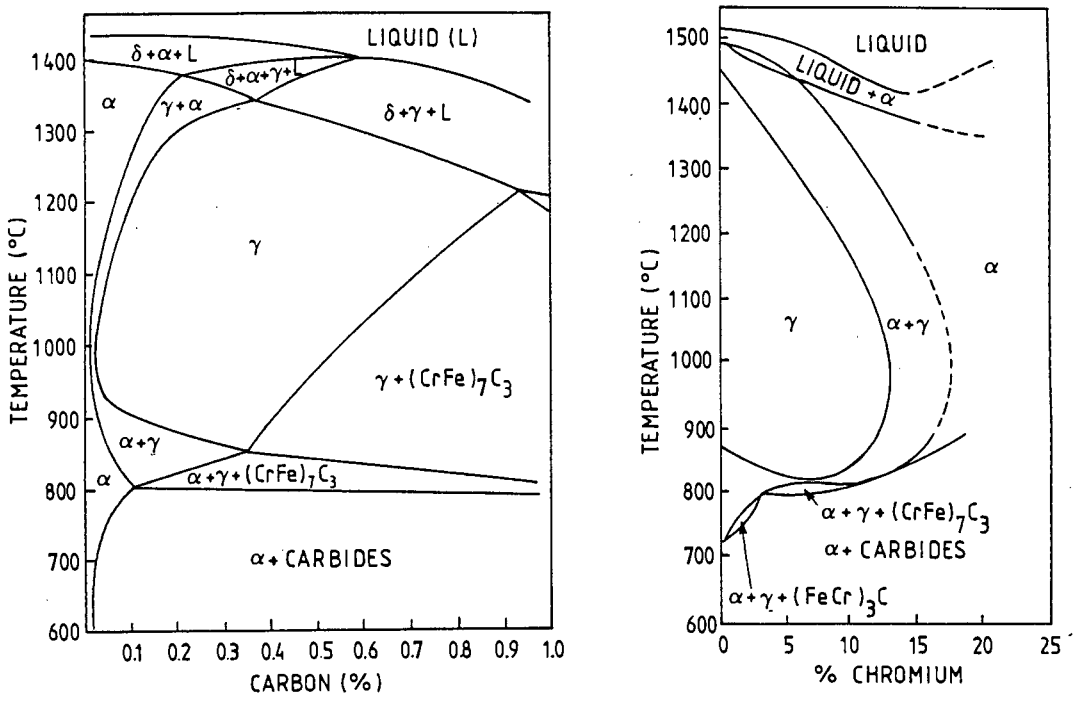

(a) (b)

FIGURE 2.3 : Equilibria of Fe-Cr-C alloys (after Ref 10).

(a) Effect of C on the constitution of Fe-Cr-C alloys containing 12% Cr.

(b) Effect of Cr on the constitution of Fe-Cr-C alloys containing 0.1% C.

From the preceding discussion it is obvious that duplex microstructures can evolve in various ways. In the simple case of dual phase steels, ferrite plus martensite structures are obtained by cooling from the intercritical region defined by the A_1 and A_3 temperatures. For more highly alloyed steels, and in this case steels containing greater than 10-12 wt % Cr, the origin of the duplex structure may not at first seem quite as clear. As indicated, 12 wt % Cr steels containing between 0.1 and 0.2 wt % C may derive ferrite-martensite structures in the same way as conventional dual phase steels, although the kinetics of transformation will be much slower due to the higher alloy content. However, in situations where the decomposition of δ-ferrite is incomplete (ie a fully austenitic microstructure is not obtained), the ferrite content in the duplex structure may be represented by a mixture of α-ferrite and residual δ-ferrite (NOTE: The terms α and δ are applied in order to distinguish between the α-ferrite which is formed by solid state transformation from austenite during cooling, and the high temperature δ-ferrite that is formed during solidification). In general, for steels containing Fe, Cr, and C, as well as other alloying elements, a more accurate assessment of the occurrence of phase transformation requires detailed examination of the Fe-Cr-Ni ternary system, and of the contribution made by additional alloying elements. The following section examines phase equilibria in the Fe-Cr-Ni system and discusses the use of "equivalents" to include alloying elements other than chromium and nickel in order to predict transformation behaviour.

2.3 CONSTITUTION OF STAINLESS STEELS

The elements chromium (Cr) and nickel (Ni) form major alloying additions to the steels investigated in this thesis. An understanding of the phase equilibria in the Fe-Cr-Ni ternary system is therefore an important factor in predicting the transformation behaviour of these steels. The development of stainless steels over the years has resulted in the constitution of the Fe-Cr-Ni ternary system being one of the most thoroughly investigated among iron ternary systems, and a critical evaluation of original literature by Rivlin and Raynor[17] forms an excellent summary. Liquidus and solidus projections, as well as isothermal sections for solid-phase equilibria from 1300°C down to 550°C, are taken from their review and presented in this section. Owing to the fact that the steels investigated in this thesis contain less than 20 wt % Cr and less than 5 wt % Ni, the ternary diagrams have been redrawn so as to include only the Fe-rich corner (extending up to 50 wt % Cr and 50 wt % Ni). The 1400°C isothermal section, assessed by Speich[18] from literature data, is also presented in the same format. More recently, a thermodynamic analysis and calculation of the Fe-Cr-Ni phase diagram has been presented by Chuang and Chang[19] and their calculations show good agreement with previous experimental data over a wide range of temperature. However, a few discrepancies do occur, and where applicable, are noted in this section.

2.3.1 CRYSTAL STRUCTURE OF IRON, CHROMIUM AND NICKEL

IRON

Three allotropes exist below the melting point of iron (1536°C). These are delta-iron (δ-Fe), gamma-iron (γ-Fe) and alpha-iron (α-Fe) and are summarised in Table 2.1. The allotropic behaviour of iron leads to the phase equilibria of binary and higher systems of iron being dependent on whether the added elements are more soluble in body-centered cubic (BCC) or in face-centered cubic (FCC) iron. In view of these crystal structure dependencies, solid solutions in the FCC phase are designated γ, whereas solid solutions in the BCC iron phase are termed α. The term δ is used when it is necessary to emphasize that the BCC solid solution originated during solidification.

TABLE 2.1 : Allotropes of iron (Fe)

TEMPERATURE RANGE	SYMBOL	CRYSTAL STRUCTURE
1536°C - 1392°C	δ-Fe	BCC
1392°C - 911°C	γ-Fe	FCC
911°C and below	α-Fe	BCC

CHROMIUM

Cr has a BCC crystal structure below its melting point. There is a degree of uncertainty as to the exact melting point and a figure of approximately 1900°C is generally accepted. Solid solutions in Cr are denoted α′. When the BCC solid solutions in Fe and Cr are continuous, as is the case over 1000°C, the symbol α is used.

NICKEL

The element is FCC below its melting point (1453°C). Solid solutions in Ni are given the symbol γ and are continuous with solid solutions in FCC iron.

2.3.2 PHASE EQUILIBRIA IN Fe-Cr AND Fe-Ni SYSTEMS

Fe-Cr

Chromium and BCC iron dissolve in all proportions from Cr to Fe. The α and δ allotropes of Fe unite at over 12 wt % Cr to form a continuous BCC solid solution, αδ-Fe, stable at all temperatures up to the solidus. Since Cr is a stabiliser for αδ-Fe but not for γ-Fe, the range of the γ-phase is restricted. The Fe-Cr binary system in fig 2.4 indicates a fall in the γ-Fe→α-Fe transformation temperature as Cr is added to Fe. This boundary passes through a minimum before rising to join the δ-Fe→γ-Fe boundary and thus closes the loop. The equilibria at low temperatures (below 800°C) are governed by the σ-phase. The σ-phase is known to form congruently from α at 820°C and 48 wt % Cr. At lower temperatures a eutectoidal decomposition to α and α′ takes place. The

sluggishness of all reactions involving the σ-phase has made its bounding temperatures and compositions a matter of some dispute[17].

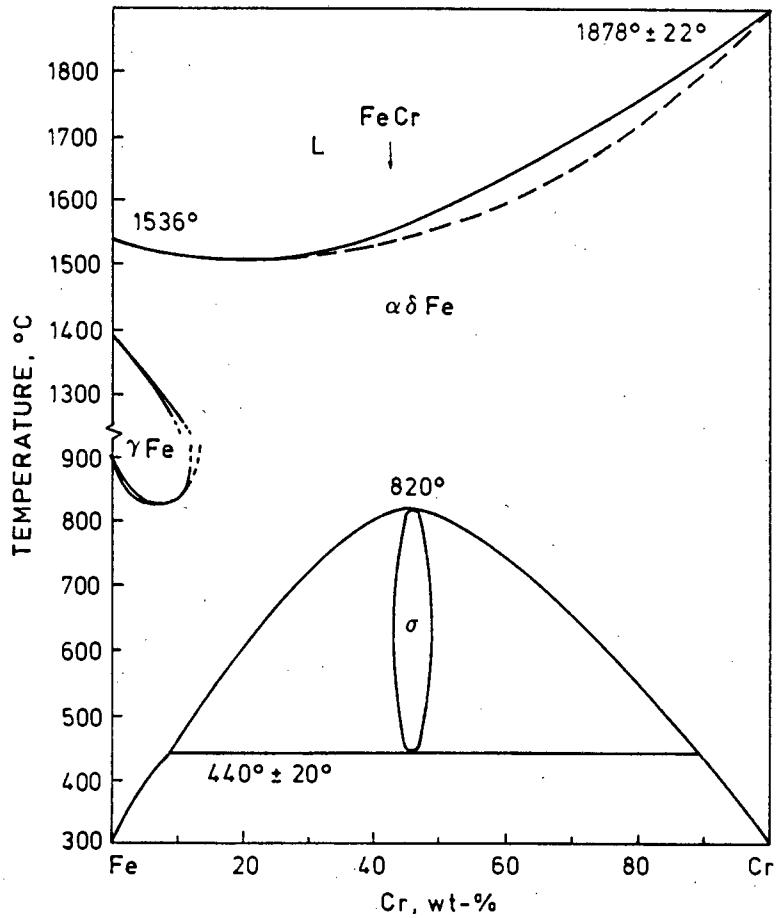

FIGURE 2.4 : Fe-Cr binary system (After Ref 17).

Fe-Ni

Ni dissolves preferentially in FCC iron (γ-Fe) so that the FCC phase accounts for most of the diagram below the solidus (fig 2.5). Solubility in the BCC allotropes of iron (α and δ) is very restricted and is limited to amounts of less than 5 wt % Ni. The γ-phase decomposes eutectoidally at 345 °C and 53 wt % Ni to α and γ'($FeNi_3$). The latter phase (ordered FCC) seems to have a wide range of stability, but below 503 °C it transforms congruently to the γ-phase.

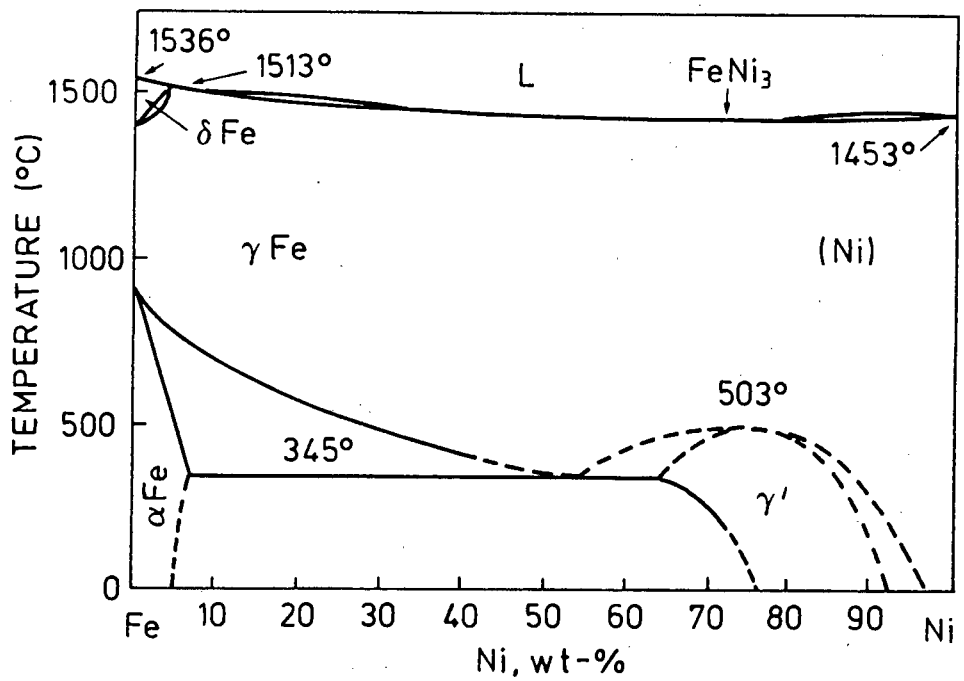

FIGURE 2.5 : Fe-Ni binary system (After Ref 17).

2.3.3 PHASE EQUILIBRIA IN THE Fe-Cr-Ni SYSTEM

As mentioned previously, only the Fe-rich corner is of interest in this investigation and therefore the following discussion of the ternary system will be limited to the composition range defined by the Fe corner, 50 wt % Ni, and 50 wt % Cr.

LIQUIDUS AND SOLIDUS (Figs 2.6(a) and (b))

A univariant line is drawn from the Fe-Ni peritectic, which occurs at approximately 6 wt % Ni ($L+\delta=\gamma$), towards the Cr-Ni eutectic ($L=\alpha'+\gamma$). As the composition moves away from the Fe corner, there is a much steeper rise in the liquidus on the Cr-Fe side of the univariant line. The slope of the liquidus towards the Fe-Ni edge is much more gradual. Solidification reactions form δ and γ.

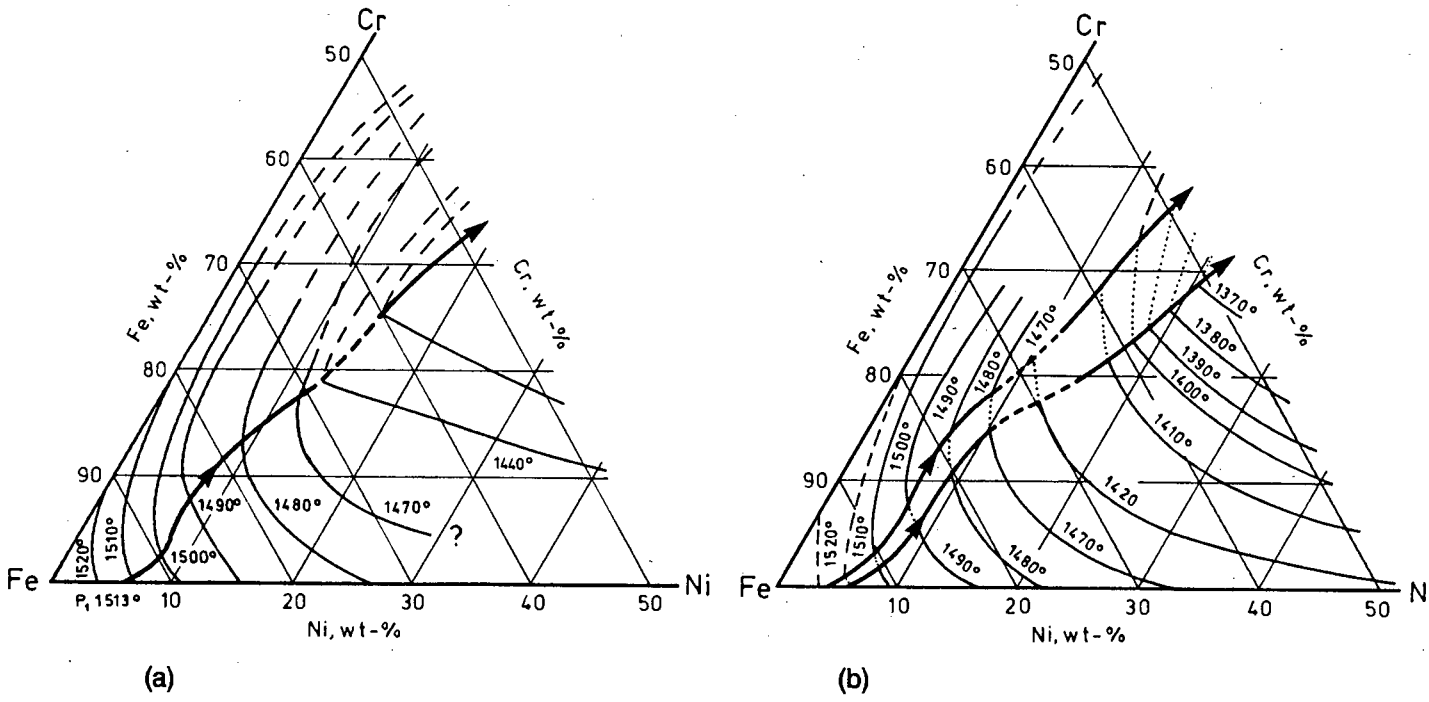

FIGURE 2.6 : Liquidus and solidus projections of part of the Fe-Cr-Ni system (After Ref 17).

(a) Liquidus projection.

(b) Solidus projection.

ISOTHERMAL SOLID SECTIONS FROM 1400°C TO 1000°C (Fig 2.7(a) to (e))

The isothermal sections in figs 2.7(a) to (e) indicate the presence of α-, γ- and $(\alpha+\gamma)$-phase fields. The extent of the γ-phase field increases along the Cr-Fe edge towards higher Cr contents as the temperature is reduced from 1400°C to 1000°C. Similarly, a widening of the $(\alpha+\gamma)$-phase field occurs as the temperature decreases.

ISOTHERMAL SOLID SECTIONS FROM 900°C TO 550°C (Figs 2.8(a) to (d))

The isothermal solid sections for 900°C and below show a decrease in the size of the γ-phase field as the temperature is reduced. The diminishing γ-phase field gives way to a widening of the $(\alpha+\gamma)$-phase field. The single phase α-field drops to lower Cr values on the Cr-Fe edge, but is restricted to Ni contents of less than 5 wt %. In addition, the isothermal section for 900°C indicates the appearance of σ-phase.

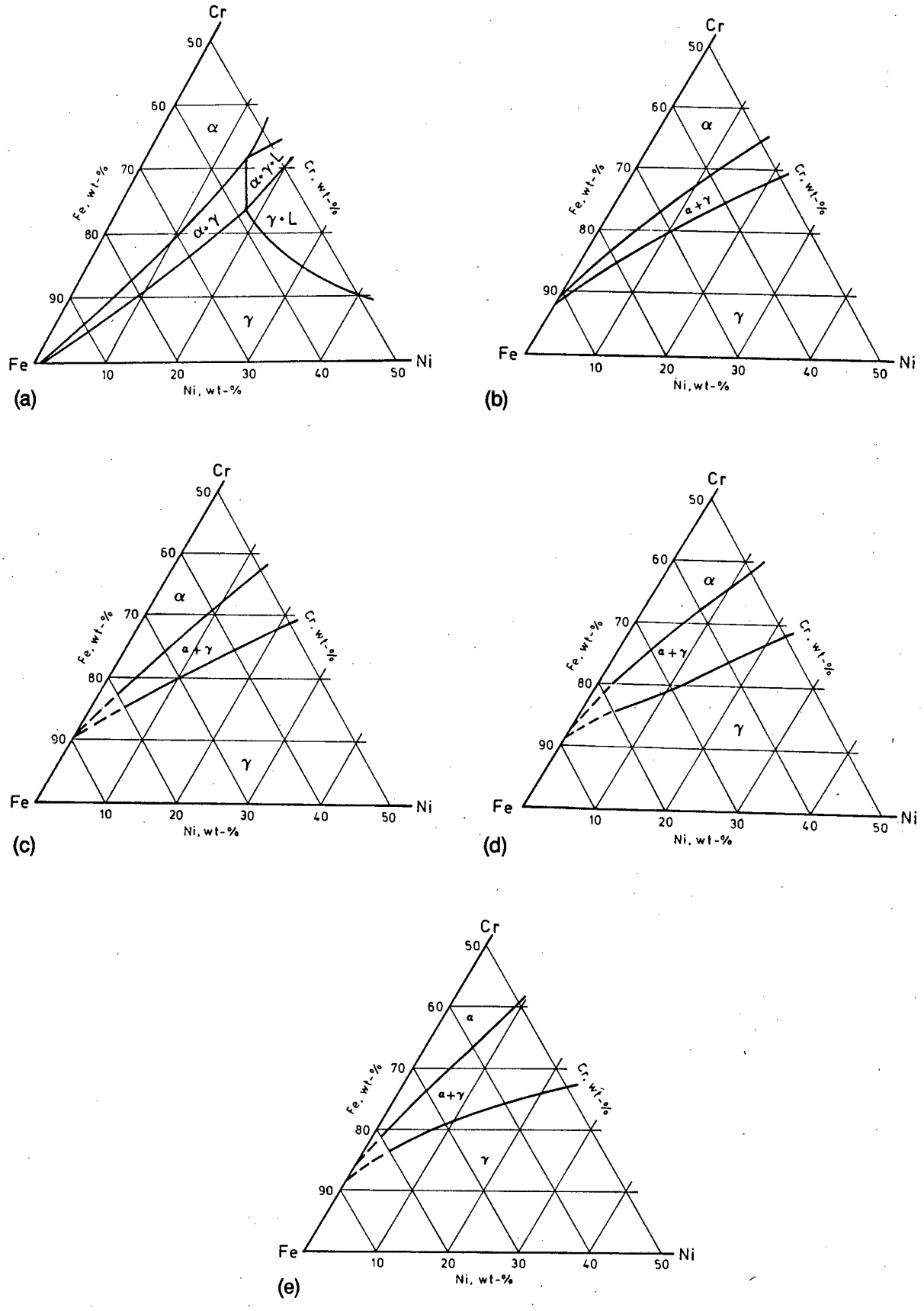

FIGURE 2.7 : Isothermal solid sections from 1400°C to 1000°C (After Ref 17).
(a) 1400°C; (b) 1300°C; (c) 1200°C; (d) 1100°C; (e) 1000°C.

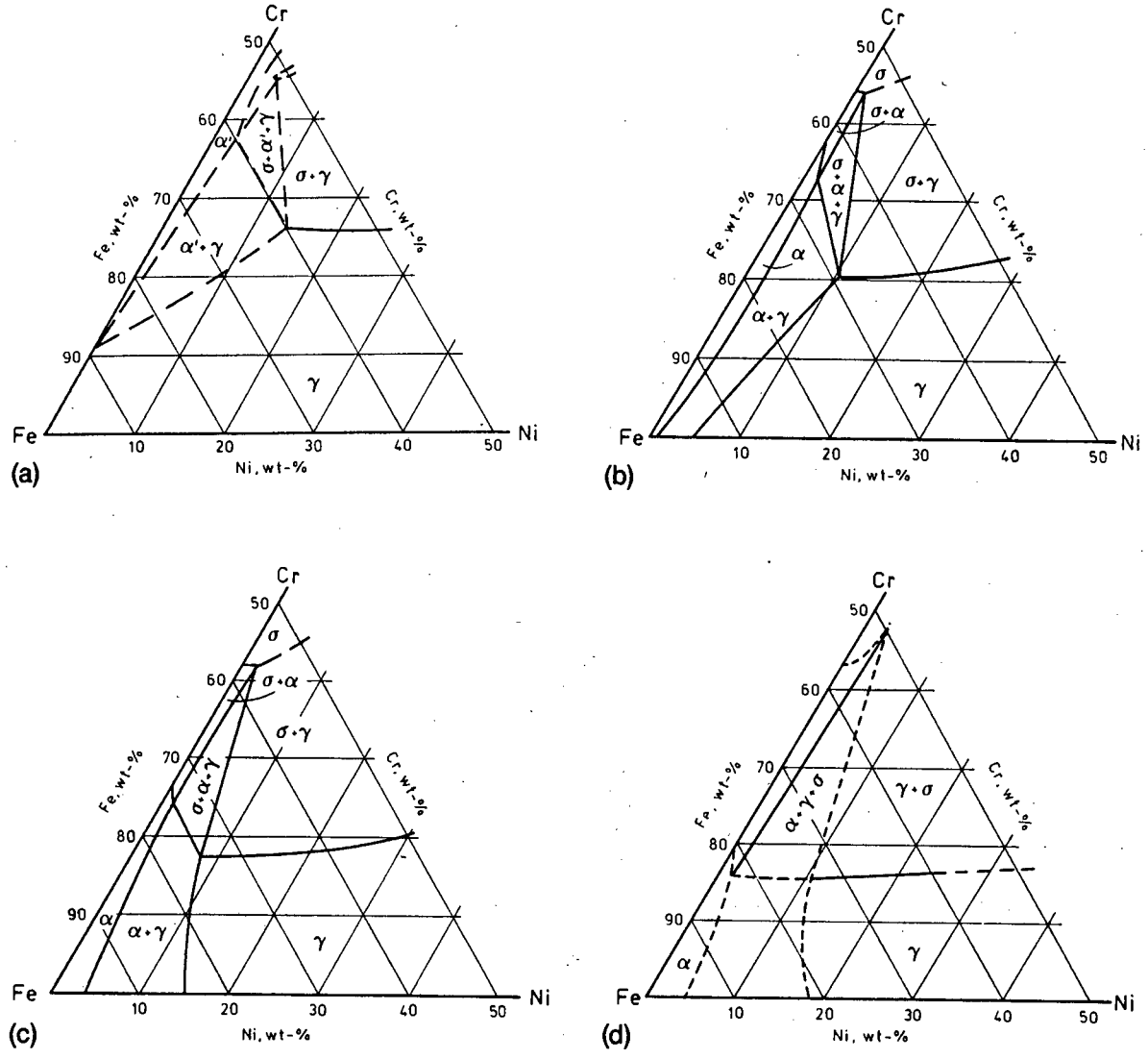

FIGURE 2.8 : Isothermal solid sections from 900°C to 550°C (After Ref 17).
(a) 900°C; (b) 800°C; (c) 650°C; (d) 550°C

Since no single publication has claimed a definitive phase diagram for the Fe-Cr-Ni system in the solid state, the isothermal solid sections in figs 2.7 and 2.8 have been derived from the experimental work of many researchers. In their review, Rivlin and Raynor[17] have often compared individual phase boundaries from a number of sources and they have selected those boundaries which indicate the most reliable approximation to equilibrium conditions. The isothermal sections calculated by Chuang and Chang[19] show reasonable agreement with the experimental data reviewed by Rivlin and Raynor[17]. However, discrepancies are noted to occur between the calculated 1400°C isotherm and the experimental data assessed by Speich[18]. As shown in fig 2.9, the calculated ($\alpha+\gamma$)-phase boundaries are slightly offset from those assessed by Speich[18].

In view of the good correlation between the calculated and experimental thermodynamic values of the various phases for the isotherms from 1300°C down to 550°C, it has been suggested by Chuang and Chang[19] that the calculated diagram at 1400°C is preferable over that given by Speich[18].

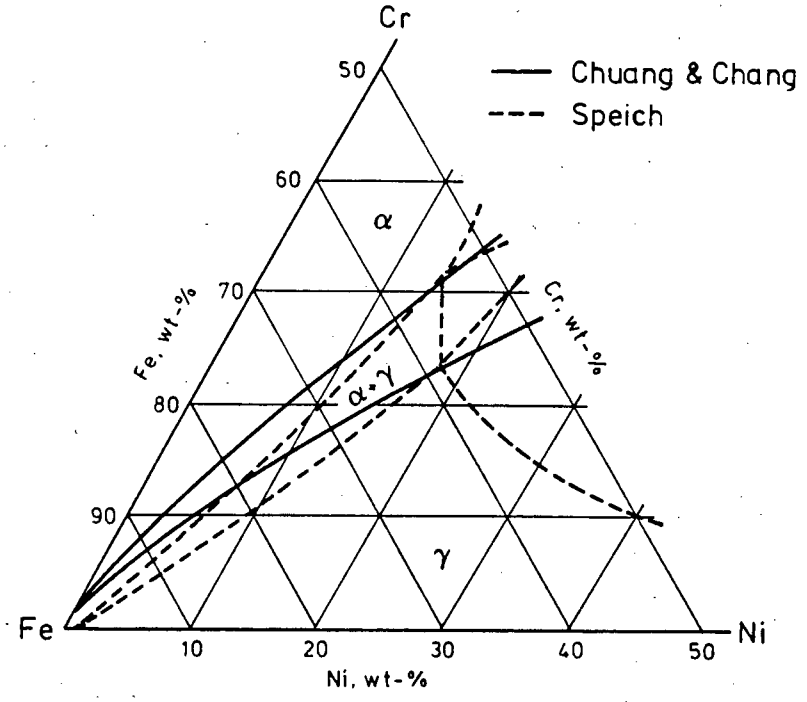

FIGURE 2.9 : Comparison of the 1400°C isothermal sections suggested by Speich[18] and Chuang and Chang[19].

2.3.4 ROLE OF ADDITIONAL ELEMENTS IN PHASE EQUILIBRIA

The preceding discussion has been concerned with phase equilibria in the ternary Fe-Cr-Ni system, whilst stainless steels as such contain many other elements present as intentional additions or as residuals. These elements have a definite influence on Fe-Cr-Ni phase equilibria and can generally be divided into two groups, namely ferrite-formers and austenite-formers. Besides chromium, an additional ferrite-forming influence is contributed by elements such as titanium (Ti), molybdenum (Mo), silicon (Si), vanadium (V), aluminium (Al), niobium (Nb), and tungsten (W). Elements contributing towards the formation of austenite are nickel, cobalt (Co), manganese (Mn), copper (Cu) and carbon (C) and nitrogen (N). The presence of these elements will affect the size and position of the α-phase and γ-phase fields in the Fe-Cr-Ni ternary phase diagram. Consequently, a direct plot of the Fe, Cr and Ni contents of a stainless steel onto an Fe-Cr-Ni ternary phase diagram would probably result in the incorrect determination of the equilibrium phase constitution of the steel. This has led to the calculation of a series of

nickel and chromium "equivalents" based on the relative ferrite- and austenite-forming tendencies of the additional alloying elements. The origin and application of a number of equivalent formulae are reviewed in the subsequent paragraphs.

Nickel and chromium equivalent expressions have mainly originated from the derivation of formulae for the prediction of phase constitution in fairly limited composition ranges, and usually under specific thermal conditions. For example, a number of equations have been formulated specifically for the determination of ferrite content in austenitic stainless steel welds and parent metal[20-22]. Schaeffler[20] combined information from the Maurer diagram (used to predict the microstructure of wrought quench-annealed Cr-Ni steels) and formulae devised by Newell and Fleischman[23] and Field et al[24] to develop a microstructure diagram from which the structure of the weld metal could be predicted. This led to the formulation of the following Ni and Cr equivalent expressions in order to take into account the "potency factors" of various minor elements :-

Cr equivalent = %Cr + 2.5(%Si) + 1.8(%Mo) + 2(%Nb)

Ni equivalent = %Ni + 0.5(%Mn) + 30(%C)

These expressions were later revised with the intention of improving their accuracy. The first to be modified was the Cr equivalent which became[21] :

Cr equivalent = %Cr + %Mo + 1.5(%Si) + 0.5(%Nb)

The Ni equivalent was later modified in order to take into account a factor for nitrogen[22] :

Ni equivalent = %Ni + 0.5(%Mn) + 30(%C + %N)

The use of equivalents was extended to predict the microstructures of cast[25] and wrought[26] austenitic stainless steels. However, potency factors were slightly modified from those originally used by Schaeffler. Pryce and Andrews[26], in particular, devised a number of equivalent equations which were dependent on the exact composition of the steel. For example, the following equivalents were derived for an 18-8 steel :

Cr equivalent = %Cr + 3(%Si)

Ni equivalent = %Ni + 0.5(%Mn) + 21(%C) + 11.5(%N).

On the other hand, an 18-8 titanium stablised steel was treated somewhat differently. In this case, notice was taken of the tendency for Ti to "fix" practically all of the nitrogen and nearly all of the carbon, except for an amount of 0.03 wt.%. In view of this, expressions were determined for soluble titanium (Ti′) and soluble carbon (C′) :

$$Ti' = \%Ti - 4\,[(\%C - 0.03) + \%N]$$

$$C' = 0.03$$

The values for Ti′ and C′ were applied to the Cr and Ni equivalent expressions as follows :-

$$\text{Cr equivalent} = \%Cr + 3(\%Si) + 10(Ti')$$

$$\text{Ni equivalent} = \%Ni + 0.5(\%Mn) + 21(C')$$

Pryce and Andrews[26] used these expressions on a modified Schaeffler diagram in order to estimate the amounts of ferrite in austenitic steels at hot-working temperatures.

More recently, Hull[27] derived equivalents based on the regression analyses of the phase composition of seventy chill cast Cr-Ni stainless steel alloys. These equivalents (listed below), when plotted onto a Schaeffler type diagram, produced similar phase boundaries to those obtained by Schneider[25] and Pryce and Andrews[26].

$$\text{Ni equivalent} = \%Ni + 0.11(\%Mn) - 0.0086(\%Mn)^2 + 0.41(\%Co) + 0.44(\%Cu) + 18.4(\%N) + 24.5(\%C)$$

$$\text{Cr equivalent} = \%Cr + 1.21(\%Mo) + 0.48(\%Si) + 2.27(\%V) + 0.72(\%W) + 2.2(\%Ti) + 0.14(\%Nb) + 0.21(\%Ta) + 2.48(\%Al)$$

The usefulness of the various equivalent expressions has been summarised by a study of thirty different austenitic stainless steel welds alloyed with manganese and/or nitrogen[28]. It was found that the ferrite content in normal and nitrogen-alloyed welds could be predicted fairly well from a conventional Schaeffler-DeJong[22] diagram. However, at higher manganese contents of 5 to 8 wt %, the equivalents formulated by Hull[27] were found to give the most satisfactory correlation between the composition and ferrite content.

The preceding discussion illustrates the fact that there are no universal expressions for chromium and nickel equivalents. The majority of expressions relate to the composition of weld metals, which in view of their very rapid cooling rates, do not represent equilibrium structures. Nevertheless, this does not diminish the usefulness of equivalents in approximating the phase constitution of Cr-Ni steels. The following more general equivalents have been formulated which take into account many of the factors determined by previous investigations.

Ni equivalent = **%Ni + %Co + 0.5(%Mn) + 0.3(%Cu) + 30(%C) + 25(%N)**

Cr equivalent = **%Cr + 2(%Si) + 1.5(%Mo) + 5(%V) + 5.5(%Al) + 1.75(%Nb) + 1.5(%Ti) +0.75(%W).**

These equivalent expressions have been widely used (29-33) to determine the transformation behaviour of stainless steels with respect to phase equilibria in the Fe-Cr-Ni ternary system, and are used to calculate the nickel and chromium equivalents for the alloys investigated in this thesis.

2.4 THE HIGH TEMPERATURE (δ) FERRITE DECOMPOSITION REACTION

Unlike the situation for low-carbon low alloy steels where the steel becomes fully austenitic at around 1400-1450°C during cooling, in the case of stainless steels the decomposition of δ-ferrite can be retarded to much lower temperatures. The temperature interval over which the transformation occurs in the latter case is also much greater (eg. 100-200°C) and the mechanism of transformation, especially when the decomposition of δ-ferrite is incomplete, is likely to have important effects on the nature of the evolved microstructure.

Firstly, in considering the nature of the solid state δ-ferrite to austenite ($\delta \rightarrow \gamma$) transformation, the solidification mode of the steel must be taken into account. Depending on the chemistry of the stainless steel, solidification may occur either as primary austenite or primary δ-ferrite, followed by later solidification of the second phase, as illustrated schematically in fig 2.10 (compositions A and B respectively)[34]. In fact it has been shown in the case of an 18-8 stainless steel that three stages of solidification occur, namely primary δ-ferrite followed by austenite, and finally a transition back to δ-ferrite solidification[35]. Under these conditions, any solid state decomposition of the δ-ferrite will be affected by the austenite already present due to solidification. Nevertheless, primary δ-ferrite alloys remote from the eutectic triangle (fig 2.10, composition C) solidify with almost 100 vol % δ-ferrite and the resultant room temperature microstructure is completely determined by the

solid state transformation[34]. The latter is more likely to be the situation when considering the modification of fully ferritic steels to form duplex ferrite-martensite microstructures.

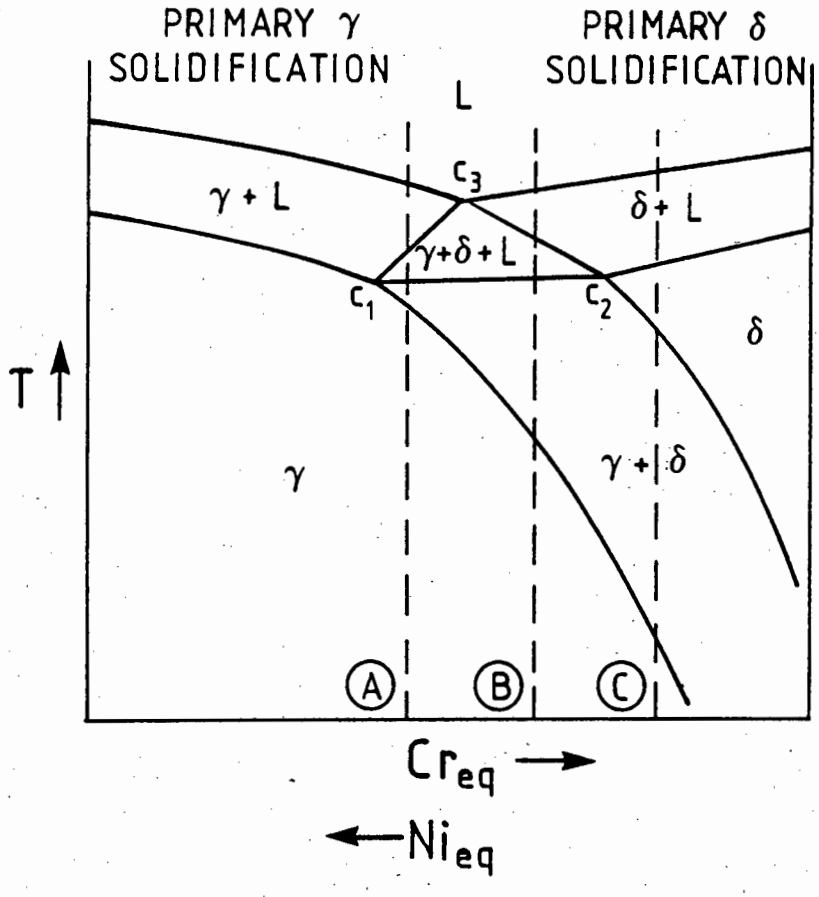

FIGURE 2.10 : Schematic constant Fe pseudobinary phase diagram. Note the use of Ni and Cr equivalents (after Ref 34).

The solid state $\delta \rightarrow \gamma$ decomposition reaction has often been referred to in connection with austenitic weld metal studies, but in many instances the exact nature of the transformation has been confused by the non-equilibrium rapid solidification of the weld metal. For example, Lyman[36] and Lippold and Savage[37] have suggested the occurrence of a massive solid state $\delta \rightarrow \gamma$ transformation giving rise to austenite of the same composition as the parent ferrite. This suggestion, however, has been disputed by Suutala et al[38] who have shown that even during the rapid cooling of welds, the solid state $\delta \rightarrow \gamma$ transformation can be interpreted as being diffusion controlled. It has been demonstrated that welds which solidify as primary δ-ferrite undergo a Widmanstätten type $\delta \rightarrow \gamma$ solid state transformation and Cr and Ni partitioning occurs to the respective ferrite and austenite phases[39]. An orientation relationship similar to Kurdjumov-Sachs (K-S) and Nishiyama-Wasserman has been identified between the ferrite and austenite. Various ferrite morphologies are known

to result from the primary ferrite solidification followed by a solid state $\delta \rightarrow \gamma$ transformation, and have been described as skeletal, vermicular, and lathy[40,41]. Each of these morphologies has been noted to have resulted from a diffusion controlled solid state transformation.

Besides welding studies, solid state δ-ferrite decomposition has been examined in a few instances involving the heat treatment of austenitic and duplex ferrite-austenite stainless steels. The high temperature decomposition of δ-ferrite to austenite has been studied in a 26%Cr-5%Ni stainless steel and austenite formation has been shown to exhibit growth kinetics intermediate between volume diffusion control and growth by a ledge mechanism[42]. Throughout the growth and coarsening stage, the austenite and ferrite have been noted to be related by the K-S orientation relationship. Similarly, the solid state decomposition of δ-ferrite in a 20-10 austenitic stainless steel has been followed and the formation of Widmanstätten austenite has been identified[43]. Once again a K-S orientation relationship is identified and Cr and Ni partitioning has been measured. The study of the crystallography of the $\delta \rightarrow \gamma$ transformation in duplex stainless steel castings has led to the proposal of a model for the evolution of the residual δ-ferrite morphology[34]. Based on the occurrence of a K-S relationship between the ferrite and austenite irrespective of the ferrite morphology, a model has been suggested analogous to those proposed for the diffusion controlled formation of Widmanstätten-type proeutectoid α-ferrite. It is proposed that at the start of the transformation, a faceted (low-energy interface) nucleus of γ(austenite) forms and growth is accomplished through the movement of curved incoherent segments of δ/γ interface. The incoherent segment possesses high energy and high mobility compared to the low mobility of the faceted portions of interface. It is further suggested that the movement of the faceted boundaries can occur via movement of interface ledges or steps parallel to the interface. The features of the residual δ-ferrite microstructure can then be viewed as evolving through the rapid movement of incoherent segments of δ/γ interface, with coherent segments being dragged along behind due to their slow movement via a ledge mechanism. A schematic diagram showing the evolution of the residual δ-ferrite morphology is shown in fig 2.11.

Evolution of the residual δ-ferrite/austenite morphology is an important factor in determining the structure of the rolled product in duplex stainless steels. The nature of the δ-ferrite decomposition reaction is critically assessed in this investigation with respect to the development of modified ferrite-martensite stainless steels.

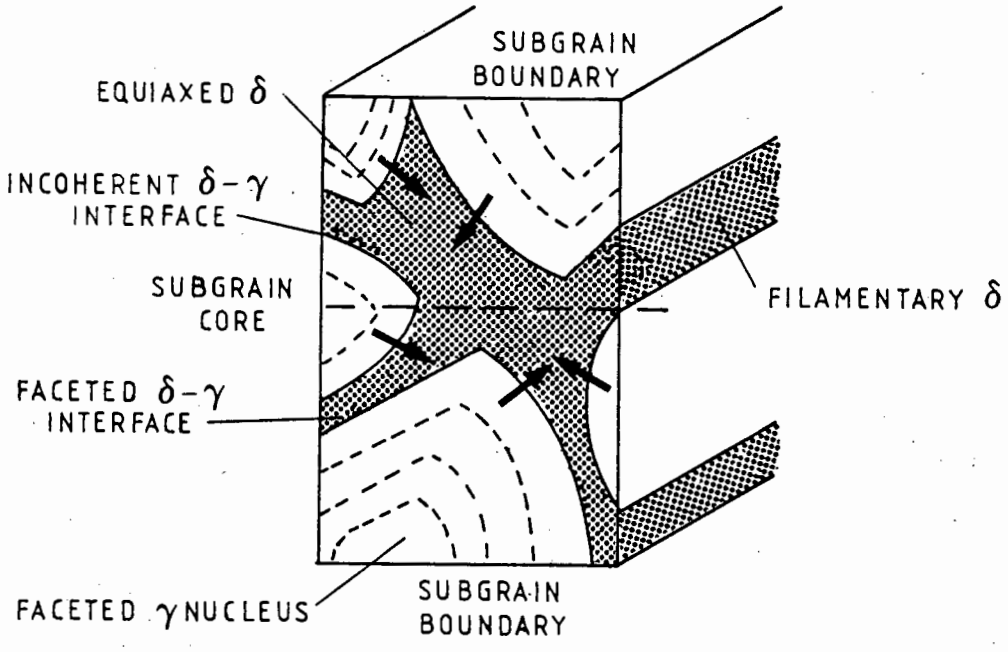

FIGURE 2.11 : Schematic diagram of the evolution of residual δ-ferrite morphology via δ→γ solid state transformation (after Ref 34).

2.5 OCCURRENCE OF NON-METALLIC INCLUSIONS IN STEEL

Non-metallic inclusions in steels can be generally divided into two groups; those of indigenous and those of exogenous origin. This classification, however, is not to be treated as a rigid division, as the origin of inclusions can be due to a combination of several factors[44]. The former group contains inclusions occurring as a result of reactions taking place in the molten or solidifying steel bath, whereas the latter contains those resulting from mechanical incorporation of slags, refractories or other materials with which the molten steel comes in contact. The indigenous inclusions form by precipitation due to homogeneous reactions in the steel and are therefore directly related to the bulk chemical composition of the molten steel. They are composed principally of oxides and sulphides and the reactions that form them may be induced either by additions to the steel, or simply by changes in solubility during cooling and freezing of the steel.

Sulphide inclusions are common in nearly all commercial steels but their specific chemical composition and distribution will in each case depend on the overall chemistry of the steel. Although sulphur levels are usually low, the insolubility of sulphur in the solid δ-ferrite phase results in fairly high concentrations of sulphur in the interdendritic liquid during solidification[45]. Consequently, sulphur reaction with an available metal source leads to

metal sulphide formation in these interdendritic regions. Precipitation commences in the remaining liquid when the solubility product for the metal-sulphur couple is exceeded. As mentioned, the sulphide composition is related to the overall steel chemistry, and in particular the relative affinities of the various metals available for sulphide formation. Kiessling and Lange[44] have suggested that the tendency for sulphide formation of the pure metals increases in the approximate sequence Ni→Fe, Cu→Mn, Ti→Al→Mg, Na, K→Ca. Nevertheless, the relative stability of different sulphides will depend on the component concentrations in the interdendritic liquid. In considering the two metal elements Ti and Mn, the lower standard free energy of formation for titanium sulphide reported at room temperature is only very marginal[44,46]. Although comprehensive data is not available on the free energies of formation of TiS over a wider temperature range, indications are that TiS forms in preference to MnS at steelmaking temperatures if sufficient titanium is available[47-49]. Figure 2.12 illustrates the variation in sulphide inclusion composition as a function of titanium and manganese levels in an 18Cr-2.3Mo-0.2S ferritic stainless steel. This series of curves indicates that above certain levels of titanium, TiS dominates in the steel even though the manganese content is fairly high. At lower levels of titanium addition, it is reported that complex manganese sulphides containing titanium form and as such have been labelled (Mn, Ti)S[48,50].

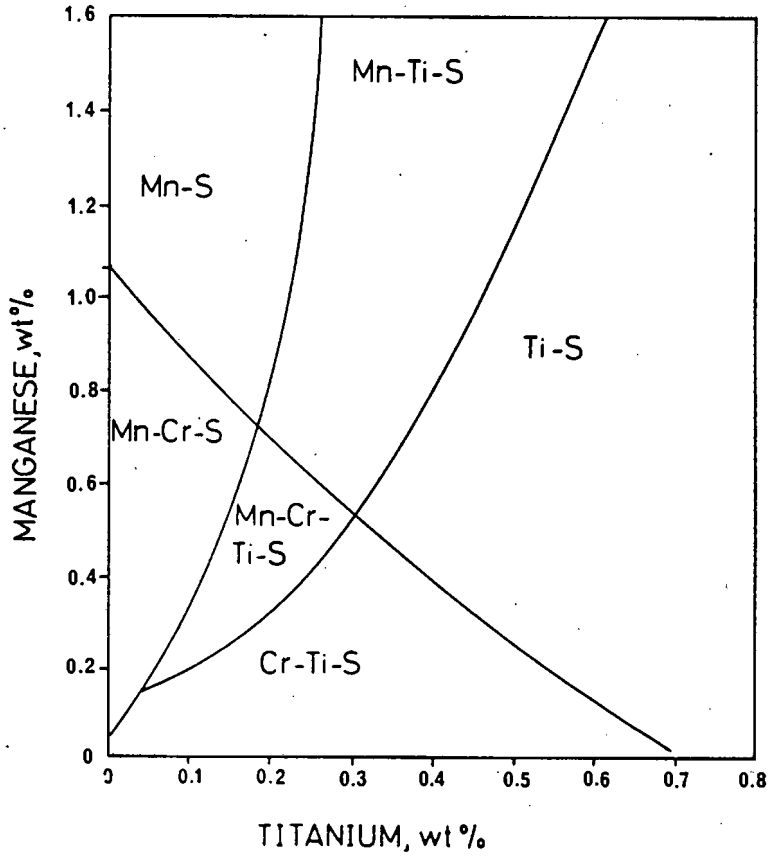

FIGURE 2.12 : Influence of Mn and Ti levels on the sulphide composition of an 18Cr-2.3Mo-0.2S ferritic stainless steel (after Ref 47).

The precipitation patterns of sulphide inclusions and their plastic behaviour is important in determining the final morphology of these inclusions in the wrought product. MnS inclusions, for instance, have been classified into three types according to their morphology in the ingot[51]. The various types are reported to originate due to specific reactions in the liquid steel and consequently lead to a range in morphologies exhibited in the wrought product. In particular, type II sulphides occur as chain-like intergranular sulphides in the ingot and, due to the high relative plasticity of MnS compared to the steel matrix[52], result in the formation of elongated stringers in the rolled steel. On account of the elongated morphology being detrimental to the transverse and through-thickness properties of the steels, investigations have been made to modify the shape of these sulphide inclusions[48,50,53]. Titanium, for example, forms sulphide inclusions which are much harder than MnS and so are not as easily deformed. As a result, these inclusions occur in a more or less globular form in the wrought steel and do not seriously impair the isotropy of the steel. Similarly, calcium and some rare earth elements are reported to function in the same way and lead to improved mechanical properties.

Carbide and nitride inclusions are also common in steels and often occur as combined carbonitride inclusions. Titanium is reported to combine with nitrogen in the melt prior to steel solidification[54] and is known to occur as well defined yellow cuboids[55] which do not dissolve, at least at temperatures up to 1250°C[54]. The very low solubility products for TiN in liquid steel determined by Wada and Pehlke support the idea of TiN precipitation in the melt[56]. TiC is more soluble in steel than TiN and an interpretation of the solubility of TiC in a type 321 austenitic stainless steel indicates that the TiC dissolves above 1100°C in a steel of this type containing 0.03 wt % C[55]. Comparison of the TiC solubility equation presented by Harries[54] and the solubility products determined for TiN[56] suggests that the solubility of TiC is greater than the solubility of TiN in steels by a factor of approximately 3.

TiC and TiN are structurally identical; both are face-centred cubic with the carbon or nitrogen occupying octahedral positions in the lattice[55]. Nitrogen can replace carbon in the carbide and vice versa, and the constituent is often referred to as titanium carbonitride, Ti(CN). With the addition of carbon to TiN, a maize colour develops. As the carbon content increases, the colour of the inclusion changes progressively from yellow to grey, the latter being the colour of TiC.

Carbon can also be incorporated into titanium sulphide compounds to form titanium carbosulphides. Although there has been some controversy as to the identification of this compound, the formula $Ti_4C_2S_2$ seems more acceptable. It would appear that on occasion this compound has been identified as Ti_2S[57], but in fact it has been suggested that Ti_2S

does not exist and the correct composition is $Ti_4C_2S_2$[58]. Titanium carbosulphide compounds are reported to be often associated with TiN, TiC, and Ti(CN) particles [50,55].

The occurrence of non-metallic inclusions is known to seriously affect the mechanical properties of alloys, and a brief account of the role played by inclusions in initiating and propagating fracture is given in the following section. In addition, the wide range in morphological and chemical behaviour of various inclusions can affect the corrosion properties of alloys in a number of ways. These corrosion aspects are considered in Appendix B.

2.6 FACTORS AFFECTING THE IMPACT STRENGTH OF WROUGHT STEELS

Factors contributing to the strength of wrought steels are numerous and can include grain size, grain shape, phase composition, texture, precipitate distributions, non-metallic inclusion content, and porosity. This implies that more often than not strength cannot be related to a single criterion. Some of these criteria are discussed below in the context of the experimentation carried out in this work.

2.6.1 EFFECT OF NON-METALLIC INCLUSIONS

Non-metallic inclusions, by virtue of their very nature, represent discontinuities within the steel matrix and are the most effective areas for crack intiation in alloys [59,60]. When a metal undergoing deformation flows past an undeformable inclusion, dislocations pile up near the inclusion-metal interface. The tensile stresses associated with these dislocation pile-ups could lead to either shearing of the inclusion or creation of a void at the interface. Such voids form more readily at those inclusions which adhere most weakly to the matrix; for instance, voids form more easily at copper oxide inclusions in copper than at aluminium oxide inclusions in aluminium, for the adhesion between copper and copper oxide is much weaker than that between aluminium and aluminium oxide.

Although most non-metallic inclusions are detrimental to the fracture properties of steels, it has been shown that the critical strain for fracture initiation at the inclusion-matrix interface is strongly affected by shape, size, orientation and rigidity of the inclusion[60]. The shape and orientation of inclusions in wrought steels is largely dependent on their deformability under hot working conditions. The alignment of inclusions during rolling develops a considerable anisotropy in fracture properties.

Manganese sulphide inclusions become soft at hot rolling temperatures and consequently smear out on the rolling plane and in the rolling direction. This results in an increase in the size of the barrier to dislocation flow, as well as an increase in the matrix/inclusion interfacial area. It is therefore not surprising that of the non-metallic inclusion types manganese sulphide inclusions are considered to have by far the most deleterious effect on the fracture properties of steels[61]. Spitzig and Sober[62] have shown a marked decrease in shelf energy with increasing sulphur content in hot-rolled carbon steels. This result has been attributed to an increase in the elongated manganese sulphide population with increase in sulphur levels. Elongated inclusions were also found to have a far more deleterious effect on the shelf energy than globular inclusions. In a comparison study of the fracture toughness of AISI 4340 steel and 18 Ni-200 maraging steel, both steels having similar strengths, the effect of inclusion size and shape on void formation was determined[63]. Both the AISI 4340 steel, which contained predominantly MnS inclusions, and the maraging steel, which contained predominantly Ti(CN) inclusions, showed similar modes of fracture associated with void formation, void growth and void coalescence. Nonetheless, it was observed that void nucleation occurred at lower strains at the larger MnS inclusions and that void growth occurred more rapidly from the large inclusions, thus reducing the resistance of the alloy to fracture. This observation has been used to explain the lower fracture toughness of the AISI 4340 steel compared to the maraging steel.

2.6.2 DELAMINATION BEHAVIOUR

The delamination or "splitting" mode of fracture, which occurs in certain wrought alloys when fractured under conditions of high triaxiality, may or may not be attributed to the occurrence of non-metallic inclusions in the metal matrix. Delaminations are noted to occur as a result of material splitting in the rolling plane. Splits are produced perpendicular to the main fracture surface and occur typically during longitudinal and transverse Charpy impact tests (notched in through thickness direction) and tensile tests. A prerequisite for the occurrence of splitting would be the potential for developing a substantial triaxial stress during loading, ie the specimen geometry and loading arrangement must be such that triaxial stresses can be generated. Numerous investigations have been carried out in order to determine the mechanism/s responsible for splitting, and contributing factors have been listed, either individually or collectively, as :

(i) Grain morphology.

(ii) Presence of precipitates and impurity inclusions leading to weak planar interfaces.

(iii) Cleavage texture.

(iv) Texture banding leading to crystal-plasticity anisotropy.

A case history relating to these various proposed mechanisms for the occurrence of delaminations is outlined in the subsequent paragraphs.

GRAIN MORPHOLOGY

Although there appears to be no common influence on the occurrence of splitting, the production of elongated grains in wrought products is a very likely contributing factor. Bramfitt and Marder[64] have observed the splitting phenomenon in high purity Fe-1% Mn alloys during impact testing and have suggested that delamination is entirely due to decohesion of grain boundaries. They have considered the delamination process to be independent of the texture of the material. Splitting was found to persist until the material completely recrystallised, thereby confirming the importance of aspect ratio and the role played by grain boundaries in the splitting phenomenon. Similarly, Baldi and Buzzichelli[65] found in a study dealing with four classes of HSLA steels that the dimensional anisotropy of the grain structure has the major influence on delamination fracture. They considered the presence of flattened manganese sulphide inclusions and of a crystallographic {100} texture component not to be essential for the formation of delaminations, although it was acknowledged that they can play an important role. The occurrence of delamination in a 13% Cr ferritic stainless has been attributed to the presence of long, straight boundaries between ferrite and martensite bands that occur parallel to the rolling direction[66]. Splitting was seen to persist even after tempering and decreased only slightly after normalising. The persistent occurrence of delamination after normalising has been ascribed to the fact that the grain boundaries remained mostly parallel after heat treatment, with the appearance of only very slight undulations. It has been suggested in this case that the easier it is for the boundary to decohese, the more likely it is that delamination will occur. Thus, greater grain elongation, thinner grains, and straight boundaries will all assist in enabling the boundary to decohese for a sufficiently long length to allow a crack to propagate in a brittle manner.

INCLUSIONS

The importance of the influence of sulphur on the formation of splits is expressed by Morrison[67]. Appreciable levels of sulphur give rise to an abundant occurrence of manganese sulphide inclusions, which due to their elongated nature after rolling, cause inclusion/matrix decohesion in the rolling plane. Splitting associated largely with these inclusions gives rise to a fracture surface with a characteristic "woody" appearance. Once again it is acknowledged that grain shape and texture also contribute towards delamination. Impact energies measured for a range of 3CR12 commercial heats have been related to the manganese sulphide population of these steels and it is shown that the impact energy for transverse Charpy impact specimens, where splitting is prominent, generally decreases with increasing manganese sulphide content[4]. Splitting in HSLA steels has also been attributed to the presence of Fe_3C precipitates located on the grain boundaries [68]. However, apart from the Fe_3C precipitates, it is noted that the presence of larger inclusions can act as nucleation sites for void formation. Once the crack is nucleated, splitting continues along the weak planar interfaces defined by the Fe_3C precipitates.

TEXTURE

Delamination in warm-rolled (650°C) low carbon steel during impact testing has been shown to be due to the development of a strong {100} texture[69]. This texture gives rise to the preferential alignment of cleavage planes parallel to the rolling direction and, as a result of the imposed triaxial stress, leads to cleavage in the rolling plane. Thus delamination has been observed to occur by transgranular cleavage and it was found that grain separation was absent. Schofield et al[70] also found the occurrence of cleavage splits in controlled-rolled pipeline steels to be largely related to the {100} texture. However, the existence of coarse-grained regions and non-metallic inclusions was also considered as a contributing influence towards delamination.

CRYSTAL-PLASTICITY

A study of the mechanism of anisotropic lamellar fracture in AISI 430 type ferritic stainless steel sheet has led to the splitting mechanism being attributed to a generalised crystal-plasticity phenomenon that is applicable to any material in which texture-orientation banding occurs[71]. It was observed that groups of grains having a common crystallographic orientation can appear in ribbon-like form in a matrix possessing a

different texture. The occurrence of these ribbon-like "grains" in the ferritic steels has been found to be associated with the segregation of Cr and Mo at hot rolling temperatures in which two phases, austenite and ferrite, are stable[72]. The proposed crystal-plasticity mechanism suggests that the deformation of a cube-on-corner matrix containing cube-on-face "ribbon-like" grains results in the occurrence of banded strain anisotropy. The prone-to-thinning orientations (cube-on-corner) produces high normal shrinkage strains and forces which cause the weak interfaces between banded regions to be prone to lamellar fracture in the rolling plane. It was noted, however, that the proposed mechanism is just one of many failure modes and it does not rule out other modes of lamellar fracture such as severe carbide or inclusion banding.

It is clear from the foregoing review that delamination can occur in various steels for different reasons. However, a necessary requirement is the development of a triaxial stress sufficient to promote delamination in the through-thickness direction. Therefore it is expected that delamination will only occur in a steel that has an inherent ductile behaviour at the test temperature.

The effect of the occurrence of delamination on the engineering properties of an alloy is so far not clearly evident. Firstly it can be argued that triaxiality can be reduced by relaxing the through-thickness stresses (σ_z) brought about by the delamination of interfaces in the rolling plane[73]. When delamination occurs, the effective thickness of the specimen is reduced, since (σ_z) decreases to zero at each delamination. Consequently, the specimen acts like a series of thin-plane stress specimens instead of one thick-plane strain specimen. The ductile-to-brittle transition temperature is noted to decrease with the increasing tendency for plane stress conditions, and therefore the greater the number of delaminations, the greater the decrease in transition temperature. It is noted, however, that the strength of the interface is an important consideration. Firstly, the interface should not be so weak that the specimen slides apart like a deck of playing cards, whilst on the other hand if the interface is too strong, delamination will not occur. Secondly, a model is proposed for the reduction of absorbed energy due to splitting behaviour. Dabkowski et al[74] proposed that when splitting occurs, the area of the main fracture behaves like a cluster of small specimens. Since the width of the plastic zone in front of an advancing shear fracture is proportional to the thickness of the material, the width of the plastic zone in each of the volumes between the splits is smaller than in a homogeneous specimen. Thus the total volume of material plastically deformed is reduced and the level of energy required for fracture consequently decreases

with the onset of splitting. Bramfitt and Marder[64] found that the absorbed energy was inversely proportional to the number of splits by :

$$E = \frac{E_0}{N + 1}$$

where N is the number of delaminations and E_0 is the absorbed energy for an unsplit full size Charpy specimen. It would therefore appear that although the transition temperature is decreased with increasing number of splits, the upper shelf impact energy could be improved by restricting the occurrence of splitting.

A third consideration is the likelihood of the occurrence of lamellar tearing of a structural component when a stress is imposed in the through-thickness direction. Obviously structural components are designed such that stresses are accommodated in directions other than the through-thickness direction of rolled plate. Nevertheless, through-thickness stresses imposed by means other than the principle stress often occur and cannot be ignored. Lamellar tearing is known to occur during welding, but it has been recognised that there is no correlation between tensile specimen splitting and the occurrence of lamellar tearing of welded structures[68]. This may be true for a particular alloy or set of alloys, but because of the many factors that can contribute towards delamination, various structural components can be expected to behave differently with respect to lamellar tearing in the rolling plane.

2.7 REVIEW OF THE PHYSICAL METALLURGY AND PROPERTIES OF 3CR12

The general physical metallurgy and engineering properties of 3CR12 are reviewed, and in many instances the advantages derived from modifying conventional ferrite steels are illustrated.

2.7.1 PHYSICAL METALLURGY

The composition of 3CR12 essentially arises from small but significant composition deviations from that of AISI 409. Ferrite and austenite forming elements have been carefully balanced in order to give a ferrite factor in the range 8-12 which is calculated from the formula given by Kaltenhauser[75].

Ferrite Factor (FF) = %Cr + 6(%Si) + 8(%Ti) + 4(%Mo) + 2(%Al) + 4(%Nb) - 2(%Mn) - 4(%Ni) - 40[%(C+N])

This composition (Table 2.2) gives rise to a banded two-phase structure of martensite and ferrite after hot rolling, which, in view of the low carbon content of the martensite, produces a ferritic microstructure after sub-critical annealing (tempering). The origin of the banded two-phase microstructure is reported to be due to hot rolling being carried out in the duplex ferrite-austenite region[1].

TABLE 2.2 : Compositional limits for 3CR12

C	N	Ni	Mn	Si	P	Cr	Ti
0.03 max	0.03 max	1.5 max	1.5 max	1.0 max	0.03 max	11.0 - 12.0	4(C+N) min

The response of the as-rolled material to heat treatment in the range 25°C to 1200°C is shown in fig 2.13, which is taken from the work of Brink and Ball [76]. On reaching 780°C, the as-rolled ferrite-martensite microstructure becomes almost completely ferritic and shows a minimum in bulk hardness. Above 800°C, which corresponds to the average dilatometrically determined A_{C1} temperature, a fine duplex microstructure is generated which is retained until at least 1200°C; the duplex structure becomes coarser with increasing temperature. A study of the microstructures by Ball et al[77] using transmission electron microscopy indicated that after the heat treatment at 700°C, the martensite becomes highly tempered and starts to lose its lath character. The dislocations within the martensite form low-angle boundaries and the structure is reminiscent of a "recovered" structure. At this temperature, the ferrite nucleation barriers are exceeded and if sufficient time is allowed, new ferrite can nucleate and grow. A further increase in temperature to 800°C provides sufficient thermal energy to induce substantial martensite decomposition to ferrite plus carbides. In this way, the hot rolled ferrite-martensite structure is essentially transformed to a stable fine-grained ferritic structure by sub-critical annealing at temperatures just below the A_{C1} temperature. The stability of this fine-grained microstructure has been attributed to the occurrence of the phase separation $\alpha \rightarrow \alpha+\gamma$ at temperatures of about 800°C. It is reported that the presence of a duplex structure during hot rolling not only restricts grain growth, but confers on the steel a very uniform state of plastic deformation[1]. This uniform plastic deformation of the duplex microstructure in turn produces a fine grain size during subsequent sub-critical annealing.

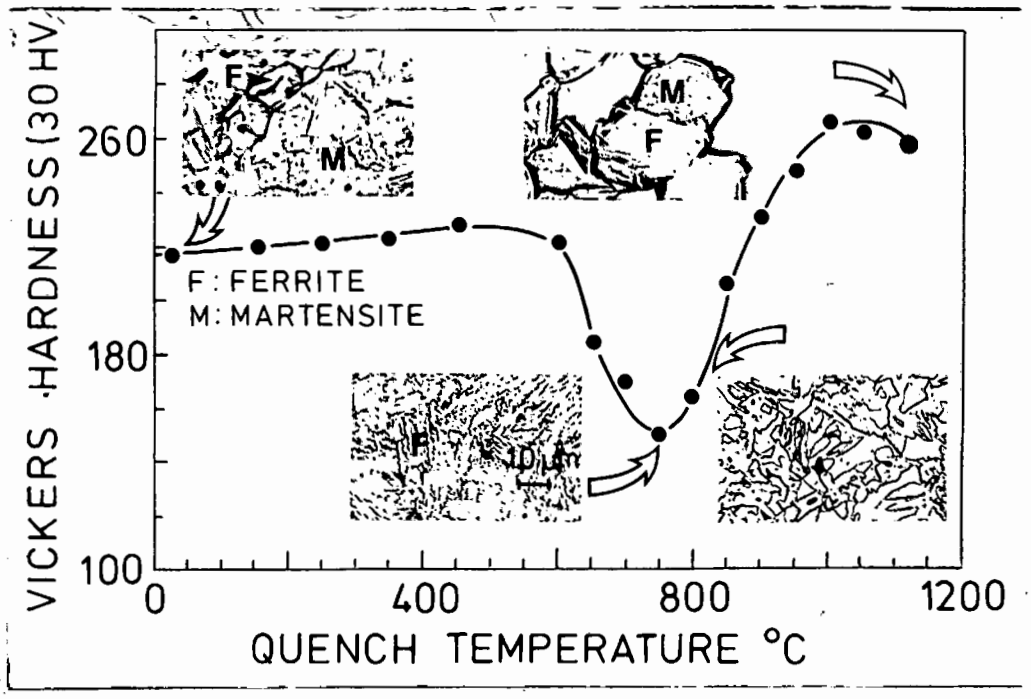

FIGURE 2.13 : Variation of room temperature bulk hardness and microstructure of 3CR12 versus annealing temperature. Each specimen was soaked at indicated temperatures for 1 hour followed by oil quenching. (After Ref 76)

Annealing above the A_{C1} temperature results in the nucleation of austenite (which forms martensite on cooling to room temperature) at the ferrite grain boundaries[77]. The austenite content increases with increasing annealing temperature, thereby resulting in an increase in hardness of material quenched from these temperatures (fig 2.13). Above 1000°C, the amount of ferrite increases and considerable grain growth occurs. This in turn causes a decrease in hardness as reflected in fig 2.13. The kinetics of the transformation from ferrite to austenite at constant temperatures between 800°C and 975°C are shown in fig 2.14. The reaction is very slow at temperatures below 850°C and at 915°C the transformation to austenite remains 90 percent complete after extended times. This tends to indicate that a small amount of ferrite remains in equilibrium with the austenite. When quenched from these duplex regions, the microhardness of the martensite is considerably greater than that of the ferrite and it is proposed that the hardness will in turn be determined by the amount of carbon in solution in the austenite prior to quenching[77,78]. The higher the holding temperature and the longer the holding period, the greater will be the amount of carbon in solution in the austenite. The martensite formed on cooling will consequently be harder. The change in the macrohardness of the steel and the volume fraction of martensite as a function of annealing temperature is shown in fig 2.15.

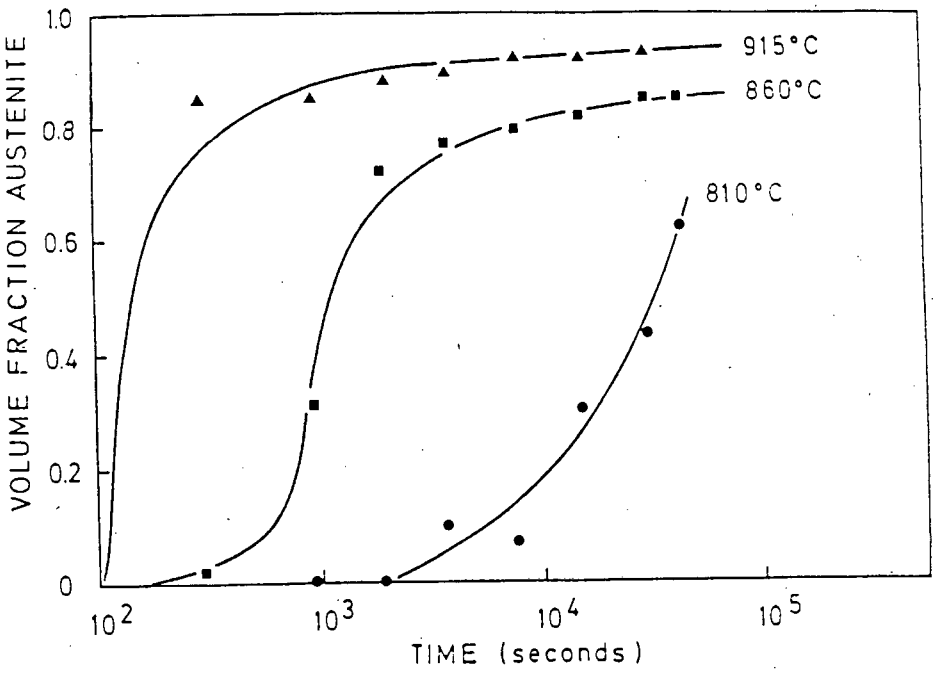

FIGURE 2.14 : Volume fraction of austenite as a function of time at various temperatures for transformation of 3CR12 steel from the ferritic structure (After Ref 77).

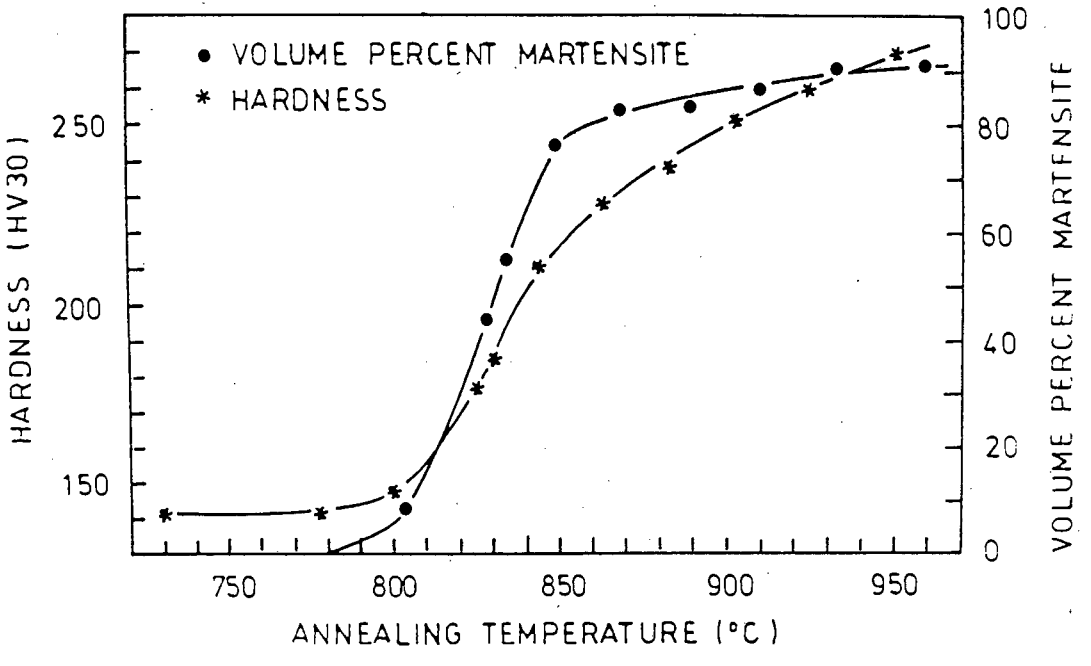

FIGURE 2.15 : The effect of annealing temperature within the duplex region on room temperature hardness and martensite content for 3CR12 (After Ref 78).

The kinetics of the reverse reaction (austenite decomposition) at temperatures below 800°C are indicated in fig 2.16. Even at 750°C, a time in excess of 1 hour is required before the regions of ferrite in the austenite begin to grow. Complete transformation to ferrite and carbides takes approximately 16 hours. These results for the austenite formation and decomposition reactions indicate that the dissolution of carbide and subsequent diffusion of carbon from the carbides into solution in austenite, and the reverse, are major factors influencing both the kinetics of reaction, and in turn the microstructural condition and mechanical properties of the final product.

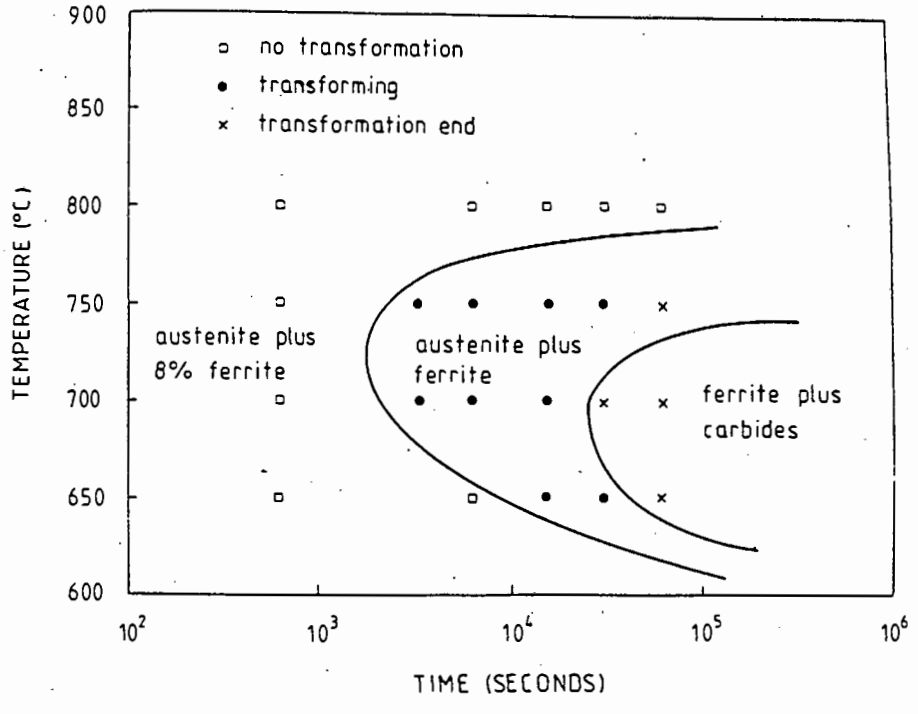

FIGURE 2.16 : Isothermal transformation for decomposition of austenite to ferrite + carbides in 3CR12 steel (After Ref 77).

2.7.2 PROPERTIES

MECHANICAL PROPERTIES

Since it is well known that refinement of the ferrite grain size not only increases the yield and tensile strengths according to the Hall-Petch relationship, but also increases the toughness, it is of little surprise that the stable fine-grained structure of 3CR12 obtained by sub-critical annealing provides attractive strength, toughness, and forming properties. In their initial study of 3CR12, Ball and Hoffmann[1] demonstrated that the impact

properties of 3CR12 were much improved as compared with those for AISI 409 type steel. They determined values of room temperature impact energy, 0°C impact energy, and the ductile-brittle transition temperature (regarded as the temperature at which the impact energy is less than 30J) to be 85J, 65J and -20°C respectively for 3CR12, compared with values of 20J, 10J and 40°C respectively for samples of AISI 409 tested under identical conditions.

The room temperature tensile properties of a typical alloy 3CR12 as a function of annealing temperature are indicated in fig 2.17. The ultimate tensile strength follows a similar pattern to the variation in hardness with annealing temperature depicted in fig 2.13, and shows a minimum at around 800°C with maxima at approximately 400°C and 1050°C. The elongation to fracture traces an inverse pattern to the tensile strength showing minima at around 400°C and 1050°C and a maximum in the region of 800°C. It has also been shown that the impact strength of 3CR12 is greatly affected by the annealing temperature[79]. The impact strength follows a similar trend to that exhibited by the elongation to fracture curve and gives rise to a maximum in impact strength of 80J at around 800°C. This means that the formation of new austenite (transforms to martensite on cooling) at temperatures above 800°C results in an increase in hardness and tensile properties, but reduces impact strength and ductility. The most attractive combination of mechanical properties is therefore obtained from material annealed at a temperature just below the A_{C1} temperature. Typical mechanical properties of material in this condition (hot-rolled-annealed, or HRA, condition) are listed in Table 2.3.

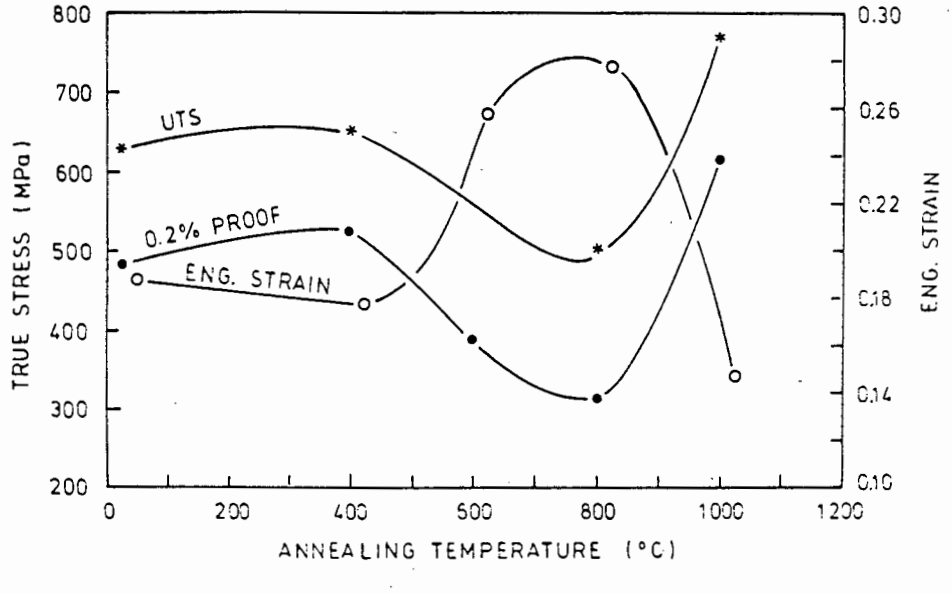

FIGURE 2.17 : The effect of annealing temperature on the room temperature tensile properties of 3CR12 (After Ref 78).

TABLE 2.3 : Mechanical properties of 3CR12 in the hot-rolled-annealed condition.

PROPERTY	UNIT	MIN.	TYPICAL
Tensile strength	MPa	460	530
Proof Stress (0.2%)	MPa	280	380
Elongation (in 50mm)	%	20	26
Hardness	HB	220*	165
Charpy V Impact	J	50	80

*MAX HARDNESS

The hot workability of 3CR12 has been assessed to some extent in a study of the mechanical properties of 3CR12 at elevated temperatures[76]. It has been found that a dramatic increase in elongation occurs in the temperature range 800°C - 900°C, along with a marked decrease in the work hardening exponent (Holloman parameter). The increase in elongation is attributed to the stable, fine-grained, duplex ferrite-austenite structure intrinsic to 3CR12 at elevated temperature. Ball and Hoffman[1] have also demonstrated the superplastic tendencies of these alloys within this temperature range. The low work hardening condition of 3CR12 between 800°C and 900°C has been explained by the rapid increase in dynamic recrystallisation of ferrite together with an increase in the rate of nucleation of austenite grains induced by a straining matrix at these temperatures. These results have led to the conclusion that for hot forming operations, minima in deformation energies occur in the temperature region between 800°C and 900°C.

WELDABILITY

The successful weldability of 3CR12 is attributed mainly to the occurrence of the second phase austenite (transforms to martensite) in the heat affected zone (HAZ) which restricts ferrite grain growth. The HAZ in 3CR12 contains between 20% and 90% martensite, depending on the ferrite factor of the steel, the heat input per pass during welding and the number of passes. These factors all contribute towards determining the strength, ductility and toughness of the welded material[80].

The grain size in the HAZ is determined by the heat input and the volume fraction of martensite. This means that steels with a high ferrite factor (ie approaching 12) will have a low martensite content and therefore ferrite grain growth is less likely to be inhibited.

On the other hand, if the steel is welded with a high heat input, the grains will be coarse anyway, with the occurrence of intergranular martensite. The weld HAZ of a steel with a low ferrite factor (8-9) will consist of 80-90% martensite and coarse grain growth is inhibited. The increase in strength (and hardness) brought about by the low carbon martensite more than compensates for the loss in strength as a result of the coarser grain. The grain growth is also restricted to a band two to three grain diameters wide. It has been determined that the tensile strength of the HAZ exceeds that of the parent material in all cases[80]. Fatigue testing has shown that fatigue values for welded 3CR12 fall within the confidence limit bands for C-Mn steel[81]. The testing of cruciform specimens is reported to give satisfactory lives with respect to weld metal failure in toe and throat of welds.

The toughness of the HAZ is determined by the volume fraction of the inherently tough, low carbon lath martensite formed. If the martensite content is maintained at not less than 45 vol %, then this second phase effectively pins grain boundaries. The synergistic effect of low carbon lath martensite and restricted grain growth is thus reported to limit the increase in the ductile-brittle transition temperature of welded 3CR12[80].

CORROSION AND ABRASION RESISTANCE

The corrosion resistance of 3CR12 is limited due to its relatively low chromium content[82]. However, the steel does have very good atmospheric corrosion resistance, even when the atmosphere is heavily polluted by contaminants such as sulphur dioxide, chlorides and nitrous fumes. Extensive atmospheric corrosion tests conducted over a two year period at various sites, have shown that 3CR12 has a low corrosion rate compared with that of mild steel, Cor-Ten A, zinc, copper and aluminium[83]. In particular, it is indicated that only in the case of a severe marine environment is the corrosion rate higher than that of aluminium alloys.

Although the abrasion resistance of 3CR12 under dry sliding conditions is similar to mild steel, conditions in a real industrial situation where corrosion is invariably present indicate that the relative wear resistance of 3CR12 is twice that of carbon and low alloy steels[84]. Simulated laboratory corrosion-abrasion tests and tests performed in-situ on mine conveyors show that when the effects of corrosion and abrasion are combined, 3CR12 out-performs not only mild steel, but certain proprietary wear alloys as well (fig 2.18).

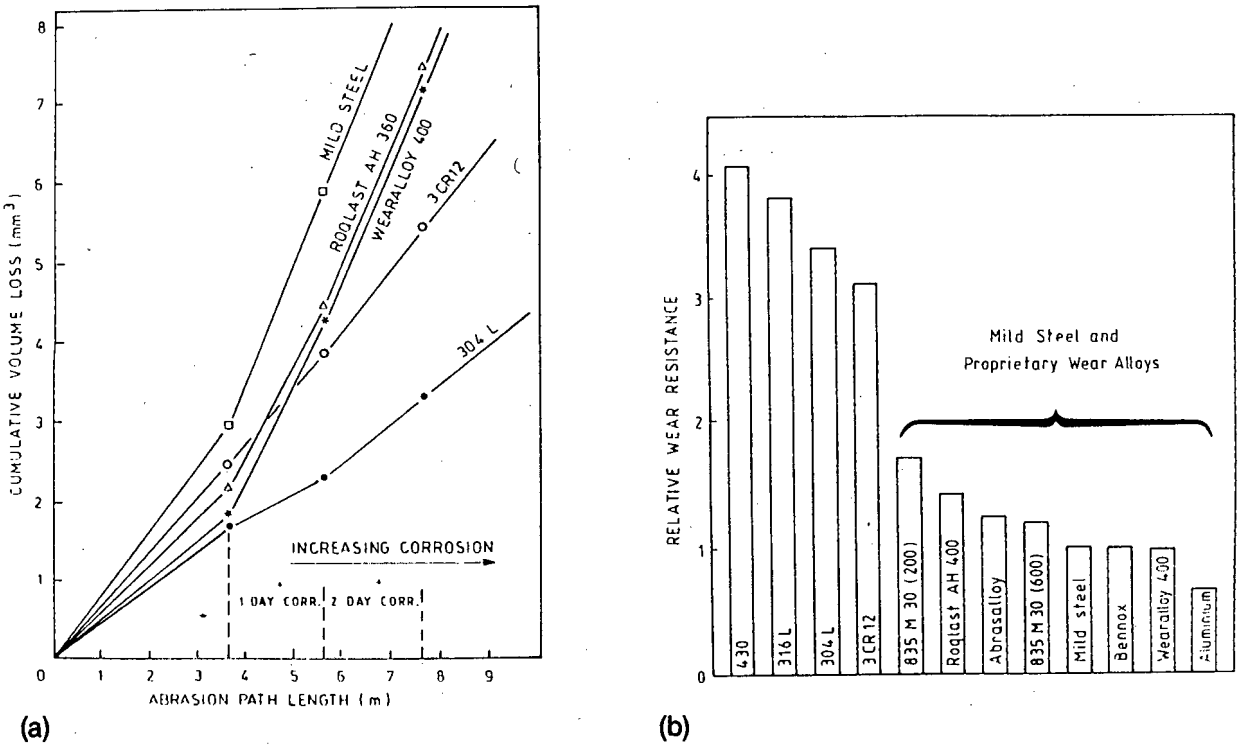

FIGURE 2.18 : Corrosion-abrasion performance of 3CR12 compared to some common alloys (After Refs 84 and 85).

(a) Simulated laboratory corrosion-abrasion tests.

(b) In-situ mine conditions.

2.7.3 OVERVIEW

The mechanical properties of 3CR12 are undoubtedly superior to those of AISI 409. The grain refining effect induced by the formation of a large volume fraction of austenite leads to the ultimate development of a fine-grained ferritic steel. In other words, huge benefits are obtained by the overall transformation of $\delta \rightarrow \gamma \rightarrow \alpha$ as a result of the slightly modified chemistry. In nearly all aspects (eg. ductile-brittle transition temperature, formability and weldability), the properties are improved over those of non-transformable, or less transformable, ferritic stainless steels.

-ooOoo-

CHAPTER 3

EXPERIMENTAL PROCEDURE AND MATERIALS

3.1 EXPERIMENTAL APPROACH

3.1.1 METALLOGRAPHY

The microstructures of the various materials were characterised using both light and electron microscopy. Samples were prepared using conventional metallographic techniques and the final surface finish was obtained by mechanically polishing with a 0.25μm diamond paste. Depending on the information required, samples were analysed either in the as-polished or etched condition. The various etching techniques used in order to fully characterise the microstructures of the test alloys involved both chemical and electrolytic etching. The etching solutions and procedures are listed below :-

(i) Dip-etched for two minutes in 10 ml HNO_3 + 20 ml HCl + 30ml H_20 ..... SOLUTION A.

(ii) Dip-etched for 20 - 30 seconds in a solution containing 100 ml of 1:5 vol/vol HCl + 2g $NH_4F.HF$ + 1g $K_2S_2O_5$ ..... SOLUTION B.

(iii) Dip-etched for 20 seconds in 50 ml of 4% picral + 1g $Na_2S_2O_5$ in 50 ml H_2O + 5 ml of 1% HCl ..... SOLUTION C.

(iv) Electrolytic etching performed in a 10% oxalic acid solution at a temperature of 70°C. The specimen was anodically polarised at 11V for 30-35 seconds.

The chemical etch solutions B and C gave rise to a tint contrast between the ferrite and martensite phases which resulted in the respective phases being easily identifiable. In

some instances double etching, using both procedures (i) and (ii) above, was performed in order to obtain optimum grain boundary definition and phase contrast.

Light microscopic examination was carried out on a REICHERT MeF2 metallograph in the brightfield mode. Oblique lighting was used to enhance the surface relief and the maximum magnification was obtained using a 125X oil-immersion objective lens. Nomarski interference contrast was also used in some instances to improve grain boundary contrast. Electron optical metallography was conducted using a CAMBRIDGE S200 scanning electron microscope (SEM). Typically images were acquired at a primary accelerating voltage of 30 kV with a conventional tungsten filament providing the electron source. However, in certain cases a lanthanum hexaboride (LaB6) filament was used to enhance the resolution of the image at higher magnifications. Image formation involved mainly secondary electron imaging, with occasional use of a back-scattered electron detector.

Metallographic sections were prepared in various orientations and are labelled according to the nomenclature illustrated in fig 3.1. In each case the planar section is referenced by two symbols which describe the orthogonal directions that are contained within the plane of interest.

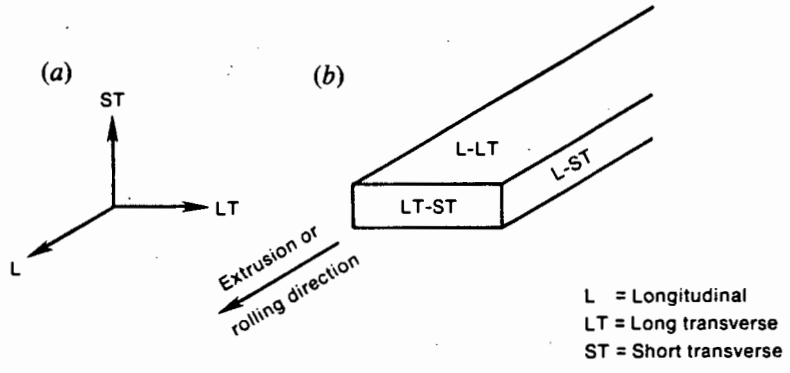

FIGURE 3.1 : Definitions of (a) axes and (b) planar section notation for metallographic specimens. After Ref 86.

3.1.2 COMPOSITION MICROANALYSIS

The determination of the composition of non-metallic inclusions and the composition of the respective ferrite and martensite phases in 3CR12 and the 16% chromium alloys was carried out using a TRACOR NORTHERN TN5400 energy dispersive X-ray microanalyser attached to the CAMBRIDGE S200 SEM. The lithium drifted silicon X-ray detector incorporated a beryllium protection window which prevented the detection

of elements lighter than sodium. Consequently, the presence of elements such as carbon and nitrogen, where necessary, had to be inferred. Details of the various analysis methods are outlined below.

3.1.2.1 Ferrite-Martensite Phase Composition Analysis

The composition of the ferrite and martensite phases in 3CR12 and the 16% chromium alloys was analysed for samples in various heat treated conditions. Since ferritising and austenitising elements favour their respective phases, it was anticipated that elemental partitioning would occur between the ferrite and prior austenite phases. Chromium is the main substitutional ferritising element and nickel and manganese are considered as dominant substitutional austenitising elements in these alloys. Nevertheless, emphasis was placed on the analysis of chromium and nickel only since the peak overlaps Cr-Kβ/Mn-Kα and Mn-Kβ/Fe-Kα result in a much more difficult interpretation of the manganese levels. The extent of element partitioning expected between the two phases, however, was very small, especially in the case of 3CR12. In addition, grain boundary widths could be as low as 5 microns in some cases. These factors meant that careful control of the analysis method was necessary in order to obtain reliable results. The selection of optimum parameters such as accelerating voltage, probe diameter, and X-ray acquisition time thus became necessary in order to provide reproducible results using a standardless semi-quantitative (SSQ) analysis routine.

It is important to note, however, that the results generated by the SSQ routine are not absolute, but can be used to compare relative phase compositions. Since the composition variation between the phases was expected to be smallest for 3CR12, the conditions pertaining to the acquisition and processing of the X-ray spectra are likely to be more critical for this alloy. The following paragraphs discuss the experimentally determined effects of accelerating voltage, probe diameter, and acquisition time on the composition analysis of the 3CR12 microstructure. This study has led to the selection of optimum parameters for the phase composition determination of both 3CR12 and the 16% chromium alloys.

Accelerating Voltage (kV)

Besides the generation of characteristic X-ray peaks, an X-ray continuum, termed the background, is also developed during the acquisition of an energy dispersive X-ray

spectrum. In order to analyse the characteristic X-ray peaks, the total background must be subtracted from the spectrum. Since the analysis routine used for this work involved background fitting and subtraction routines based on Kramer's law[87], it was necessary to acquire spectra having backgrounds which closely resembled that predicted by Kramer's law.

Figure 3.2 illustrates the effect which the primary accelerating voltage (Eo) had on the shape of the spectrum background. The backgrounds displayed in this figure were obtained by subtracting the characteristic peaks from spectra acquired for 3CR12 at operating accelerating voltages of 20, 25 and 30 kV. These results indicated that the background for 20 kV (operating voltage) most closely corresponded to that expected from the classical Kramer's law[87], whereas the background acquired at 30 kV showed a second maximum at approximately 12 keV. This anomalous contribution to the background in the region of 12keV has been attributed to a significant number of back-scattered electrons penetrating the beryllium window of the EDS detector at high primary accelerating voltages[88]. The background generated at 30 kV would therefore give rise to poor analysis. The resultant background acquired at 25 kV did not show a second maximum, but if one considers the position of the Kα peaks for chromium and nickel, it can be seen that the background contribution was lowest for 20 kV, and therefore more favourable peak-to-background ratios would be obtained at this latter accelerating voltage. It is important to note that a consideration of accelerating voltages less than 20 kV was not feasible in this instance due to the limiting primary energy required to produce Ni-Kα X-rays.

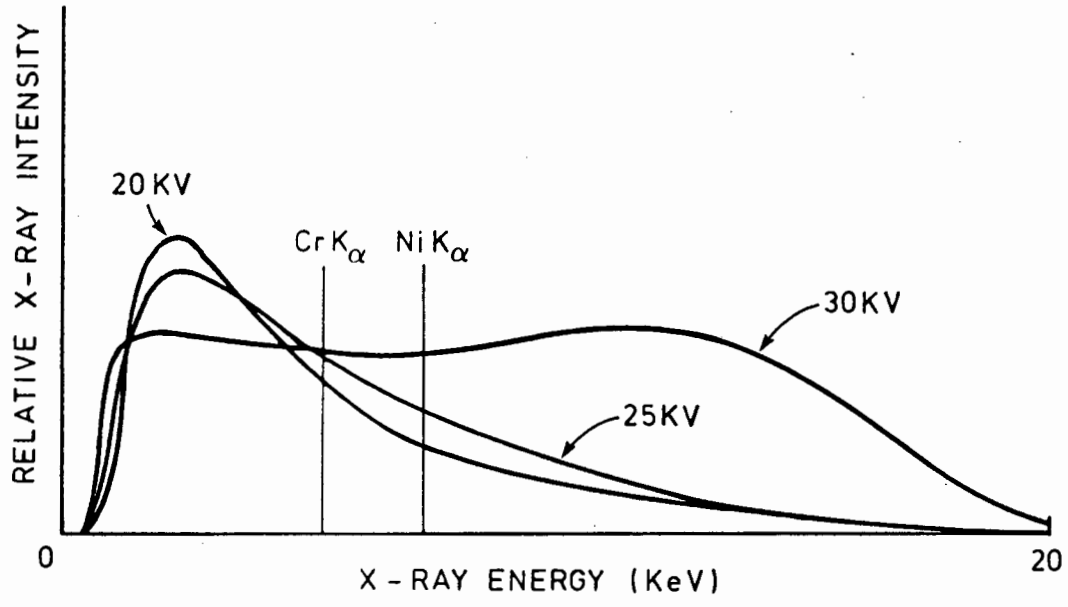

FIGURE 3.2 : Effect of accelerating voltage (kV) on the shape of the spectrum background acquired for 3CR12.

Probe Diameter

When performing single spot analysis, the electron probe diameter is an important factor in determining the size of the area from which X-rays are produced. Since the grain width can be as low as 5 micrometres, it was necessary to obtain a fine probe diameter in order to achieve the smallest possible interaction area. However, it was also necessary to maintain an acceptable X-ray count rate which is related to the electron probe current. In view of 20kV being a more favourable accelerating voltage in terms of background fitting, it was decided to select an acceptable count rate of approximately 3000 counts/sec and measure the resultant probe diameter at this voltage. A specimen working distance of 20 millimetres and a specimen tilt angle of 30° were chosen in order to optimise the X-ray take-off angle.

The probe diameter was measured according to the edge sweep method illustrated in fig 3.3. The curve represents an intensity line scan performed across a very sharp edge which is mounted above a hole in a carbon block. The distance over which the intensity changed from 10% to 90% was calculated as the probe diameter. A total of 10 measurements were performed under constant settings and yielded a probe diameter in the range of 250-350 nanometres. This measurement was well within the limits of the grain size.

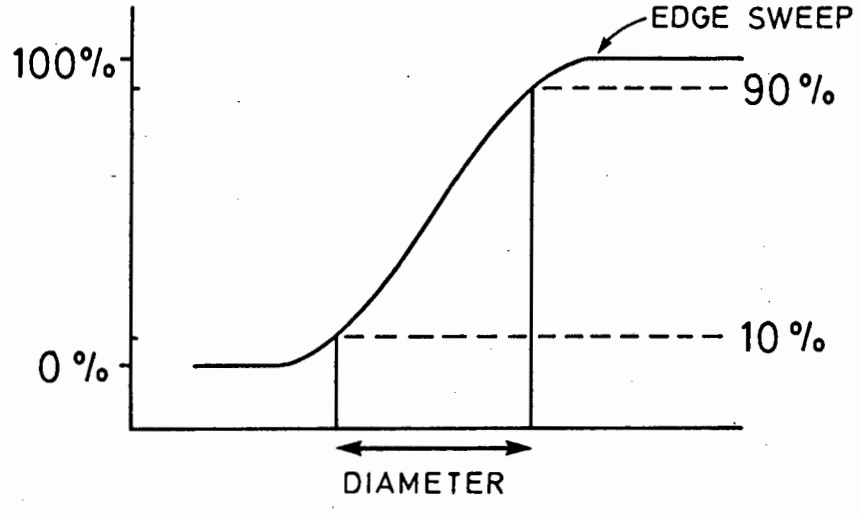

FIGURE 3.3 : Schematic illustration of the edge sweep technique used for the probe diameter measurement.

The electron range in 3CR12 at 20 kV, as calculated according to the equation by Kanaya and Okayama[89], is of the order to 1.57 micrometres. Therefore, as a conservative estimate, the surface interaction area is not likely to exceed 2 - 3

micrometers in diameter and the sampling depth should not exceed 2 micrometres. A schematic representation of the probe/sample interaction is shown in fig 3.4. This model does not take into account the fact that X-ray flourescence can occur over a much larger range, but the results discussed later indicate that this contribution is insignificant.

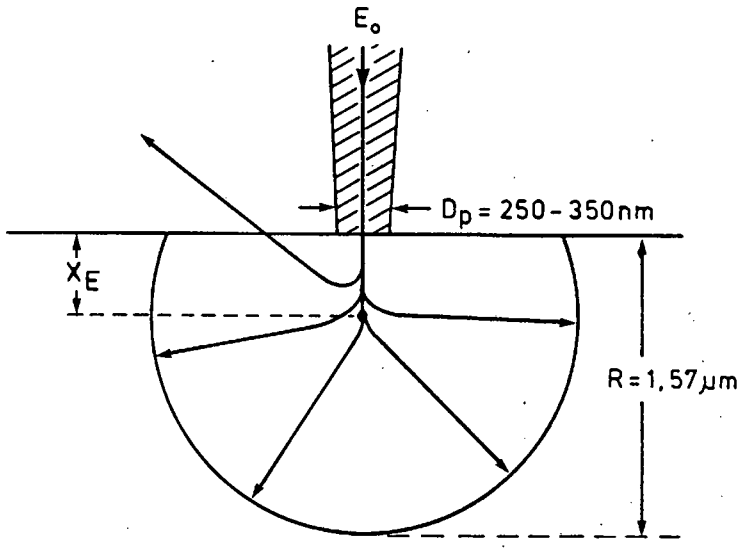

$$R = \frac{2.76 \times 10^{-11} A E_o^{5/3}}{\rho Z^{8/9}} \cdot \frac{(1 + 0.978 \times 10^{-6} E_o)^{5/3}}{(1 + 1.957 \times 10^{-6} E_o)^{4/3}} \quad *$$

E_o = incident electron energy (eV); A = atomic weight; Z = atomic number; ρ = density ($g.cm^{-3}$); D_p = probe diameter; R = electron range; Xe = electron penetration due to kinetic energy.

* After Ref 89

FIGURE 3.4 : Probe/sample interaction for 3CR12 at 20 kV.

Acquisition Time

The statistical accuracy of the analysis depended on the resolution of the X-ray spectrum. The generation of an X-ray photon in a sample irradiated with an electron probe is independent of previous or subsequent electron-photon events and hence it is random in these terms. Since there is nothing which will formalise either the number of X-rays reaching the detector or the pulse train in the multi-channel analyser, it follows that the random nature of the generation of X-rays is reflected by a random nature in the detection and counting of X-ray photons. Therefore the counting of X-rays obeys the statistics of independent random events ; Poisson statistics, which for

large numbers are well approximated by Guassian probability distributions. This means that the standard deviation will be determined by the number of counts, although other factors such as background intensity and the sum of any overlaps also play a role in determining the standard deviation. In particular, the subtraction of a high background from under a small characteristic peak can result in a large relative error being produced as noted in the previous section. This can only be improved by counting for a longer time.

In order to determine the X-ray acquisition period necessary to provide meaningful results, a total of 10 X-ray spectra were acquired for each period of 60, 200, 400 and 600 seconds on the same area of 3CR12 matrix under the optimum microscope conditions discussed in the previous paragraphs. The spectra were analysed using the SSQ routine and the mean and standard deviations were determined for the chromium and nickel contents for each acquisition time. The results shown in fig 3.5 indicate a fairly large standard deviation for a 60 second acquisition period whereas acquisition times greater than 200 seconds gave rise to more acceptable results. In order to maintain a reasonably small error, an acquisition period of 400 seconds was chosen for all analyses.

In summary, reliable results in terms of measuring the extent of substitutional element partitioning between ferrite and martensite phases in 3CR12 could be achieved under the following operating conditions :

- **Primary accelerating voltage = 20 kV**
- **X-ray count rate = 2800 - 3000 counts/second**
- **Specimen tilt angle (towards X-ray detector) = 30°**
- **Specimen working distance = 20 mm**
- **X-ray acquisition time = 400 seconds.**

These conditions were used for all phase composition determinations (3CR12 and 16% chromium alloys) and each result presented in the following chapter is an average of a minimum of four analyses of each phase.

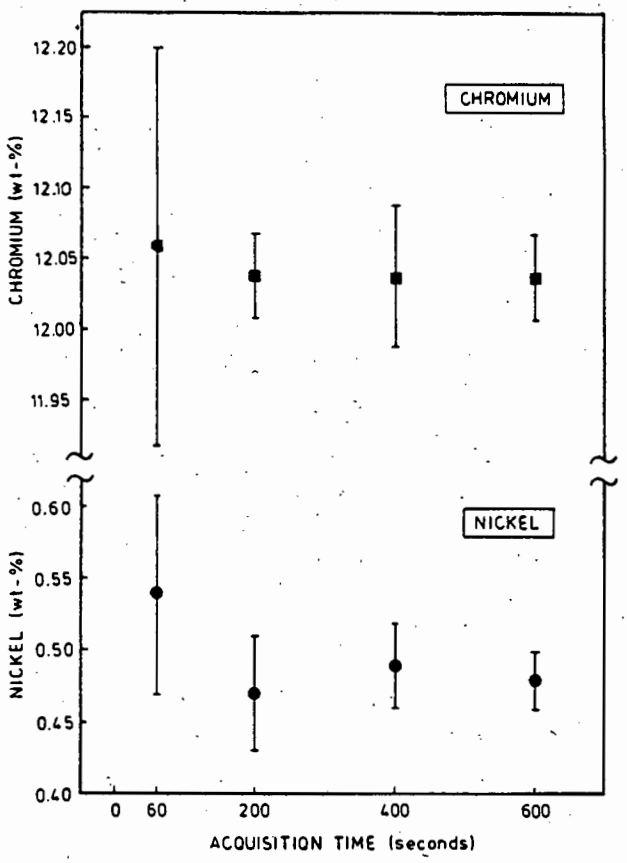

FIGURE 3.5 : Mean Cr and Ni content as a function of X-ray acquisition time. Standard deviations are indicated.

3.1.2.2 Non-metallic Inclusion Analysis

Energy-dispersive X-ray spectroscopy (EDS) was used to determine the composition of non-metallic inclusions on both polished surfaces and fracture surfaces. In view of the very small inclusion size (sulphides can be of the order of 1 micron thick) and the uneven topography of the fracture surfaces, the inclusion compositions were determined on a qualitative basis only. Quantitation of their composition would be misleading due to the fact that the X-ray interaction volume often included a portion of the steel matrix and, secondly, the presence of elements such as carbon and nitrogen, which were undetectable, would be excluded from the analysis. This meant that the inclusion compositions were essentially identified by the elements detected and not necessarily by their stoichiometric composition. However, the relative element contents could often be inferred to some degree from the X-ray peak heights.

In order to enable an approximate allowance to be made for the matrix contribution during inclusion analyses, X-ray spectra were obtained for the individual inclusions as

well as for the general matrix. The inclusion spectra were processed by subtracting the matrix spectrum from the inclusion spectrum after normalisation with respect to the Fe-Kα peaks. In this way a more accurate assessment could be made of the inclusion composition from the processed spectra. An example is illustrated in fig 3.6 which shows spectra for an inclusion, the general matrix, and the resultant inclusion spectrum after matrix subtraction. The inclusion spectra are displayed in a bi-polar mode with respect to X-ray intensity so as to allow the identification of negative peaks which would be generated if more than just the matrix contribution were subtracted from the inclusion spectrum. In this example the identification of the manganese sulphide inclusion containing small amounts of titanium is much clearer in fig 3.6(c) compared to the original inclusion spectrum in fig 3.6(a).

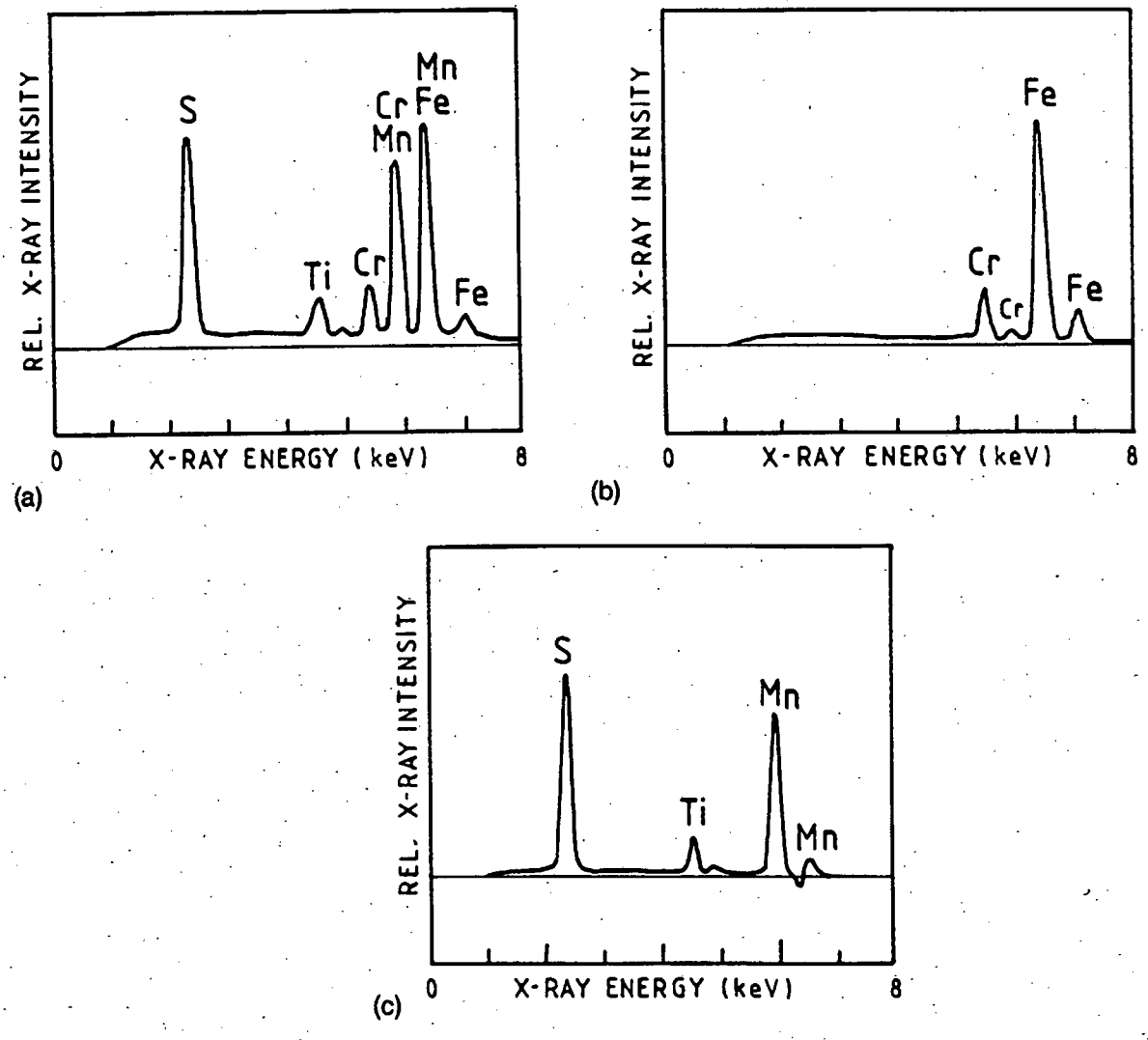

FIGURE 3.6 : An example of inclusion qualitative analysis by matrix subtraction.

a) Analysis of inclusion surface

b) General matrix analysis

c) Net inclusion spectrum after matrix subtraction

3.1.3 HEAT TREATMENT

The heat treatment of the various alloys was carried out in either chamber or tube furnaces, depending on the size of the specimens and the temperatures required. The various procedures are described as follows :-

(i) Charpy V-notch impact test specimens and tensile specimens were heated in a chamber furnace which had an eleven litre capacity. The prevention of oxidation was effected by wrapping the specimens in stainless steel foil and continuously purging the furnace chamber with argon.

(ii) The heat treatment of small metallographic specimens, involving temperatures not exceeding 1100°C, was carried out in horizontally supported tube furnaces. The furnaces had a tube diameter of 30mm and a uniform hot zone of 80mm in length. These furnaces were also continuously purged with argon gas and specimens were protected with a ceramic coating. Under conditions where specimens were soaked at alternate upper and lower temperatures, two horizontally opposed tube furnaces were used which were connected via an extension tube. Specimens were attached to a stainless steel push-rod and could be easily moved from one furnace to the other. Where necessary, quenching was carried out by transferring the specimens directly into a 25 litre oil bath.

(iii) Heat treatments performed at temperatures greater than 1100°C were carried out using a vertically supported Pt-Rh winding furnace equipped with a vacuum pumping system. This allowed metallographic specimens to be heated in a vacuum of 10^{-4} - 10^{-5} Torr. The specimens were suspended from a nichrome wire fuse which allowed them to be released from the hot zone by applying a voltage across the fuse terminals. In this way specimens could be quenched into the oil bath situated below the furnace without interrupting the vacuum. Specimens were also cooled within the furnace by either switching the furnace off (uncontrolled cooling) for fast furnace cooling, or by cooling at a controlled rate of 1°C per minute. The temperature-time profile for uncontrolled furnace cooling is illustrated in fig 3.7.

3.1.4 DILATOMETRY

The transformation temperatures for the 3CR12 and the 16% chromium alloys were determined dilatometrically during both heating and cooling cycles. Specimens

measuring 50mm in length were heated at a constant rate of 4°C per minute in a controlled argon atmosphere, and were furnace cooled either in an uncontrolled manner (furnace switched off), or at a constant rate equal to 1°C per minute. Change in specimen length was measured using a displacement transducer and transformation start and finish temperatures were defined as the temperature at which the dilation curve either deviated from or resumed linearity. An example of transformation temperature measurement is indicated schematically in fig 3.8.

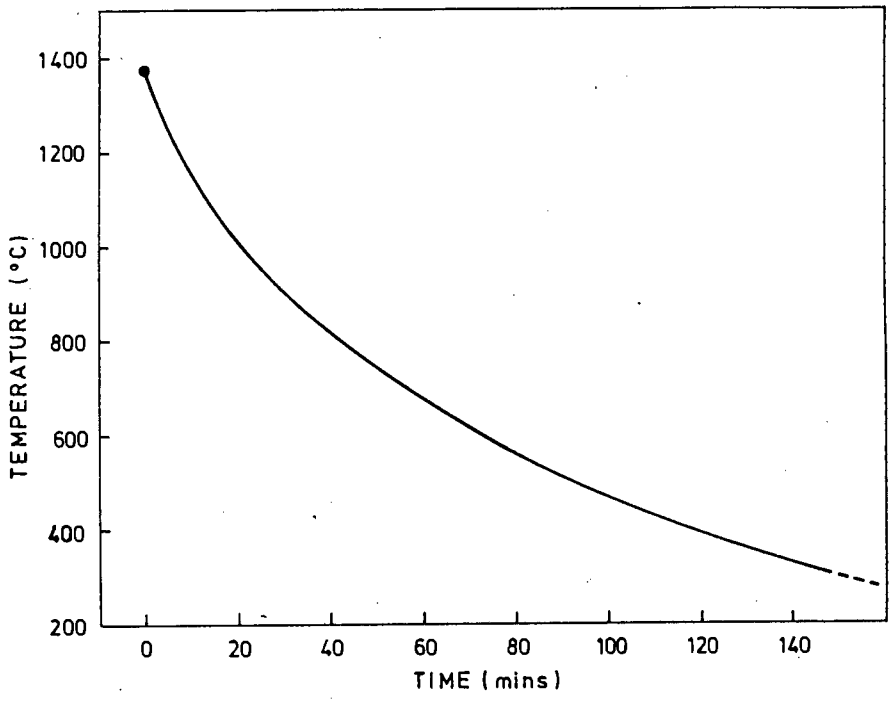

FIGURE 3.7 : Temperature-time profile for uncontrolled furnace cooling.

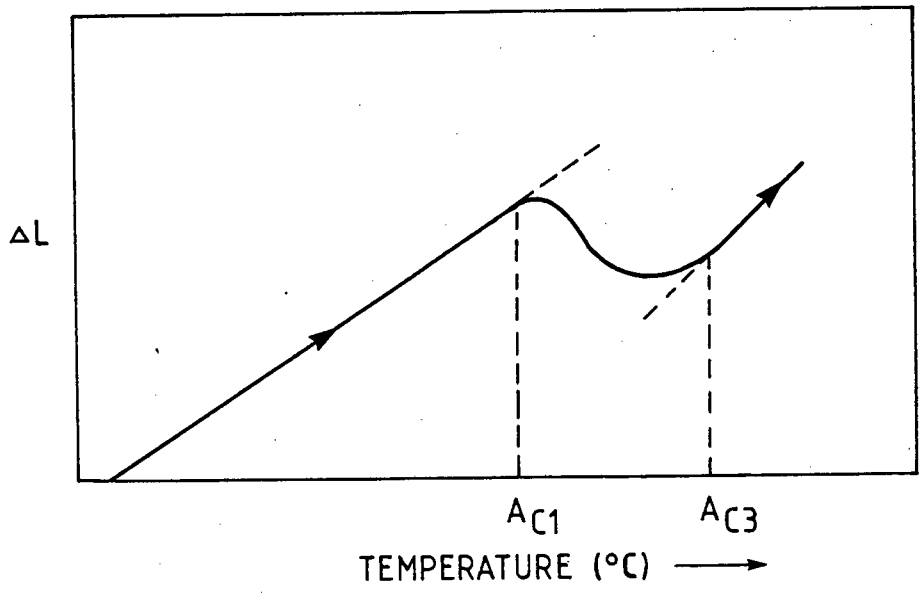

FIGURE 3.8 : Definition of transformation temperatures measured.

3.1.5 MECHANICAL TESTING

IMPACT TESTING

Impact testing was carried out at room temperature using Charpy V-notch specimens. The specimen dimensions varied according to the plate thickness, but where direct comparisons were made, all specimens had the same dimensions and orientation with respect to the rolling direction. For instance, impact test specimens used to determine the effect of inclusion content on the impact properties of 3CR12 had dimensions 7.5 x 10mm and were machined in the T-L orientation (fig 3.9). Where necessary specimen geometries are noted along with the results. Four specimens were tested for each condition.

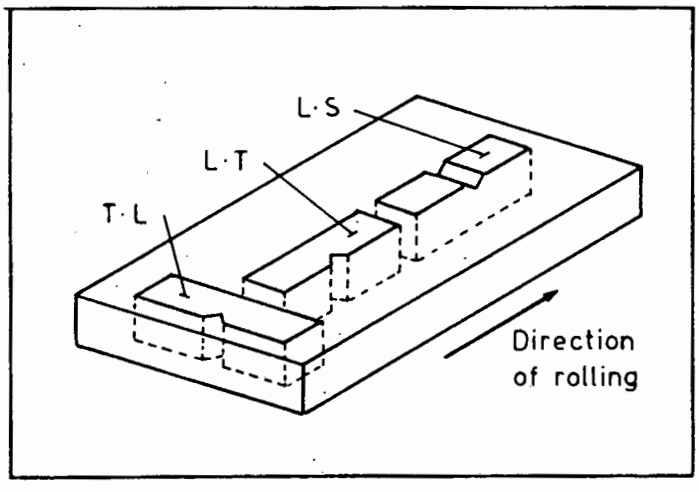

FIGURE 3.9 : Orientation of Charpy specimens with respect to direction of rolling. (TL = transverse-longitudinal, LT = longitudinal-transverse, LS = longitudinal-short transverse).

TENSILE TESTING

Tensile properties were determined using a ZWICK universal tester equipped with a 200 kN load cell. Conventional Hounsfield metric specimens were used to determine the properties of the alloys in both the as-rolled and heat treated conditions. These specimens had a gauge length and gauge diameter of 25.2 mm and 5.04 mm respectively. The orientation of the tensile axis was always parallel to the rolling direction. All tensile tests were performed at room temperature and at a strain of 10^{-3} per second.

3.1.6 VOLUME FRACTION ANALYSIS

The volume fractions of cuboid inclusions occurring in 3CR12 steel and the ferrite/martensite phase ratios in the 16% chromium alloys were determined using the point counting technique. Manual counting was carried out on a conventional light microscope. In order to achieve reasonable accuracy during the volume fraction analysis of cuboid inclusions, a minimum of 800 fields of view were counted for each sample. This gave rise to a total sample area size of 128 mm^2 for each material. In the case of the determination of the ferrite/martensite phase ratios only 30 fields of view were required for good accuracy.

3.1.7 LABORATORY ROLLING SCHEDULES

Laboratory rolling was carried out on a DINKEL laboratory rolling mill. In the case of the hot rolling of 3CR12, attempts were made as far as possible to simulate the commercial hot rolling conditions. Specimens were presoaked at 1100°C prior to rolling and reduction was terminated at temperatures above 700°C.

3.2 COMPOSITION OF 3CR12 EXPERIMENTAL MATERIALS

INCLUSION, IMPACT FRACTURE AND CORROSION STUDIES

Investigations concerning the inclusion, impact fracture, and corrosion studies on 3CR12 were carried out on a range of commercial heats. The heats examined were manufactured by Middleburg Steel and Alloys (Transvaal, RSA) and supplied in the hot rolled and annealed condition in plate thicknesses varying from 8-12 mm. A summary of the production schedule and typical thermal history for these alloys is illustrated in fig 3.10.

The object of investigating a reasonably large number of commercial heats was to analyse the possible variations in microstructure and non-metallic inclusion content that might be encountered as a result of subtle variations in steel chemistry, with particular emphasis on variations in impurity levels. The fact that the heats are divided into two groups, A1-A14 and B1-B14 does not reflect any difference in their production procedures or gross composition, but rather that impact fracture studies were performed using the alloy group A1-A14 only. The reason for this was that insufficient material was supplied for the machining of impact test specimens from the heats labelled B1-B8. The composition of the heats A1-A14 and B1-B8 are listed in Tables 3.1 and 3.2 respectively.

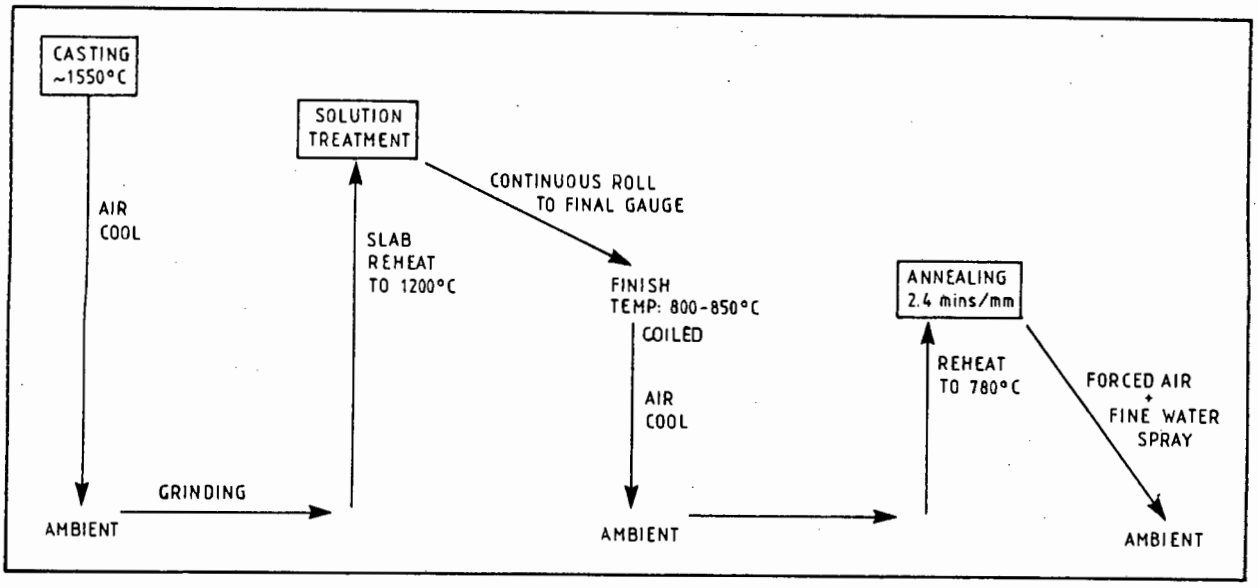

FIGURE 3.10 : Brief summary of the commercial 3CR12 production procedures

TABLE 3.1 : Composition of heats A1-A14. All figures represent wt% [FF = ferrite factor]

ALLOY	C	S	P	Mn	Si	Cu	Ti	Mo	Cr	Ni	Al	N	O	FF
A1	.022	.009	.022	1.13	.74	.06	.25	.05	11.00	.61	.008	.019	.008	11.2
A2	.023	.018	.020	1.17	.40	.01	.26	.04	11.22	.62	.006	.016	.007	09.5
A3	.024	.013	.020	1.20	.43	.06	.30	.05	11.06	.58	.010	.016	.007	09.5
A4	.022	.008	.014	1.22	.42	.12	.30	.05	11.42	.60	.012	.013	.003	10.4
A5	.022	.008	.019	1.19	.44	.07	.31	.05	11.01	.61	.012	.014	.000	10.1
A6	.026	.015	.023	1.16	.44	.06	.35	.02	11.26	.68	.008	.014	.006	10.2
A7	.028	.020	.018	1.22	.44	.05	.36	.01	11.24	.61	.005	.012	.009	10.3
A8	.027	.015	.026	1.23	.40	.13	.34	.07	11.30	.67	.010	.011	.006	10.1
A9	.025	.012	.026	1.23	.41	.04	.47	.02	11.11	.63	.026	.010	.004	11.2
A10	.027	.008	.020	1.20	.34	.03	.39	.02	11.32	.56	.007	.013	.004	10.3
A11	.028	.009	.019	1.22	.35	.06	.30	.05	11.23	.61	.001	.017	.005	09.3
A12	.025	.009	.017	1.16	.49	-	.37	-	11.31	.62	-	.017	-	10.9
A13	.021	.013	.020	1.15	.42	-	.37	.04	11.28	.59	.005	.012	-	10.9
A14	.024	.023	.017	1.13	.46	-	.36	-	11.10	.60	-	.014	-	11.0

TABLE 3.2 : Composition of heats B1-B8. All figures represent wt % [FF = ferrite factor]

ALLOY	C	S	P	Mn	Si	Cu	Ti	Mo	Cr	Ni	Al	N	O	FF
B1	.017	.014	.022	1.24	.35	.11	.52	.04	11.40	.57	.009	.012	.009	12.0
B2	.019	.011	.015	1.09	.28	.07	.46	.04	11.00	.60	.018	.017	.006	10.5
B3	.030	.008	.019	1.28	.42	.03	.46	.04	11.52	.66	.014	.014	.003	11.0
B4	.026	.006	.019	1.20	.55	.06	.23	.04	11.29	.55	.002	.027	.005	09.9
B5	.024	.006	.019	1.27	.36	.01	.48	.03	11.49	.57	.012	.009	.011	11.5
B6	.024	.023	.019	1.13	.37	.07	.21	.04	11.15	.61	.009	.019	.009	08.8
B7	.024	.024	.021	1.18	.42	.09	.35	.04	11.27	.61	.001	.011	.010	10.6
B8	.024	.023	.022	1.07	.40	.10	.40	.04	11.00	.65	.019	.031	.006	09.9

MICROSTRUCTURAL EVOLUTION OF 3CR12

In addition to the examination of the conventional 3CR12 commercial heats, two heats representative of different stages in the production process were also examined in order to trace the evolution of the 3CR12 microstructure (Table 3.3). Alloy C1 represents hot rolled plate which was allowed to air cool to room temperature with no subsequent sub-critical annealing having been carried out. Alloy S1 represents material from the initial cast slab form. This latter heat was employed in the laboratory hot rolling investigations. A third special alloy containing twice the normal nickel level in 3CR12 was included in the investigation and the evolution of its microstructure was compared to that of conventional 3CR12. This alloy, referred to as 3CR12Ni and labelled N1 is included in Table 3.3

TABLE 3.3 : Composition of alloys C1, S1 and N1. All figures represent wt % [FF = ferrite factor]

ALLOY	C	S	P	Mn	Si	Ti	Cr	Ni	N	FF
C1	.023	.005	.027	1.18	.36	.44	11.23	0.58	.011	11.1
S1	.027	.006	.025	1.22	.48	.35	11.40	0.58	.013	10.9
N1	.027	.011	.022	0.90	.47	.23	11.71	1.21	.019	7.9

CHROMIUM AND NICKEL EQUIVALENTS

The average chromium and nickel equivalents for 3CR12 commercial heats and the special 3CR12Ni alloy were calculated according to the following equations (Chapter 2, section 2.3.4) :-

Cr equivalent = %Cr + 2(%Si) + 1.5(%Mo) + 5(%V) + 5.5(%Al)
+ 1.75(%Nb) + 1.5(%Ti) + 0.75(%W)

Ni equivalent = %Ni + %Co + 0.5(%Mn) + 0.3(%Cu)
+ 30(%C) + 25(%N)

The equivalents for 3CR12 and 3CR12Ni are listed in Table 3.4 below.

TABLE 3.4 : Cr and Ni equivalents for 3CR12 and 3CR12Ni

ALLOY	Cr EQUIVALENT	Ni EQUIVALENT
3CR12	12.5	2.3
3CR12Ni	12.9	3.0

-ooOoo-

CHAPTER 4

RESULTS

4.1 GENERAL INTRODUCTION

The experimental results are presented in the following order :-

(i) Characterisation of the 3CR12 microstructure

(ii) Composition analysis of inclusions in 3CR12

(iii) Fracture study of 3CR12

(iv) Microstructural characteristics of 16%Cr duplex ferrite-martensite steels.

It is the intention to present mainly experimental observations and data in this chapter, and to continue with a comprehensive discussion in Chapter 5. However, in order to present the results as clearly as possible, it has been necessary in certain situations to include some discussion.

4.2 CHARACTERISATION OF THE 3CR12 MICROSTRUCTURE

4.2.1 OVERVIEW

The characterisation of the 3CR12 microstructure involved a study of the transformation behaviour of 3CR12 during cooling from 1380°C, and the subsequent composition analysis of the evolved phases. These results were related to the microstructures

developed during laboratory and commercial hot rolling and annealing procedures. The results of this investigation are presented in three parts, namely :-

(i) Transformation behaviour of 3CR12 during cooling from 1380°C
(ii) Morphology and composition of hot rolled and tempered microstructures.
(iii) Reaustenitisation reaction during reheating into the intercritical $\alpha+\gamma$ region.

4.2.2 TRANSFORMATION BEHAVIOUR OF 3CR12 DURING COOLING FROM 1380°C

4.2.2.1 Transformation start-finish temperatures

The delineation of equilibrium transformation temperature regimes for 3CR12 during cooling from just below the solidus temperature was carried out by constructing a pseudo-binary Cr-Ni phase diagram for an isopleth at 85 wt % Fe, (Fig 4.1). Phase boundaries were plotted using the isothermal sections for solid-phase equilibria in the Fe-Cr-Ni system and the vertical composition line for 3CR12 was calculated according to the Ni and Cr equivalent equations discussed in chapter 2. Although a phase diagram of this nature should be interpreted with caution, the binary section is roughly parallel to the tie-lines interpreted from the various isothermal sections for solid phase equilibria and only relatively minor variation in the Fe content is expected. The position of the 3CR12 composition line indicates the existence of a single phase delta-ferrite (high temperature ferrite) structure down to a temperature of approximately 1300°C. Delta-ferrite transforms to austenite below 1300°C and the phase diagram shows that the steel should be fully austenitic in the region extending from approximately 1150°C to 900°C. Below 900°C the austenite structure transforms to alpha-ferrite (low temperature ferrite).

These equilibrium transformation start-finish temperatures are compared in fig 4.2 to the transformation temperatures which were experimentally determined for 3CR12 (Alloy A2) by high temperature dilatometry. After heating to 1380°C, the dilatometer specimens were cooled to room temperature either by switching off the furnace (uncontrolled furnace cooling) or by cooling at a controlled rate of 1°C/minute. The transformation temperatures recorded under both cooling rate conditions are illustrated. In some instances the transformation temperatures are indicated by a range in temperature due to the combination of results for at least three tests for each cooling condition. This is particularly marked in the case of the austenite-finish temperatures due to the difficulties experienced in determining the exact point of inflection on the transformation curve. The cooling interval per 100°C is shown for uncontrolled cooling conditions.

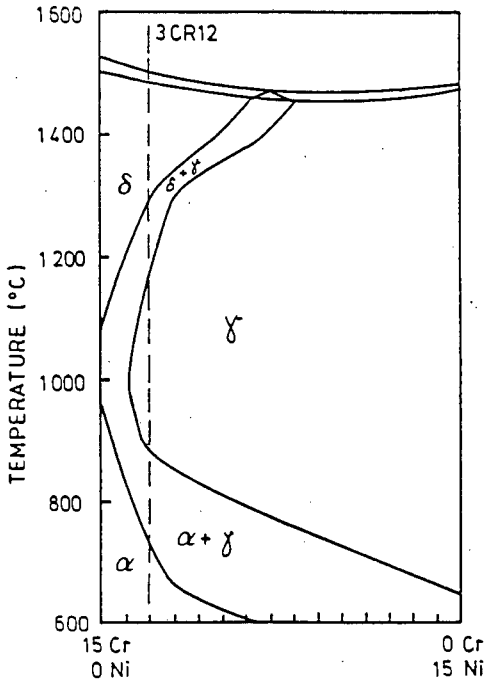

FIGURE 4.1 : Pseudo-binary Cr-Ni phase diagram for 85 wt % Fe drawn from isothermal data presented in chapter 2. Vertical line indicates 3CR12 composition (Cr and Ni equivalents).

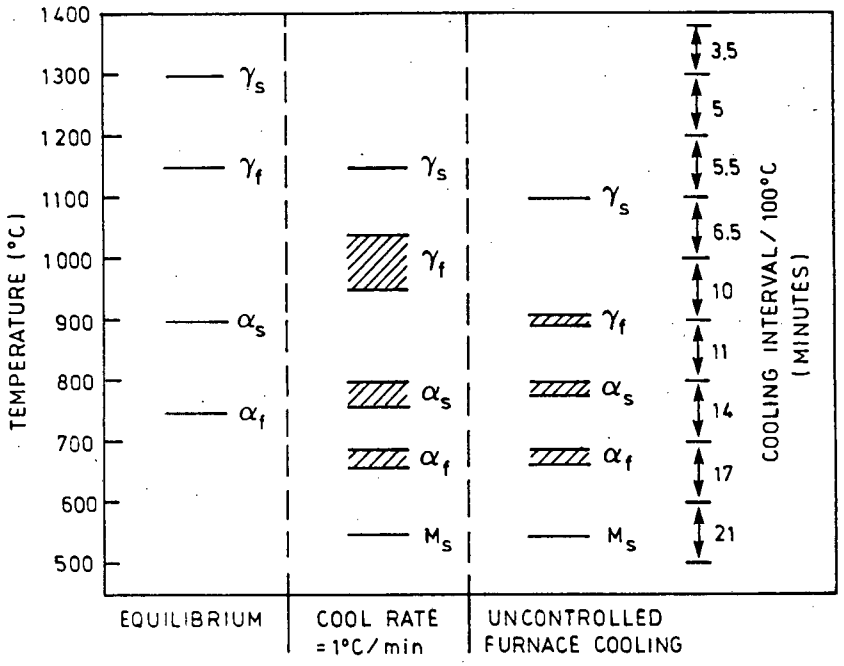

FIGURE 4.2 : Transformation start-finish temperatures for 3CR12 determined from a pseudo-binary equilibrium phase diagram (fig 4.1) and experimental dilatometry [γ_s = austenite start, γ_f = austenite finish, α_s = ferrite start, α_s = ferrite finish, M_s = martensite start, M_f = martensite finish.]

4.2.2.2 Metallography

QUENCH STRUCTURE (1380°C)

The microstructure which resulted after rapidly cooling (oil quenching) alloy A2 from a solution treatment at 1380°C for 1 hour is shown in fig 4.3(a). It is evident from this structure that a single phase (δ-ferrite) existed at this elevated temperature and resulted in extensive grain growth. The appearance of a second phase at the grain boundaries can be identified and indicates the start of the transformation from δ-ferrite to austenite. The majority of these grain boundary precipitates have a "chunky" appearance which resembles the formation of grain boundary allotriomorphs (GBA). However, it seems that in some cases the planar interface of the chunky precipitates has given way to a "sawtooth" growth pattern. This is clearly indicated in fig 4.3(b).

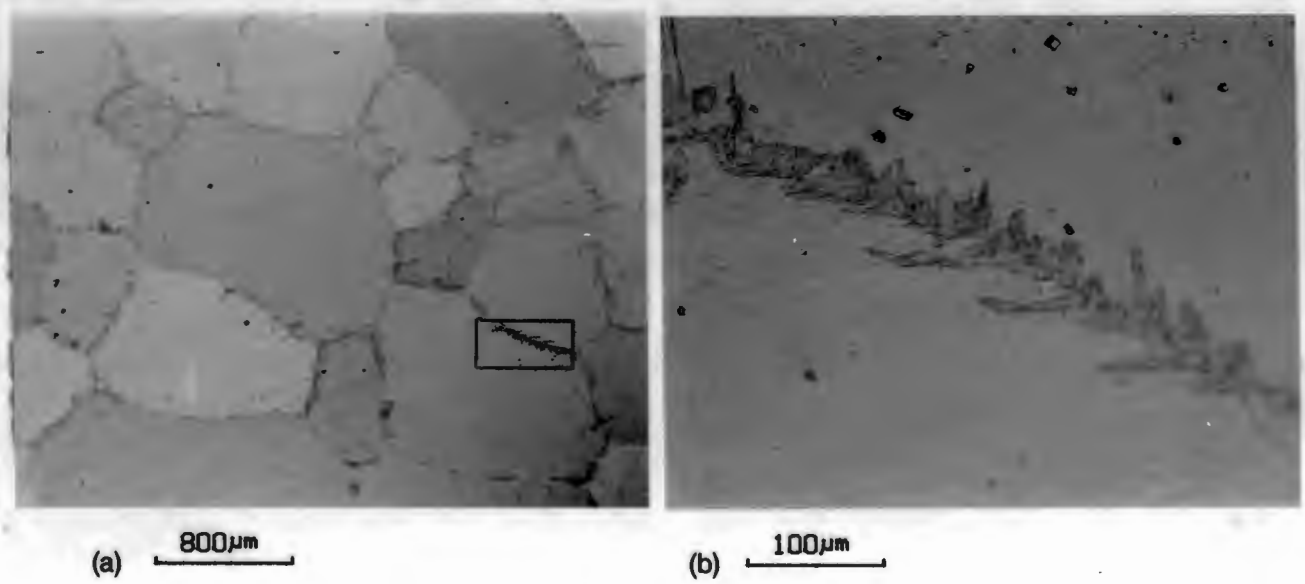

FIGURE 4.3 : 3CR12 microstructure developed after oil quenching from 1380°C [Alloy A2]

(a) Large grained ferrite structure showing second phase precipitation at the grain boundaries.

(b) "Sawtooth" growth pattern of some grain boundary precipitates. [Enlargement of boxed area in (a)].

CONTINUOUS COOLING FROM 1380°C

The microstructure developed after continuous uncontrolled furnace cooling from 1380°C to 950°C followed by rapid quenching from 950°C, is shown in fig 4.4(a). This microstructure indicates the "lathy" phase morphology produced as a result of the transformation from δ-ferrite to austenite. Traces of the first austenite to form outline the original δ-ferrite grain boundaries and residual untransformed ferrite is seen to occur as interlaths. Microhardness measurements in the respective phases indicate that the austenite has transformed to martensite during quenching from 950°C (fig 4.4(b)).

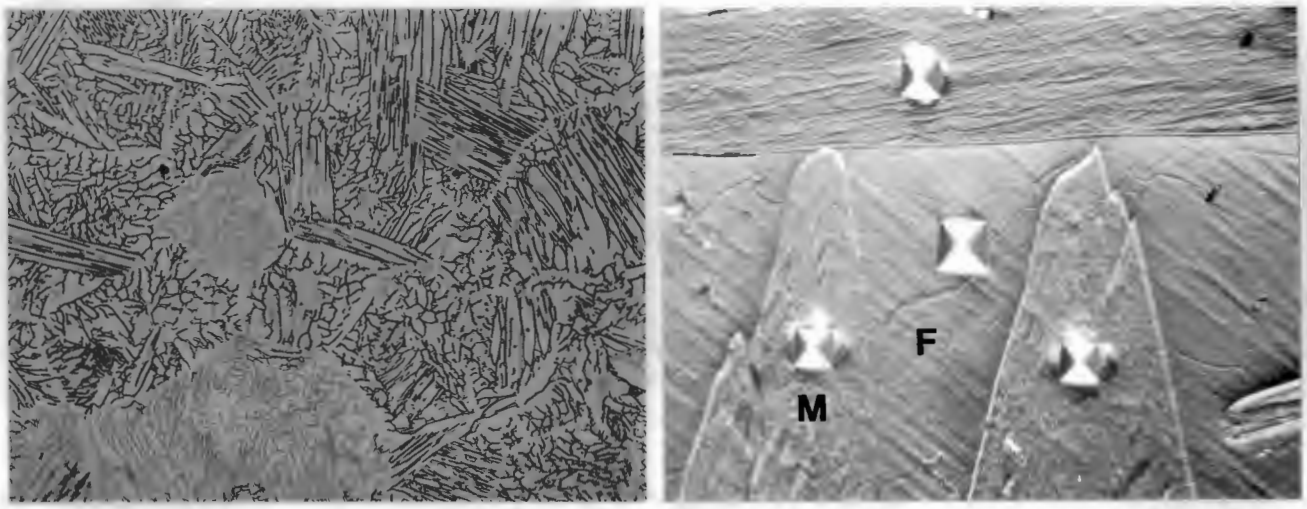

FIGURE 4.4 : Microstructure developed during continuous cooling from 1380°C to 950°C followed by oil quenching [Alloy A2]

(a) "Lathy" ferrite-austenite (now martensite) phase morphology.

(b) Microhardness indentations in ferrite and martensite phases (F = ferrite, M = martensite).

Continuous uncontrolled furnace cooling from 1380°C down to room temperature resulted in the formation of a similar microstructural pattern to that shown in fig 4.4(a). The transformation from δ-ferrite to austenite remained incomplete and the interlath ferrite structure can once again be identified in fig 4.5(a). There is also evidence, however, for the growth of new ferrite (α-ferrite) extending from the δ-ferrite boundaries into the austenite. This growth pattern is shown in fig 4.5(b) using

Nomarski interference contrast. The δ-ferrite interlaths thicken more or less symmetrically and maintain a planar interface. Microhardness indentations indicate a very slight increase in hardness in the now martensite phase compared to the old and new ferrite phases (fig 4.5(c)).

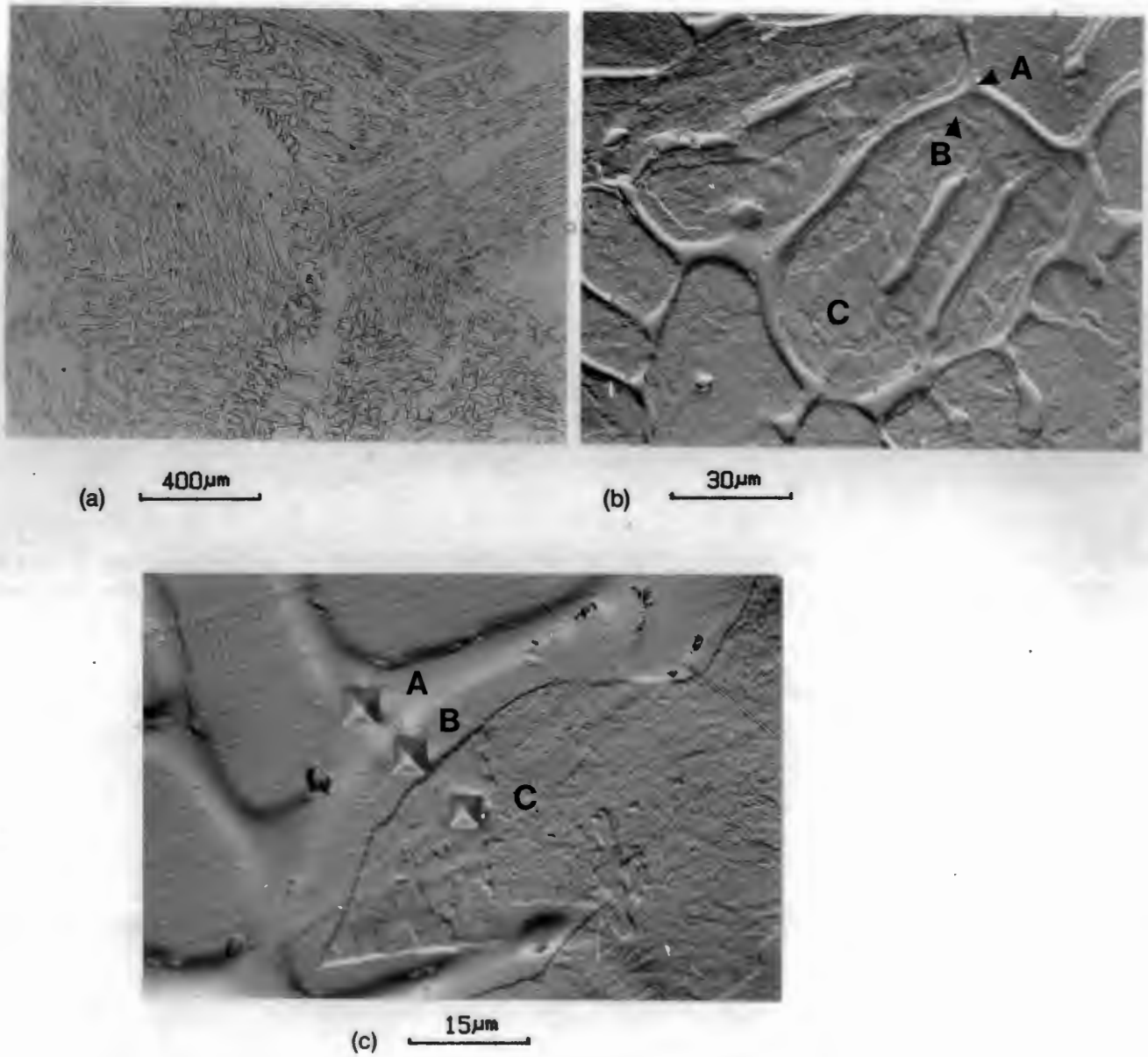

FIGURE 4.5 : Phase morphology due to continuous uncontrolled furnace cooling from 1380°C to 25°C [Alloy A2]. (A = Residual δ-ferrite, B = New α-ferrite, C = Martensite).

(a) Residual δ-ferrite interlaths

(b) Growth of new α-ferrite from δ-ferrite

(c) Microhardness indentations in martensite and ferrite phases

Slower cooling at a rate of 1°C/min from the solution temperature (1380°C) still did not give rise to the complete decomposition of the δ-ferrite phase. Residual δ-ferrite is clearly identified and the interlath patterns are similar to the two aforementioned situations, except that the original δ-ferrite grains were much larger in this instance (fig 4.6(a)). This larger grain size is hardly surprising considering the longer interval sustained in the δ-ferrite phase field due to the slower cooling rate. The growth of α-ferrite has occurred to a much greater extent in this instance and in some cases a vague "sawtooth" ferrite/austenite interface could be identified (fig 4.6(b)). Of further interest is the occurrence of inclusions in the residual δ-ferrite phase.

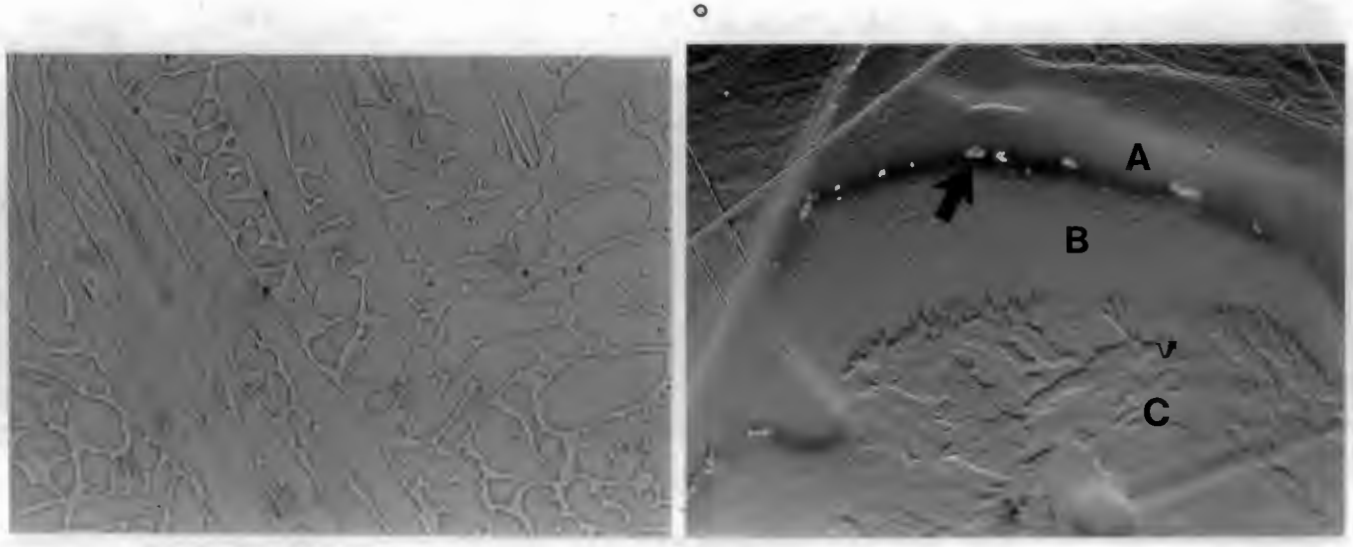

FIGURE 4.6 : Microstructure developed during continuous cooling at 1°C/min from 1380° to 25°C [Alloy A2]. (A = Residual δ-ferrite, B = New α-ferrite, C = Martensite).

(a) Incomplete δ-ferrite to austenite transformation.

(b) "Sawtooth" type α-ferrite growth. Note inclusions in "old" δ-ferrite (arrowed).

The overall hardness of the three microstructures developed during continuous cooling at the various cooling rates is indicated in Table 4.1. Hardness tests were performed using a 1kg load in order to measure the combined effect of the two phase structure. The lower hardness of the two samples continuously cooled to room temperature reflects the growth of α-ferrite and the possible softening of martensite due to the slow cooling rate (auto-tempering).

TABLE 4.1 : Hardness of 3CR12 as a function of cooling rate from 1380°C.

COOLING RATE	HARDNESS (HV_{1Kg})
1380 $\xrightarrow{FC}$ 950 $\xrightarrow{OQ}$ 25°C	280
1380 $\xrightarrow{FC}$ 25°C	180
1380 $\xrightarrow{1°C/min}$ 25°C	140

FC = Furnace cool (uncontrolled); OQ = Oil quench.

PHASE STRUCTURE OF 3CR12Ni AFTER CONTINUOUS COOLING FROM 1380°C.

The 3CR12Ni alloy (Alloy N1), containing double the nickel content of 3CR12 (ie 1.2 wt%), was allowed to continuously furnace cool from 1380°C at an uncontrolled rate. The resultant microstructure is illustrated in fig 4.7(a). Once again a "lathy" ferrite structure in an austenite (now martensite) matrix is generated. The structure appears very similar to that evolved from 3CR12 even though the higher austenite promoting element content favours a more complete transformation from δ-ferrite to austenite. The commercial hot rolled microstructure of 3CR12Ni is reproduced in fig 4.7(b). It is clear that residual δ-ferrite occurs as long thin bands parallel to the rolling direction.

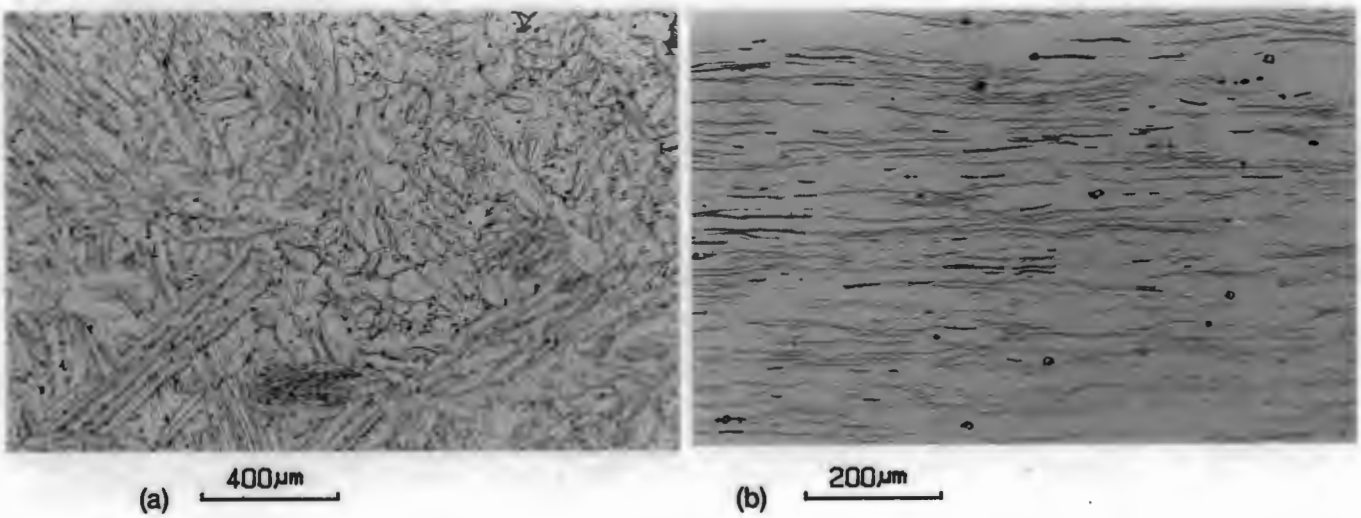

FIGURE 4.7 : Ferrite-martensite microstructure of 3CR12Ni [Alloy N1].

(a) Continuous cooling from 1380°C ("lathy" ferrite-martensite structure)

(b) Hot rolled microstructure (thin bands are residual δ-ferrite in a martensitic matrix)

4.2.2.3 Microanalysis

Energy dispersive X-ray spectroscopy (EDS) analysis of the microstructures developed during the δ-ferrite to austenite transformation indicated element partitioning between the ferrite and austenite phases during the transformation. Results show that the main ferritiser, chromium, has partitioned to the residual δ-ferrite phase, whereas the austenite forming substitutional elements, nickel and manganese, have partitioned to the transformed austenite phase. It is important to note, however, that EDS analysis of the austenite precipitated during rapid cooling from 1380°C did not indicate any partitioning with respect to substitutional elements. Table 4.2 lists the compositions obtained for the δ-ferrite and martensite phases formed after furnace cooling from 1380°C to 950°C followed by oil quenching to room temperature.

TABLE 4.2 : Microanalysis of δ-ferrite and martensite phases evident after furnace cooling from 1380°C to 950°C followed by oil quenching. (Figures indicate weight percentage).

ELEMENT	δ-FERRITE	MARTENSITE
Si	0.5 ± 0.1	0.4 ± 0.1
Ti	0.2 ± 0.1	0.2 ± 0.1
Cr	11.1 ± 0.1	9.1 ± 0.1
Mn	0.7 ± 0.1	0.9 ± 0.1
Ni	0.3 ± 0.1	0.8 ± 0.1

Similar partitioning trends in the residual δ-ferrite and martensite phases were observed during continuous cooling from 1380°C to room temperature. The composition of the new ferrite which has grown from the residual δ-ferrite into the austenite has also been determined and has the same substitutional element composition as the parent austenite (now martensite) phase. Table 4.3 lists the compositions analysed for the residual δ-ferrite, new ferrite (α-ferrite), and martensite phases. These compositions were determined for the areas indicated as A, B, and C in fig 4.5 (c).

TABLE 4.3 : Microanalysis of the residual δ-ferrite, new α-ferrite, and martensite phases indicated in fig 4.5(c) (Wt %).

ELEMENT	δ-FERRITE	α-FERRITE	MARTENSITE
Cr	11.4	9.9	9.8
Mn	0.8	1.0	1.0
Ni	0.4	0.6	0.6

Composition analysis of the inclusions identified in the specimen cooled from 1380°C to 25°C at 1°/min (see fig 4.6(b)) indicated significant concentrations of titanium and phosphorous as well as iron and chromium. An example of the analysis of these inclusions observed in the SEM (fig 4.8(a)) is illustrated in fig 4.8(b). Much of the iron and chromium content illustrated in this spectrum (fig 4.8(b)) probably resulted from the interaction of the electron beam with the steel matrix. This interaction is due to the sub-micron size of the precipitates. The chromium and nickel concentrations are also indicated for the residual δ-ferrite and prior austenite phases.

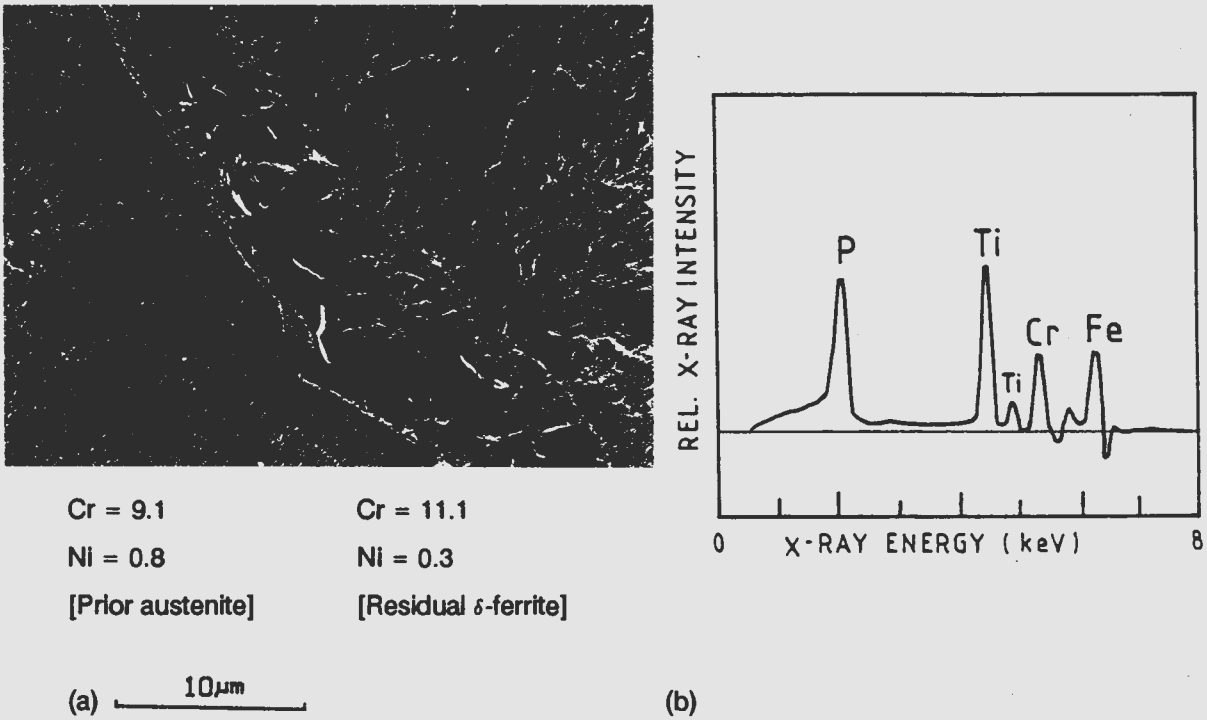

FIGURE 4.8 : Microanalysis of inclusions occurring in the residual δ-ferrite phase. (Continuous cooling at 1°C/min from 1380°C to room temperature).

(a) SEM image

(b) Analysis of fine precipitates arrowed in (a).

4.2.3 MORPHOLOGY AND COMPOSITION OF HOT ROLLED AND TEMPERED MICROSTRUCTURES

4.2.3.1 Metallography of rolled structures

LABORATORY ROLLING

A 10 mm thick sample cut from the slab material (Alloy S1) was hot rolled to a total reduction of 80%. The sample was soaked at 1100°C for 30 minutes prior to rolling and then steadily reduced until rolling was terminated at approximately 700°C - 750°C. Following the rolling procedures, the rolled strips were either oil quenched immediately after the last pass, or immediately reheated to approximately 800°C and cooled down slowly in the furnace to room temperature.

The oil quenched microstructure is indicated in fig 4.9. Alternating ferrite and martensite bands exist parallel to the rolling plane with the martensite bands generally occurring thicker than the ferrite bands. The higher magnification secondary electron micrograph in fig 4.9(b) reveals a sharp interface between the two phases. During etching the ferrite phase has dissolved at a much faster rate than the martensite phase.

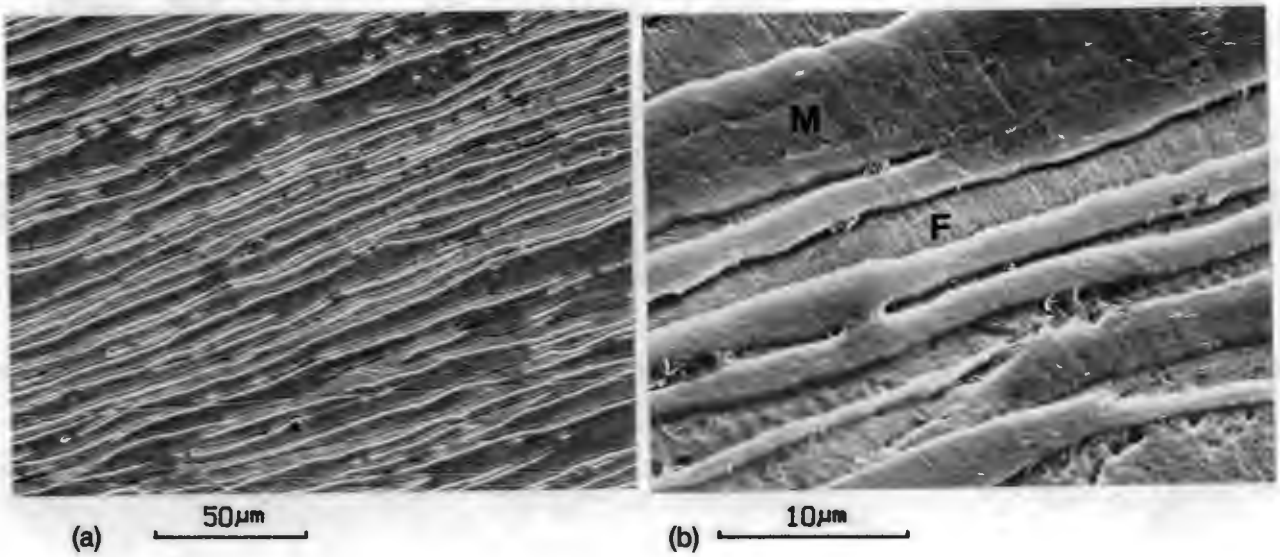

FIGURE 4.9 : Rolled ferrite - martensite microstructure evident after directly quenching from the finish roll temperature of 700°C (Alloy S1 etched in solution B. F = ferrite, M = martensite). [L-ST orientation]

(a) Banded ferrite-martensite microstructure

(b) Well defined ferrite-martensite interface

The microstructures of the rolled strips which were furnace cooled after the last reduction are illustrated in fig 4.10. The strips were furnace cooled at two different rates in order to determine the transformation behaviour of the rolled structure. In fig 4.10(a), after cooling at 5°C/min between 800° and 500°C, the banding is still very prominent, but in some instances the ferrite boundaries appear to have migrated into what was previously the austenite bands. However, in the case of much slower cooling at 1°C/min between 800°C and 500°C, the coarse banding has disappeared and long indulating grain boundaries parallel to the original banding remain (fig 4.10(b)). The thickness and orientation of the new elongated grain structure is reminiscent of the original two phase banded structure depicted in fig 4.9.

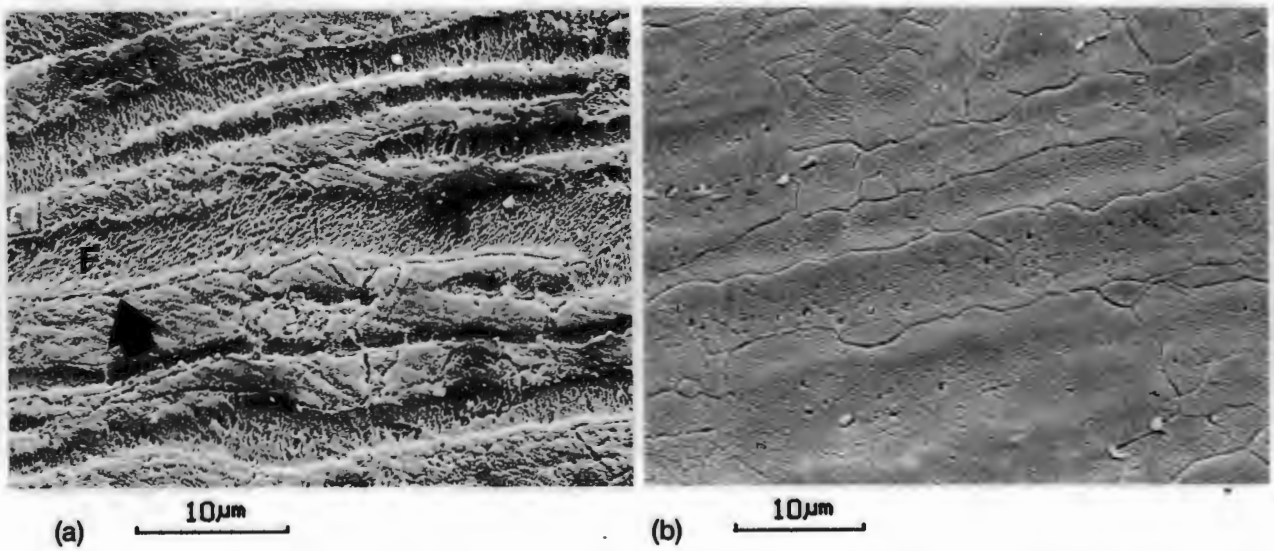

FIGURE 4.10 : Rolled strip furnace cooled from approximately 800°C to room temperature after hot rolling. (Alloy S1 etched in solution B). [L-ST orientation]

(a) Evidence of migrating ferrite grain boundaries (arrowed) [5°C/min]

(b) Undulating boundaries parallel to the original banding [1°C/min]

PRODUCTION PLANT ROLLING

As illustrated in section 3.2, the rolled plate is coiled and allowed to air cool to room temperature subsequent to the termination of reduction in the temperature range between 800°C and 850°C. The microstructure developed as a result of this procedure is exhibited in fig 4.11 (a),(b),(c) and (d). Once again a banded ferrite / prior austenite structure exists parallel to the rolling direction and the original ferrite bands appear to have recrystallised. Figure 4.11(b) illustrates the recrystallisation in

the ferrite more clearly. Similar evidence of ferrite grain boundary migration to that indicated in fig 4.10(a) is shown in fig 4.11(c). In the case of fig 4.11(d), ferrite grain boundaries are seen to migrate towards each other from either side of a prior austenite band. The centre region of the prior austenite band (labelled A) is now martensite whereas the new α-ferrite regions (labelled B) border either side of the martensite band. The residual δ-ferrite band is labelled C.

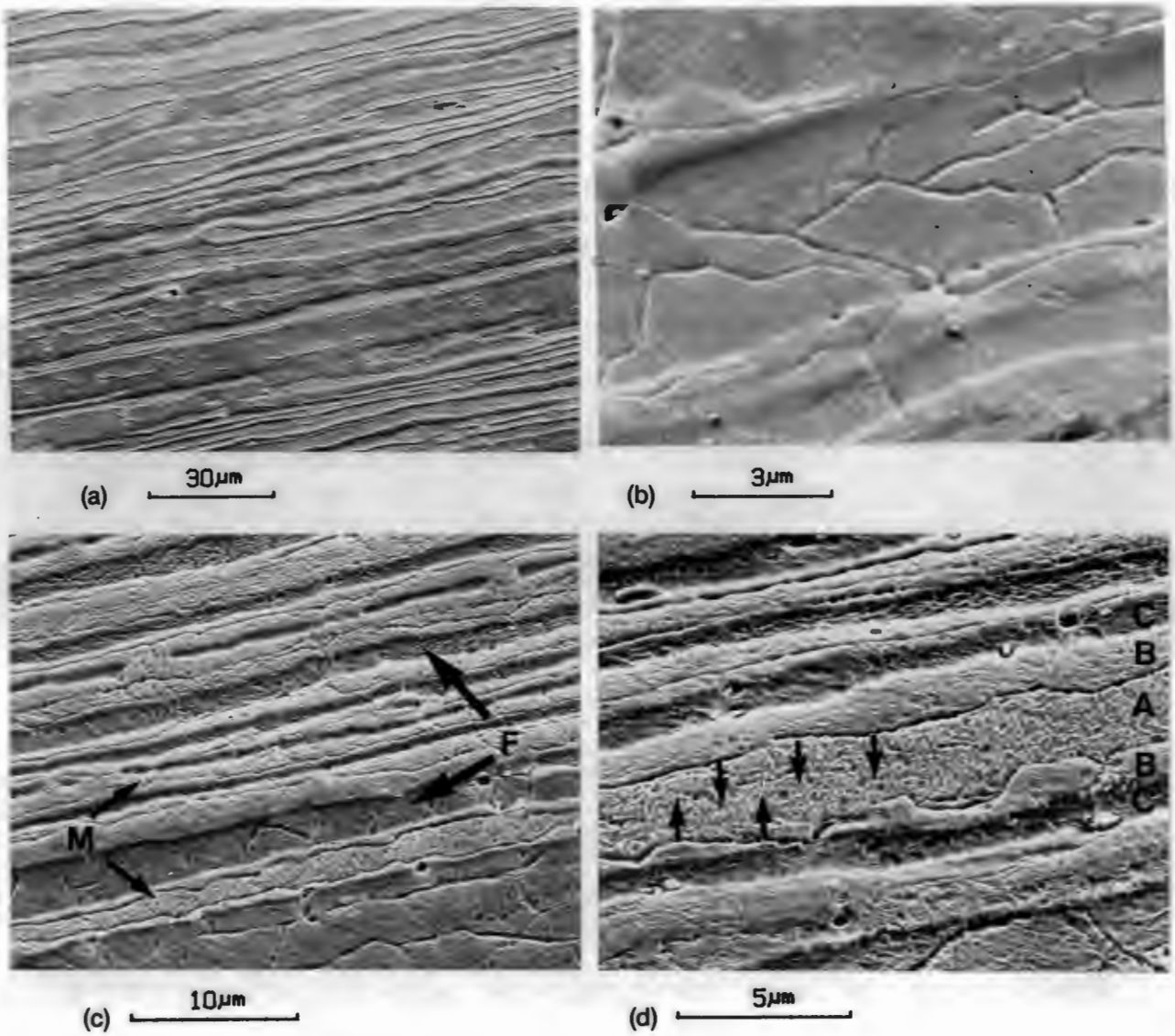

FIGURE 4.11 : Microstructure of production hot rolled 3CR12 (Alloy C1 etched in solution B). A = Martensite, B = α-ferrite, C = Residual δ-ferrite. [L-ST orientation]

(a) Banded phase structure

(b) Recrystallisation within the original δ-ferrite band

(c) Evidence for the migration of the original δ-ferrite/austenite interface into the austenite.

(d) Original austenite band transformed to α-ferrite and martensite.

4.2.3.2 Tempered microstructures

Subsequent tempering of the hot rolled structure illustrated in fig 4.11 was carried out at 780°C for holding intervals of 5, 10 and 20 minutes. The bulk hardness after each treatment (Table 4.4) indicates a gradual, although very slight, softening of the microstructure which is consistent with the decomposition of the remaining low carbon martensite. Figure 4.12 indicates the start of grain coalescence which is evident even after five minutes and increases with longer holding periods. The shadow effect produced by the remnant banded structure can still be seen.

TABLE 4.4 : Hardness vs tempering time at 780°C.

TEMPERING TIME	HARDNESS (HV_{30})
HOT ROLLED	174
5 minutes	162
10 minutes	161
20 minutes	159

FIGURE 4.12 : Ferrite grain coalescence visible after 5 minute temper at 780°C. Electrolytically etched in oxalic acid). [L-ST orientation]

A typical microstructure produced as a result of continuous sub-critical annealing, or tempering, carried out in the production plant is indicated in fig 4.13. Under these conditions plate material is soaked at 750° - 780°C for 2 - 3 minutes per millimetre thickness. The resultant microstructure is fully ferritic with a pronounced pancake morphology. Figures 4.13(a) and 4.13(b) represent the same specimen, but have been etched differently. In the case of fig 4.13(b) the shadow effect reminiscent of the original banded structure is still visible. The reason for this shadow effect is investigated in section 4.2.3.3.

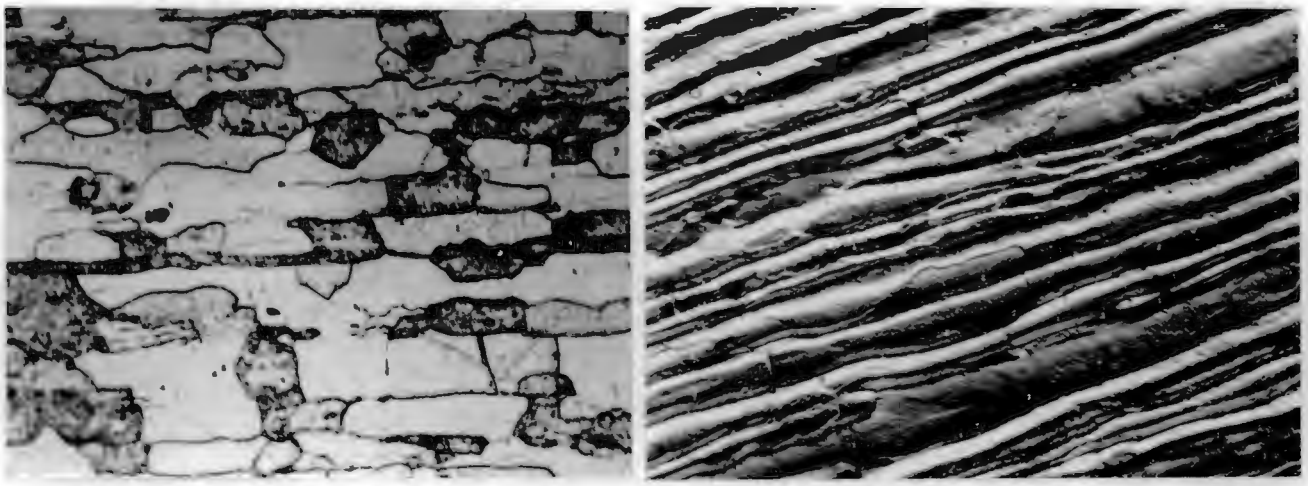

FIGURE 4.13 : Microstructure of 3CR12 in the hot rolled and tempered condition. [L-ST orientation]
(a) Etched in solution A
(b) Electrolytically etched in oxalic acid

4.2.3.3 Microanalysis

Composition analysis of the banded features distinguishable in the laboratory rolled and quenched, production hot rolled, and continuously tempered structures reported in the preceding sections was carried out using EDS. Analysis of the ferrite and martensite bands visible in the laboratory rolled and quenched structure (fig 4.9) indicates marked substitutional element partitioning which is consistent with partitioning trends observed during the δ-ferrite decomposition study (section 4.2.3). Average Cr, Ni, and Mn concentrations for the respective ferrite and martensite

bands are indicated in Table 4.5(a). A similar degree of partitioning is detected in the production hot rolled structure. Relative concentrations for the areas A, B, and C annotated in fig 4.11(a) are listed in Table 4.5(b). These analyses show similar substitutional element concentrations for the new ferrite (α-ferrite) grains and the prior austenite bands

TABLE 4.5 : Microanalysis of banded structures [(a) = Alloy S1; (b) = Alloy A2]

(a) Laboratory hot rolled and quenched

PHASE	Cr	Ni	Mn
MARTENSITE	11.1±0.1	0.6±0.1	1.4±0.1
FERRITE	12.8±0.2	0.4±0.1	1.2±0.1

(b) Production hot rolled (see fig 4.11 for areas A, B and C)

AREA	Cr	Ni	Mn
A (Martensite)	10.8	0.7	1.6
B (α-ferrite)	10.9	0.7	1.6
C (δ-ferrite)	12.1	0.5	1.4

The commercial hot rolled and tempered microstructure (alloy A2), which is fully ferritic, was etched in solution C in order to produce a tint banding effect. This is illustrated by the appearance of dark bands in fig 4.14. The average relative Cr and Ni concentrations in the alternating dark and light tint bands exhibit element partitioning consistent with the partitioning trends detected for the alternating δ-ferrite/prior austenite bands in the case of the previously analysed hot rolled structures. Typical results are listed in Table 4.6. The shadow effect produced when etching tempered structures in oxalic acid (fig 4.13(b)) can thus be explained by the occurrence of compositional banding which is still evident in the tempered condition.

TABLE 4.6 : Average Cr and Ni concentrations (wt%) for the alternating dark and light bands in fig 4.14.

AREA	Cr	Ni
DARK	12.2 ± 0.2	0.5 ± 0.1
LIGHT	10.9 ± 0.2	0.7 ± 0.1

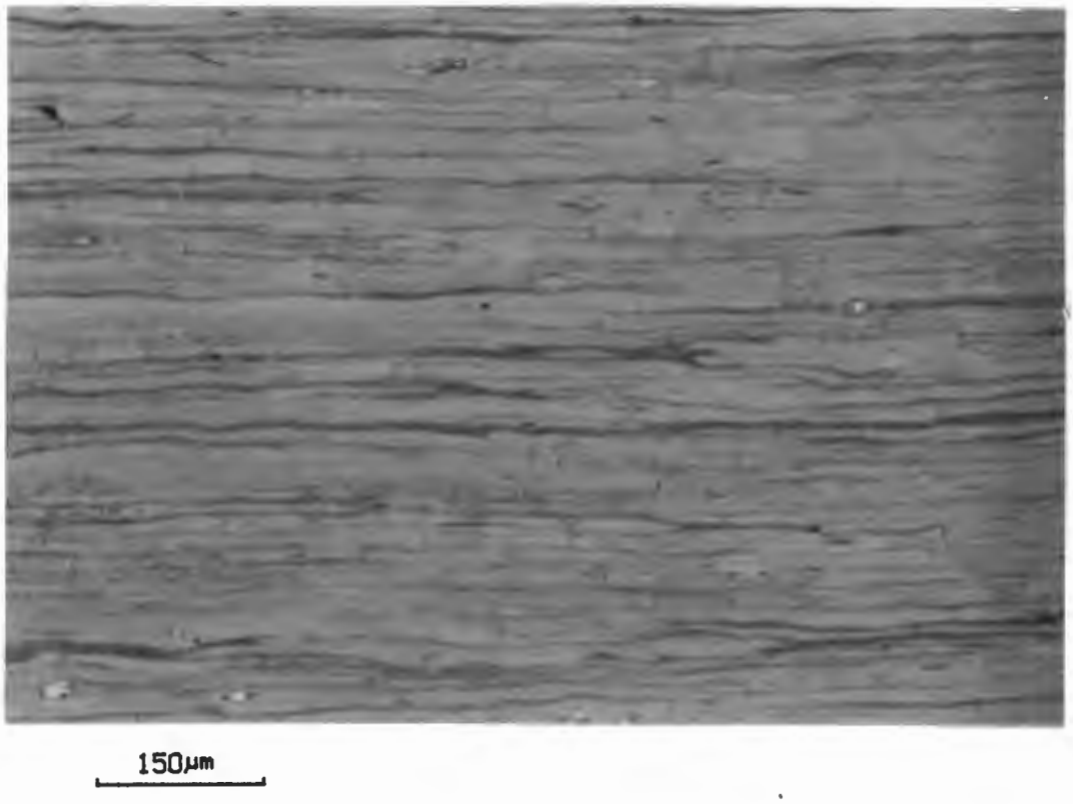

FIGURE 4.14 : Tint banding evident in commercially tempered (at 780°C) 3CR12. (Alloy A2 etched in solution C). [L-ST orientation]

4.2.4 REAUSTENISATION REACTION DURING REHEATING INTO THE INTERCRITICAL $\alpha + \gamma$ REGION

Reheating of the tempered (now fully ferritic) microstructure (Alloy A2) to temperatures between 850°C and 950°C resulted in the formation of austenite which subsequently transformed to martensite when cooled (oil quenched) to room temperature. The microstructures for specimens held at 850°C, 900°C and 950°C, for 1 hour, are shown in fig 4.15 (a), (b), and (c) respectively. It is evident from these three micrographs that the austenite (now martensite) content has increased with increasing temperature. This is also reflected in the increase in bulk hardness which is listed in Table 4.7. Although reaustenitisation has occurred to a greater or lesser extent in each case, directionality is still maintained with respect to the ferrite content. The ferrite banding exhibited after quenching from 950°C is of a similar scale to that indicated by the darker etched bands in the tempered structure illustrated in fig 4.14. This points to the preferential transformation to austenite of the areas richer in austenite forming elements (light bands in fig 4.14), and the corresponding retention of ferrite in the areas which are richer in ferrite forming elements (dark bands in fig 4.14).

Re-tempering of the microstructure previously heated to 950°C was carried out at 780°C. The resultant microstructure, which is reproduced in fig 4.15(d), illustrates that the compositional banding inherent in the original rolled structure is responsible for the maintenance of a directional structure even after cyclic heat treatment of this nature.

TABLE 4.7 : Hardness of 3CR12 after oil quenching from 850°, 900° and 950°C (Alloy A2).

SOAK TEMPERATURE (°C)	HARDNESS (HV_{30})
TEMPER CONDITION	175
850	197
900	227
950	254

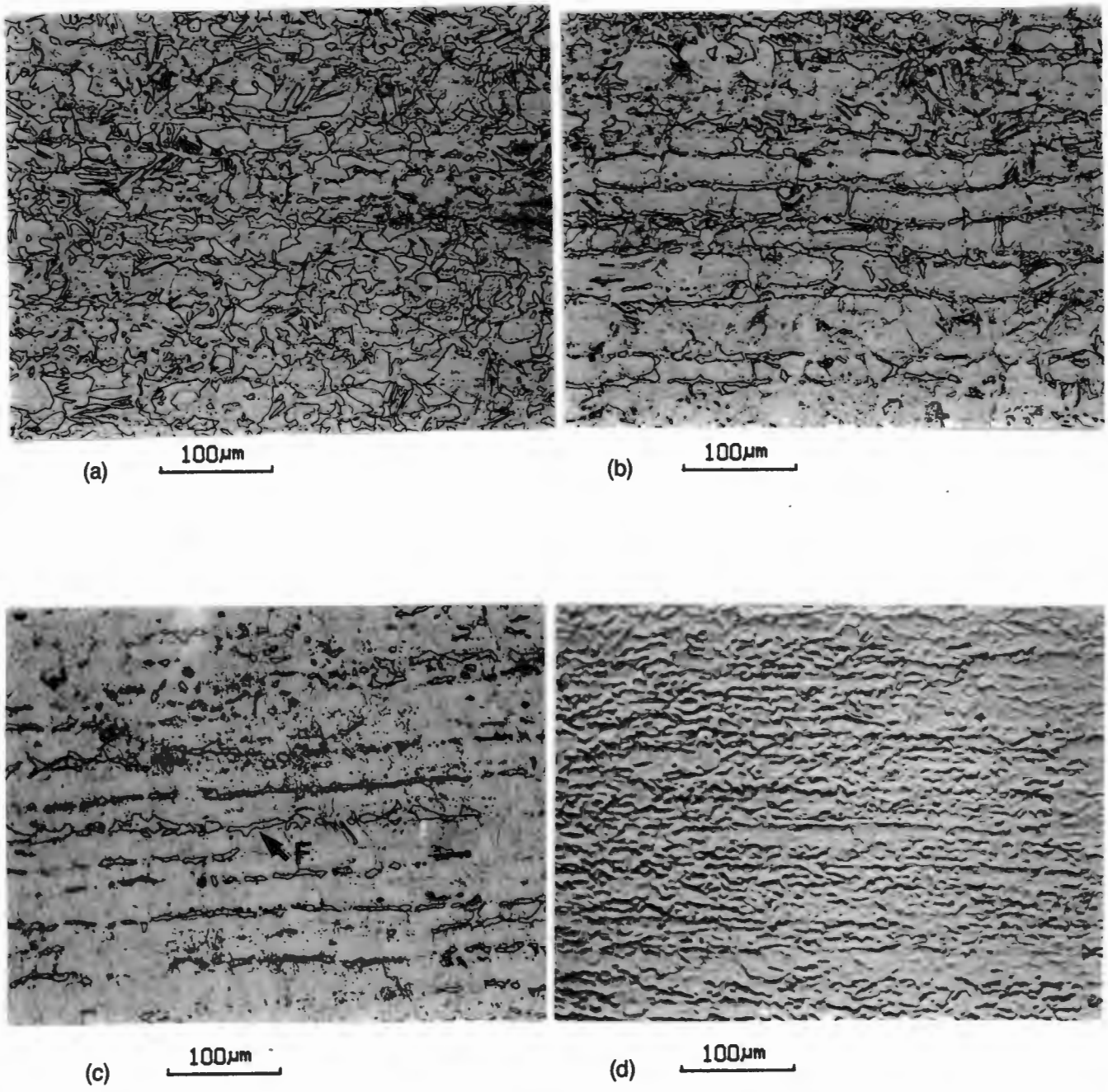

FIGURE 4.15 : Commercially tempered 3CR12 microstructure (alloy A2) reheated into $\alpha+\gamma$ phase region. (Etched in oxalic acid). [L-ST orientation]

(a) Quenched from 850°C after 1 hour

(b) Quenched from 900°C after 1 hour

(c) Quenched from 950°C after 1 hour

S (d) Re-tempered at 780°C after 950°C quench.

4.3 COMPOSITION ANALYSIS OF INCLUSIONS IN 3CR12

4.3.1 OVERVIEW

The composition of non-metallic inclusions occurring in typical run-of-the-mill commercially produced 3CR12 heats was examined (alloy groups A1-A14 and B1-B8). The chemical analysis of these inclusions was related to the bulk composition of the individual alloys.

4.3.2 ANALYSIS OF CUBOID INCLUSIONS

Cuboid titanium containing inclusions are by far the most commonly occurring non-metallic inclusions in 3CR12. Individual cuboid inclusions ranged up to 10 microns in size and occurred both as random dispersions, and as distinct clusters which appeared stringered parallel to the rolling direction (fig 4.16). They were yellow in colour and often had a pink/grey second phase around their boundaries.

FIGURE 4.16 : Typical cluster occurrence of titanium containing cuboid inclusions in commercial 3CR12. (Optical image - etched in oxalic acid).

The composition of these inclusions is illustrated by considering two isolated cuboids occurring in alloy A2 (fig 4.17(a)). A typical X-ray spectrum of the centre of these cuboids can be seen in fig 4.17(b). Because of the limitations of EDS, only titanium was detected, but carbon and nitrogen have been previously identified by means of scanning auger microscopy[90]. In a spectrum of the boundary area, the surrounding phase is shown to consist of titanium and sulphur (fig 4.17(c)).

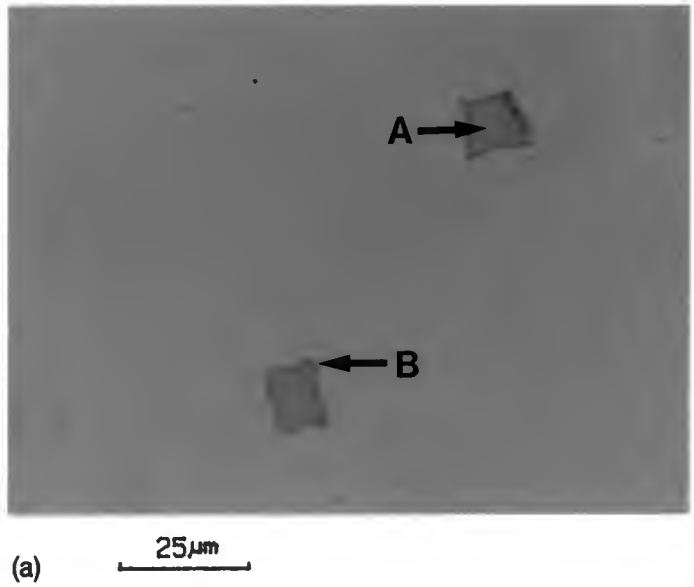

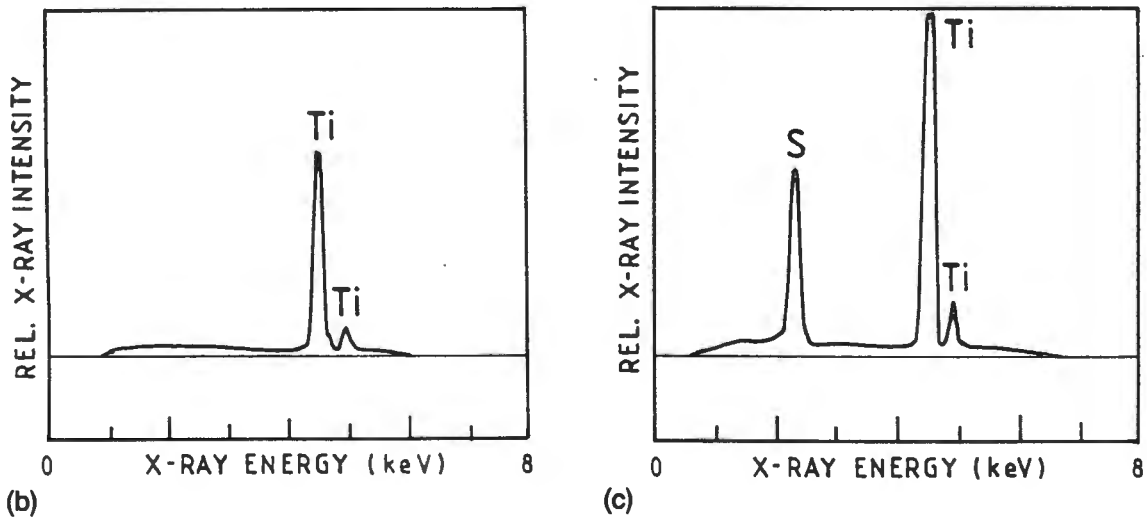

FIGURE 4.17 : Analysis of cuboid inclusions (Alloy A2)

(a) Two isolated cuboids (A,B) show the presence of second phases at their boundaries.

(b) X-ray spectrum from centre of particle A indicates titanium only.

(c) Sulphur is seen to be present in addition to titanium in boundary phase associated with particle B.

In some cases minor amounts of manganese have also been detected at the boundaries and the cuboids do not always appear as well formed as those shown in fig 4.17(a). The presence of manganese and sulphur associated with these titanium bearing inclusions is illustrated in fig 4.18.

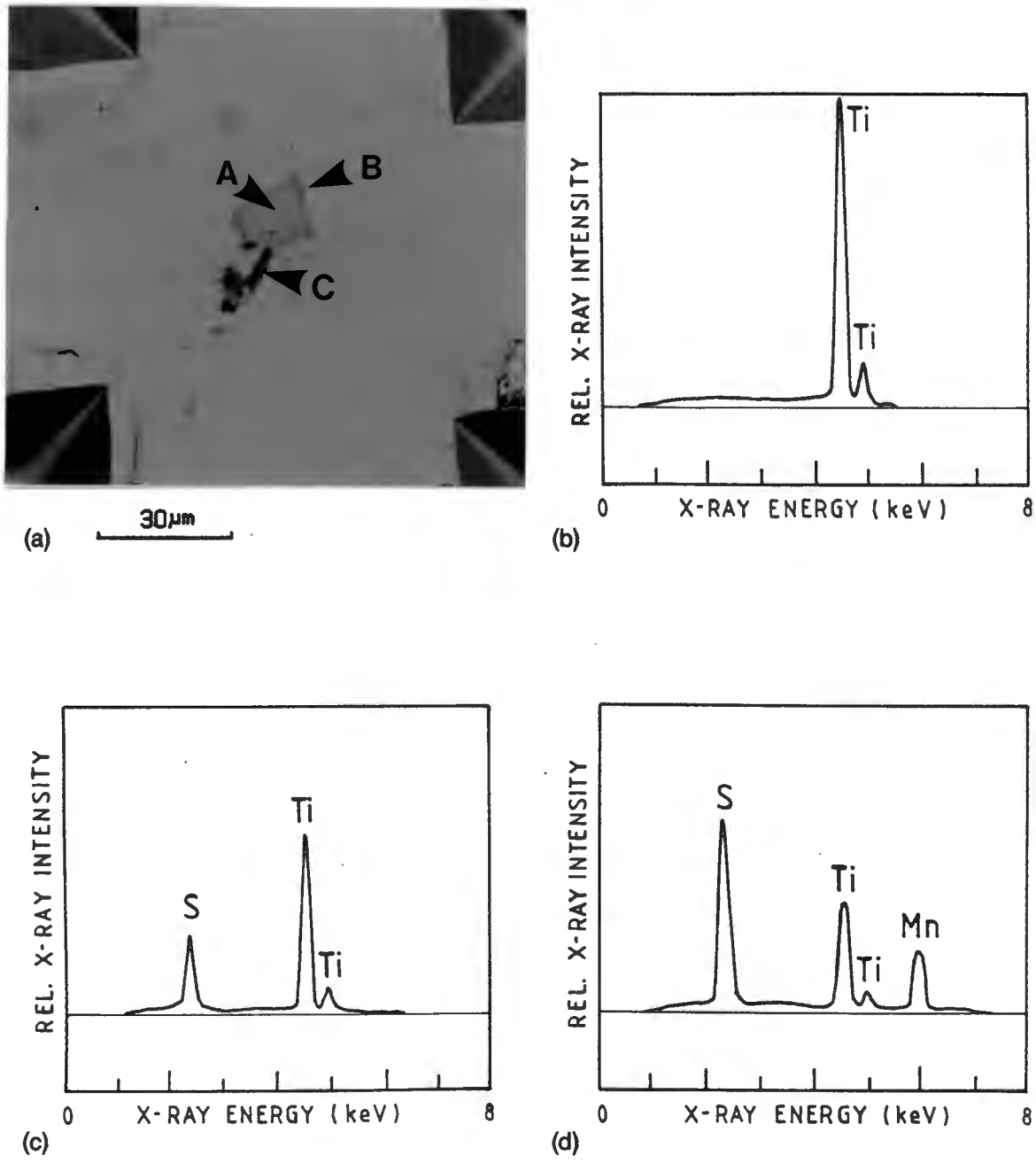

FIGURE 4.18 : Detection of manganese and sulphur at cuboid boundaries (Alloy B6).

(a) Titanium containing cuboid inclusion plus associated phases.

(b) X-ray spectrum of area A

(c) X-ray spectrum of area B

(d) X-ray spectrum of area C

The cuboid inclusion volume fractions were determined for alloys B1 - B8 and are listed in Table 4.8. The large standard deviation values reported are indicative of the wide scattered distribution of these inclusions. An attempt at correlating the volume fractions with the steel compositions indicates a volume-dependence on the nitrogen content of the steel. This is shown in fig 4.19.

TABLE 4.8 : Cuboid inclusion volume fractions for alloys B1 - B8.

ALLOY	VOLUME FRACTION (%)		
	MEAN	STD. DEV.	95% C.L.
B1	0.18	0.47	0.15 - 0.21
B2	0.14	0.48	0.10 - 0.17
B3	0.19	0.51	0.16 - 0.23
B4	0.35	0.80	0.29 - 0.40
B5	0.12	0.36	0.09 - 0.15
B6	0.24	0.59	0.20 - 0.28
B7	0.20	0.59	0.16 - 0.24
B8	0.36	0.94	0.29 - 0.43
	C.L. = confidence limits		

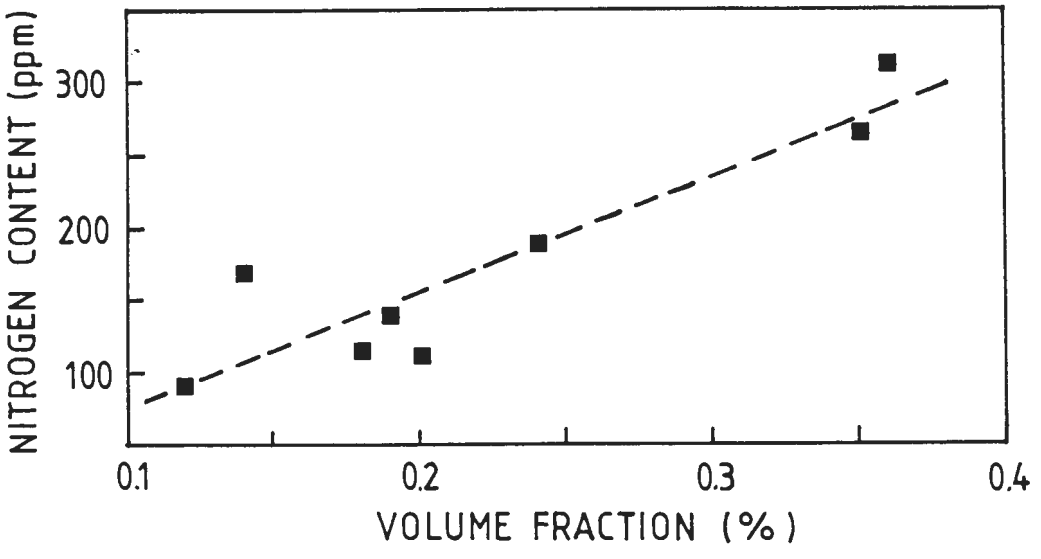

FIGURE 4.19 : Relationship between cuboid inclusion volume fraction and nitrogen content for alloys B1 - B8.

4.3.3 SULPHIDE INCLUSIONS

Manganese sulphide (MnS) inclusions identified in the 3CR12 alloys generally occurred as stringers, but it was noted that their presence is very much dependent on the bulk chemistry of the steel. These inclusions were elongated parallel to the rolling direction and ranged from less than 1 micron up to 20 microns in length. The stringered microphology of a MnS inclusion viewed in the longitudinal-short [L-ST] plane is shown in fig 4.20(a). When viewed in the rolling plane [L-LT], these inclusions appear almost "disc-shaped", as can be seen in figs 4.20(b) and (c), and it can be inferred that they resemble a "pancake" morphology.

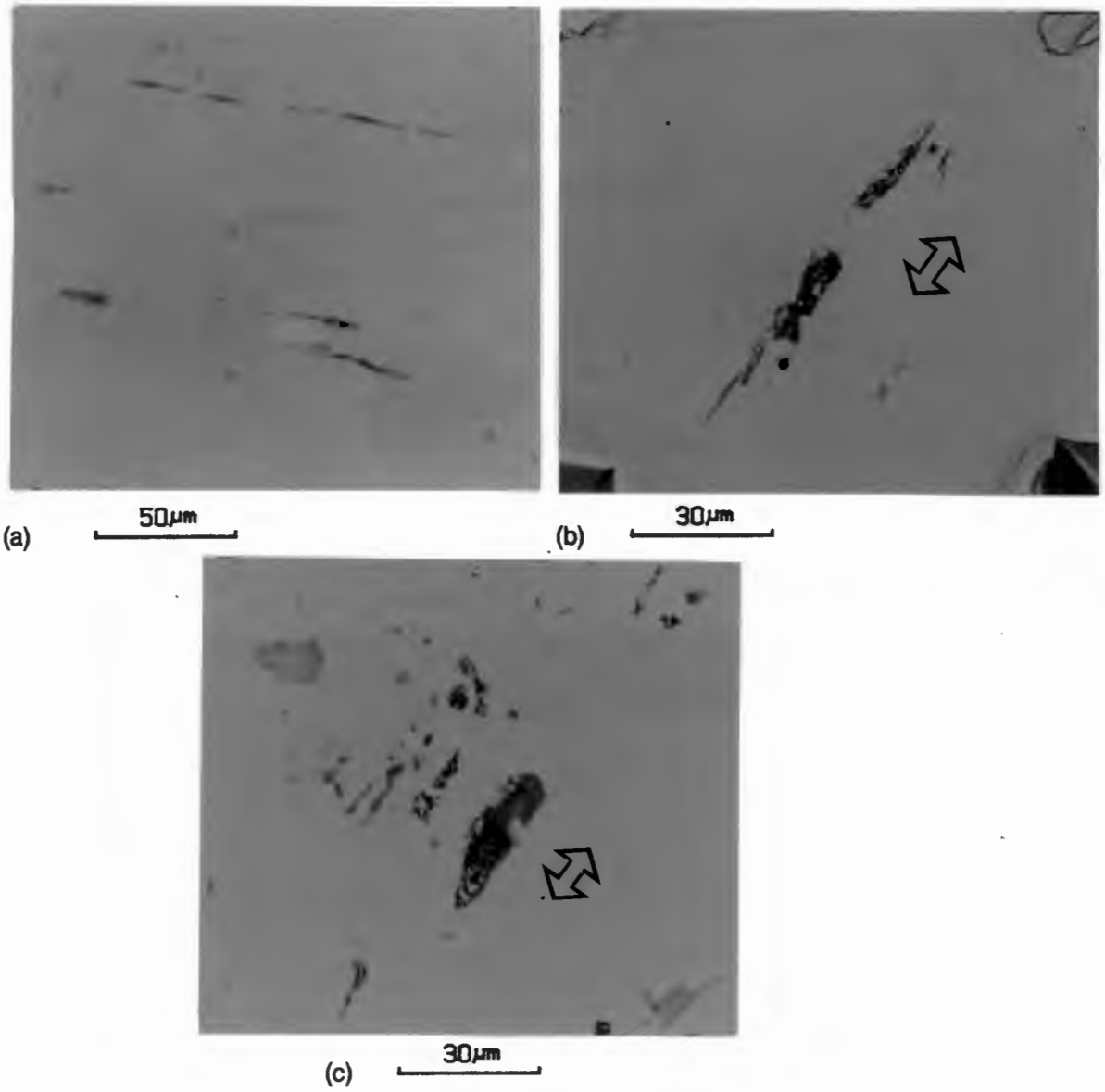

FIGURE 4.20 : Manganese sulphide morphology in alloy B6.

(a) Longitudinal-short plane [L-ST]

(b) and (c) Rolling plane [L-LT]. Arrow indicates rolling direction.

Although isolated homogeneous manganese sulphide inclusions were common in some of the steels examined, varying amounts of titanium were often associated with such inclusions. After considering relative peak intensities from numerous X-ray spectra, it was generally found that the titanium content in these inclusions increases as the Ti/S ratio in the steel increases. Alloy A5, for example, having a Ti/S ratio of 38.75, has shown titanium to be the major metallic element in the sulphide inclusions, with only small amounts of manganese occasionally detected. Alloy A2, on the other hand, has a low Ti/S ratio (14.44) and has shown that manganese is nearly always present in the sulphide inclusions and is often the major metallic element. Typical spectra for sulphide inclusions occurring in alloys A5 and A2 are shown in figs 4.21 (a) and (b) respectively. This variation in the metallic content of the sulphides is hardly surprising since TiS appears to be thermodynamically more stable than MnS, and hence forms in preference to MnS. Further, it confirms that free titanium was available, not all of it being tied up in the carbonitrides. This situation would be different in steels containing more carbon and/or nitrogen.

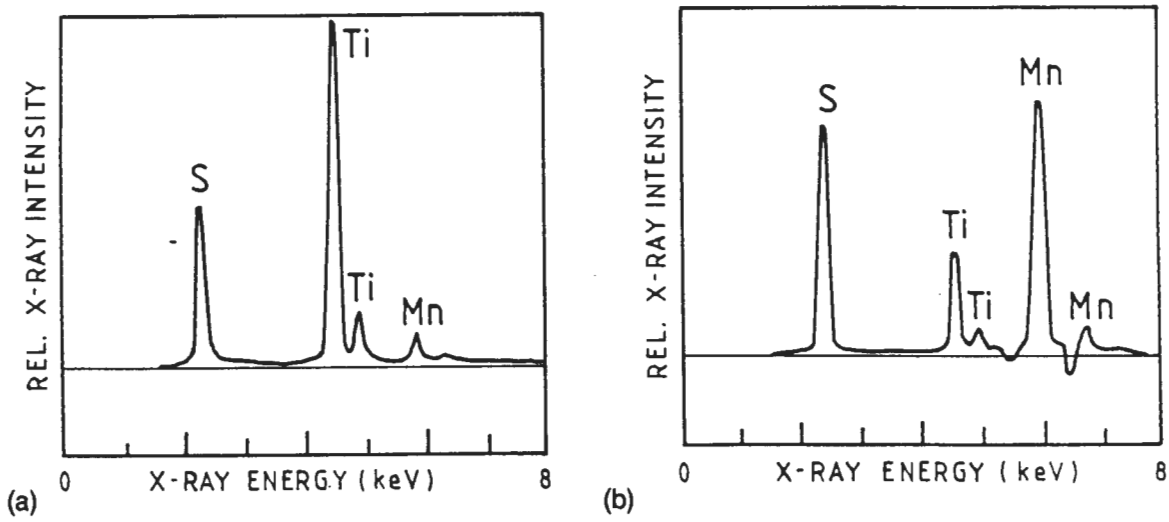

FIGURE 4.21 : Comparison of the composition of sulphide inclusions occurring in alloys A5 and A2.

(a) Alloy A5 - Ti/S ratio = 38.8

(b) Alloy A2 - Ti/S ratio = 14.4

The morphology of the sulphide inclusions changed with increasing titanium content, becoming more globular and less continuous. This variation in morphology is clearly illustrated by considering the inclusions shown in fig 4.22. The stringered sulphide inclusion (labelled A) contains manganese and sulphur with only very minor amounts of

titanium. The inclusion labelled B appears more globular and is seen to contain large amounts of titanium. Cuboid inclusions containing titanium and sulphur at the boundaries are also visible. Steels having Ti/S ratios greater than 40 generally had few or no stringered sulphide inclusions present, and the sulphides occurred mostly at the boundaries of the cuboid inclusions.

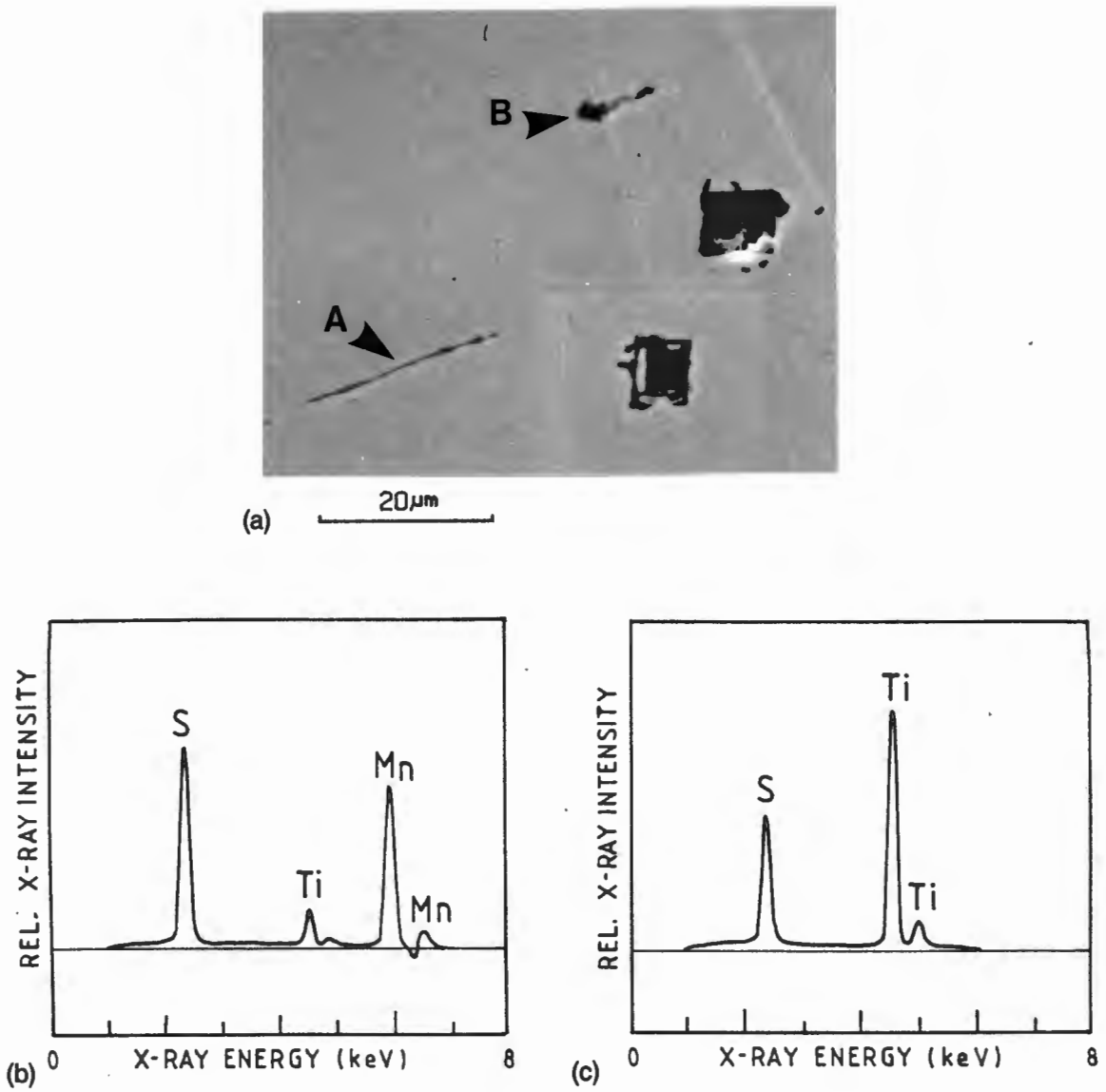

FIGURE 4.22 : Variation in the morphology of sulphide inclusions as a function of inclusion composition.

(a) Inclusions occurring in alloy A3 (Ti/S ratio = 23.1). [L-ST orientation]

(b) X-ray spectrum for inclusion A

(c) X-ray spectrum for inclusion B

Analysis of the predominantly titanium containing sulphide inclusions, occurring either as isolated inclusions or as the boundary phase associated with cuboids, often indicated a

2:1 ratio for the relative intensities of the titanium and sulphur peaks. This is clearly evident from the spectra in figs 4.17, 4.18, and 4.22. This would seem to indicate that the composition in this case is Ti_2S rather than TiS. However, in view of the titanium carbosulphide compound having been previously identified[57], it is more likely that these inclusions have the composition $Ti_4C_2S_2$. Obviously in this case the carbon content is not detected by EDS. The composition of these compounds could be identified using X-ray diffraction and/or electron diffraction techniques, but unfortunately facilities for analytical work of this nature were not readily available.

4.3.4 PRECIPITATE PHASES

Much less obvious non-metallic inclusion distributions were noted when examining specimens which were lightly etched. Fine inclusions, mostly sub-micron in size, were seen to occur in long arrays parallel to the rolling direction. Examination in the SEM showed these inclusions to occur at what could be identified as the prior δ-ferrite/austenite interfaces. This is illustrated in fig 4.23(a) where the fine inclusion arrays appear to delineate the original hot rolled banded structure. EDS analysis, although difficult due to the fine particle size, has shown some particles to contain titanium only, whereas others are seen to contain titanium and phosphorous. However, there appears to be no recognisable difference in the morphology of those inclusions containing phosphorous and those containing titanium only. A typical spectrum of an inclusion containing titanium and phosphorous is indicated in fig 4.23(b).

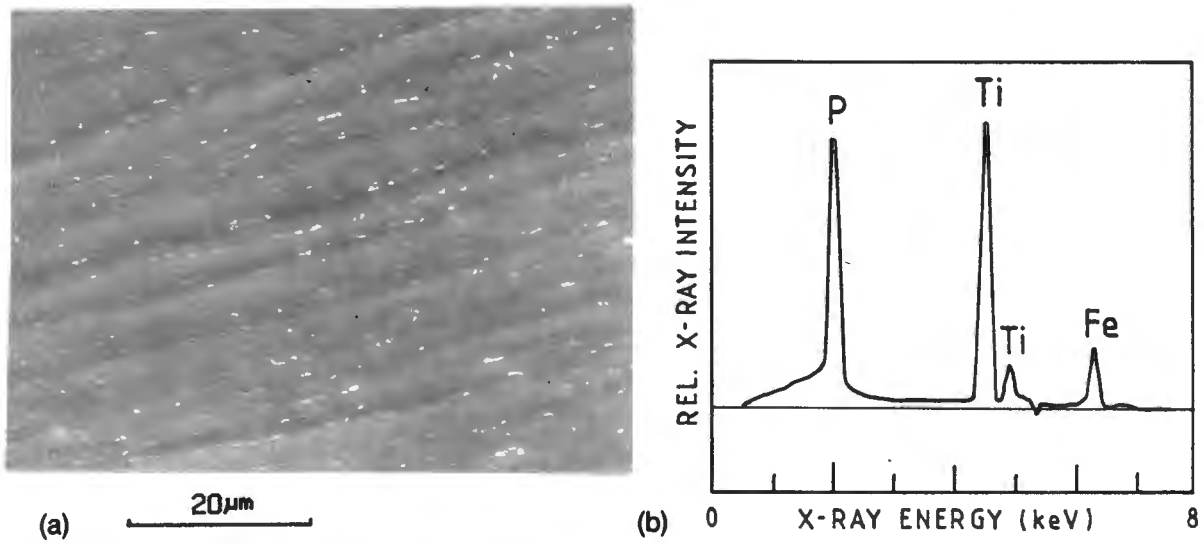

FIGURE 4.23 : Fine inclusions detected in commercially hot rolled and tempered 3CR12 after light etching in oxalic acid.

(a) Occurrence of fine inclusions in alloy A8 (SEM image). [L-ST orientation].

(b) Analysis of a fine inclusion in (a) containing titanium and phosphorous

4.4 FRACTURE STUDY OF 3CR12

4.4.1 OVERVIEW

Charpy V-notch impact testing was performed on fourteen commercial 3CR12 heats (alloys A1-A14) after subjecting all the specimens to a standard heat treatment. Impact energies were compared to the alloy bulk composition and fractography was related to both the occurrence of non-metallic inclusions and the matrix grain morphology.

4.4.2 MICROSTRUCTURAL FEATURES OF TEST SPECIMENS (ALLOYS A1 - A14)

Due to the fact that the sub-critical annealing (or tempering) conditions of the commercially produced heats, A1 - A14, may have varied slightly during the steel production process, all test pieces were subjected to a final laboratory anneal at 800°C for 1 hour, followed by slow cooling in the furnace. This was performed in order to standardise the microstructural condition of the specimens before testing. In this way it was able to more accurately assess the mode of failure, with particular reference to the grain morphology and non-metallic inclusion distributions.

The laboratory heat treated microstructures of all the heats showed fully ferritic grain structures. The ferrite grains were elongated parallel to the rolling direction (Fig 4.24(a)) and also appeared flattened in the transverse plane (fig 4.24(b)). The average grain aspect ratios for the longitudinal direction and transverse direction were determined as 3:1 and 2:1 respectively. Although the ferrite factors for the fourteen heats were not identical, there were no significant differences in the microstructures when comparing the individual heats. The bulk hardness values were all consistent with ferritic microstructures and ranged from 145 to 175 Vickers hardness (30kgf). Random microhardness measurements performed on all of the alloys indicated very little variation in hardness throughout the matrix. The absence of martensite in the annealed microstructure was confirmed by carrying out dilatometric measurements under similar thermal conditions to that experienced during the annealing treatments. A minor amount of austenite was seen to form during the soaking period (1 hour) at 800°C, but subsequently transformed to α-ferrite during cooling to room temperature. There was no indication of a martensite-start transformation.

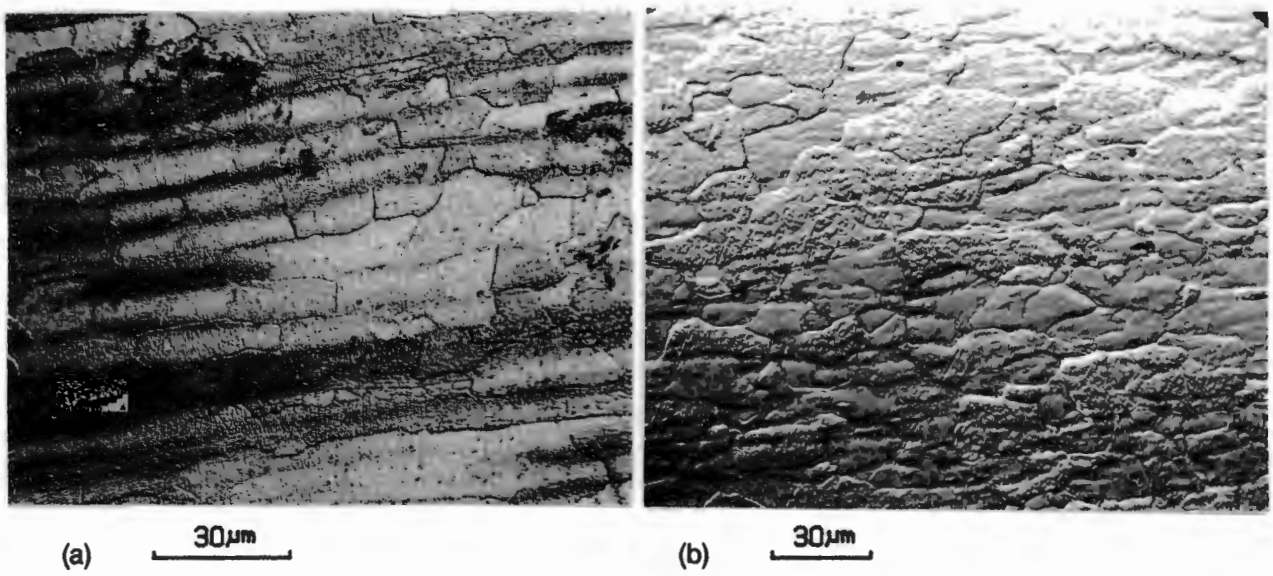

FIGURE 4.24 : Ferrite microstructure of alloy A1 after laboratory annealing.
(a) Longitudinal-short surface [L-ST orientation]
(b) Transverse surface [LT-ST orientation]

4.4.3 CHARPY IMPACT RESULTS

A considerable range of impact energy was obtained for the 14 compositions tested, although results for each composition were fairly consistent (Table 4.9). An attempt at correlating impact energies with elemental compositions and ratios of the various elements yielded two trends as shown in fig 4.25. In fig 4.25 (a), a general decrease in impact energy with increasing sulphur content is indicated. This result is in agreement with Spitzig and Sober[62] who showed a definite decrease in upper shelf energy with increasing sulphur content for 0.10 and 0.20 wt. % carbon steels. They have noted the effect to be particularly marked for through thickness specimens and can be attributed to the increase in volume fraction of stringered manganese sulphide inclusions with increase in sulphur content. In fig 4.25(b), however, the impact energy is shown to increase with increasing Ti/S ratio and the data points correlate slightly better than the previous graph. Since increasing the titanium content decreases the probability of manganese sulphide formation and also changes the morphology of the inclusions, it appears that the presence of titanium sulphide is less deleterious to the impact energy than stringered manganese sulphide inclusions. However, Ti(CN) cuboids may also contribute towards impact energy losses, although variations are not very evident.

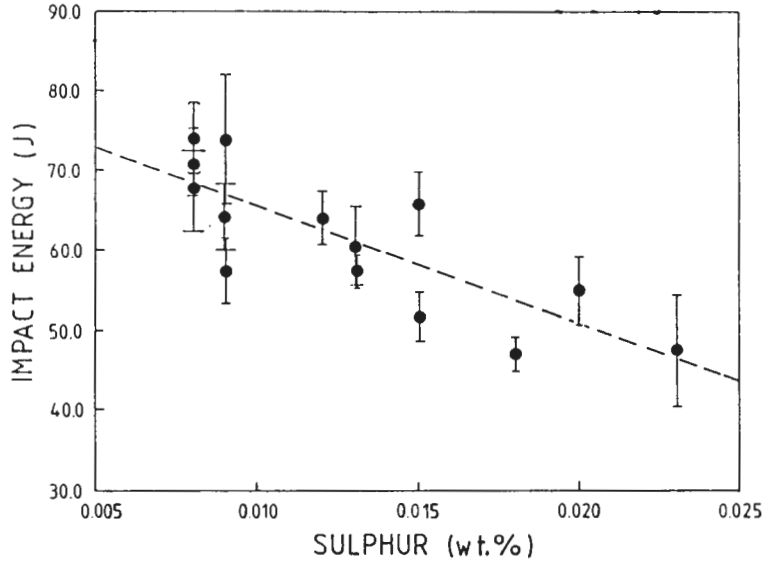

(a)

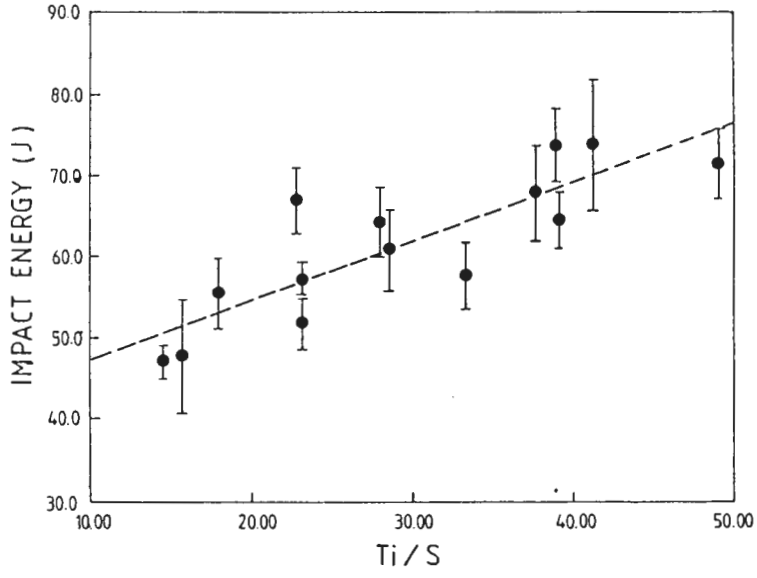

(b)

FIGURE 4.25 : Dependence of room temperature impact energy on titanium and sulphur contents of 3CR12 alloys A1-A14.

(a) Sulphur content

(b) Ti/S ratio

In view of the increased activity of titanium as the nitrogen content is decreased, and the effective increase in titanium available to associate with sulphur, it follows that a steel with a reasonably low nitrogen level and a high Ti/S ratio should show optimum impact values. Plotting impact energy as a function of both nitrogen content and Ti/S ratio (fig 4.26) shows an area to the right hand side of the dashed curve which has impact energy values greater than 60J. A graph of impact energy as a function of ferrite factor (from

values given in Table 4.9) is shown in fig 4.27. No obvious trend is indicated owing to the wide scatter of points.

TABLE 4.9 : Summary of titanium, sulphur, and nitrogen contents as well as impact results for alloys A1-A14 (FF = ferrite factor, S.D. = std deviation).

ALLOY	Ti	S	N	Ti/S	F.F.	IMPACT ENERGY (J) MEAN	S.D.
A1	.25	.009	.019	27.8	11.3	64.2	4.3
A2	.26	.018	.016	14.4	9.5	47.0	2.2
A3	.30	.013	.016	23.1	9.9	57.3	1.9
A4	.30	.008	.013	37.5	10.4	67.6	5.9
A5	.31	.008	.014	38.8	10.2	74.0	4.4
A6	.35	.015	.014	23.3	10.2	51.7	3.1
A7	.36	.020	.012	18.0	10.4	55.5	4.1
A8	.34	.015	.011	22.7	10.1	66.7	3.9
A9	.47	.012	.010	39.2	11.2	64.2	3.4
A10	.39	.008	.013	48.8	10.3	70.6	4.2
A11	.30	.009	.017	33.3	9.3	57.4	4.1
A12	.37	.009	.017	41.1	10.9	73.9	8.6
A13	.37	.013	.012	28.5	10.9	60.5	5.0
A14	.36	.023	.014	15.7	11.0	47.5	7.4

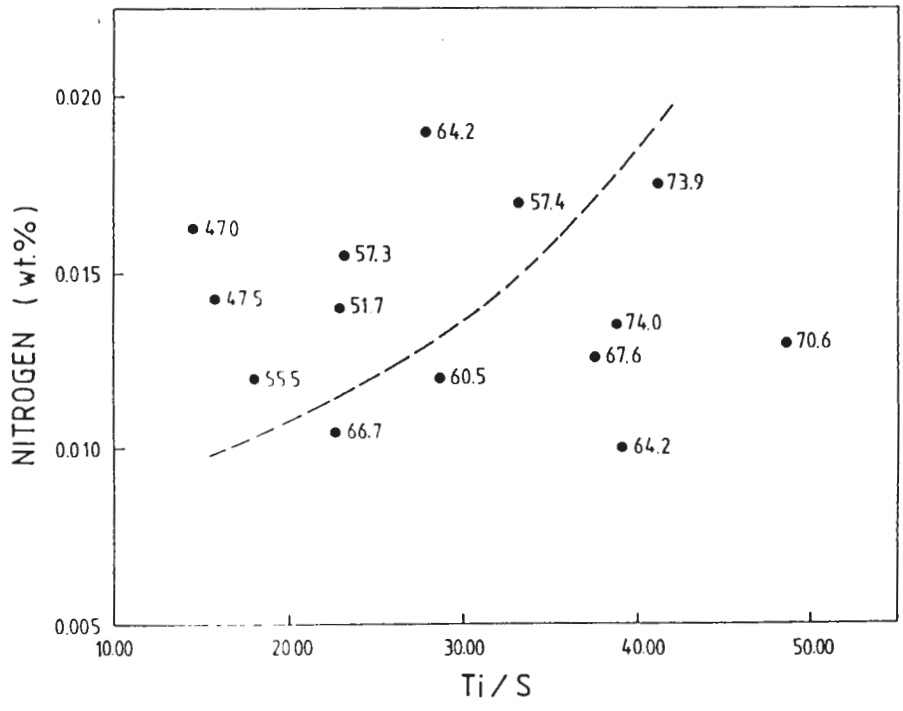

FIGURE 4.26 : Impact energy shown in relation to both nitrogen content and Ti/S ratio. Numbers next to data points indicate impact energies (J)

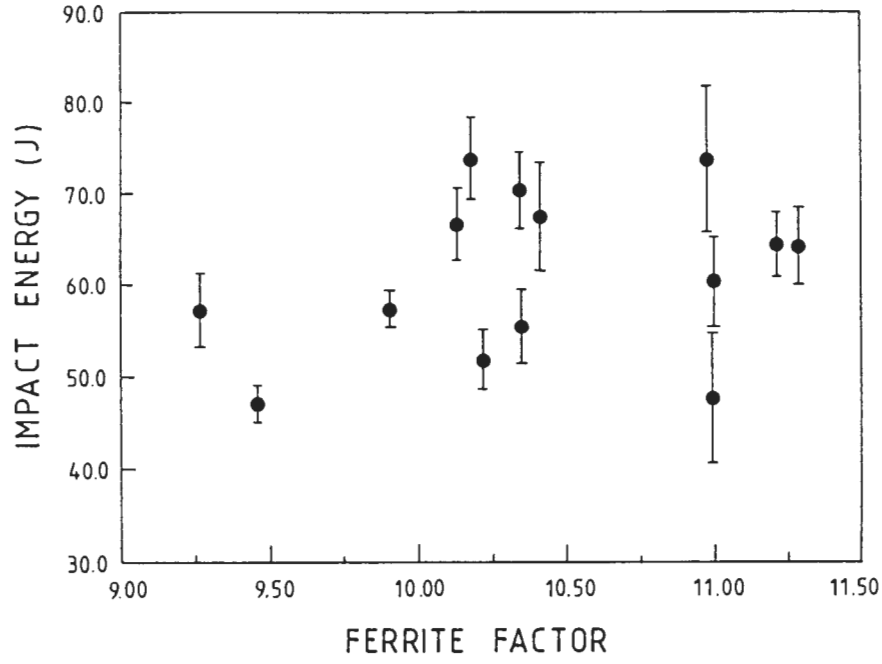

FIGURE 4.27 : Impact energy as function of ferrite factor (values from Table 4.9)

4.4.4 FRACTOGRAPHY

MACROSCOPIC OBSERVATIONS

The impact fracture surfaces were all characterised by a number of splits which occurred at regular spacings perpendicular to the parting surface. Splitting occurred parallel to the rolling plane and gave rise to a highly contoured surface which appeared jagged in profile. This is illustrated by rematching the Charpy specimens after fracture, and a series of secondary necking systems (ligaments) produced by the splitting can be identified (fig 4.28). The number of major splits varied from 2 to 4 but was not related to the impact energy. In fig 4.28(a), a major split is seen to coincide with the centre of the specimen width, whereas the splitting shown in fig 4.28(b) is off-centre. However, the spacing between the splits in a particular specimen was always equal.

Despite the occurrence of splitting in all the specimens, the reduction in surface area exhibited on the fracture surfaces of the individual test pieces can be roughly related to the impact energy. This is illustrated qualitatively in fig 4.29 which compares the fracture surfaces of alloys A2 and A5. It is clear that a greater amount of reduction in area is associated with the testpiece having the higher impact energy (alloy A5 in fig 4.29(a)).

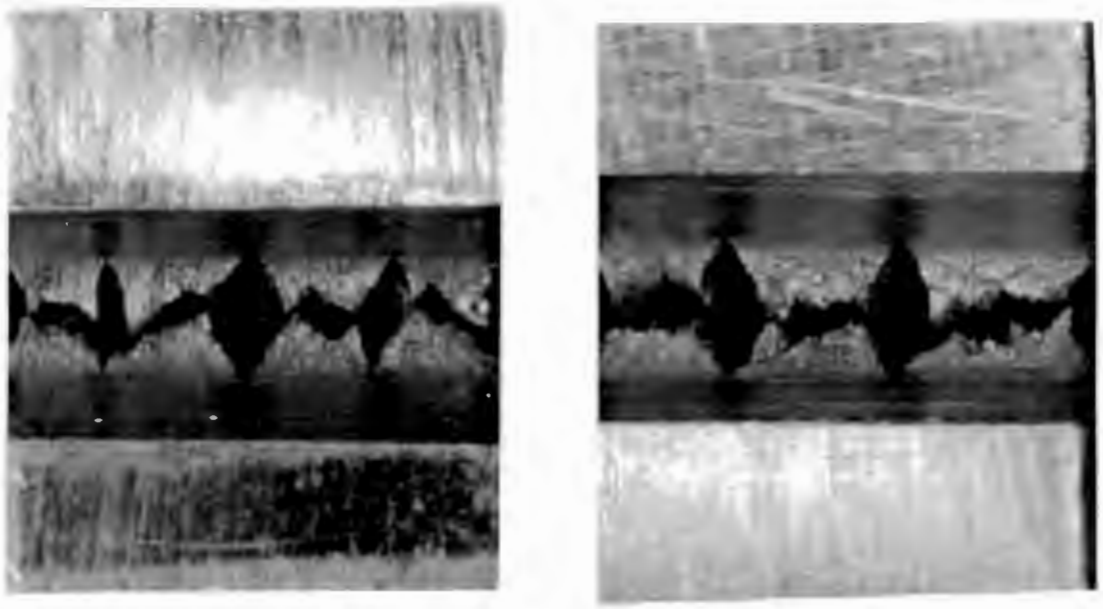

(a) (b)

FIGURE 4.28 : Profile of impact fracture surfaces.

(a) Major split at centre of specimen width (alloy A6)

(b) Off-centre splitting (alloy A2)

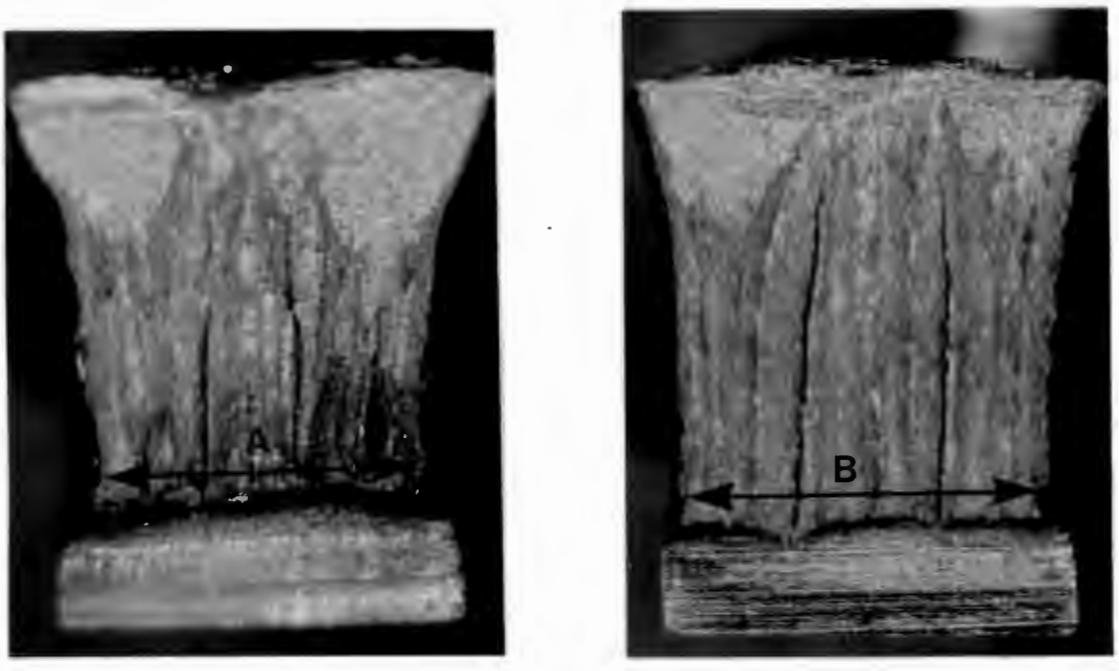

(a) (b)

FIGURE 4.29 : Comparison of the reduction in area of the fracture surfaces of alloys A5 and A2. The greater reduction for A5 is demonstrated by comparing the dimensions A and B where A<B.

(a) Alloy A5 - impact energy = 74J

(b) Alloy A2 - impact energy = 47J

MICROSCOPICAL FEATURES

Examination of the fracture surfaces in the SEM revealed a variety of fracture modes. If the topography produced by splitting is considered to consist of a number of ridges and valleys (fig 4.30), the ridges are typically associated with ductile-dimple fracture, whereas the valleys show a relatively smooth surface, indicative of failure by a low energy mode.

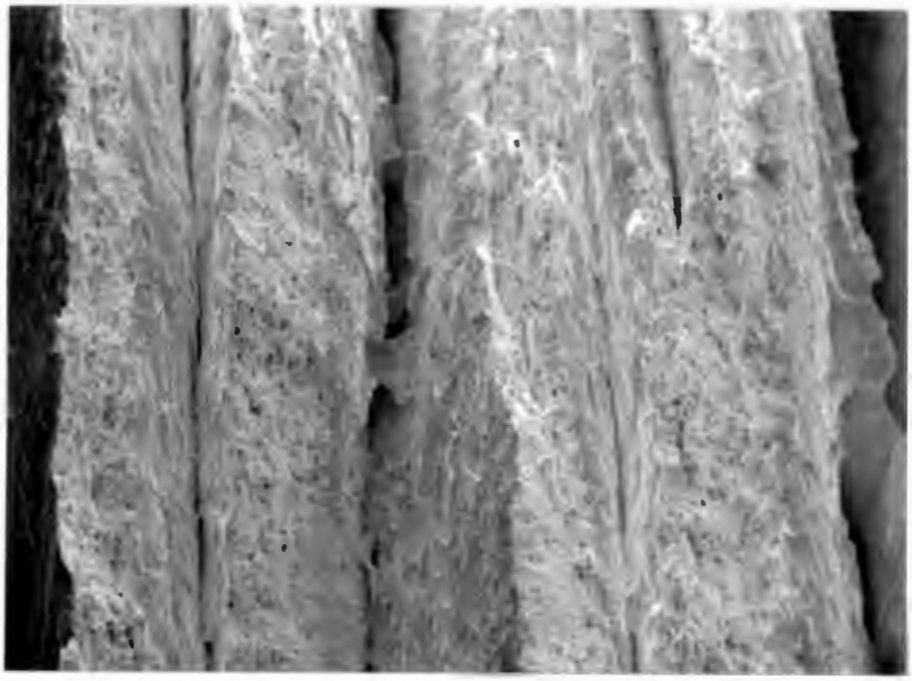

FIGURE 4.30 : General view of fracture surface displaying characteristic features associated with splitting (Alloy A1)

From a closer inspection of the fracture surface at higher magnifications, it was clear that inclusions played a large role in both splitting and in microvoid nucleation. McDonald and Ludwigson[91] have described four modes of fracture associated with inclusions in steel which can be briefly summarised as follows :

DUCTILE RUPTURE. *Dimples, resulting from microvoid formation and coalescence, are characteristic of ductile rupture. Microvoids are generally initiated at inclusions which can sometimes be observed within the dimples.*

DECOHESION. *Fields of inclusions, interrupted by little, if any, ductile rupture, are charateristic of decohesion at the inclusion/matrix boundaries.*

CLEAVAGE. *Stepped facets are caused by fracture through regions of different crystallographic orientation. Cleavage occurs by rapid propagation of a crack along crystallographic planes, and may be initiated by inclusion/matrix decohesion. This is a very low energy type of fracture.*

QUASICLEAVAGE. *A less well defined fracture mode, known as quasicleavage, is associated with tear ridges which represent limited plastic deformation separating cleavage facets. Unlike pure cleavage, energy is absorbed as a result of the limited plastic deformation.*

All these fracture modes could be identified on each of the fracture surfaces. The inclusions associated with the various fracture modes have been monitored using EDS. Inclusions were seen to occur within the ductile dimples as well as in areas where splitting is assumed to have initiated. A typical association of inclusion fragments with ductile failure on the ridge areas is shown in fig 4.31. Particles are clearly visible within the cuplike features. The presence of inclusions along a split surface is clearly indicated in fig 4.32 which displays a characteristic inclusion/matrix decohesion mode of fracture.

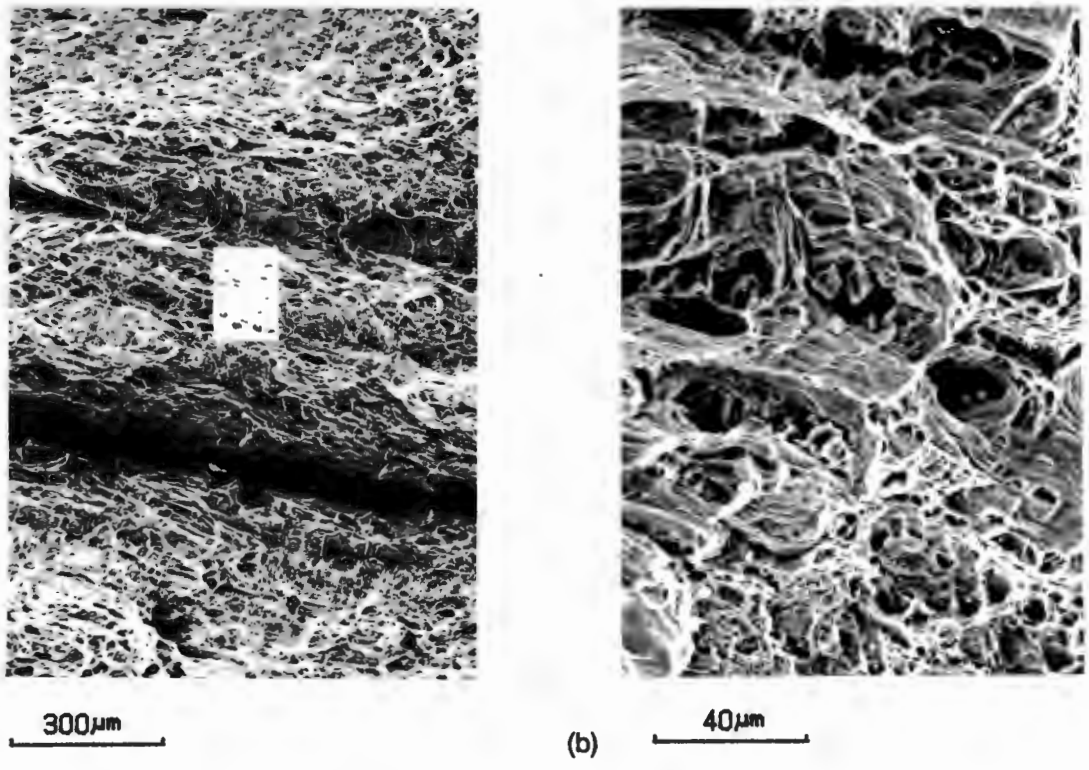

FIGURE 4.31 : Association of inclusions with ductile fracture (Alloy A2)

(a) General area

(b) Inclusion fragments within ductile dimples.

FIGURE 4.32 : Typical example of inclusions (circled) on fracture surface at top of split (Alloy A2)

The EDS analysis has shown all types of inclusions to be associated with splitting and in fig 4.33 even titanium sulphide fragments are identified along the edge of a split. The fact that the inclusions are commonly exposed at the top of the split surface seems to indicate that splitting was often initiated at the inclusion sites. Large numbers of manganese sulphide inclusions were also often associated with splitting, as shown in fig 4.34. A chainlike formation of titanium carbonitrides seen in fig 4.35 clearly shows the separation of the matrix from the cuboid inclusions, although a considerable amount of ductile tearing of the material is also evident.

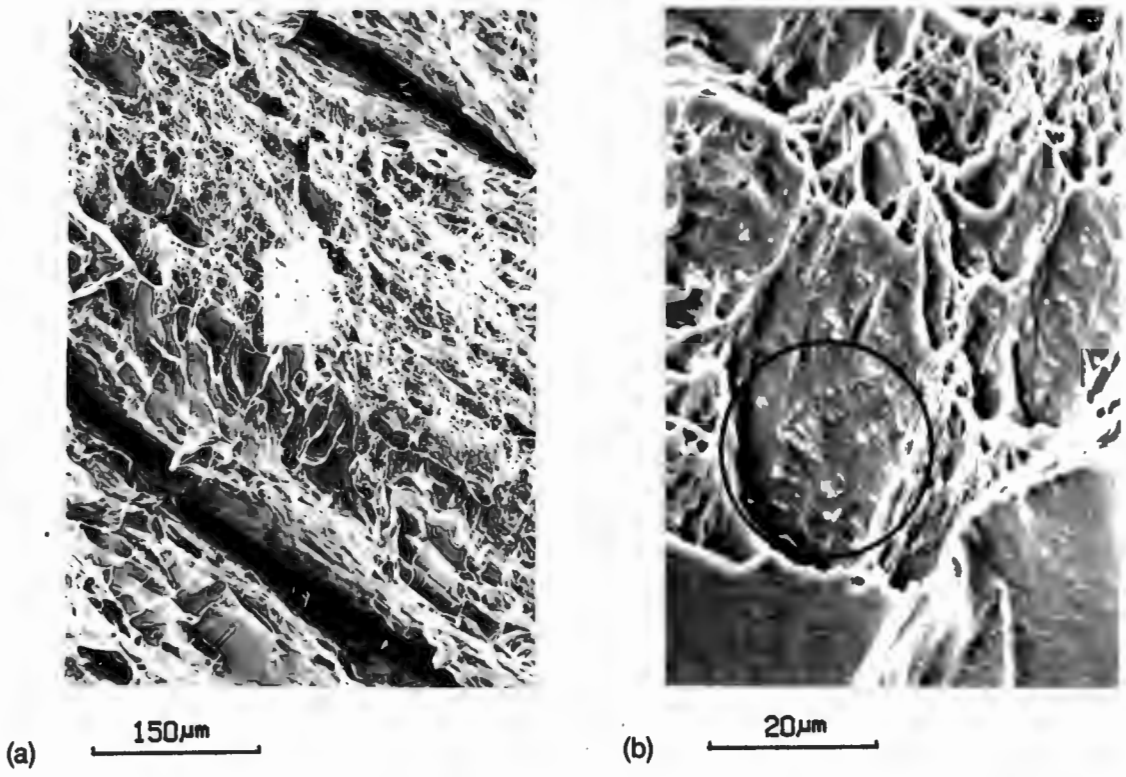

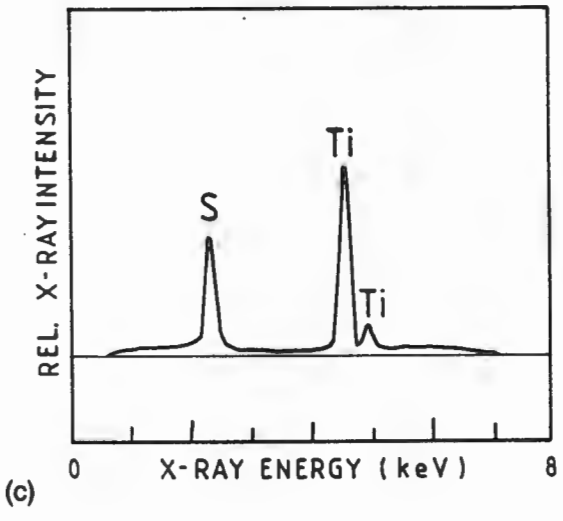

FIGURE 4.33 : Titanium sulphide inclusions (circled) along edge of split (Alloy A5)

(a) SEM image

(b) Higher magnification of boxed area in (a)

(c) X-ray spectrum of inclusions in (b).

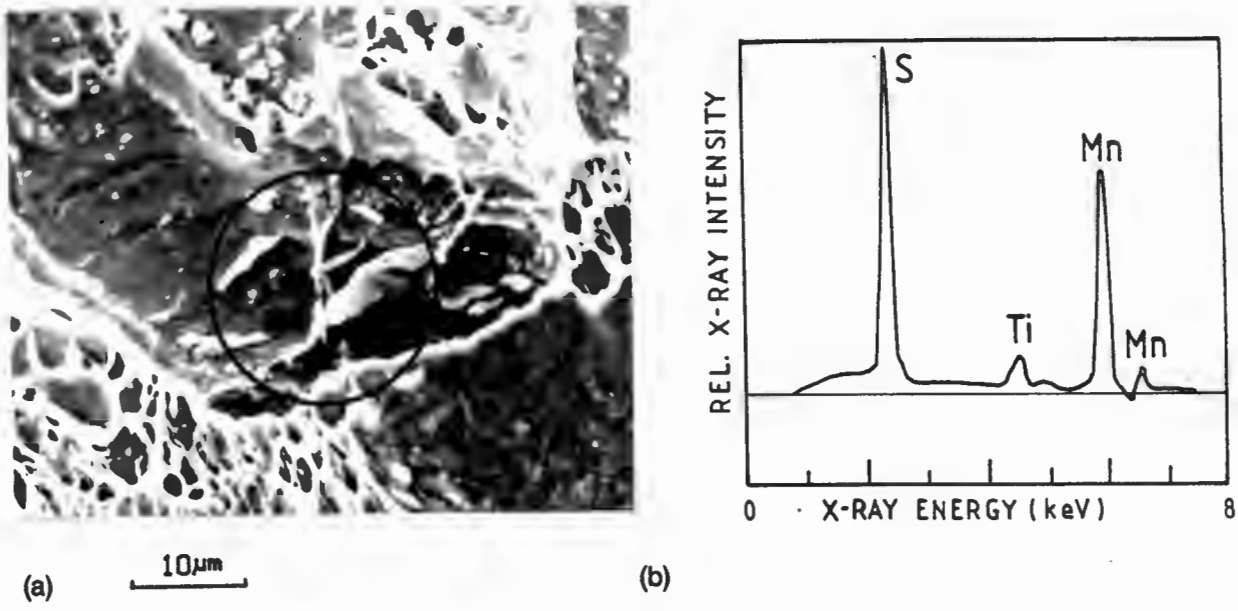

FIGURE 4.34 : Fragmented manganese sulphide inclusion (circled) exposed on split surface (Alloy A2).

(a) SEM image

(b) X-ray spectrum of inclusion fragments in (a).

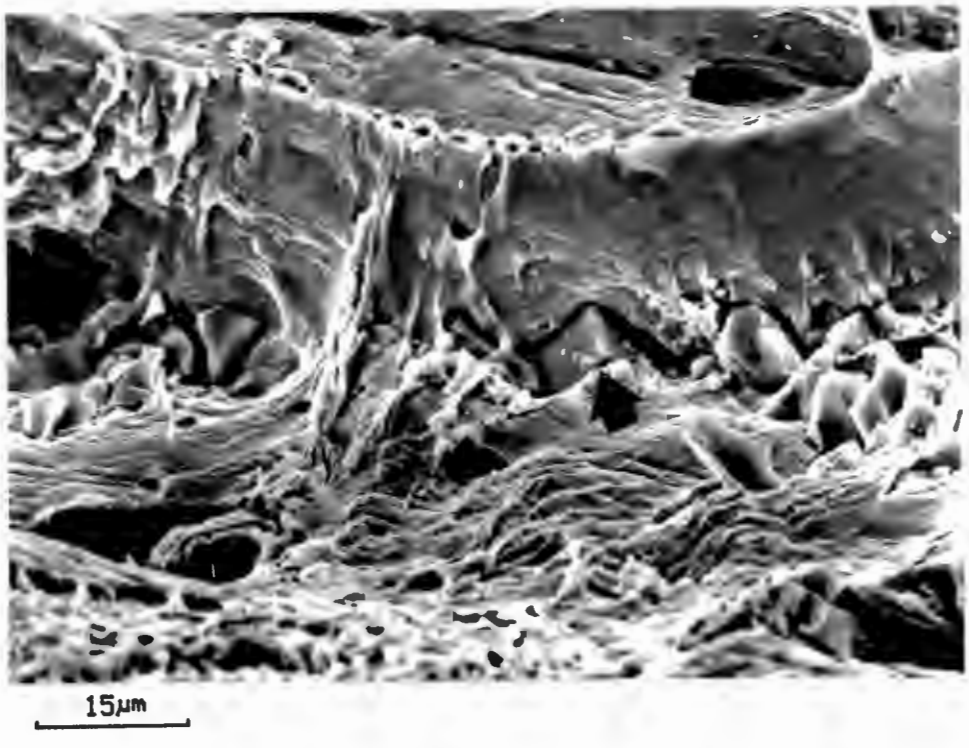

FIGURE 4.35 : Inclusion/matrix decohesion (arrowed) occurring along chain of titanium-containing cuboid inclusions (Alloy A3)

A polished cross-section of a split surface in fig 4.36(a) reveals void formation around a cuboid inclusion in association with splitting. Further polishing of the same surface has resulted in the removal of the carbonitride cuboid and the extent of the void formation can be identified (fig 4.36(b)).

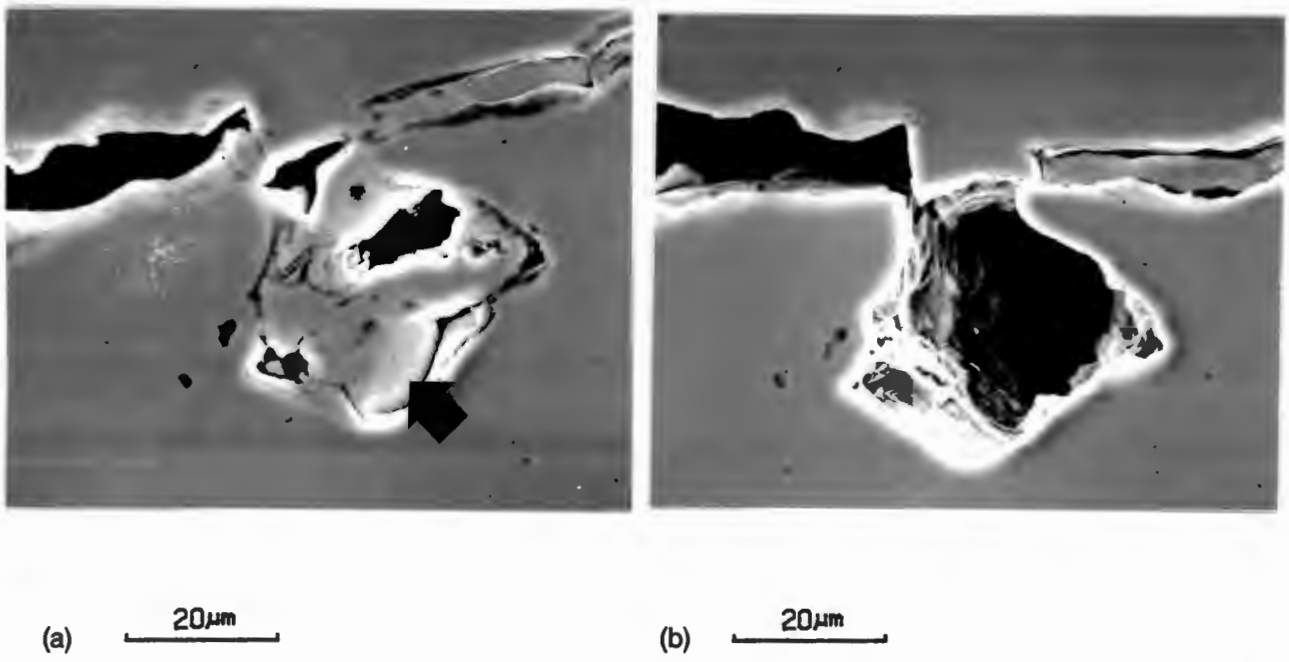

FIGURE 4.36 : Cross-section of split surface showing a cuboid associated with splitting phenomena (Alloy A5)

(a) Initially polished section. Cuboid edge is arrowed.

(b) Further polishing has resulted in removal of the cuboid inclusion.

A quantitative assessment of the relative contribution of the various inclusion types is not feasible because of the complex nature of the fracture surfaces. However, inclusion analyses using EDS on polished surfaces have shown that those alloys in which stringered manganese sulphide inclusions occur more abundantly have lower impact values. Fig 4.37(a) and (b) illustrate the relative inclusion distributions in alloys A2 and A5 respectively.

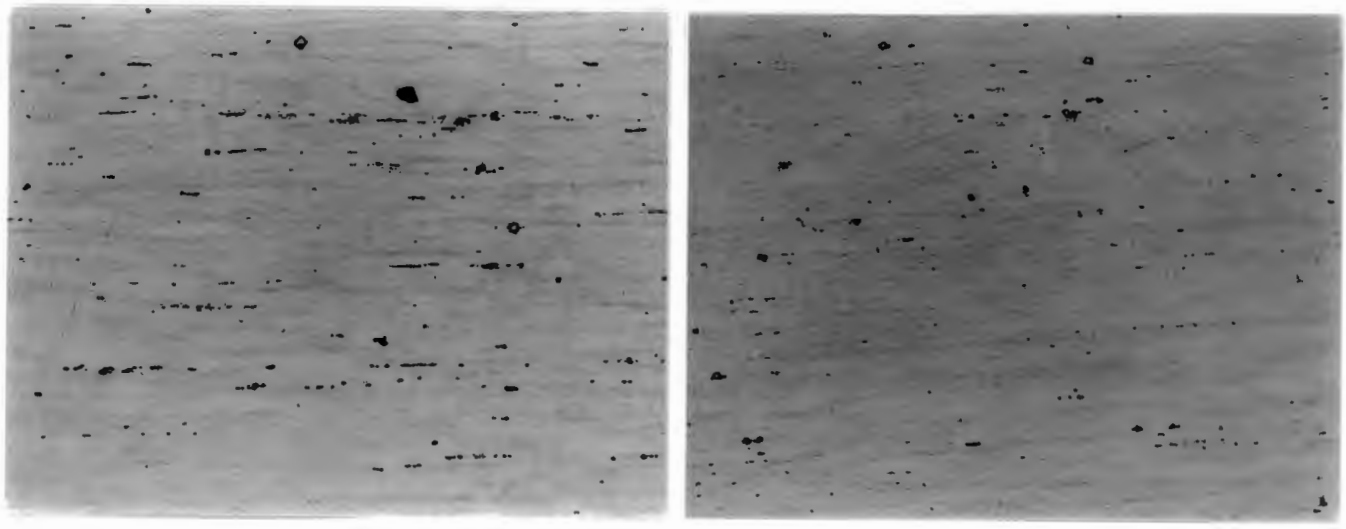

FIGURE 4.37 : Inclusion distributions in Alloys A2 and A5.

(a) High density of inclusions in alloy A2. Charpy impact energy = 47J

(b) Much lower density of inclusions in alloy A5 when compared to A2. Charpy impact energy = 74J.

A polished and etched cross-sectional view of a split surface is shown in fig 4.38(a). It appears that as the split propagates, crack opening occurs at points of weakness ahead of the main crack. The subsidiary cracks then join up to give the split a fairly irregular appearance in profile. The tearing associated with the joining up of the cracks gives rise to the so-called quasicleavage as indicated in fig 4.38(b).

The general mode of crack propagation along a split is seen to be mostly intergranular, although transgranular fracture is also apparent. Figure 4.39(a) clearly illustrates the occurrence of grain boundary separation. The crack often follows a fairly straight path over a number of grain lengths, thus emphasing the occurrence of continuous, flat grain boundaries in this steel. In addition, the crack path is usually coincident with the "shadow" banding effect reminiscent of the original δ-ferrite/austenite banding. This is demonstrated in fig 4.39(b) which exhibits splitting coincident with the "shadow" banding. The fact that the crack does not always travel in a straight line is illustrated in figs 4.39(c) and (d) where it is evident that the crack path has deviated due to the separation of grains whose grain boundaries are not always coincident with the banding interface.

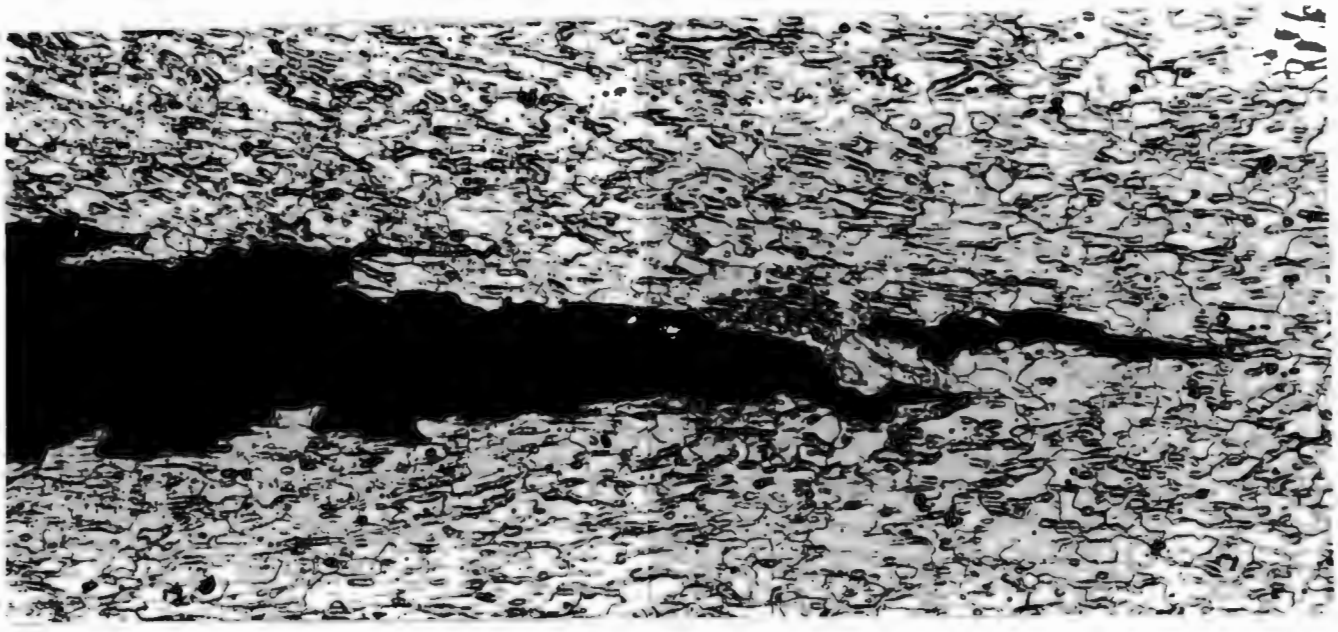

(a) 200μm

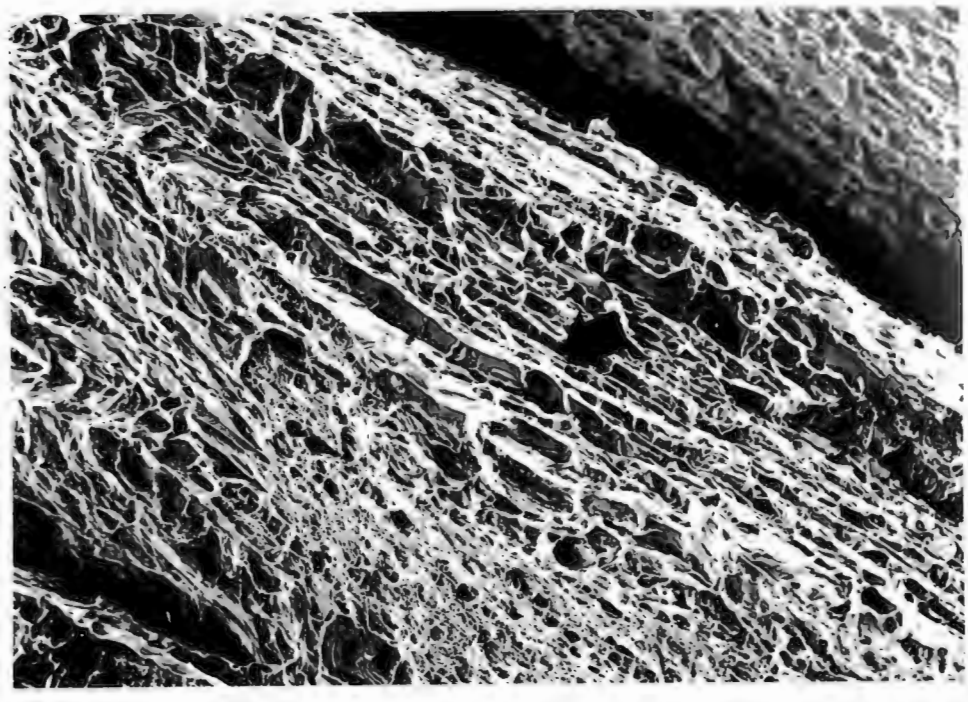

(b) 150μm

FIGURE 4.38 : Fracture behaviour associated with splitting.

(a) Cross-sectional view (transverse surface) of split surface. Crack opening occurs ahead of the main crack (alloy A2)

(b) Quasicleavage is visible along split surface in area arrowed (alloy A5)

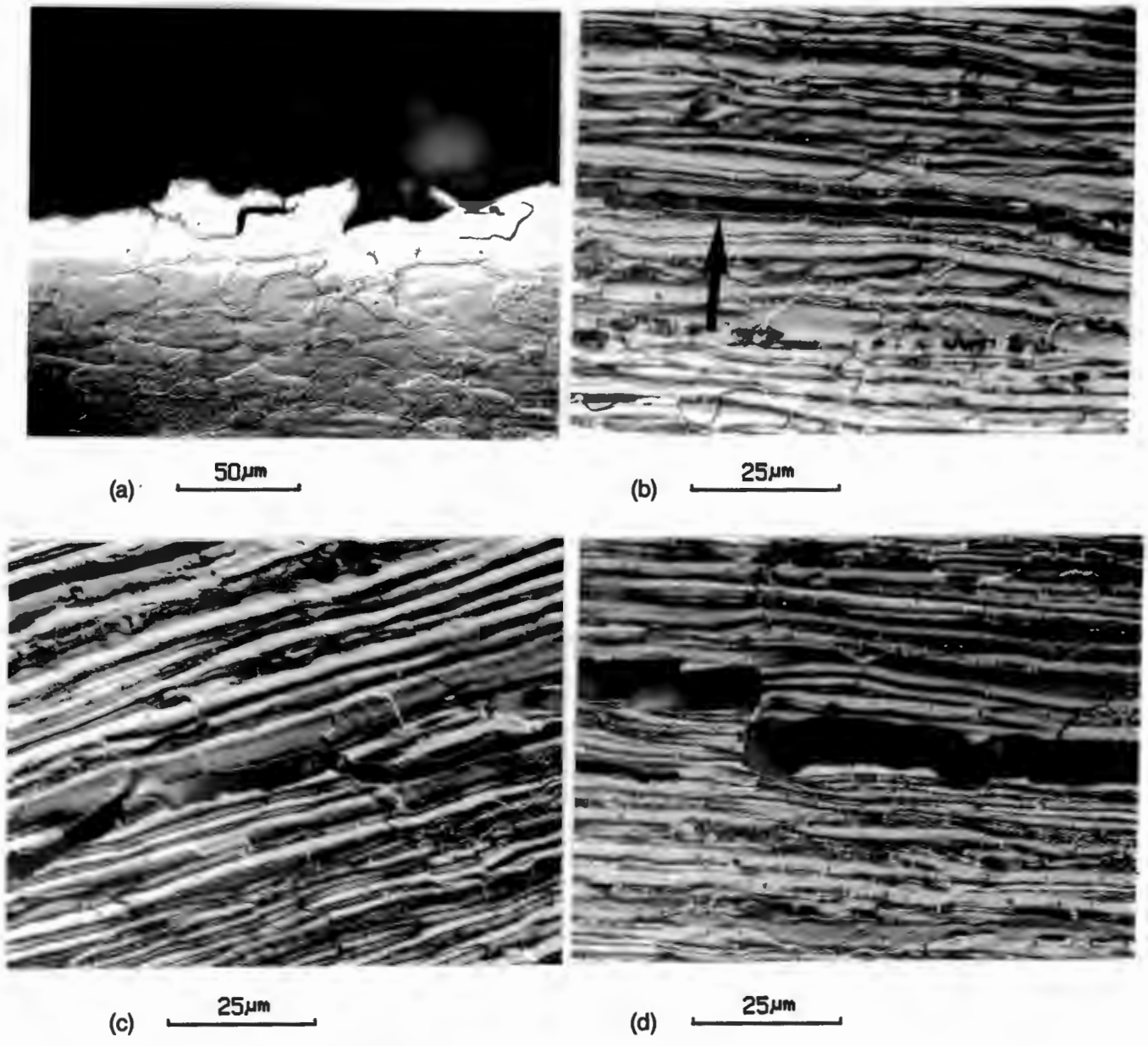

FIGURE 4.39 : Crack path during delamination

(a) Grain boundary separation

(b) Splitting (arrowed) coincident with "shadow" banding effect

(c) and (d) Deviation of crack path around grain boundaries

The actual appearance of the split surface is indicated in fig 4.40. The use of back-scattered electron imaging in fig 4.40(b) reveals more clearly the predominantly smooth nature of the split surface. It is not difficult to envisage the preponderance of grain boundary separation from these micrographs. In this particular instance quasicleavage is generally absent, thus resulting in a very low energy fracture. Figure 4.41 illustrates the appearance of the split surface at the top of a split (i.e. near the major parting surface).

Although the split surface is fairly smooth, the fine ripple effect demonstrates evidence of stretching which probably occurred during elongation of the individual ligament formed as a consequence of splitting.

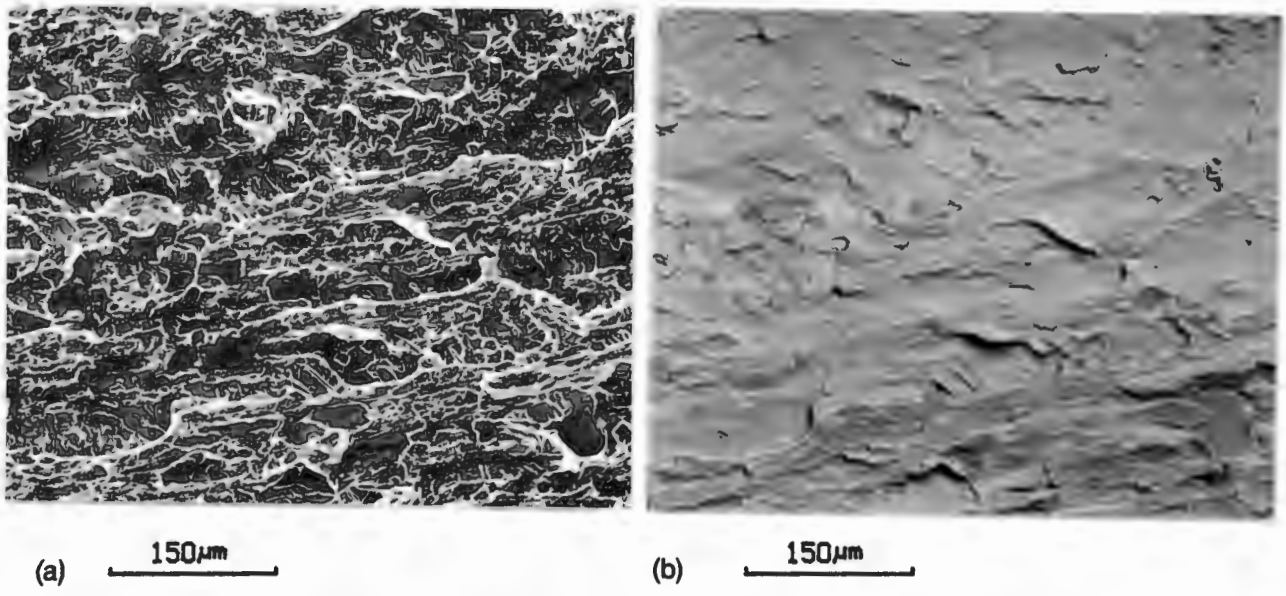

FIGURE 4.40 : Grain boundary separation revealed by back-scattered electron imaging of surface of split

(a) Secondary electron image

(b) Backscattered electron image of area indicated by (a)

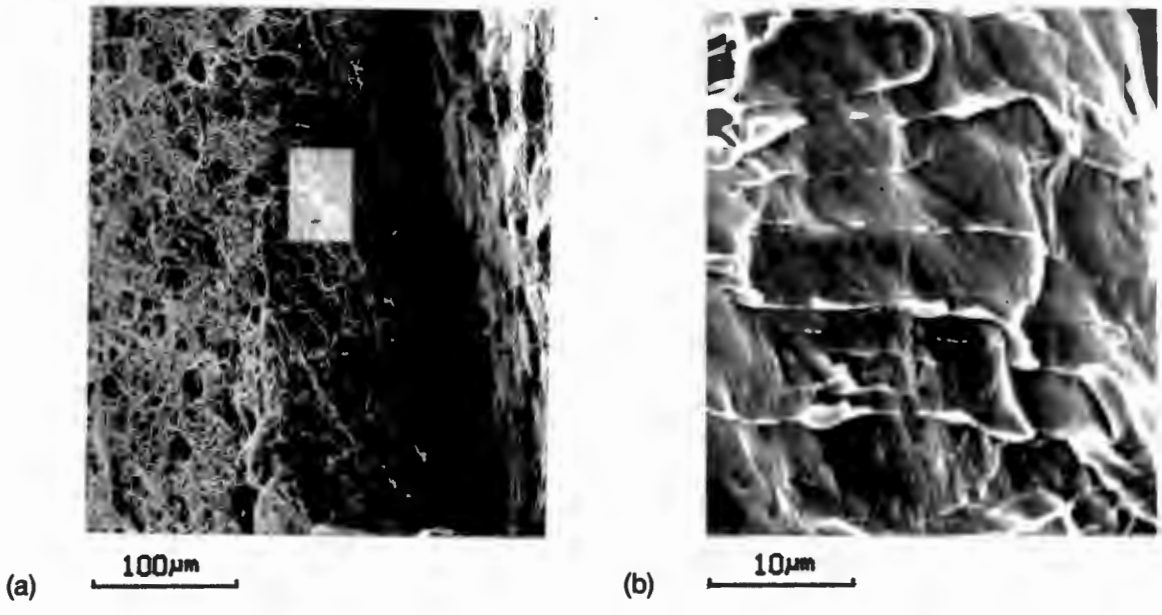

FIGURE 4.41 : Appearance of relatively smooth split surface near the top of the split.

(a) Low magnification of split area

(b) Higher magnification of area boxed in (a).

4.5 MICROSTRUCTURAL ANALYSIS OF 16-17 wt% CHROMIUM FERRITE-MARTENSITE ALLOYS

4.5.1 OVERVIEW

The microstructure and mechanical properties were examined for duplex 16-17 wt % chromium containing ferrite-martensite steels whose compositions were derived by balancing the ferrite to austenite forming element ratios (Appendix A). This study involved an investigation of the stability of the duplex structure over the temperature range 500°-1000°C, as well as an analysis of the transformation behaviour of alloys containing varying nickel levels. In addition, tensile and impact properties were measured in relation to various heat treatments, and the tempered microstructures were examined.

4.5.2 ALLOY COMPOSITIONS

The compositions of four experimental alloys possessing ferrite-martensite duplex structures are listed in Table 4.10. Alloy E3 has been referred to in the initial investigation in Appendix A and alloys E4-E6 represent alloys possessing similar base chemistries but varying nickel contents.

TABLE 4.10 : Chemical composition of experimental alloys E3-E6. (All figures represent wt %).

ALLOY	C	N	S	P	Mn	Si	Cr	Ni	FF	Cr'	Ni'
E3	.021	.028	.007	.019	0.90	.34	16.87	3.22	2.3	17.6	5.0
E4	.028	.029	.009	.025	0.97	.42	15.95	2.14	5.9	16.8	4.2
E5	.027	.026	.008	.019	1.00	.35	15.98	2.44	4.2	16.7	4.4
E6	.028	.024	.009	.019	0.96	.36	16.14	3.03	2.2	16.9	5.0

[F.F. = ferrite factor; Cr' = Cr equivalent; Ni' = Ni equivalent].

4.5.3 CONSTITUTION OF ALLOY E3

The phase constitution of alloy E3 was determined over the temperature range 500°C - 1000°C. Heat treatments involved prior soaking at 1100°C for 1 hour followed by cooling to lower holding temperatures in the range 500°C - 1000°C for a further 1 hour

soak period. Specimens were oil quenched from the lower soak temperature. The Cr and Ni levels of the respective phases and the ferrite/martensite phase ratios were measured as a function of each quench temperature. These results are plotted in figs 4.42 and 4.43 respectively.

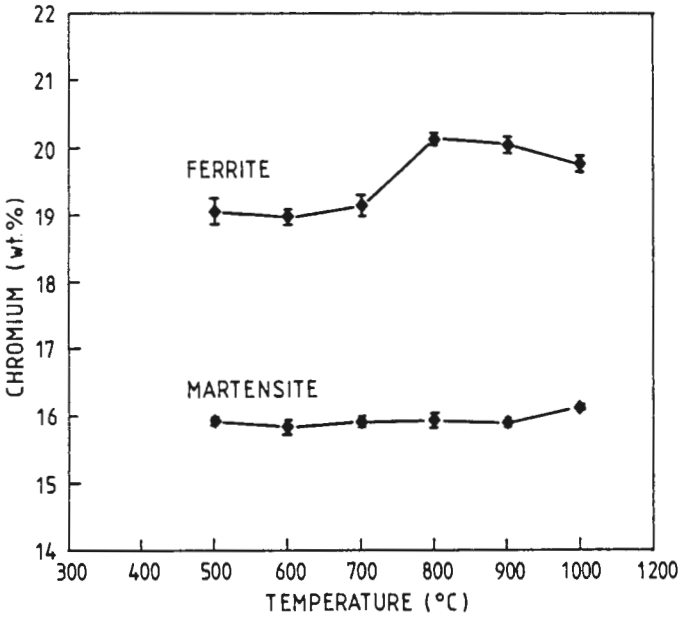

(a)

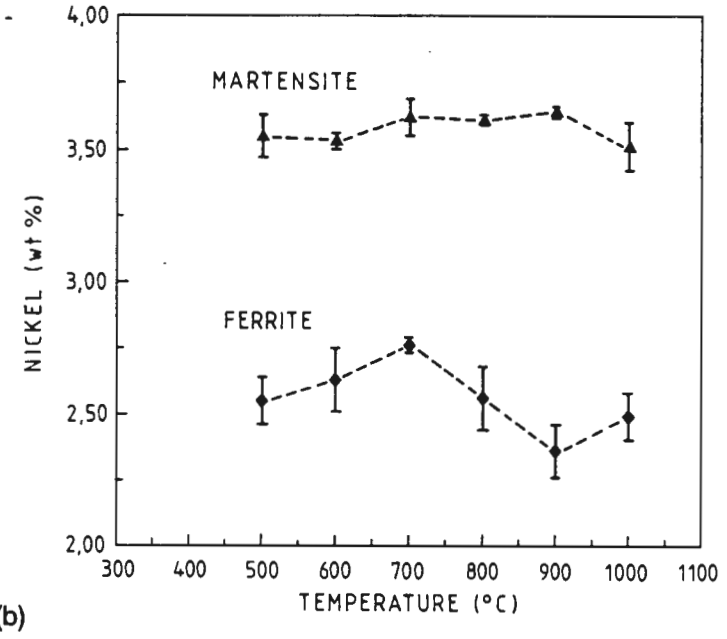

(b)

FIGURE 4.42 : Phase composition as function of final soak temperature (Alloy E3).

(a) Cr levels in ferrite and martensite phases.

(b) Ni levels in ferrite and martensite phases.

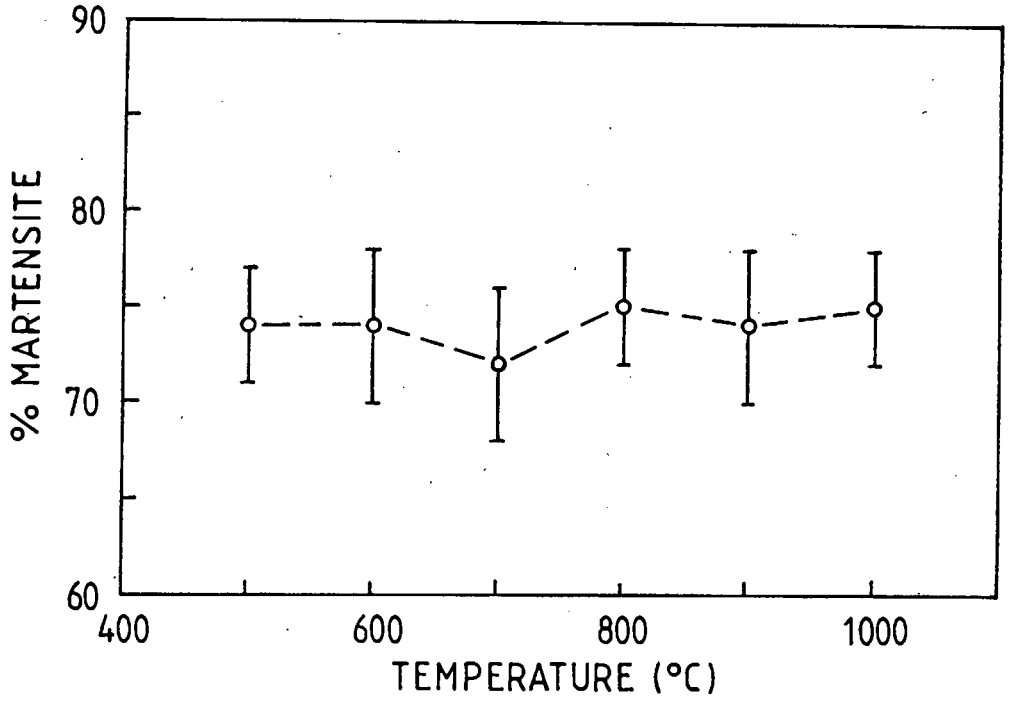

FIGURE 4.43 : Martensite content in duplex ferrite-martensite microstructure as function of final soak temperature (Alloy E3).

4.5.4 TRANSFORMATION BEHAVIOUR OF ALLOYS E4-E6

The transformation behaviour of the three alloys (E4-E6) possessing similar base chemistries but varying nickel contents was assessed. Alloys E4, E5, and E6 contained 2.14, 2.44, and 3.03 wt% Ni respectively (Table 4.10). The dilatometrically determined phase transition temperatures measured during both heating and cooling at 4°C/min are reproduced in fig 4.44. An explanation of the phase transition points indicated in fig 4.44 is given below :-

Heating Cycle

A = Start of austenite formation
B = Austenite formation completed
C = Start of δ-ferrite formation from austenite
D = δ-ferrite formation completed

Cooling Cycle

E = Start of δ-ferrite decomposition to austenite
F = Decomposition of δ-ferrite completed
M_s = Start of martensite formation
M_f = Completion of martensite formation.

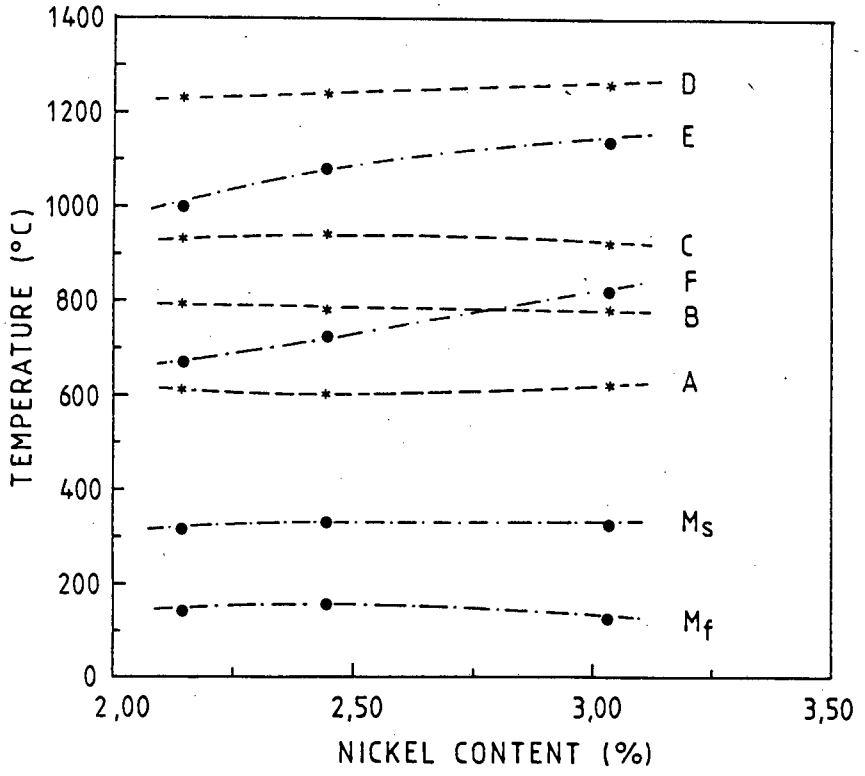

FIGURE 4.44 : Transformation temperatures of alloys E4-E6 during heating and cooling at 4°C/min. Test specimens were in the hot rolled condition prior to testing.

In order to compare alloys E4-E6 in the as-rolled condition, the ferrite volume fraction and the macrohardness was measured for each alloy. The results are indicated in Table 4.11.

TABLE 4.11 : Ferrite volume fraction and macrohardness for alloys E4-E6 in the as-rolled condition.

ALLOY	FERRITE CONTENT	HARDNESS (HV_{30})
E4	27%	343
E5	17%	360
E6	13%	362

4.5.5 MECHANICAL PROPERTIES OF ALLOYS E4-E6 AS FUNCTION OF HEAT TREATMENT

TENSILE STRENGTH

The ultimate tensile strengths of alloys E4-E6 were determined after normalising at 1000°C for 2 hours (air cool) followed by soaking at 500°, 600°, 700° and 800°C for 2 hours (oil quench to room temperature). These strengths were compared to the normalised condition. Results are reproduced in fig 4.45.

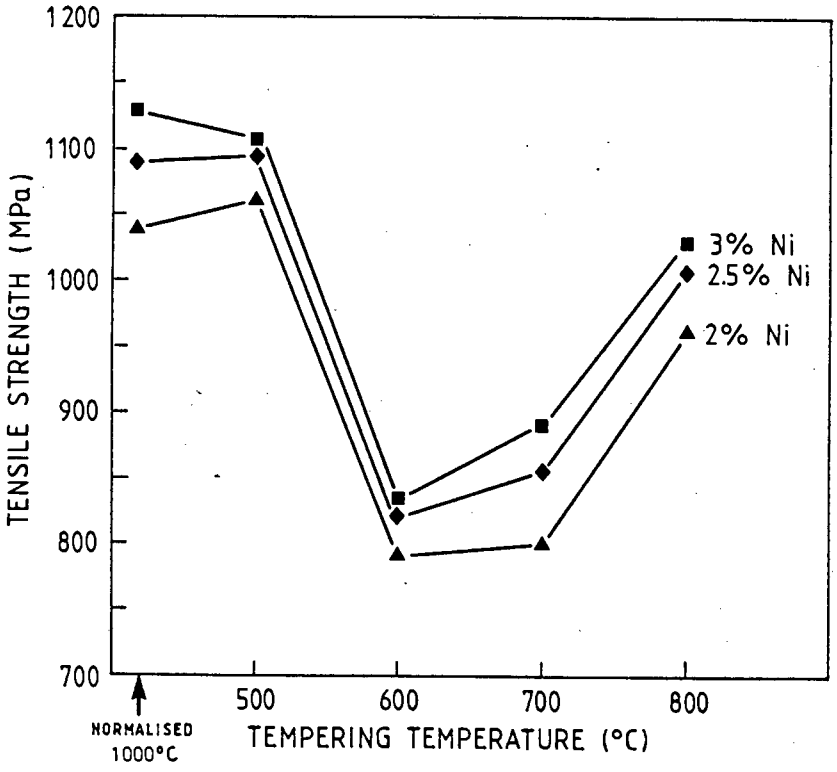

FIGURE 4.45 : Room temperature ultimate tensile strengths of alloys E4-E6 after heat treatment (2 hours at temperature followed by oil quenching).

IMPACT ENERGY

Charpy V-notch impact energies were measured for alloy E5 following identical heat treatments to those performed on the tensile test specimens. In each case sub-size specimens (7.5 mm) machined in the L-T orientation were tested. The results are presented in fig 4.46.

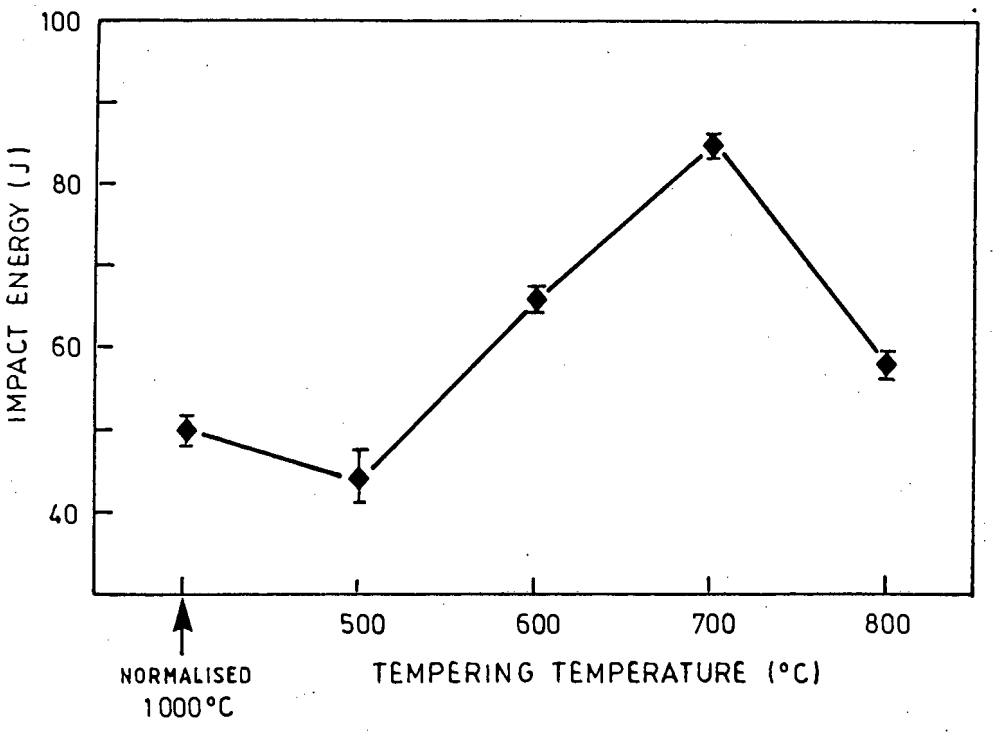

FIGURE 4.46 : Room temperature impact energies for alloy E5 after heat treatment (2 hours at temperature followed by quenching). Values for the normalised condition are also indicated.

TEMPERING RESPONSE

Alloy E5 was soaked at 500°, 600°, 700°, and 800°C for 2 hours and 5 hours following normalisation. The macrohardness measured after each heat treatment is indicated in Table 4.12.

TABLE 4.12 : Hardness values (HV_{30}) for alloy E5 as function of temperature and time.

	TEMPERING TEMPERATURE (°C)			
TIME	**500**	**600**	**700**	**800**
2hrs	366	263	252	320
5hrs	370	263	270	322

*NORMALISED CONDITION = 360 HV_{30}

4.5.6 ANALYSIS OF PHASE REACTIONS DURING TEMPERING OF ALLOY E5

The microstructure of alloy E5 was examined in the normalised condition and after tempering at 500°, 600°, 700°, and 800°C for 2 hours following normalisation. In addition, the microstructure was examined after tempering at 700°C for 5 hours and 8 hours. These microstructures are reproduced in figs 4.47(a) to (g). In the normalised condition, shown in fig 4.47(a), residual δ-ferrite (primary ferrite) is seen to occur in a martensitic matrix. After tempering at 500°C there appears to be little change in the martensite except for the occurrence of precipitates which delineate the prior austenite grain boundaries (fig 4.47(b)). It can also be inferred that a certain degree of interlath precipitation has occurred within the martensite due to the more distinctive etching of the martensite in fig 4.47(b) compared to fig 4.47(a). Nevertheless this observation is not conclusive from SEM imaging. The microstructure heated at 600°C (fig 4.47(c)) indicates considerable tempering of the martensite which is also emphasised by the decrease in hardness (Table 4.12). Precipitates occur not only on the prior austenite grain boundaries but also within the prior austenite grains themselves. The primary ferrite grains are unaffected. In the case of the microstructure heat treated at 700°C for 2 hrs, 5 hrs and 8 hrs (fig 4.47(a) to (f)), the primary ferrite once again appears to be unaffected. However, the martensite has decomposed substantially to form secondary ferrite and new austenite (transforms to martensite). The degree of this transformation has increased with tempering time, but remains similar after 5 hrs and 8 hrs. The resultant room temperature microstructure can be described as primary ferrite (δ-ferrite) in a matrix consisting of a fine mixture of secondary ferrite and new martensite. After tempering at 800°C a fine woven structure of secondary ferrite and martensite is again evident in the original martensitic regions, although in this case a greater proportion of new martensite is formed. The greater amount of new martensite formed is also reflected by the sizable increase in hardness (Table 4.12).

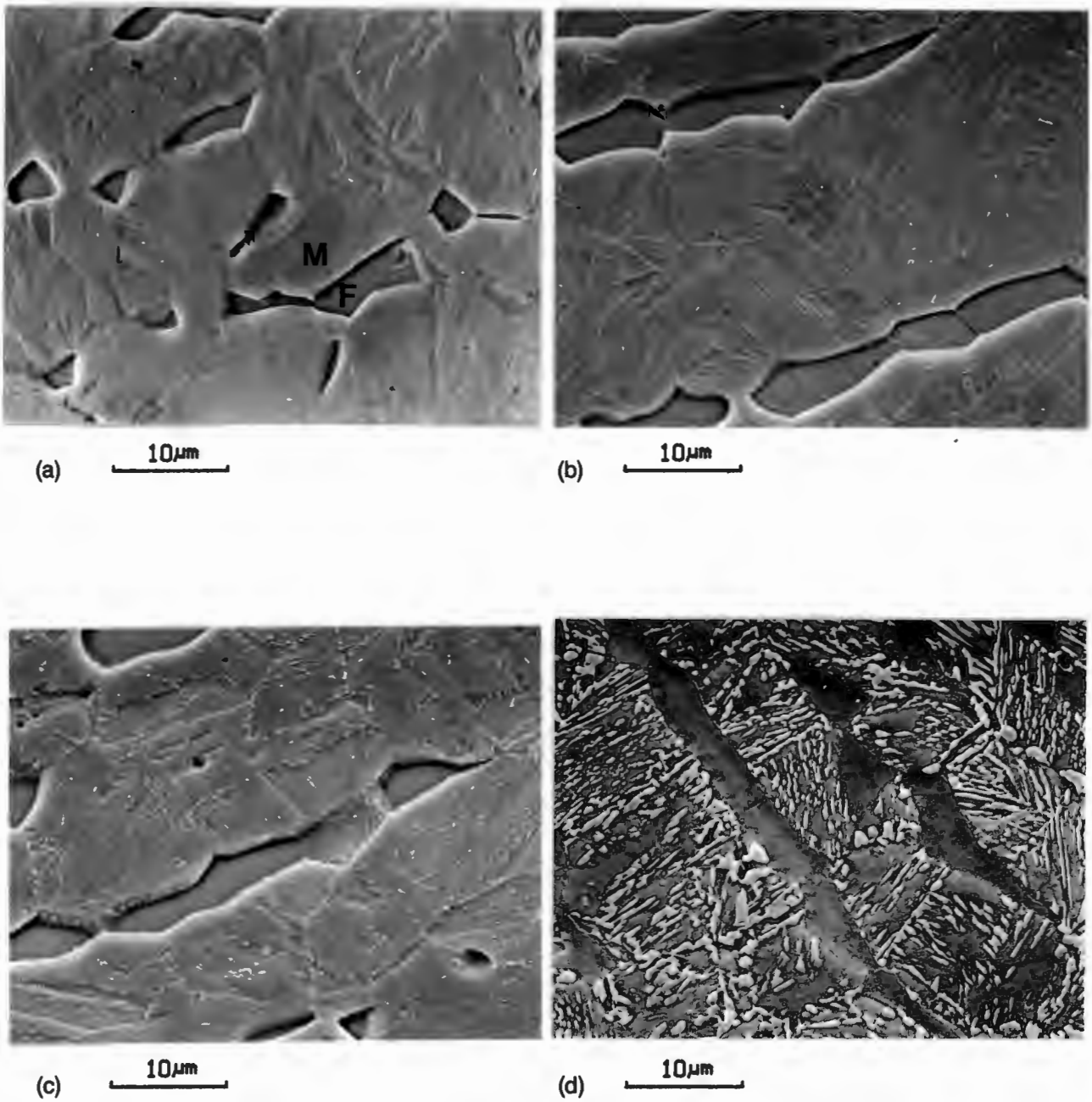

FIGURE 4.47 : Comparison of the microstructures of alloy E5 in the normalised and tempered conditions. Tempering was carried out subsequent to normalising at 1000°C for 2 hours (air cool to room temperature).

(a) Normalised condition

(b) Temper 500°C 2 hrs

(c) Temper 600°C 2 hrs

(d) Temper 700°C 2 hrs

FIGURE 4.47 /contd...

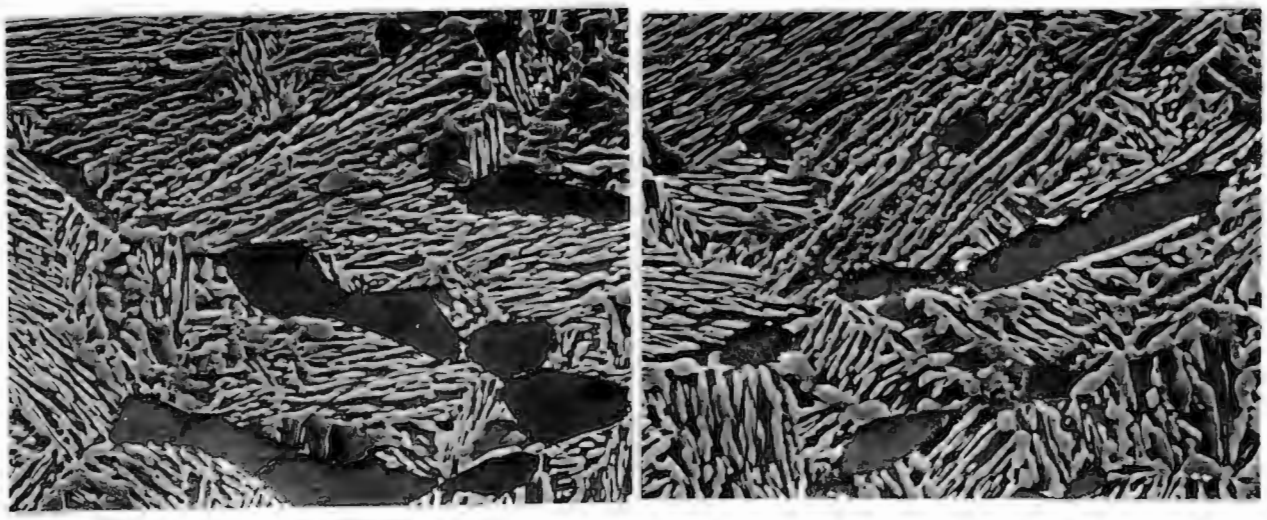

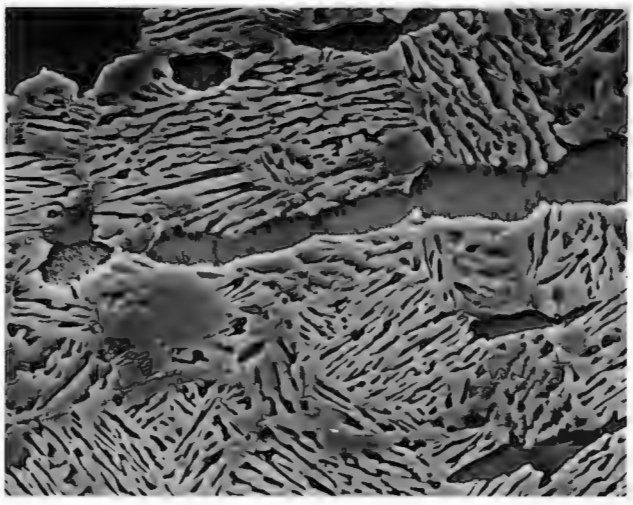

FIGURE 4.47 : Comparison of the microstructures of alloy E5 in the normalised and tempered conditions. Tempering was carried out subsequent to normalising at 1000°C for 2 hours (air cool to room temperature).

(e) Temper 700°C 5 hrs

(f) Temper 700°C 8 hrs

(g) Temper 800°C 2 hrs

Energy dispersive X-ray spectroscopy (EDS) analysis of the microstructures produced after tempering at 700°C indicates partitioning of chromium and nickel between the new martensite and secondary ferrite which was formed as a result of the decomposition of the original martensite. During the decomposition of the original martensitic matrix it appears that the growing secondary ferrite grains caused the rejection of nickel to the austenite phase (Table 4.13(a)), and in addition the growing ferrite became enriched in chromium (Table 4.13(b)). It is also apparent that the amount of partitioning is related to time at temperature and to the extent to which the transformation has occurred. This is supported by the results presented in Table 4.13(a) where it is indicated that there is a marked difference in the nickel content in the secondary ferrite when comparing the microstructures after tempering at 2 hours and 5 hours. The composition of the residual δ-ferrite (primary ferrite) showed very little change when comparing the analysis before and after tempering . (Compare with * below).

TABLE 4.13 : Average Ni and Cr levels of the phases identified after tempering alloy E5 at 700°C. All figures represent wt %.

(a) Ni Levels

TEMPERING TIME	PRIMARY FERRITE	SECONDARY FERRITE	MARTENSITE
2 hrs	1.9	2.5	3.7
5 hrs	2.0	1.7	3.5
8 hrs	1.9	1.9	3.5

(b) Cr levels

TEMPERING TIME	PRIMARY FERRITE	SECONDARY FERRITE	MARTENSITE
2 hrs	18.7	15.2	14.6
5 hrs	18.7	15.3	14.3
8 hrs	18.8	15.3	14.1

*Composition of primary ferrite and martensite (wt %) in the normalised condition is :-

PRIMARY FERRITE : Cr = 18.3 Ni = 1.7 MARTENSITE : Cr = 14.8 Ni = 2.7

CHAPTER 5

DISCUSSION

5.1 EVOLUTION OF 3CR12 MICROSTRUCTURE

5.1.1 DECOMPOSITION OF δ-FERRITE

The microstructural and microchemical results indicate a deviation from the predicted transformation behaviour of 3CR12. Examination of the evolution of the 3CR12 microstructure during cooling from temperatures marginally below the solidus to room temperature shows that the $\delta \rightarrow \gamma$ decomposition reaction is incomplete. This results in remnants of the original δ-ferrite being retained at room temperature. On the contrary, the phase equilibria for 3CR12 represented in fig 4.1 predict the occurrence of a fully austenitic structure between 1150°C and 900°C. The reasons for these differences in transformation behaviour are discussed.

The equilibrium phase diagram illustrated in fig 4.1 indicates that the 3CR12 compositional system has the potential for the composition-invariant transformation of δ-ferrite to austenite. However, it is also clear from this phase diagram that the $\delta \rightarrow \gamma$ transformation will proceed via a diffusion controlled reaction during continuous cooling, and partitioning of elements is expected. Given sufficient opportunity to reach equilibrium, though, a fully austenitic structure should be obtained which has the same composition as the parent δ-ferrite. Examination of the microstructural evolution during various cooling conditions from the 1380°C solution treatment has allowed the characteristics of the solid state $\delta \rightarrow \gamma$ transformation in 3CR12 to be analysed.

The phase structure evident after rapidly quenching from the solution temperature (1380°C) displays large ferrite grains which have occurred as a result of the unrestricted growth of single phase δ-ferrite at high temperature (fig 4.3(a)). It follows then that the

precipitates identified at these large ferrite grain boundaries after quenching to room temperature are indicative of the start of the $\delta \rightarrow \gamma$ decomposition reaction which has occurred even at the fast cooling rate. The predominant occurrence of these precipitates in the form of grain boundary allotriomorphs illustrates the favourable grain boundary nucleation site. It is also evident, however, that the planar allotriomorphic austenite-ferrite interface has become unstable and given way to Widmanstätten precipitation in some instances (fig 4.3(b)). The etched appearance of the precipitate phase indicates a subsequent transformation of the austenite precipitates to martensite on cooling to room temperature.

The absence of measureable partitioning of chromium and nickel to the respective ferrite and austenite phases during this rapid transformation at first appears somewhat surprising in view of the predicted diffusion behaviour from fig 4.1. Any possibility of a diffusionless massive transformation having occurred can be ruled out due to the occurrence of the Widmanstätten growth morphologies. This leads to the assumption that interstitial carbon and nitrogen diffusion has occurred resulting in local para-equilibrium of the austenite phase. Evidence supporting this assumption follows from observations made by Castro and Tricot[92]. They identified very rapid diffusion of carbon and nitrogen towards austenite precipitates during rapid quenching of a 17% Cr stainless steel from the single phase δ-ferrite region.

Continuous furnace cooling from 1380°C to 950°C followed by quenching to room temperature has resulted in a greater degree of $\delta \rightarrow \gamma$ transformation, yet incomplete (fig 4.4(a)). The lathy phase morphology indicates an extension of the Widmanstätten plate growth initially identified in the microstructure quenched from 1380°C. Widmanstätten plates are seen to occur as both secondary side plates which develop from grain boundary allotriomorphs of austenite and as intragranular plates which grow within the δ-ferrite grains. These morphologies are consistent with the Dubè classifaction for the formation of Widmanstätten ferrite from austenite in hypoeutectoid steels[93]. Once again it seems that the $\delta \rightarrow \gamma$ transformation has been initiated by the formation of grain boundary allotriomorphs which are seen to outline the prior δ-ferrite grain boundaries (fig 4.4(a)). The favourable grain boundary nucleation site and the faster grain boundary diffusion paths would have led to a fairly rapid initial growth of the austenite. However, the growth of austenite allotriomorphs would have slowed down when the ferrite grain boundaries became site-saturated with austenite precipitates. Following this stage, it is apparent that the mode of Widmanstätten side plate growth was favoured rather than the continued growth of the allotriomorphs by the normal mode of planar interface displacement. Similar austenitisation behaviour has been shown to occur during the transformation of large grained α-ferrite to austenite in an Fe-C-Si-Mn dual phase

steel[94] when reheated into the intercritical region, and it has been suggested that the Widmanstätten plates are more effective than the normal growth mode of planar interface displacement to rapidly increase the austenite volume fraction.

The change in growth mode from the initial planar interface displacement (GBA) to the Widmanstätten growth mechanism occurs due to the growth kinetics of a plate structure being more favourable for a large grained microstructure[95]. For the migration of the planar interface of a chunky precipitate, long range diffusion is required. The composition profile along an advancing precipitate, in this case austenite, is shown in fig 5.1(a). Area A1 in fig 5.1(a) is proportional to the mass of solute rejected from the austenite precipitate as it grew a distance Z. All of this solute is piled up directly in front of the interface so that the area marked A2 must equal A1. Since the interface concentration gradient may be determined as a function of the parameter L, the further the austenite precipitate grows, the bigger L becomes and the diffusion range increases. Therefore the growth rate is time dependent and continually decreases with time.

In contrast, the composition profile along an advancing plate is shown in fig 5.1(b). As the austenite plate grows, most of the solute ejected from the tip will diffuse laterally to the sides of the thin plate. Since all the solute is not piled up ahead of the advancing tip, area A1 does not equal area A2. In this way, the solute profile at the centreline of the tip is essentially independent of time and diffusion occurs over much shorter distances with plate growth. This means that plate lengthening will occur at a steady state velocity.

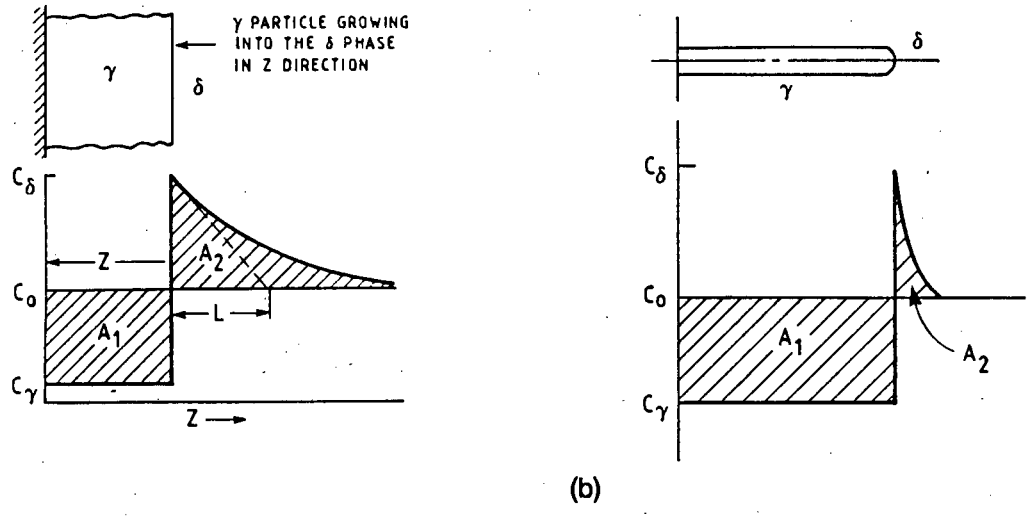

FIGURE 5.1 : Comparison of the composition profiles expected for allotriomorphic and plate precipitate growth (After Ref 95).

(a) Migration of a planar interface

(b) Advancing plate precipitate

The occurrence of the Widmanstätten precipitation of austenite during the decomposition of δ-ferrite in stainless steels has been previously reported [34,42,43,92]. Of importance in this study, however, is the restriction of such a transformation mechanism on the extent to which decomposition of the δ-ferrite structure to austenite occurs, and the effect that the presence of the residual δ-ferrite has on subsequent transformations occurring in the steel and on its properties. Even during relatively slow continuous furnace cooling, at a rate of 1°C/min, a complete $\delta \rightarrow \gamma$ transformation is still not produced (fig 4.6(a)). The amount of residual δ-ferrite interlaths in this case is similar to that produced during the faster uncontrolled furnace cooling previously mentioned. Under both furnace cooling conditions partitioning of chromium and nickel to the respective ferrite and austenite phases is identified. In addition, the degree to which this partitioning has occurred, as identified by EDS, is of the same order for both cooling rates. Transformation temperatures determined by dilatometry, however, indicate a lower austenite-start temperature (γ_s) for the faster cooling rate condition (fig 4.2). This tends to indicate the temperature-time dependence for the nucleation of grain boundary allotriomorphs and therefore the later start of transformation in the case of the faster cooling rate. Although the austenite-finish temperature (γ_s) also appears lower, little confidence can be attached to this result due to the difficulty previously mentioned in determining the transformation point. The fact that similar degrees of transformation occur during both fast and slow cooling may well indicate that equilibrium is already obtained during the faster furnace cooling condition. However, the barriers required to be overcome during complete transformation via Widmanstätten growth are worthy of discussion.

On account of the fact that an interlath structure is maintained irrespective of the cooling rates considered, attention is focussed on the phase structure relationship developed during Widmanstätten growth. It is well known that epitaxial matching usually occurs at the precipitate/matrix interface during plate growth in order to create a low energy interface. This implies a specific crystallographic orientation relationship between the matrix and precipitate. The δ-ferrite/austenite interlath morphologies are seen to exhibit a considerable degree of regularity and there seems little doubt from previous research[34,42,43] that retained δ-ferrite and austenite are Kurdjumov-Sachs (K-S) related as a consequence of the $\delta \rightarrow \gamma$ solid-state transformation via Widmanstätten growth. In the case of the $\delta \rightarrow \gamma$ transformation, the K-S relationship implies that the $\gamma(111)$ and $\delta(110)$ close-packed planes are parallel, thereby giving rise to a coherent, or at least semi-coherent, interface as a result of the atomic matching across the interface. Although coherent boundaries of this type have low surface energy, the surrounding material may be strained for considerable distances[96]. Consequently their movement is believed to be arrested by the accumulation of volume strain energy and therefore the

boundaries have low mobility. This means that despite austenite plate lengthening occurring fairly rapidly during the δ-ferrite decomposition reaction, the actual thickening of the austenite plates could possibly be interface controlled rather than diffusion controlled. The model suggested by Brown et al[34] for the decomposition of δ-ferrite in duplex stainless steel castings illustrates a mechanism for the generation of the interlath morphologies which is dependent on the existence of both fast and slow moving interfaces. In their model the restricted movement of semi-coherent interfaces is outlined. Furthermore, it is possible that solute build-up on the sides of the advancing plates could result in the solute content of the interlath ferrite exceeding the equilibrium composition in terms of ferrite promoters. This would lead to increased stabilisation of the residual δ-ferrite and therefore diminish the driving force for further transformation. These factors could account for restricted δ→γ transformation in 3CR12 and perhaps the presence of more residual interlath δ-ferrite than might be expected.

Simonen and Trivedi[97] indicate that volume diffusion and interfacial structure are known to control the growth kinetics and shape of Widmanstätten precipitates, and that plate thickening is argued to be dependent on a ledge mechanism. More particularly Southwick and Honeycombe[42] have shown that the growth kinetics of the austenite during δ-ferrite decomposition are intermediate between interface and volume diffusion control. Nevertheless, they have indicated that despite the δ-ferrite and austenite being related by the K-S orientation relationship throughout the growth and coarsening stage, the constant values for the aspect ratios of the austenite indicated no serious barrier to growth in the thickening direction. If this is true for the present situation as well, then it is possible that the interpretation of the reported phase equilibria and the calculation of the nickel and chromium equivalents (chapter 2) has resulted in the incorrect determination of the 3CR12 equilibrium phase diagram. This may imply that the 3CR12 vertical composition line does not pass through the austenitic region at all, but in fact is maintained in the ferrite + austenite two phase region during cooling. However, examination of the δ-ferrite decomposition in the 3CR12Ni alloy, which contains a greater proportion of austenite promoting elements (ie, 1.2 wt % Ni) also indicates an incomplete δ→γ transformation. Even allowing for error in the construction of an equilibrium phase diagram for this alloy, the indications are that this alloy should definitely pass through the austenitic region during cooling. Previous investigations concerning the reaustenitisation of thermomechanically processed 3CR12 and 3CR12Ni have indicated that 92-95 vol % austenite is achieved in 3CR12 and a fully austenitic structure is obtained for 3CR12Ni[77,98]. Therefore it is possible that the transformation mechanisms occurring during the cooling conditions presently investigated may well restrict the δ-ferrite to austenite decomposition reaction to certain extents in alloys such as 3CR12. The low carbon content in solution in 3CR12 places more emphasis on the

diffusion of substitutional elements in controlling complete transformation. Consequently, the considerable decrease in volume diffusion of substitutional elements with decrease in temperature means that solute build-up in the δ-ferrite interlaths could exacerbate the already retarded plate thickening kinetics. The implications of the presence of residual δ-ferrite on further transformations in 3CR12 are discussed in the subsequent paragraphs.

5.1.2 FORMATION OF α-FERRITE

Continuous cooling from the 1380°C solution temperature to room temperature has led to the partial regression of austenite to α-ferrite. The transformation start temperatures for this reaction are indicated in the range 750° to 800°C and are approximately 100° lower than the α-ferrite-start temperature predicted from the equilibrium diagram in fig 4.2. The lower α-ferrite-start temperature would seem to indicate a significantly more stable austenite than that predicted from the phase diagram in fig 4.1. This may well be expected in view of the suggestion that the residual δ-ferrite contains more ferrite stabilisers than the equilibrium situation. However, the time-temperature dependence of these reactions must not be ignored and the delayed reaction start may be a function of the cooling rate.

Ferrite growth is identified by the planar migration of the δ-ferrite/austenite interface into the austenite phase. There is no direct evidence for the nucleation of new ferrite at either prior ferrite-austenite or austenite-austenite grain boundaries. It is understood from classical nucleation theory that a greater driving force is required to nucleate a new grain than is required to grow an existing grain. Since in this instance the reaction is occurring during cooling, the initial driving force for transformation is not very high. Therefore it is understandable that the start of ferrite formation will take place such that the change in surface free energy will be lowest, and hence interface migration rather than nucleation occurs. Similar observations have been noted in a previous study concerning austenite decomposition in 3CR12[98]. Energy dispersive spectroscopy analysis has indicated that the new ferrite has the same composition with respect to Cr and Ni content as the parent austenite phase. Consequently, it would appear that the diffusion of Cr and Ni is not necessary for this transformation to occur, but rather that possibly only interstitial elements (carbon and nitrogen) play an important role.

The origin of the microstructure of the commercially produced 3CR12 plate can now be traced through an understanding of the evolution of the 3CR12 microstructure during cooling from temperatures just below the solidus. Evidence for the existence of a duplex ferrite-austenite structure during hot rolling is provided by the rolled strip which was

quenched immediately after the final reduction. The phase composition and morphology of this banded ferrite/martensite microstructure can be compared to the microstructure developed after furnace cooling from 1380°C to 950°C, followed by quenching to room temperature. Partitioning trends expected from the $\delta \rightarrow \gamma$ transformation are identified in the alternating bands of ferrite and martensite, and the sharp interface between these two phases is reminiscent of the incomplete $\delta \rightarrow \gamma$ transformation. This suggests that the duplex structure present during hot rolling is composed of austenite and residual untransformed δ-ferrite. The incomplete $\delta \rightarrow \gamma$ transformation has been shown to produce a lathy ferrite-austenite structure which obviously gives rise to a banded microstructure after rolling, i.e. the alternating thin lamellae of ferrite and austenite are reminiscent of the filamentary structure developed during Widmanstätten growth.

The transformation behaviour of the duplex structure after hot rolling is illustrated by the microstructures developed during slow cooling of the laboratory rolled strips. Regression of the austenite to α-ferrite occurs in the same way as that identified during continuous cooling of the solution treated (1380°C) specimens. This is illustrated in fig 4.10(a) by the migration of the original δ/γ interface into the austenite band. Slower cooling (1°C/min) below the reduction temperature indicates the tendency towards an almost complete regression of the austenite to α-ferrite. The initial transformation mechanism by boundary migration, as opposed to nucleation, has resulted in the formation of long undulating grain boundaries parallel to the rolling direction. Although the ferrite grain thickness can in many cases be related to the thickness of the original bands, it is apparent that grain coalescence has also occurred, thereby giving rise to much larger grains.

Similar phase banding and substitutional element partitioning is illustrated by the production hot rolled 3CR12 plate (alloy C1) which has been allowed to air cool after final reduction. It is also apparent that the continuous air cooling of the rolled coil has allowed partial regression of some of the austenite to α-ferrite. Once again the $\gamma \rightarrow \alpha$ transformation has involved the migration of the δ/γ interface into the austenite bands. Although recrystallisation has occurred within the ferrite bands, continuous boundaries are still produced as the interface migrates. Since the initial recrystallisation of ferrite at the δ/γ interface produces a flat boundary corresponding to this interface, migration of a number of recrystallised ferrite boundaries into the austenite appears as a long, more or less straight boundary. This is clearly illustrated in fig 4.11(c). Directionality of the original δ/γ interface that existed during rolling is therefore maintained even during the subsequent recovery events and regression of austenite.

Tempering of the rolled structure leads to recovery of the martensite (transformed residual austenite) and grain coalescence. The low carbon martensite loses its lath structure fairly rapidly between 700°C and 800°C[77] and it is apparent that the annealing out of dislocations gives rise to so called "recrystallisation" of the martensite (fig 4.12). This "recrystallisation", which is noted to really only be a form of subgrain growth resulting from the general coarsening of the carbide particles[99], can lead to the formation of equiaxed areas of ferrite. But, in view of the general 3CR12 microstructure being elongated, the subgrain growth and grain coalescence mostly results in larger "pancake" shaped ferrite grains being formed. The commercially rolled and tempered steel (Alloy A2) exhibits a fully ferritic microstructure which is clearly anisotropic with respect to grain morphology. Long flat grains are identified in a section parallel to the rolling direction. Despite the fully ferritic phase structure, the microstructure still displays compositional banding as shown by EDS analysis of the coloured bands developed during tint-etching. The fact that the total redistribution of Cr and Ni is not necessary during the $\gamma \rightarrow \alpha$-ferrite transformation is consistent with results obtained during the continuous furnace cooling of the solution treated (1380°C) specimens. A model summarising the events leading up to the development of the final annealed 3CR12 ferritic microstructure is illustrated in fig 5.2.

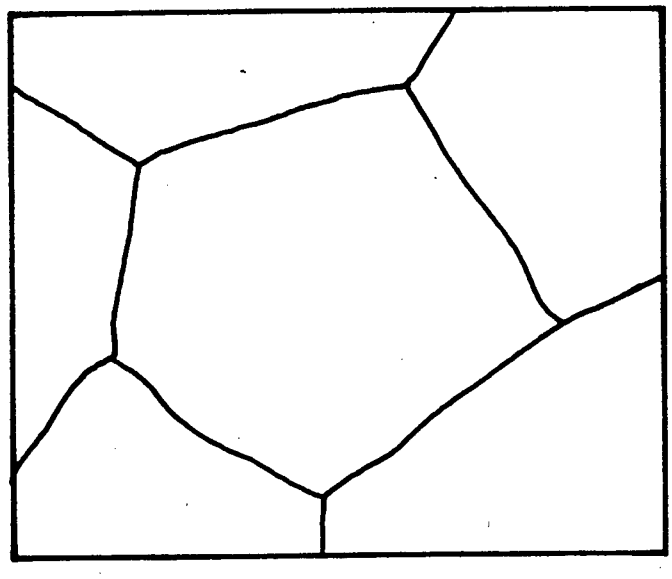

(a) Single phase δ-ferrite structure above 1200°C. Homogeneous distribution of ferrite and austenite forming elements.

FIGURE 5.2 : A model depicting the events leading up to the evolution of the final annealed 3CR12 microstructure.

FIGURE 5.2/contd...

(b) δ-ferrite transforms to austenite via Widmanstatten growth to produce a lathy structure. Element partitioning occurs between the two phases.

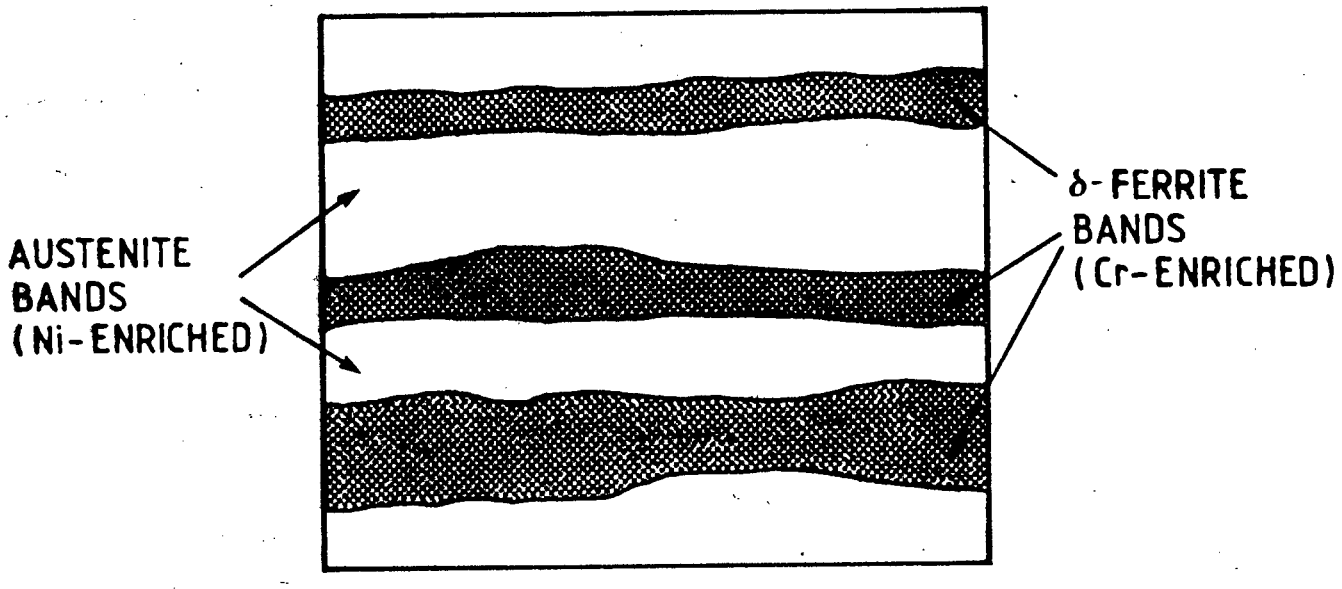

(c) Hot rolling (terminated at approx. 800°-850°C) gives rise to a banded residual δ-ferrite/austenite structure.

FIGURE 5.2 : A model depicting the events leading up to the evolution of the final annealed 3CR12 microstructure.

FIGURE 5.2/contd...

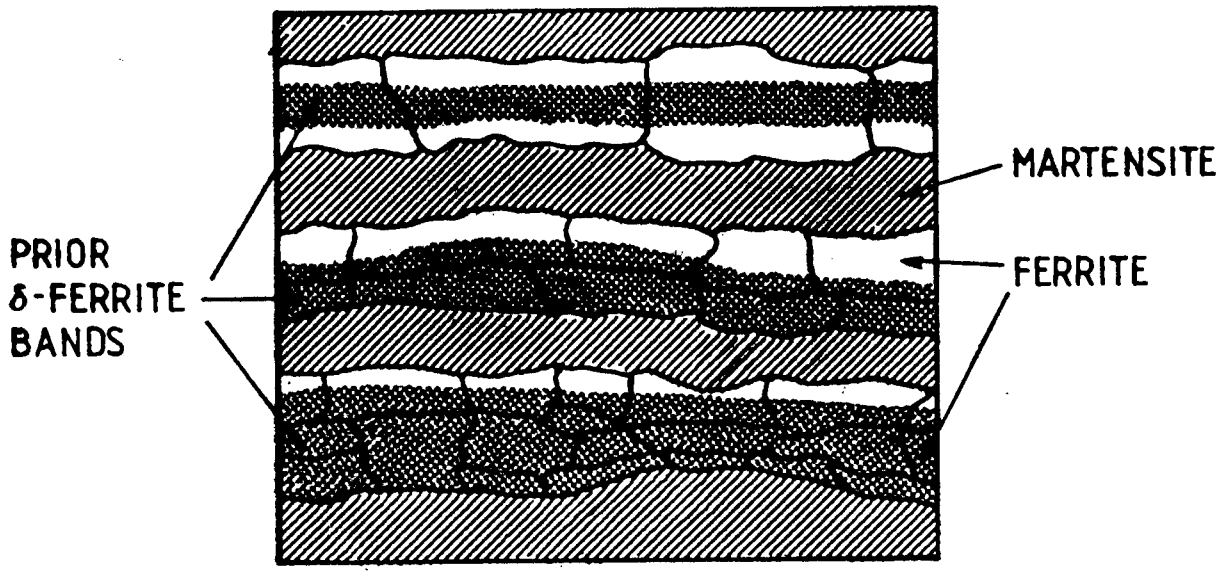

(d) Partial austenite regression occurs during cooling to room temperature after rolling. α-ferrite growth occurs via planar migration of the δ/γ interface into the austenite bands.

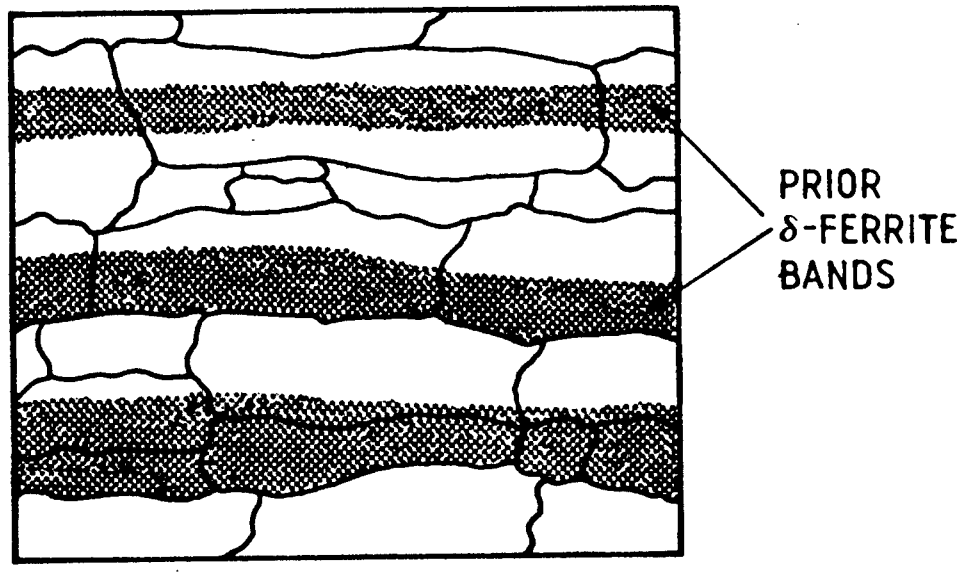

(e) Sub-critical annealing leads to recovery of martensite and grain boundary coalescence. Original δ/γ composition banding is still evident.

FIGURE 5.2 : A model depicting the events leading up to the evolution of the final annealed 3CR12 microstructure.

In view of the compositional banding evident in the tempered microstructure, reheating into the two phase α-ferrite plus austenite region gives rise to the preferential reaustenitisation of areas rich in austenite promoters. Therefore, even after soaking at 950°C for 1 hour, directional banding with respect to ferrite and austenite is maintained. Although the ferrite bands tend to break up to some extent, and become more undulated, the general elongated structure is still maintained during subsequent transformation.

It is clear then that the persistent occurrence of the ferrite "pancake morphology", even after reheating into the $\alpha+\gamma$ region, is largely due to the incomplete decomposition of the δ-ferrite structure and the resultant compositional banding. This gives the steel a "fingerprint" which cannot be eliminated by conventional metallurgical treatments.

5.2 OCURRENCE OF NON-METALLIC INCLUSIONS IN 3CR12

Although the inclusion compositions reported in this work have been determined semi-quantitatively and are limited by the detection of those elements only with atomic number greater than 10, a comparison of these results with previous inclusion studies reported in the literature gives rise to a reasonable assessment of the composition and origin of the non-metallic inclusions occurring in 3CR12 steel. Therefore, in order to validate a discussion on the occurrence of non-metallics in 3CR12, much emphasis is placed on the elements contained in the inclusions and not necessarily their exact stoichiometric ratios, although these can be inferred in most cases.

Considering the average chemical composition of 3CR12, it is not surprising to find inclusions containing titanium, manganese, carbon, nitrogen, sulphur, and phosphorous dispersed throughout the matrix. The presence of titanium carbides and nitrides is to be tolerated since titanium is purposefully added to the steel as a stabliser in order to lower the carbon and nitrogen interstitial levels. However, unlike carbon and nitrogen which contribute strongly towards the strength and transformation behaviour of steels of this nature, the elements sulphur and phosphorous are considered to be unfortunate impurities inherent in the steel making process. Manganese sulphides are not uncommon in steels and the addition of titanium has led to the occurrence of titanium sulphides and phosphides as well. Consequently, it is evident that the two principal metals contained in the inclusions in 3CR12 are titanium and manganese and it is therefore reasonable to divide the inclusions into two main groups based on the relative contents of these two metals.

5.2.1 TITANIUM CONTAINING INCLUSIONS

On the basis of the EDS analysis of the Ti-rich inclusions and their size, shape and distribution in 3CR12, five compositional categories are proposed for these inclusions. These are (i) N-rich carbonitrides, Ti (NC), (ii) carbosulphides, $Ti_4C_2S_2$, (iii) C-rich carbonitrides, Ti (CN), (iv) Ti-rich mixed sulphides, (Ti, Mn)S, and (v) Ti-rich phosphide inclusions. Differentiation among these five categories is important in determining the evolution of inclusions in 3CR12 and the effect they may have on the properties of the steel. The reasons for this classification are discussed in the following paragraphs.

(i) N-rich carbonitrides, Ti (NC)

It is well known that titanium can combine with both carbon and nitrogen and the yellow cuboid inclusions such as those identified in 3CR12 are often referred to as titanium carbonitrides. This nomenclature, however, does not infer any particular balance between carbon and nitrogen in the inclusion composition. Nevertheless, it can be demonstrated that the nitrogen content is much greater than the carbon content in cuboid inclusions occurring in 3CR12. This is apparent for two reasons. In the first instance it has been reported, although not in great detail, that direct analysis of cuboid inclusions using secondary ion mapping indicates far more intense spectra for TiN^+ than for TiC^+ [100]. Secondly, and much more conclusively, the present work has shown a direct dependence of the volume fraction of cuboids on the steel nitrogen levels. In contrast, there does not appear to be any direct relationship between the carbon content and the cuboid inclusion population. These observations tend to indicate that the cuboid inclusions in 3CR12 might behave more like TiN inclusions and are thus referred to as Ti(NC).

Bearing in mind the solubility behaviour of TiN inclusions[54,56], it can be strongly suggested that the titanium containing cuboid inclusions in 3CR12 precipitate from temperatures above the alloy liquidus. Furthermore, it has been reported that yellow cuboid inclusions have been identified in the ladle which is used to add titanium to the melt during the 3CR12 production process[101]. Although large clusters of these inclusions can be identified in the steels in certain instances, their more or less homogeneous distribution does not indicate preferential precipitation from either a ferrite or austenite phase. In view of the fact that titanium partitions to the ferrite phase and both carbon and nitrogen partition to the austenite phase, it would be expected that some phase relationship might exist had the inclusions precipitated from the solid. This is clearly not the case and although it has been proposed by Brink[78] that the yellow

cuboid inclusions preferentially precipitate from the ferrite phase, there is no substantial evidence for this proposal. The fact that the cuboids sometimes occur in fairly large clusters or chain-like formations is possibly due to a settling phenomena during the steel solidification process coupled with the displacement of these solid particles by the solidification front to pockets of residual liquid. Reheating the steel to temperatures just below 1400°C does not appear to change the distribution of the cuboid inclusions in any way.

(ii) Carbosulphides, $Ti_4C_2S_2$

The detection of sulphur at the edges of the yellow cuboid inclusions implies that a titanium sulphide phase has formed at the surface of the cuboids. The relative peak intensities for Ti and S indicate the formation of titanium carbosulphide, $Ti_4C_2S_2$, as opposed to TiS. Although some of the globular inclusions containing Ti and S are not directly associated with the cuboid inclusions, it is accepted that they are similar in composition in view of the relative peak intensities. Unfortunately the solubility product for $Ti_4C_2S_2$ is not available at present in the literature, but the association of this sulphur compound with the cuboid inclusions seems to suggest similar solubility behaviour for these two inclusion types.

(iii) C-rich carbonitrides, Ti (CN)

The inhomogeneous distribution of very fine Ti-rich precipitates at the prior δ/γ interface gives the impression that these inclusions precipitated from the solid phase at temperatures significantly lower than the solidus. These inclusions are presumed to be rich in carbon in view of the much greater solubility of TiC in steel than TiN. It has been demonstrated that the solubility of TiC is greater than the solubility of TiN in steels by a factor of approximately 3, and that TiC is known to dissolve above 1100°C in 0.03 wt.%C stainless steels (section 2.5). In addition, a study of the precipitation of titanium carbonitride inclusions in microalloyed austenite during stress relaxation has led to a distinction being made between undissolved carbonitrides rich in nitrogen and reprecipitated carbonitrides rich in carbon[102]. The latter inclusions precipitated subsequent to austenite deformation in the temperature range 950°-1050°C. These observations support the proposal that the fine Ti-rich particles stringered parallel to the rolling direction in 3CR12 are C-rich and indicates that they possibly precipitated during the hot rolling process. The occurrence of precipitates at the δ/γ interface suggests that this is a favourable nucleation site.

(iv) Ti-rich mixed sulphides, (Ti, Mn)S.

It seems unlikely that a pure stoichiometric titanium sulphide, TiS, occurs in a steel of this nature. The Ti-S system has not yet been fully explained and a complicated range in inclusion formulae has been proposed[44,57]. As shown in (ii) above, the Ti/S peak ratios imply the presence of a carbosulphide phase in many instances. However, the occasional detection of minor amounts of manganese associated with inclusions rich in Ti and S requires an explanation. It is recognised that metal solid solubility can occur in sulphide inclusions[44] and the Mn-Ti-S system has been identified to some extent. On account of the formation of titanium sulphide being more favourable than the formation of manganese sulphide from the point of view of free energies of formation, it is reasonable to predict that the mixed Mn-Ti sulphides should contain predominantly Ti if there is sufficient Ti available for their formation. This is supported by the fact that the addition of Ti to steels reduces the MnS content [49]. The mixed (Ti, Mn)S inclusions found in 3CR12 are generally spherical in shape and owing to the fact that TiS is considerably harder than MnS[44], it is less likely that these inclusions were plastically deformed during the hot rolling process. Apart from this occurrence, it is also evident that manganese can be associated with the sulphide phase identified on the surface of the yellow cuboid inclusions, as has been detected in some instances.

(v) Ti-rich phosphide inclusions

Inclusions containing titanium and phosphorous are distributed in a similar manner to the fine Ti-rich inclusions which are proposed to be Ti(CN) precipitates, ie, they also appear at the δ/γ interface. Similar Ti-P inclusions have been identified in the δ-ferrite phase during slow cooling from the fully δ-ferrite condition to room temperature. These fine inclusions are, however, absent when the steel is slow cooled from the δ-ferrite condition to 950°C followed by oil quenching to room temperature. This seems to suggest that they precipitate from the solid phase at, or near to, the δ/γ interface during cooling below 950°C.

The grain boundary segregation of phosphorous is common in low alloy steels during ageing in the temperature range 400°-800°C. This occurs as a result of the decreased solubility of phosphorous in ferrite over this temperature range and often leads to the embrittlement of steels. Nevertheless, the degree of phosphorous segregation can be affected by other elements in the steel[103]. Carbon is seen to compete with phosphorous for grain boundary positions and a mutual displacement occurs for these elements at the grain boundaries. With increasing carbon bulk concentration, segregation of carbon

increases, and the grain boundary concentration of phosphorous decreases. The addition of elements such as chromium and titanium affect the segregation of phosphorous differently. Chromium lowers the activity of carbon and results in less competition between carbon and phosphorous for grain boundary positions, and therefore leads to increased phosphorous grain boundary segregation. Titanium, on the other hand, can affect the phosphorous segregation in two ways. Like chromium, titanium lowers the carbon activity by the precipitation of stable TiC and reduces the competition between carbon and phosphorous as mentioned above. On the other hand, if excess titanium is available in the bulk, then the solubility of phosphorous is reduced by the precipitation of a phosphide phase. It has been shown that increasing the bulk titanium content can lead to decreased grain boundary segregation of phosphorous[103]. Although the activity of titanium is lowered considerably by the presence of carbon, nitrogen and sulphur in 3CR12, there appears to be sufficient titanium available to form some phosphide. A possible consequence of the low titanium activity is the fairly late precipitation of the phosphide phase which can explain the inhomogeneous distribution of these inclusions near to, or on, the δ/γ boundaries. That is to say, the migration of phosphorous to the grain boundaries with decrease in temperature has resulted in the precipitation of the phosphide phase in this grain boundary region. The EDS analysis of these inclusions also indicates the presence of Fe which suggests some similarity to the phosphide composition $(Ti,Fe)_3P$ determined by Erhart et al[103].

5.2.2 MANGANESE SULPHIDE INCLUSIONS

As mentioned in part (iv) of the preceding discussion, manganese is occasionally detected in inclusions rich in titanium and sulphur. Apart from this, however, inclusions containing manganese and sulphur only (EDS analysis) have also been identified and are seen to occur as long, flat inclusions elongated parallel to the rolling direction (fig 4.20). Manganese sulphide inclusions of this nature are not uncommon in steels and may contain variable amounts of iron as well as other elements such as chromium in solid solution. In view of the fairly high relative plasticity of manganese sulphide inclusions with respect to the steel matrix during hot rolling, these inclusions are easily deformed and thus derive their pancake morphology[52]. Apart from the occurrence of homogeneous MnS inclusions in 3CR12, small amounts of titanium can often be associated with some of these stringered inclusions. Generally, as the amount of titanium increases in the inclusion, there is a morphological change from a pancake shaped inclusion to the more globular inclusions discussed in part (iv) of the previous section.

5.2.3 VARIATION IN INCLUSION POPULATIONS WITH STEEL COMPOSITION

Although the variations in bulk composition for the 3CR12 commercial heats examined (A1-A14 and B1-B8) are relatively subtle, changes in the inclusion populations have been identified. However, these reported differences in inclusion populations only concern the larger, more eaily identifiable inclusions. Any variation in the distribution of the fine Ti(CN) and Ti-Fe-P inclusions is difficult to assess and therefore it is unable to directly relate the dependence of their occurrence on the bulk chemistry of the steel.

The yellow cuboid inclusions, Ti (NC), are present in all the steels, and as has been shown for heats B1-B8, their exact volume fraction is dependent on the nitrogen content of the steel. Sulphur is often detected at the cuboid boundaries ($Ti_4C_2S_2$), but since this can vary within a particular heat, no correlation can be made between the amount of sulphur occurring on the cuboid boundaries and the bulk steel composition. Isolated titanium carbosulphide inclusions and titanium sulphide inclusions containing small amounts of manganese also occur to some extent in all the 3CR12 alloys, but their relative volume fractions appear to be related to the occurrence of stringered manganese sulphide inclusions. In considering once again the free energies of formation for titanium sulphide and manganese sulphide inclusions, and the trends previously noted for relative distributions of these inclusions (fig 2.12), titanium sulphide should form in preference to manganese sulphide. This means that on condition there is sufficient "free" titanium available, little or no manganese sulphide should occur in the steel. However, the Ti and S contents of the 3CR12 heats vary fairly considerably and it is clear that there may not always be sufficient free titanium available to combine with all the sulphur. Furthermore, since the Ti (NC) inclusions form fairly early in the melt, the free titanium available for sulphide formation will be further affected by the nitrogen content of the steel. For these reasons then, it is feasible to suggest that the lower the Ti/S ratio of the steel, the more likely is the occurrence of MnS inclusions and mixed (Mn, Ti)S inclusions, whereas for higher Ti/S ratios, $Ti_4C_2S_2$ and mixed (Ti,Mn)S inclusions will be more dominant. This observation has an important effect on the morphology of sulphide inclusions in 3CR12. Titanium containing sulphide inclusions are much harder than manganese sulphide inclusions[44] and are therefore less likely to be deformed during hot rolling. The result is that sulphide inclusions rich in titanium tend to be spherical whilst MnS inclusions are elongated parallel to the rolling direction.

The investigations concerned with the fracture and corrosion behaviour of 3CR12 clearly outline the influences of the various sulphide compositions and morphologies in these steels.

5.3 IMPACT FRACTURE BEHAVIOUR OF 3CR12

Two important facts have emerged from the impact fracture studies on annealed 3CR12 heats :-

(i) A trend exists between the impact fracture energy and the sulphur content and Ti/S ratio, and

(ii) Delamination parallel to the rolling plane occurs in all the heats tested.

The occurrence of delamination and the effect of inclusions on the impact toughness are no doubt related, but several other factors relating to the microstructure need to be taken into account in determining the modes of impact failure in 3CR12 alloys.

5.3.1 FACTORS INFLUENCING IMPACT ENERGY

Since a notable variation in impact energy is observed when considering a range of 3CR12 commercial heats tested in the T-L orientation, fracture initiation must be influenced slightly differently in each heat. In view of all the heats being subjected to similar rolling schedules during production and the fact that all testpieces were given a standard anneal prior to testing, the grain structure of the different heats should not vary in any considerable manner. This is confirmed by the absence of any notable differences in hardness and grain distribution within the heats examined. Furthermore, if grain structure and composition were likely to affect the range in impact energy, then a relationship should exist between impact energy and ferrite factor. Clearly this is not so, as shown in fig 4.27. It thus makes sense to consider the influence of non-metallic inclusions on fracture initiation and propagation.

It is clear from the preceding discussion (section 5.2) that a variety of inclusions and precipitate phases occur in 3CR12 steel. The size, shape, coherency, and deformation characteristics of the various particles will obviously affect fracture in different ways. As has already been shown, the population of the larger titanium containing cuboid inclusions and the manganese sulphide inclusions can be related to the chemistry of the steel. It follows that if a trend is identified with respect to impact energy and the element content affecting these inclusion distributions, then a more substantial argument can be put forward for the inclusion type mostly responsible for the variation in impact energy. Such a relationship exists between the impact energy and the sulphur level of the steel. In addition, the titanium level, when considered in conjunction with the sulphur level, is

also seen to play a role. Since it has been shown that the sulphur and titanium levels both affect the manganese sulphide content of the steel, it follows that the variations in the populations of the flattened manganese sulphide inclusions are most likely to be responsible for the range in impact energy observed.

To illustrate the importance of titanium in controlling the morphology of sulphide inclusions and the deleterious effect of MnS on impact fracture, the impact fracture behaviour of a Ti-free 3CR12 alloy was compared to normal 3CR12. A comparison of the impact fracture surfaces (T-L orientation) of the Ti-free alloy and alloy A7 is illustrated in fig 5.3. Apart from the much lower impact energy recorded for the Ti-free alloy, the fracture surface shows some resemblance to the "woody" appearance which has previously been related to the occurrence of appreciable amounts of MnS inclusions. This suggests that increasing MnS populations enhance the role played by these inclusions in determining the mode of fracture and the fracture energy.

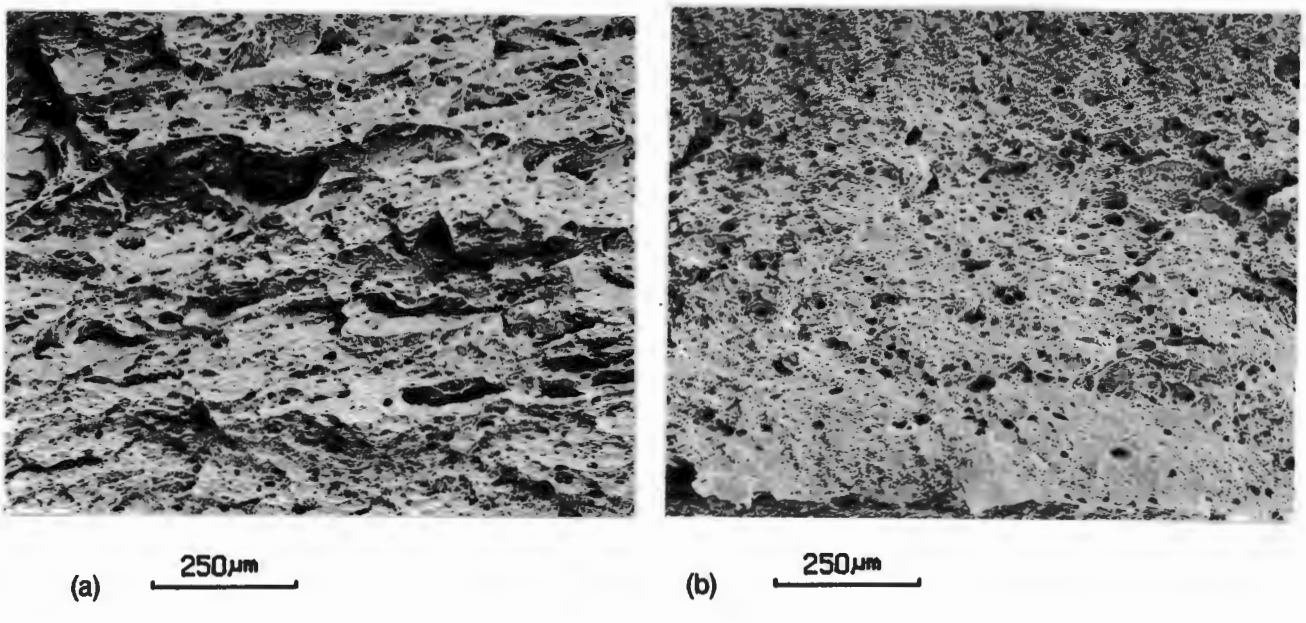

FIGURE 5.3 : Comparison of the fracture surfaces of a Ti-free alloy and alloy A7
(a) Ti-free alloy : impact energy = 35J
(b) Alloy A7 : impact energy = 55J.

The fact that MnS inclusions mostly affect the impact strength of 3CR12 is not surprising when considering the findings of previous studies[61-63]. However, the contributions from other inclusions cannot be ignored since numerous inclusion types have been identified both within the ductile-dimples and in association with the split surfaces. Non-

deformable inclusions which form as clusters during solidification are known to have similar effects to MnS inclusions on fracture[67]. This is due to the tendency for the clusters to be elongated to the same extent as the matrix and therefore form stringer-type inclusions. Titanium cuboid inclusions have been noted to occur in this manner in 3CR12 and likewise are identified in connection with fracture initiation. Although these inclusions do not override the effect of MnS inclusions, their relative proportions must affect the change in impact strength of 3CR12. Since the nitrogen level is seen to control the volume fraction of the cuboid inclusions, steels with lower nitrogen levels should have slightly better impact properties. This is apparent from fig 4.26 which indicates higher impact energies for alloys possessing favourable nitrogen levels and Ti/S ratios.

These results suggest that the impact energy of 3CR12, for a particular test direction, can be modified by even relatively small changes in the chemistry of the steel. Careful control of the sulphur and nitrogen levels (less than 0.010 wt %) should ensure low volume fractions of both manganese sulphide and titanium containing cuboid [Ti(NC)] inclusions. On the other hand, moderate titanium additions (0.30 - 0.40 wt %) should be maintained in order to ensure the formation of globular titanium sulphide compounds instead of the easily hot deformable manganese sulphide inclusions. In this way optimum impact properties for 3CR12 can be maintained.

5.3.2 FACTORS DETERMINING MODE OF FRACTURE

Two distinct modes of failure have been observed during the impact fracture of Charpy specimens notched in the through thickness direction (T-L orientation test specimens, fig 3.8). These are :-

(i) Ductile rupture characterised by a dimple fracture appearance, and

(ii) Low-energy delamination due to the formation of splits parallel to the rolling plane.

The causes of the ductile-dimple fracture can be attributed to void coalescence, mainly resulting from the initiation of voids at inclusion sites. Dimples occur almost exclusively on the ridge areas (fig 4.30) and are associated with the fracture of the individual ligaments which are developed as a result of splitting. This type of fracture typically represents a fairly high-energy failure mode. The occurrence of delamination, however, is not as simple, and can be related to a number of factors.

The stress causing the splitting can be explained in terms of the triaxial stress system set up at the root of the Charpy V-notch. With reference to fig 5.4(a), the applied stress, σ_1, causes the material to yield at the root of the notch (area 1), while the material above and below the notch (area 2) is still contrained by the unloaded volumes. This results in secondary stresses being imposed in the σ_2 and σ_3 directions. It is these secondary stresses (σ_2) which occur perpendicular to the rolling plane that are responsible for the splitting.

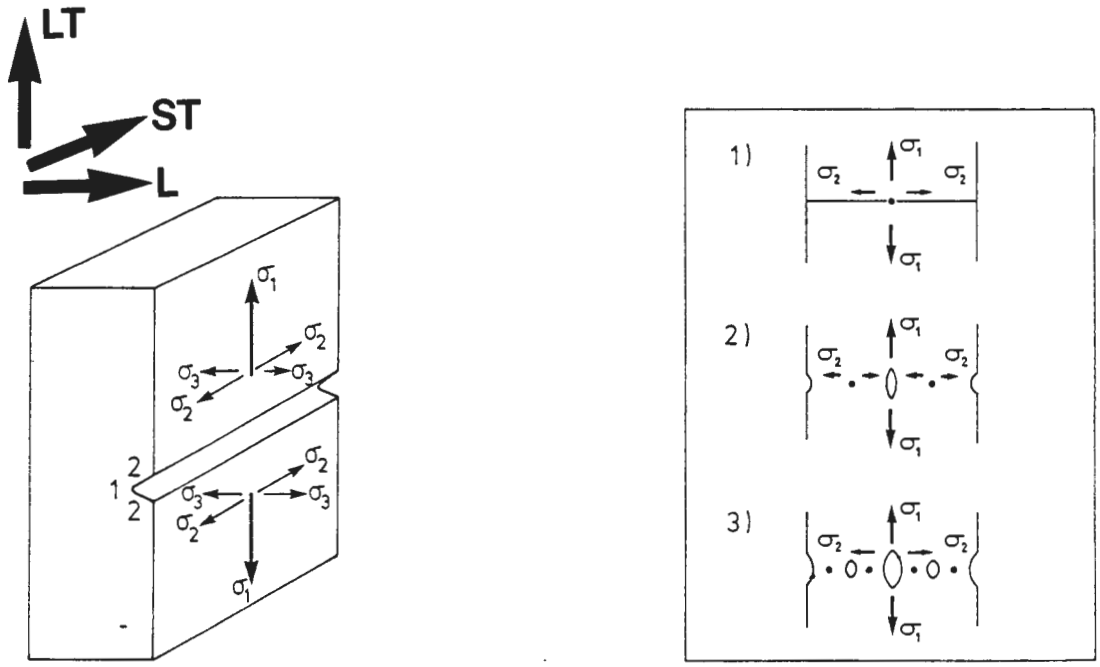

(a) (b)

FIGURE 5.4 : Development of triaxial stress system at root of notch and subsequent events leading to splitting.

(a) Triaxial stresses (L = Longitudinal, LT = Long transverse, ST = Short transverse)

(b) Simple model of splitting events (see text for explanation)

(1) initial maximum σ_2 stress concentration;

(2) two necking systems produced by first split;

(3) new maximum σ_2 produces further splitting.

A model of the splitting events shown in fig 5.4(b) indicates the initial maximum σ_2 stress concentration to be in the centre of the test specimen. Therefore, the first split is expected to occur in this region and subsequently two necking systems (ligaments) are produced. If a slightly weaker planar orientation exists off-centre, then it is likely that

initial splitting could correspond to this weakness (see fig 4.28(b)). A new maximum in the σ_2 stress concentration is now set up in the centre of each secondary necking system and results in further splitting at regular spacings. During initial loading, and before delamination occurs, the plane-strain situation gives rise to a σ_2 stress which is about twice the yield stress of the material at the elastic/plastic interface at the notch root[69]. However, σ_2 is always smaller than σ_1, and therefore the stress required to cause delamination must be less than the stress required to fracture the principle fracture plane (in this case the plane defined by the longitudinal and through-thickness directions). Since the development of triaxial stresses is inherent in the Charpy V-notch impact testing of ductile materials, the factors which determine the occurrence of splitting are chiefly microstructural, and are discussed for 3CR12 in the subsequent paragraphs.

Certainly one of the most striking factors contributing to delamination is the elongated grain morphology of 3CR12. Characterisation of the 3CR12 microstructure has shown that even after sub-critical annealing, the grain structure of the steel remains elongated in the rolling direction. This gives rise to long, flat grain boundaries which have been shown by previous studies to favour delamination in the rolling plane[64,66]. The fact that the ferrite grains grow outwards from the original δ-ferrite bands during cooling after final reduction means that a continuous grain boundary front is often maintained over a number of grains. This makes grain boundary decohesion and crack propogation even easier since the longer the length over which the grain boundaries can decohese, the more favourable are the conditions for crack propogation, i.e. extended grain boundary areas parallel to the rolling plane give rise to large fracture paths nearly equi-oriented for a crack propagated along this plane. These arguments are supported by the planar orientation of the delamination surface and the predominant occurrence of intergranular failure as observed on cross-sections of the split surfaces (fig 4.39(a)). Limited ductile tearing is also observed on the split fracture surface due to the crack path being altered by minor delaminations ahead of the main propagating split (fig 4.38). Ductile tearing arises from the joining up of the minor cracks associated with intergranular and/or transgranular failure. The term "quasi-cleavage" described by McDonald and Ludwigson[91] may be applied to describe this combination of both ductile and low energy failure.

As previously mentioned, the energy to part these grain boundaries must of course be less than the energy required to fracture the material in the plane perpendicular to the principle stress (σ_1). Bramfitt and Marder[64] have shown that the triaxial stress is sufficient to part the grains in a plane parallel to the principle stress when the aspect ratio is of the order of 2.4:1 in the longtudinal direction (L-T orientation testpiece) and

3.4:1 in the transverse direction (T-L orientation testpiece) when testing high purity Fe-1% Mn alloys. In the present situation concerning the fracture of transverse 3CR12 specimens (T-L orientation) in the annealed condition, the average aspect ratio in the transverse direction is of the order of 2:1. This value is much less than the limiting value for the occurrence of delamination in the transverse specimens tested by Bramfitt and Marder[64]. Since ferrite-ferrite interfaces are being considered in both cases, it would seem to suggest that additional factors other than aspect ratio are important in controlling the occurrence of delamination in 3CR12. A possible solution to this is the fact that the aspect ratios of the grains themselves may not indicate long grain boundaries, but the parallel alignment of the prior δ/γ interfaces and the subsequent transformation mechanisms has resulted in the planar orientation of the ferrite grains (fig 5.2). Therefore it is the continuous alignment of the grain boundaries rather than the length of the individual boundaries in the transverse direction that encourages delamination. Grain boundaries coincident with prior δ-ferrite/austenite interfaces (shadow banding) have been observed to present favourable crack paths (fig 4.39).

It is likely that non-metallic inclusions also play a large role in promoting grain boundary decohesion. The elongated shape of the inclusions in the rolling plane favour void initiation at the inclusion/matrix interface. This is especially true for MnS inclusions which, due to their high plastic deformability at hot rolling temperatures, have a large surface area in contact with the matrix in the rolling plane. In addition, the difference in the thermal expansion coefficients between the matrix and MnS (where matrix < MnS)[104] facilitates the formation of voids at the inclusion/matrix interface. MnS inclusions, along with titanium sulphides and cuboid inclusions, have often been identified on the split surfaces in 3CR12. However, it is unlikely that inclusions play a major role in causing splitting due to the absence of the "woody" fracture appearance which is synonymous with inclusion related delamination[67].

The titanium carbide and titanium phosphide particles which have been shown to precipitate at the δ/γ interface during cooling below 950°C must not be ignored in terms of contributing towards delamination. In fact the distribution of these precipitates often coincides with the arrangement of the grain boundaries in view of the alignment of both the precipitates and the ferrite grains being determined by the prior δ-ferrite/austenite structure. It is highly likely that in many instances the migrating ferrite grain boundaries may be pinned by the small precipitates. Thus the precipitates are aligned in arrays parallel to the rolling plane and are located on (or near) grain boundaries which are themselves elongated in the rolling direction. It has been shown by DeArbo[68] that the precipitation of Fe_3C particles on ferrite grain boundaries is largely responsible for tensile specimen splitting of high strength low alloy steels. Grain boundary decohesion is

likely to be promoted by the presence of these precipitates, and in the case where precipitate arrays occur within grains, transgranular cleavage is encouraged. The fact that the crack is often coincident with the "shadow" banding effect reminiscent of the original δ-ferrite/austenite banding suggests itself that splitting might be promoted by the parallel alignment of the titanium carbide and titanium phosphide particles.

The texture of 3CR12 could also certainly play a role in the splitting phenomenon. Texture determinations on hot rolled 3CR12 plate have shown that the {100}<011> texture component forms within the ferrite after rolling in the dual phase ferrite and austenite phase region[105]. This obviously corresponds to the deformation of the residual δ-ferrite bands at hot rolling temperatures. A texture similar to the ferrite has also been found to have formed in the martensite due to the influence of the strongly textured neighbouring ferrite grains[105]. The production of a {100} texture in BCC materials preferentially aligns cleavage planes parallel to the rolling plane. Although σ_1, (principle stress) is greater than σ_2 (stress in through-thickness direction), the favourable cleavage orientation has been shown to permit cleavage in the rolling plane[69] and transgranular-fracture results. The occurrence of transgranular cleavage during splitting in 3CR12 is certainly identified although it is not dominant. It is likely that the combination of easy grain boundary decohesion and cleavage plane orientation leads to the favourable cleavage of grains in certain situations. Cleavage crack propagation is probably not continuous due to crack tip blunting at grain orientations not favouring cleavage and the fact that cracking can occur ahead of the main split at weaknesses such as long grain boundaries and inclusions which then reduces the energy at the tip of the main crack. Cracking ahead of the main split leads to tearing and therefore the presence of quasi-cleavage is an indication of the more minor role played by transgranular cleavage. As mentioned previously, the alignment of any precipitates within grains can also encourage transgranular cleavage.

More recent work by Matthews et al[106] has indicated the presence of bands of orientations of {100}<uvw> and {111}<uvw> type textures in annealed 3CR12 plate. They have suggested that this crystallographic banding contributes to grain boundary decohesion by the crystal-plasticity mechanism proposed by Chao[71]. The presence of banded crystallographic orientations are not explained but it would seem that they arise from the combination of the existence of a two phase ferrite+austenite structure during hot deformation and the subsequent structural changes which occur during cooling to room temperature and during later tempering operations (section 5.1.2).

From the preceding discussion, it would seem that the most likely cause of delamination in 3CR12, and hence the very large difference between impact properties for specimens

notched in the through-thickness direction and in the rolling plane, is the parallel alignment of grain boundaries in the rolling plane. This is reflected by the occurrence of mostly intergranular separation. Reheating into the intercritical region followed by sub-critical annealing has been shown in a previous study to still produce delamination[107] and therefore highlights the suggestion that the grain boundary morphology is dependent on the original δ-ferrite/austenite banding in 3CR12. However, other factors such as the occurrence of non-metallic inclusions (in particular MnS) and precipitates parallel to the rolling direction certainly play an additional role in determining the extent of delamination. The more minor occurrence of transgranular-cleavage could be texture related and it is possible that differential straining of the two textures could enhance grain boundary decohesion.

5.4 DUPLEX FERRITE-MARTENSITE STEELS CONTAINING APPROXIMATELY 16 wt% CHROMIUM

5.4.1 GRAIN REFINEMENT

The microstructure of low carbon ferritic stainless steels (16-17 wt % Cr) can be refined by increasing the austenitising ability of the steel. This leads to the decomposition of the coarse-grained high temperature δ-ferrite and the formation of a duplex ferrite-martensite microstructure. The extent to which the $\delta \rightarrow \gamma$ transformation occurs is very important in that it controls the final grain size of the alloy. The solid state $\delta \rightarrow \gamma$ transformation occurs mainly via the Widmanstätten growth mechanism which follows the initial formation of allotriomorphic austenite at the prior δ-ferrite grain boundaries. However, when only minor δ-ferrite decomposition is permitted, austenite is formed mostly as grain boundary allotriomorphs and plate growth is generally absent. The formation of austenite precipitates at the δ-ferrite grain boundaries does little to reduce the overall grain size of the ferritic structure since the diameter of the ferrite grains are only marginally reduced by the average diameter of the austenite precipitates. In the case of more advanced δ-ferrite decomposition, the Widmanstätten growth mechanism dominates and the formation of austenite plates leads to considerable reduction in the grain size of the original δ-ferrite. This gives rise to the formation of a "lathy" microstructure which when rolled produces a banded duplex ferrite-austenite structure; the austenite forms martensite during cooling to ambient.

The alloy system which has been investigated considers nickel to be the main variable in terms of austenitising ability due to the strict requirement for low interstitial levels, especially carbon. The extent to which the solid state $\delta \rightarrow \gamma$ transformation occurs is therefore related to the nickel content of the alloy. In addition it is also necessary to consider the balance between the ferrite forming and austenite forming elements in the steel chemistry since an increasing Cr equivalent will counteract an increasing Ni equivalent and vice versa. Thus a more cost effective modified alloy, in terms of an alloy based on the AISI 430 ferritic stainless steel, has been demonstrated to require a chromium level in the region of 16-16.5 wt % and a nickel level of approximately 2.5-2.8 wt % in order to effectively refine the grain structure. It is important that the alloy remains titanium-free as the presence of titanium will increase the ferrite forming ability of the alloy and therefore invoke larger nickel additions.

The above composition has been shown to give rise to a microstructure consisting of ferrite bands in a martensitic matrix in the hot rolled condition. A 3-dimensional impression of the microstructure is shown in fig 5.5. The stability of this duplex structure is such that very little variation in the microstructure is identified during cooling below 1000°C. Attempts at inducing isothermal transformations in the range 500-1000°C after a presoak at 1100°C have shown negligible changes in the phase ratios (fig 4.43). It is also apparent that there is very little variation in the composition of the ferrite and martensite phases over the temperature range examined, although there is a marked difference between the composition of the two phases. The difference in phase composition suggests the preferential partitioning of nickel to the austenite (now martensite) phase and the enrichment of chromium in the ferrite phase. This partitioning is consistent with the diffusion controlled solid state $\delta \rightarrow \gamma$ transformation. In the case of the isothermal heat treatments, composition analysis of the martensite phase indicated negligible variation in both the Cr and Ni levels as function of the final soak temperature (fig 4.42). The composition of the ferrite also varied only slightly, although there is a drop in the Cr content below 800°C. This probably reflects the precipitation of chromium carbides below this temperature. The consistency of both the ferrite-martensite phase ratios and the respective phase compositions reflects the sluggishness of diffusion below 1000°C and the fact that the large degree of partitioning between the two phases has further stablised these phases. This means that the duplex structure developed during the solid state $\delta \rightarrow \gamma$ transformation is stable down to room temperature although the austenite does transform to martensite.

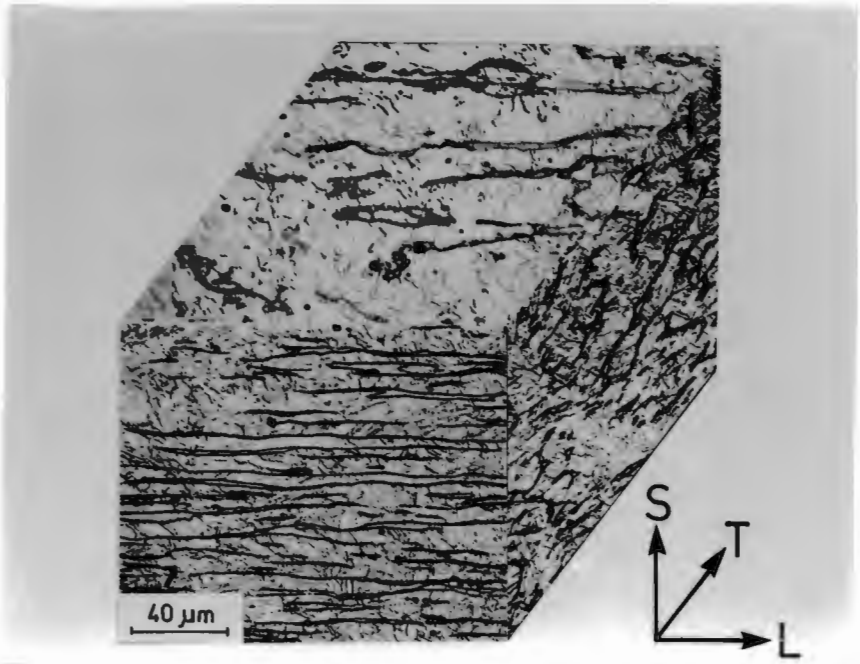

FIGURE 5.5 : Microstructure of alloy E5 in the hot rolled condition. Dark areas indicate residual δ-ferrite and light areas are martensite.

5.4.2 NICKEL CONTENT

The effect of nickel content on the transformation behaviour of the duplex alloys has been illustrated by examining the transformation temperatures of alloys E4-E6 during both heating and cooling cycles (fig 4.44). It is clear that during heating there is little difference in the transformation temperatures relative to the nickel content. On cooling, however, the temperature at which the start of the $\delta \rightarrow \gamma$ transformation occurs varies as a function of the nickel content. It has been shown that the higher the nickel level, the higher the temperature at which the start of the δ-ferrite decomposition occurs. The temperature at which the $\delta \rightarrow \gamma$ reaction is terminated is affected in a similar way and increases with increasing nickel content. This observation implies that the stability of the δ-ferrite can be altered by even relatively small changes in the nickel levels. One might imagine that under welding conditions where some regions will almost certainly be transformed to single phase δ-ferrite at temperature, there is a greater tendency for the higher nickel alloys to decompose to austenite during cooling and therefore form substantial amounts of low carbon martensite in the heat affected zone. In this way the grain size is more likely to be reduced and the combination of the ferrite-martensite structure could lead to improved toughness in the heat affected zone. The martensite-start and -finish temperatures are not affected by the change in nickel content over the considered nickel range.

In addition to the variation in the $\delta \rightarrow \gamma$ transformation temperatures, the extent to which this transformation occurs is also affected by the nickel content. This is clearly evident from the bulk hardness and phase ratios measured for the hot rolled material. Increased nickel content leads to a lower ferrite content and correspondingly higher hardness in the rolled condition. What is surprising is the much smaller difference in the ferrite content and hardness of alloys E5 and E6, despite the substantial difference in nickel level. This may indicate that the extent of the δ-ferrite decomposition is influenced by the nature of the Widmanstätten growth mechanism. In other words the decomposition reaction has reached a stage whereby in both situations further transformation is largely controlled by the movement of interfaces and thus the rate of transformation in each case is similarly retarded. Apart from the benefits that may be obtained in welding alloy E6 due to the earlier decomposition of δ-ferrite during cooling, the microstructures of alloys E5 and E6 appear similar. From the point of view of refining the grain size of ferritic steels with minimum additional cost, it would appear more sensible to choose alloy E5 in order to lower the nickel requirement.

The tensile strengths of the three alloys (E4-E6) also illustrate the effect of nickel on the microstructure and properties of the alloys. In the normalised condition it is quite clear that the strength is proportional to the nickel content of the alloys. Identical trends are followed by the three alloys in relation to tempering temperature and under each condition the actual strength is related to the nickel content. There is an obvious decrease in strength after tempering at 600°C and 700°C, the tensile strength recorded for the latter tempering temperature being slightly higher than that recorded after tempering at 600°C. Tempering at 800°C also resulted in a decrease in the tensile strength compared to the normalised condition although this was not as marked.

5.4.3 TEMPERING REACTIONS

The term tempering has been applied to the heat treatments in the range 600-800°C although by definition this is not quite correct. The A_{C1} temperature for these alloys occurs at approximately 600°C and therefore heat treatments above these temperatures are expected to form new austenite which is not consistent with tempering treatments. Nevertheless, the overall softening of the original martensite has led to the term tempering being used in this case. Analysis of the phase reactions during the tempering of alloy E5 has allowed an understanding of the microstructural characteristics giving rise to the observed trends in the tensile properties. Tempering at 500°C has resulted in a microstructure which is not significantly different from the microstructure representative of the normalised condition, although a slight increase in hardness is

observed. This increase in hardness is possibly due to the precipitation of fine $M_{23}C_6$ carbides (both at prior austenite grain boundaries and at interlath sites) which are not readily identified by the SEM micrographs (fig 4.47(b)). The microstructure produced as a result of tempering at 600°C indicated substantial softening of the martensite and the formation of fairly coarse precipitates both at the prior austenite grain boundaries and within the grains themselves. Although it is expected that much coarser $M_{23}C_6$ carbides would form at 600°C compared to the temper at 500°C and hence a significant reduction in hardness, it cannot be concluded that the coarse precipitates identified in the SEM micrographs are representative of $M_{23}C_6$ carbides. Dilatometry has been carried out in order to identify the possible formation of new austenite during tempering at this temperature (fig 5.6(a)). A normalised specimen heated to 600°C at 8°C/min and held at temperature for 2 hours has indicated a decrease in specimen length recorded during soaking at 600°C which is consistent with the formation of new austenite. On cooling to room temperature, however, martensite formation was not observed. This would seem to suggest that the austenite formed at 600°C is subsequently retained at room temperature. The coarse precipitates occurring both inter-and intra-granularly (fig 4.47(c)) could therefore be identified as retained austenite. A similar occurrence of retained austenite has been identified during the tempering of a 0.024C-16Cr-1.5Mo-5Ni stainless steel[16]. Tempering at 700°C has resulted in much more obvious changes in the appearance of the original martensitic matrix. Fine acicular precipitates are produced after tempering for 2 hours (fig 4.47(d)) and it is shown that increasing the tempering time up to 5 hours leads to the formation of a more closely knit lamellar structure (fig 4.47(e)). It is evident that the martensite has decomposed to form new austenite, but in this case the amount of austenite is indeed much greater. The transformation of the martensitic matrix during tempering at 700°C has therefore resulted in the formation of fine secondary ferrite intermixed with austenite. Dilatometry has once again aided the identification of the formation of austenite at the tempering temperature (700°C) but in this instance the formation of new martensite has occurred during cooling to ambient (fig 5.6(b)). Nevertheless, it cannot be concluded whether or not all the austenite forms martensite. In the case of tempering at 800°C a similar structure is produced to that observed at 700°C, but the extent to which new austenite has formed is much greater. This is illustrated by the greater decrease in specimen length during soaking at 800°C for 2 hours (fig 5.6(c)) and by the higher bulk hardness of the heat treated microstructure (Table 4.12). It is also apparent from the SEM micrograph (fig 4.47(g)) that much larger areas of austenite have formed. The dilatometer trace in this instance shows more martensite formed compared to the temper at 700°C.

Composition analysis of the microstructure formed after tempering at 700°C (Table 4.13) has indicated partitioning of chromium and nickel between the new martensite and

secondary ferrite which was formed as a result of the decomposition of the original martensitic matrix. The relative partitioning of nickel is the most obvious and it is observed that as the amount of secondary ferrite decreases (tempering time = 5 hours), the nickel content within this phase also decreases. Similar phase reactions have been identified by Grobner and Biss[16] but the exact mechanism has not been established. It would seem that the precipitation of carbides (most likely chromium carbides) from the low carbon martensite during reheating fairly rapidly recovers the martensite, thereby reducing the tetragonality of the martensite and forming secondary ferrite. Since reheating occurs above the A_{C1} temperature (overtempering), austenite is able to form and nickel is rejected from the recovered martensite into the growing austenite regions. This rejection of nickel in turn encourages the ferritic character of the recovered martensite. The similarity in the microstructures after tempering for 5 hours and 8 hours indicates that a state of reasonable equilibrium has been reached. This demonstrates the ability to achieve a very fine grained, stable two phase ferrite-martensite structure in what were originally martensitic regions. The development of a lamellar structure reveals that the austenite has nucleated at tempered martensite lath boundaries and therefore has developed a growth habit related to the orientation of the original martensite laths in view of the constraint imposed by the existing laths. Similar nucleation and growth of austenite has been shown to occur during the low temperature (750°C) reaustenitisation of low alloy steels[108].

The absence of a martensitic transformation after forming reverted austenite at 600°C can be explained by the lowering of the M_s temperature due to the higher nickel content of the new austenite. In view of the precipitates being too small to analyse after tempering for 2 hours, a specimen was soaked at 600°C for 20 hours and the austenite precipitates were analysed (Table 5.1). In this case the precipitates, which reached a size of up to 4 microns, were seen to contain nearly 5 wt % nickel which is sufficient to reduce the M_S temperature to below room temperature.

TABLE 5.1 : Composition of phases present in alloy E5 after tempering at 600°C for 20 hrs. All figures represent wt %.

PHASE TYPE	Cr	Ni
PRIMARY FERRITE	17.6±0.1	1.8±0.1
SECONDARY FERRITE	15.2±0.4	2.4±0.1
RETAINED AUSTENITE	14.9±0.2	4.7±0.3

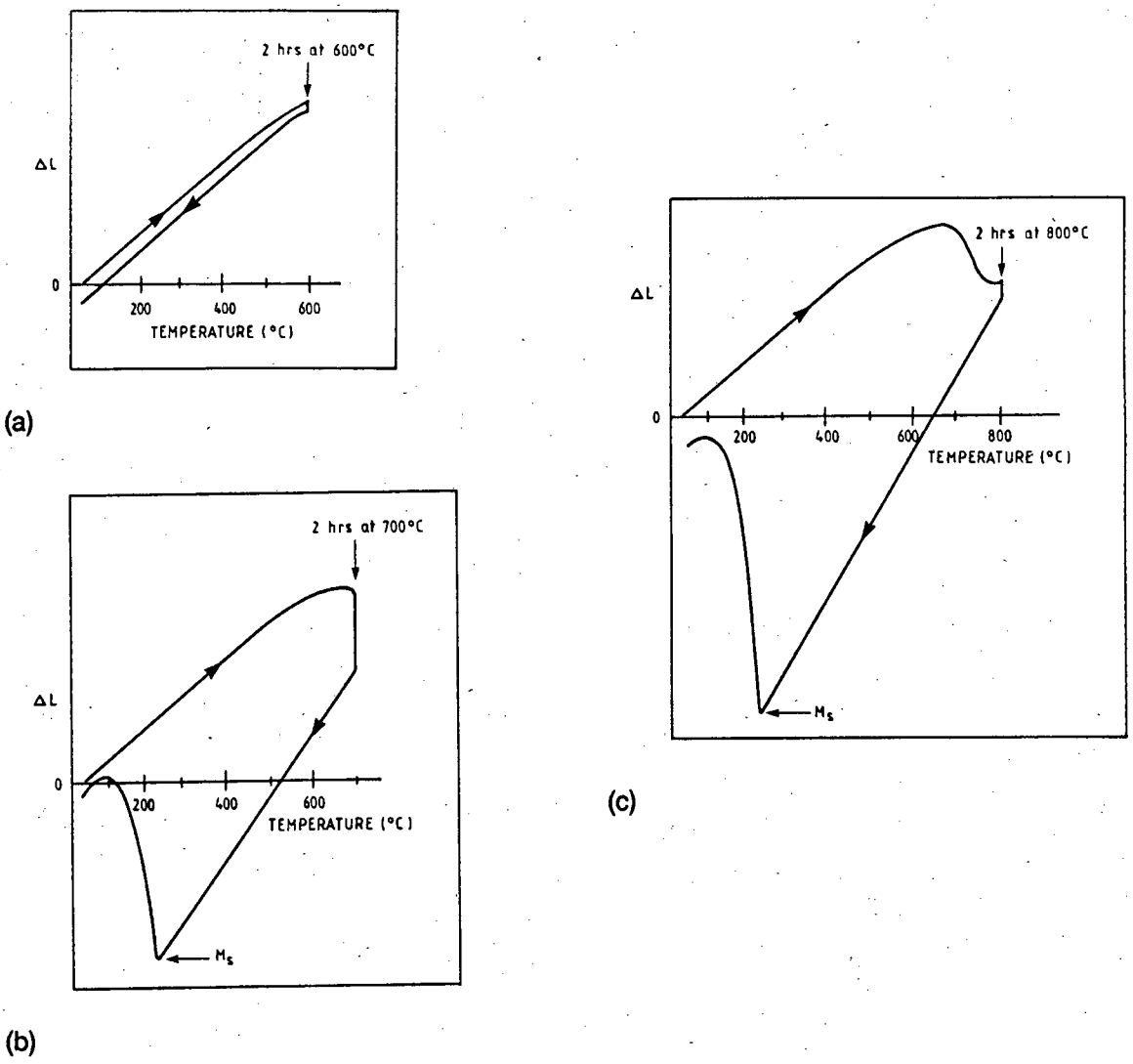

FIGURE 5.6 : Dilatometer traces representative of tempering treatments (Alloy E5).
(a) 600°C
(b) 700°C
(c) 800°C

The rapid recovery of the martensite above 600°C and the rejection of nickel from the growing secondary ferrite regions has reduced the hardness and strength of the duplex alloys considerably. The impact toughness of alloy E5 is shown to follow an inverse trend compared to that observed for the tensile strength. The highest impact energy was recorded after tempering at 700°C which illustrates the resistance to crack initiation and propagation of the lamellar ferrite-martensite microstructure. Previous work concerning in situ observations of tensile fracture in lamellar dual phase structures has demonstrated that

martensite lamellae possess good ductility and can sustain a certain degree of plastic deformation[109]. Consequently propagating cracks may be blunted by the retardation effect of the lamellar structure. This suggests that an excellent combination of mechanical properties can be obtained for this alloy when heat treated at 700°C. Furthermore, the fact that these alloys are hardenable by heating at 800°C, with acceptable loss in impact toughness, makes them more versatile in their application. The potential displayed by such a microstructure demonstrates the ability to bridge the gap between the mechanical properties of ferritic stainless steels (Type AISI 430) and austenitic stainless steels (Type AISI 304) with minimal additional cost in view of the relatively low nickel additions (2.5 wt %) compared to conventional austenitics (8-10 wt %).

-ooOoo-

CHAPTER 6

SUMMARY

The small, yet significant composition deviations from AISI 409 have led to the design of an alloy, 3CR12, which has improved formability, weldability, and mechanical properties. These improvements can be largely attributed to the achievement of a much finer grained ferritic microstructure which originates from the grain refining effects caused by the presence of a duplex ferrite-austenite structure at hot rolling temperatures. It is apparent, though, that in spite of the advantages gained by the refined grain structure, the effects of the transformations occurring in 3CR12 need to be carefully understood in order to appreciate the limitations of such a modified alloy and the requirements for designing alloys with similar microstructures but of different compositions.

The low carbon, titanium stabilised chemistry of 3CR12 has been shown to form a duplex ferrite-austenite structure at hot rolling temperatures which has its origin due to the incomplete transformation of δ-ferrite to austenite. This fact alone illustrates the difference in the transformation behaviour between 3CR12 and low carbon low alloy dual phase steels. The ultimate aim in the manufacture of 3CR12 is the attainment of a fine grained very low carbon ferritic steel. Titanium stabilisation of 3CR12 leads to an extremely low effective carbon content and it has been demonstrated that even when the nickel content is increased, a fully austenitic structure is not obtained during the decomposition of δ-ferrite. Thus instead of the fine grained ferrite structure evolving from a fully austenitic structure during cooling, or from the formation of equiaxed ferrite during the subsequent tempering of low carbon martensite, the presence of residual δ-ferrite plays a major role in determining the morphology of the final structure. Compositional banding arises due to element partitioning during the incomplete $\delta \rightarrow \gamma$ transformation and the final ferrite grain shape is influenced by the elongated residual δ-ferrite stringers. Consequently, a directional microstructure is present even after heat treatment. In addition to the directional grain structure is the occurrence of non-metallic inclusions stringered in the rolling direction, and the parallel alignment of titanium carbide and titanium phosphide particles which originate from the precipitation at or near to the prior δ/γ interfaces. The combination of all these effects, along with the development of certain textures, promotes

the occurrence of delamination fracture behaviour which is persistent even after heat treatment. Although the impact properties of this alloy are still generally considered to be excellent, especially the low ductile-brittle cleavage transition temperature, the potential for the development of a high performance steel is lost in view of the anisotropy pertaining to this alloy. The mechanisms leading to the decomposition of the coarse grained δ-ferrite, coupled with hot rolling, ultimately gives rise to a finer grained ferritic structure when compared to non-transformable single phase ferritic steels, but, it is clear that the consequences of the existence of the banded phase structure cannot be avoided.

It has been shown that although the occurrence of delamination behaviour cannot be directly related to non-metallic inclusion populations, it is obvious that their presence exacerbates splitting and lowers the upper shelf impact energy. The inclusions found to most strongly influence the fracture behaviour are the elongated MnS inclusions, which occur more prominently in steels with higher sulphur levels and low Ti/S ratios. Likewise it has been demonstrated that the presence of numerous MnS inclusions have a deleterious effect on the corrosion performance of 3CR12 alloys. This is especially noticeable under conditions where the potential exists for crevice corrosion. In view of MnS inclusions affecting both impact properties and corrosion resistance, it is clear that strict control on the sulphur levels in this steel will provide optimum properties.

Attempts at refining the grain structure of ferritic steels containing 16 - 17 wt % chromium have shown that nickel additions in the order of 2.5 - 2.8 wt % are required in order to sufficiently refine the grain size of the high temperature δ-ferrite phase. The nature of the solid state $\delta \rightarrow \gamma$ transformation is similar to that identified in 3CR12 and gives rise to a duplex ferrite-austenite phase structure at hot rolling temperatures. Unlike 3CR12, however, regression of austenite to α-ferrite does not occur during cooling to room temperature and instead all the austenite originating from the solid state $\delta \rightarrow \gamma$ transformation transforms to martensite. Thus the hot rolled structure consists of residual δ-ferrite stringers in a martensitic matrix. Comparison of this duplex structure to alloys containing much smaller volumes of martensite, i.e. alloys which have undergone much less advanced $\delta \rightarrow \gamma$ transformation, has shown that more desirable properties are obtained from the finer grained high volume martensite alloys.

The hardness of the 16-17 wt % chromium duplex ferrite-martensite alloys is much greater than 3CR12, but this hardness can be reduced considerably by heat treating in the 600°-700°C range. In doing so, the martensitic matrix decomposes to a fine structure consisting of secondary ferrite and austenite, the austenite of which may or may not transform to martensite, depending on the tempering temperature. These heat treatments lead to a reduction in strength but greatly improve the impact toughness, especially when the

lamellar secondary ferrite-martensite structure is formed after tempering at 700°C. Thus the fine grained structure achieved as a result of the formation of austenite during the solid state $\delta \rightarrow \gamma$ transformation and the subsequent tempering of the steel at 700°C produces an alloy with considerably more attractive properties than single phase ferritic steels. Obviously additional cost is implemented by the addition of nickel, but the more versatile properties of this steel could prove its cost effectiveness, especially in relation to conventional austenitic stainless steels.

6.1 CONCLUSIONS

1. 3CR12 does not undergo a complete $\delta \rightarrow \gamma$ transformation during cooling from the single phase δ-ferrite region. The solid state $\delta \rightarrow \gamma$ transformation occurs via a Widmanstätten growth mechanism and it is possible that the nature of the Widmanstätten transformation retards the extent of the $\delta \rightarrow \gamma$ transformation. The incomplete $\delta \rightarrow \gamma$ transformation gives rise to a banded duplex microstructure after hot rolling.

2. Continuous cooling to room temperature leads to partial regression of austenite to α-ferrite. The formation of α-ferrite occurs via planar migration of the δ/γ interface into the austenite grains. Indications are that the diffusion of substitutional elements, Cr and Ni, is not necessary during the $\gamma \rightarrow \alpha$ transformation.

3. The growth of α-ferrite from the banded δ/γ phase structure leads to the formation of an elongated ferritic structure possessing long undulating grain boundaries parallel to the rolling direction.

4. The persistent composition banding in 3CR12, which originates from the solid state $\delta \rightarrow \gamma$ transformation, restricts the formation of an equiaxed grain structure even during subsequent reheating into the intercritical region.

5. Non-metallic inclusions containing Ti, Mn, C, N, S and P are common in 3CR12 steel. These inclusions have been identified as :-

   (a) Nitrogen-rich titanium carbonitrides, Ti(NC);
   (b) Titanium carbosulphides, $Ti_4C_2S_2$;
   (c) Carbon-rich titanium carbonitrides, Ti(CN);
   (d) Mixed sulphides (Ti,Mn)S;
   (e) Titanium containing phosphides, and
   (f) Manganese sulphides, MnS

6. The yellow cuboid Ti(NC) inclusions form in the liquid steel and their occurrence is related to the nitrogen content of the steel. $Ti_4C_2S_2$ compounds are often associated with these inclusions as a boundary phase.

7. Sulphide inclusions containing titanium are noted to form in preference to manganese sulphide inclusions and it is generally found that the occurrence of MnS inclusions is inversely related to the Ti/S ratio of the steel. The morphology of MnS sulphide inclusions changes from pancake shaped to globular as the titanium content in the inclusions increases.

8. Fine carbon-rich titanium carbonitrides, Ti(CN), and titanium phosphide particles precipitate from the solid phase at, or near to, the prior δ/γ interfaces and result in inclusion arrays stringered parallel to the rolling direction.

9. The fracture of 3CR12 in the annealed condition gives rise to a series of complex fracture modes. These fracture modes can be attributed to a combination of the elongated nature of the ferrite grains, the presence of non-metallic inclusions and other precipitate phases, and textural relationships developed during rolling. Impact energy is noted to vary for a range of commercial heats and the following relationships between bulk chemistry and impact energy have been observed:

   (a) Impact energy decreases as the sulphur content of the steel increases.
   (b) Impact energy increases with increasing Ti/S ratio.
   (c) Good impact energies are consistent with high Ti/S ratios and low nitrogen contents.

10. Although all inclusions would be expected to play some role in fracture initiation and propagation, the trends outlined indicate that manganese sulphide has the most deleterious effect. Stringered manganese sulphide inclusions appear to be very effective in causing inclusion/matrix decohesion because of their pancake-shape and differences in thermal expansion coefficients.

11. It has been shown that by the correct control of impurities, the toughness of 3CR12 can be optimised. To achieve such optimisation, it is necessary to meet the following requirements:

    (a) Sulphur contents of less than 0.008 wt %
    (b) Moderate titanium levels (0.30-0.40 wt %)
    (c) A low nitrogen content (0.010 wt %)

12. The mode of splitting in the rolling plane occurs predominantly by the separation of elongated ferrite grains. The continuous alignment of grain boundaries in the rolling plane provides a favourable crack path for low energy failure. The exposure of inclusions on the split surfaces indicates that delamination is aided considerably by inclusion/matrix decohesion. The parallel alignment of titanium carbide and titanium phosphide precipitates which is often coincident with grain boundaries exacerbates delamination. It is also suggested that crystallographic texture may play a role in aiding delamination.

13. The persistent occurrence of splitting even after heat treatment is related to the events leading to the microstructural evolution of 3CR12.

14. The presence of MnS inclusions in 3CR12 affects the corrosion behaviour of the steel. Increasing occurrence of MnS decreases the general stability of passive film formation and increases the susceptibility of the steel to crevice attack. Lower sulphur levels and improved Ti/S ratios will avoid many of the deleterious effects associated with large populations of MnS. Negligible effect on corrosion performance was observed for titanium sulphide and titanium carbonitride inclusions.

15. Nickel additions in the order of 2.5-2.8 wt % are required in order to refine the grain structure of ferritic steels containing 16-17 wt % chromium. Grain refinement caused by the solid state $\delta \rightarrow \gamma$ transformation gives rise to a banded duplex ferrite-martensite microstructure in the hot rolled condition. Tempering at 700°C results in a lamellar ferrite-martensite structure which produces optimum impact properties whilst maintaining acceptable tensile strengths.

16. The attractive microstructural and mechanical properties of a low interstitial (C=0.03 wt %) steel containing 16-17 wt % Cr and 2.5-2.8 wt % Ni demonstrates the ability to cost effectively bridge the gap between conventional ferritic and austenitic stainless steels.

-ooOoo-

REFERENCES

1. BALL A and HOFFMAN J P, *Met. Technol.*, 1981, **8**(9), pp.329-338.

2. KNUTSEN R D, BALL A, HEWITT J, HOFFMAN J P and HUTCHINGS R, in Proc. "Stainless Steels '87", Sept.87, York, The Inst. Met., London, 1988, pp.512-520.

3. GROBLER C and VAN ROOYEN G T, in Proc "25th Annual Conference of Metallurgists", Aug.1986, Toronto, Ont., paper 34.1.

4. KNUTSEN R D and HUTCHINGS R, *Mater. Sci. Technol.*, **4**, 1988, pp.127-135.

5. RASHID M S, *Ann. Rev. Mater. Sci.*, 1981, **11**, pp.245-266.

6. DAVIES R G, *Metall. Trans.*, 1978, **9A**, pp. 671-679.

7. BALLIGER N K and GLADMAN T, *Met. Sci.*, Mar. 1981, pp. 95-108

8. SZEWCZYK A F and GURLAND J, *Metall. Trans.*, 1982, **13A**, pp. 1821-1826

9. KORZEKWA D A, MATLOCK D K and KRAUSS G, *Metall. Trans.*, 1984, **15A**, pp. 1221-1228.

10. PICKERING F B, in Proc "Stainless Steels '84", Sept. 1984, Goteborg, The Inst. Met., London, 1985, pp. 2-28.

11. TIAINEN T, NIEMI K and KETTUNEN P, in Proc. "Stainless Steels '84", Sept 1984, Goteborg, The Inst. Met., London, 1985, pp. 37-42.

12. OSADA K, UEKOH S and EBATO K, in Proc. "Stainless Steels '87", Sept. 1987, York, The Inst. Met., London, 1988, pp. 490-497.

13. OLSSON J and NORDIN S, in Proc. "Int. Conf. on Duplex Stainless Steel", Oct. 1986, The Hague, paper 48.

14. HAYDEN H W and FLOREEN S, *Metall. Trans.*, 1970, **1**, pp 1955-1959.

15. WRIGHT R N and WOOD J R, *Metall. Trans.*, 1977, **8A**, pp. 2007-2011.

16. GROBNER P J and BISS V, *Metall. Trans.*, 1984, **15A**, pp. 1379-1387.

17. RIVLIN V G and RAYNOR G V, *Int. Met. Rev.*, 1980, **1**, pp. 21-28.

18. SPEICH G R, Metals Handbook, 8th edn., vol. **8**, "Metallography, Structures and Phase diagrams", ASM International, Metals Park, OH, 1973, p.424.

19. CHUANG Y Y and CHANG Y A, *Metall. Trans.*, 1987, **18A**, pp. 733-745.

20. SCHAEFFLER A L, *Weld. J.*, 1947, **20**, (10), pp.601s-620s.

21. SCHAEFFLER A L, *Metal Progress*, 1949,**56**, pp. 680 and 680b.

22. SCHAEFFLER A L, *Metal Progress*, 1960, **77**, p. 100b.

23. NEWELL H D and FLEISCHMAN M, US Patent No 2, 118, 683.

24. FIELD A L, BLOOM F K and LINNERT G E, "Development of Armour Welding Electrodes", OSRD Report Nos. 1636 and 3034, 1943.

25. SCHNEIDER H, *Foundry Trade Journal*, 1969, (May), pp. 562-563.

26. PRYCE L and ANDREWS K W, *JISI*, 1960, (August), pp. 415-417.

27. HULL F C, *Weld. J. Res. Suppl.*, 1973, **52** (5), 193s-203s.

28. SUUTALA N, *Metall. Trans.*, 1982, **13A**, pp. 2121-2130.

29. MARSHALL P, "Austenitic Stainless Steels - microstructure and mechanical properties", pp. 19-20, 1984, London, Elsevier Applied Science Publishers.

30. HONEYCOMBE R W K, "Steels - microstructure and properties", pp. 214-215, 1981, London, Edward-Arnold Ltd.

31. HARRIES D R, "Physical metallurgy of Fe-Ni-Cr austenitic steels", Int. Conf. Mech. Behaviour and Nuclear Applications of Stainless Steel at Elavated Temperatures", Varese, May 1981, London, Metals Society.

32. BRIGGS J Z and PARKER T D, "The super-12% Cr Steels", 1965, Climax Molybdenum Co.

33. PICKERING F B, *Int. Metals. Rev.*, 1976, Review **211**, pp. 227-268.

34. BROWN E L, WHIPPLE T A and KRAUSS G, in Conf. Proc. "Duplex Austenitic - Ferritic Stainless Steels", Oct 25-28, 1982, St. Louis, USA, pp. 665-691, ASM, Metals Park, Ohio, 1983.

35. FREDRIKSSON H, *Metall. Trans*, 1972, **3**, pp. 2989-2997.

36. LYMAN C E, *Weld J Res. Suppl.*, 1979, **58**(7), pp. 189s-194s.

37. LIPPOLD J C and SAVAGE W F, *Weld J Res. Suppl.*, 1979, **58**, pp. 362s-374s.

38. SUUTALA N, TAKALO T and MOISIO T, *Weld J Res. Suppl.*, 1981, **60**(5), pp. 92s-93s.

39. SUUTALA N, TAKALO T and MOISIO T, *Metall. Trans.*, 1979, **10A**, pp. 1183-1190.

40. BROOKS J A, WILLIAMS J C and THOMPSON A W, *Metall. Trans.*, 1983, **14A**, pp. 23-31.

41. BROOKS J A, WILLIAMS J C and THOMPSON A W, *Metall. Trans.*, 1983, **14A**, pp. 1271-1281.

42. SOUTHWICK P D and HONEYCOMBE R W K, *Met. Sci.*, July 1980, pp. 253-261.

43. SINGH J, PURDY G R and WEATHERLY G C, *Metall. Trans.*, 1985, **16A**, pp. 1363-1369.

44. KIESSLING R and LANGE N, in "Non-metallic Inclusions in Steel", 2 edn, part III, p. 1 and part II, p97, 1978, London, The Metals Society.

45. GASPARD C, MESSEIN P and GREDAY T, *Met. Scl.*, 1982, **16**, pp. 105-117.

46. ELLIOT J F and GLEISER M, in "Thermochemistry for Steelmaking", vol **1**, 1960, Addison-Wesley, Reading, USA.

47. SEDRIKS A J, Int. *Met. Rev.*, 1983, **28**(5), pp. 295-307.

48. BANKS T M and GLADMAN T, *Met. Technol.*, Mar. 1979, pp. 81-94.

49. BANDI W R, LUTZ J L and BUYOK E G, in "Sulfide Inclusions in Steels", eds, JJ deBarbadillo and E Snape, 1975, p. 178, American Society for Metals, Metals Park, Ohio.

50. WILSON W G and McLEAN A, in "Desulfurisation of Iron and Steel and Sulfide Shape Control", 1980, chap 5, AIME, Iron and Steel Society.

51. SIMS C E and DAHLE F B, *Trans. AFS*, 1938, **46**, p 65.

52. MURTY Y V, KATTAMIS T Z, MEHRABIAN R and FLEMINGS M C, *Metall. Trans.*, 1977, **8A**, pp.1275-1282.

53. DAIZHONG L, *Arch. Eisenhüttenwes*, 1983, **54**(12), pp.507-512 (in English).

54. HARRIES D R, "Physical Metallurgy of Fe-Cr-Ni austenitic steels", in Proc. "Int. Conf. on Mechanical Behaviour and Nuclear Applications of Stainless Steel at Elevated Temperatures", Varese, May 1981, London, The Metals Society.

55. NOVAK C J, in "Handbook of Stainless Steels", eds, D Peckner and I M Bernstein, 1977, chap 4, McGraw-Hill, New York.

56. WADA H and PEHLKE R D, *Metall. Trans.*, 1977, **8B**, pp.443-450.

57. BANDI W R and KRAPF G, *Analyst*, 1979, **104**, pp.812-821.

58. BALL C J, *Met. Sci.* 1984, **18**, pp.577-579.

59. HAYDEN H W, MOFFAT W G and WULFF J, "The Structure and Properties of Materials", vol III, pp.153-159, 1965, New York, John Wiley and Sons,

60. TANAKA M and IIZUKA H, *J Mat. Sci.*, **20**, 1985, pp.3750-3762.

61. RAGHUPATHY V P, SRINIVASAN V, KRISHNAN H and CHANDRASEKHARAIAH M N, *J Mat. Sci.*, 17, 1982, pp.2112-2126.

62. SPITZIG W A and SOBER R J, *Metall. Trans.*, **12A**, 1981, pp.281-291.

63. COX T B and LOW J R, *Metall. Trans.*, **5A**, 1974, pp.1457-1470.

64. BRAMFITT B L and MARDER A R, *Metall. Trans.*, **8A**, 1977, pp.1263-1273.

65. BALDI G and BUZZICHELLI G, *Met. Sci.*, **12**, 1978, pp.459-472.

66. MINTZ B, *Met. Technol.*, **7**(3), 1980, pp.127-129.

67. MORRISON W B, *Met. Technol.*, **2**(1), 1975, pp.33-41.

68. DeARBO A J, *Metall. Trans.*, **8A**, 1977, pp.473-485.

69. HAWKINS D N, *Met. Technol.*, **3**(9), 1976, pp.417-421.

70. SCHOFIELD R, ROWNTREE G, SARMA N V and WEINER R T, *Met. Technol.*, **1**(7), 1974, pp.325-331.

71. CHAO H C, *Metall. Trans.*, **9A**, 1978, pp.509-514.

72. DEFILIPPI J D and CHAO H C, *Metall. Trans.*, **2**, 1971, pp.3209-3216.

73. HERTZBERG R W, "Deformation and Fracture Mechanics of Engineering Materials", 2nd edn., 1983, USA, John Wiley and Sons, pp.357-360.

74. DABKOWSKI D S, KONKOL P J and BALDY M F, paper presented at Canadian Metallurgical Society Symposium on "Artic line pipe", Toronto, Ontario, Aug. 1974.

75. KALTENHAUSER R H, *Met. Eng*, 1971, **11**(2), pp.41-47.

76. BRINK A B and BALL A, in Proc. "Stainless Steels '84", Sept. 1984, Götenburg, The Inst. Met., London, 1985, pp.69-76.

77. BALL A, CHAUHAN Y and SCHAFFER G B, *Mat. Sci. and Technol.*, 1987, **3**, pp.189-196.

78. BRINK A B, M.Sc. Thesis, Univ. of Cape Town, South Africa, 1983.

79. MATTHEWS L M and DeMARSH E A, Mintek Report No M213, 1985, Council for Mineral Technology, Randburg, South Africa.

80. HOFFMAN J P, ASM International Conference on New Developments in Stainless Steels Technology, 1984, Detroit, Michigan, paper 8410-014.

81. TUBBY P J, Proc. Inaugural International 3CR12 Conf., 1984, Johannesburg, South Africa, pp.263-280.

82. THOMAS C, Proc. Conf. Duplex Stainless Steels, St.Louis, Mo, USA, 25-28 Oct. 1982, ASM, Metals Park, Ohio, 1984, pp.649-664.

83. HOFFMAN J P, Proc. Inaugural International 3CR12 Conf. 1984, Johannesburg, South Africa, pp.82-96.

84. ALLEN C, BALL A and PROTHEROE B E, *Wear 74*, 1981-82, pp.287-305.

85. ALLEN C, PROTHEROE B E and BALL A, *J. S. Afr. Inst. Min. Metall.*, 1981, **81**(10), pp.289-297.

86. PICKENS J R, *Metall. Trans.*, **17A**, 1986, p.1095.

87. RUSS J C, in "Fundamentals of Energy Dispersive X-ray Analysis", chap 12, pp. 151-163, 1984, London, Butterworths.

88. HUTCHINGS R, in Proc. Electron Microsc. Soc. South. Afr., 1985, vol. **15**, pp. 31-32.

89. KANAYA K and OKAYAMA S, *J. Phys. D*, 1972, **5**, pp. 43-58.

90. BLUM F, STANDER C M and COMINS N R, in Proc. Electron Microsc. Soc. South Afr., 1984, 14, pp.9-10.

91. McDONALD M M and LUDWIGSON D C, *J Test Eval.*, 1983, **11**, pp.165-173.

92. CASTRO R and TRICOT R, in "The Metallurgical Evolution of Stainless Steels", ed. F B Pickering, The Metals Society (London), 1979, pp.230-244.

93. TOWNSEND R D and KIRKALDY J S, *Trans. ASM*, 1968, **61**, pp.605-619.

94. YI J J, KIM I S and CHOI H S, *Metall. Trans.*, 1985, **16A**, pp.1237-1245.

95. VERHOEVEN J D, in "Fundamentals of Physical Metallurgy", pp.424-426, John Wiley and Sons, New York, 1975.

96. BARRETT C and MASSALSKI T B, in "Structure of Metals", 3rd edn., 1980, Pergamon Press, Oxford, England, p.493.

97. SIMONEN E P and TRIVEDI R, *Acta Met.*, 1977, **25**, pp.945-950.

98. SCHAFFER G B, "A Constitutional Study of a Dual Phase Steel Containing 12% Chromium", M.Sc Thesis, University of Cape Town, South Africa, 1983.

99. LITTLE E A, HARRIES D R, PICKERING F B and KEOWN S R, *Met. Technol.*, 1977, **4**, pp. 205-217.

100. BLUM F, WEISS B-Z and COMINS N R, Project No. 420/94052, National Inst. for Mat. Res.-CSIR, Pretoria, RSA, May 1987.

101. HEWITT J, Middelburg Steel & Alloys, Middelburg, Transvaal, RSA, - private communication

102. LIU W J and JONAS J J, *Metall. Trans.*, 1988, **19A** pp.1415-1424.

103. ERHART H, GRABKE H J and ÖNEL K, in Proc. Conf. "Advances in the Physical Metallurgy and Applications of Steels", Univ. Liverpool, 21-24 Sept. 1981, pp.282-285, The Metals Society, London, 1982.

104. BROOKSBANK D and ANDREWS K W, *J. Iron. Steel Inst.*, April 1972, pp.246-255.

105. MATTHEWS L M and SCHWARZER R A, in Proc. "EUREM 88", York, England, 1988, Inst. Phys. Conf., vol. **2**, chap.13.

106. MATTHEWS L M, NANA S and CORTIE M B, in Proc. "Fracture '89", June 29-30 ,1989, World Trade Centre, Johannesburg, Univ. Witwatersrand / S.A.I.M.E.

107. GROBLER C and VAN ROOYEN G T, *Can. Metall. Quart.*, 1988. **27**, (1), pp. 49-58.

108. LENEL U R and HONEYCOMBE R W K, in Proc. "Advances in the Physical Metallurgy and Applications of Steels", Sept.21-24, 1981, Liverpool, pp.38-46, The Metals Society, London, 1982.

109. SU M, SUN S M and YANG D Z, *Scripta Met.*, 1987, **21**, pp. 801-804.

-ooOOoo-

APPENDIX A

DERIVATION OF A SUITABLE COMPOSITION FOR A DUPLEX FERRITE-MARTENSITE STEEL CONTAINING 16-17 wt % CHROMIUM

A1 INTRODUCTION

Analysis of the evolution of the 3CR12 microstructure has clearly indicated that the most important consideration in refining the microstructure is the extent of the decomposition of the high temperature δ-ferrite phase. Grain refinement in 3CR12 has been successfully achieved by balancing the ferrite forming and austenite forming elements in order to give a ferrite factor in the range 8-12. At the same time a low interstitial content is desired which implies a carbon level less than 0.03 wt%. Similar factors should therefore be taken into account in order to refine the microstructure of ferritic steels containing 16-17 wt.% chromium.

Using a steel base chemistry containing 16-17 wt % chromium and carbon levels less than 0.03 wt %, sufficient nickel is required to be added in order to provide the necessary $\delta \rightarrow \gamma$ decomposition reaction to refine the δ-ferrite grain structure. A pseudobinary Fe-Ni phase diagram for 17 wt% chromium has been drawn in fig A1 to illustrate the effect of nickel on the nature of phase transformations. This diagram indicates that if one assumes equilibrium cooling conditions, then complete decomposition of δ-ferrite to austenite can only be achieved for nickel equivalents greater than 4. Nickel additions above this equivalent value will increase the tendency to achieve a fully austenitic structure at intermediate temperatures. However, in deciding on the upper limit of nickel addition, the essential cost factor needs to be taken into account. The idea of modifying ferritic stainless steels is to achieve improved engineering alloys whilst still maintaining low cost. Careful consideration is therefore required in determining a suitably balanced chemical composition.

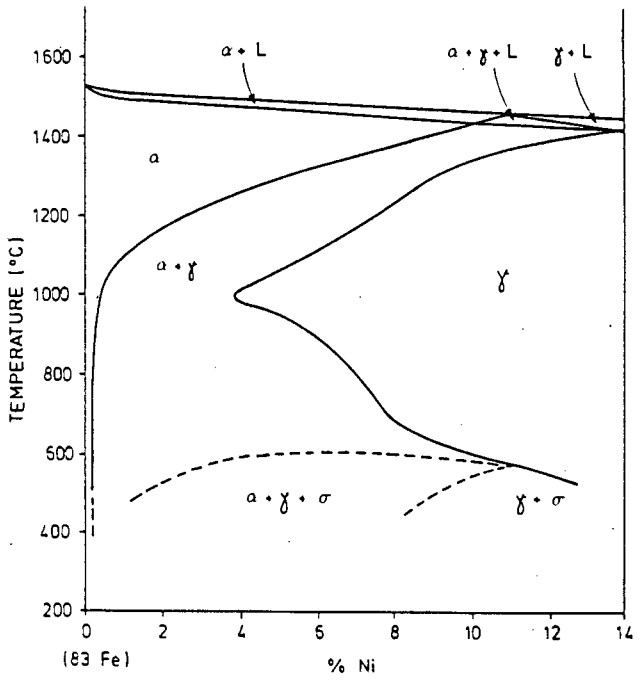

FIGURE A1 : Pseudobinary Fe-Ni phase diagram for an isopleth at 17wt% Cr. Drawn from isothermal sections for solid phase equilibria presented in Chapter 2 (Ref 17).

A2 EXPERIMENTAL ALLOYS

The microstructural behaviour of three experimental alloys was initially assessed. Two of the alloys (E1 and E2) were titanium stabilised and gave rise to ferrite factors in the range 8-12, whereas the third alloy (E3) had a ferrite factor equal to 2.3. The compositions of the three alloys, along with their computed ferrite factors and chromium and nickel equivalents are listed in Table A1.

TABLE A1 : Composition of alloys E1-E3

ALLOY	C	N	S	P	Mn	Si	Ti	Cr	Ni	FF	Cr′	Ni′
E1	.013	.030	.010	.017	1.42	.49	.29	18.19	2.00	11.1	19.7	3.9
E2	.025	.029	.010	.018	1.48	.28	.34	16.70	1.97	8.3	17.9	4.2
E3	.021	.028	.007	.019	0.90	.34	.00	16.87	3.22	2.3	17.6	5.0

[F.F = ferrite factor ; Cr′ = Cr equivalent ; Ni′ = Ni equivalent]

Alloys E1-E3 were laboratory cast into 5kg ingots (thickness = 50 mm) and were hot rolled to plate thicknesses in the range 6-8 mm. Final reduction was terminated at 850°C. The as-rolled microstructure, normalised (1000°C for 2 hours) microstructure, and dilatometer trace

for each of these alloys are shown in figs A2 to A4. Phase transformation temperatures are indicated by the points of inflection in the dilatometer traces which were produced at heating and cooling rates equal to 4°C/min. The macrohardness of the as-rolled and normalised conditions are indicated in Table A2.

TABLE A2 : Macrohardness (HV_{30}) of alloys E1-E3 in as rolled and normalised conditions.

ALLOY	AS ROLLED	NORMALISED
E1	250	180
E2	290	255
E3	340	335

Alloy E1 exhibited a coarse banded ferritic microstructure (fig A2(a)) in the hot rolled condition and after normalising the occurrence of very minor martensite was detected at the boundaries of the large grained (200-300 μm) ferritic matrix (fig A2(b)). The dilatometer trace in fig A2(c) does not indicate the occurrence of any substantial transformations during the heating and cooling cycles, although minor austenite formation is indicated between 500°C and 600°C during heating. It is apparent that any austenite that might have formed as a result of partial δ-ferrite decomposition during cooling has regressed to α-ferrite in the region of 600°C. There is no evidence of a martensite-start (M_s) temperature.

Alloy E2, in the as-rolled condition, indicated the occurrence of elongated fibres of martensite in a predominantly ferritic matrix (fig A3(a)). The duplex ferrite-martensite microstructure was maintained after normalising, with little change in the distribution of the martensite fibres (fig A3(b)). The dilatometer trace (fig A3(c)) indicated a reasonably well defined point of inflection just below 600°C during the heating cycle and a well defined M_S temperature at 300°C during cooling.

Alloy E3, on the other hand, exhibited an elongated ferritic structure in a martensitic matrix after hot rolling (fig A4(a)). The phase ratios did not appear to have changed after normalising, although the ferrite seemed to have recrystallised to some extent (fig A4(b)). The dilatometer trace for this alloy showed a much more exaggerated inflection just below 600°C during the heating cycle (fig A4(c)). During cooling a considerable degree of δ-ferrite decomposition is indicated and a corresponding degree of martensite formation is detected at approximately 220°C.

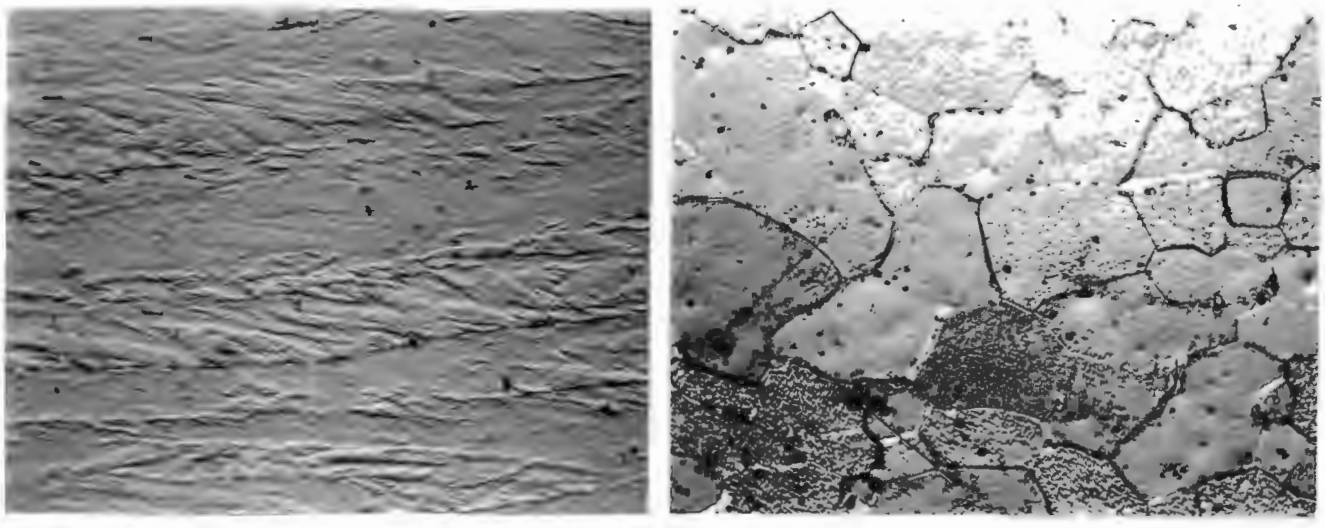

(a) (b)

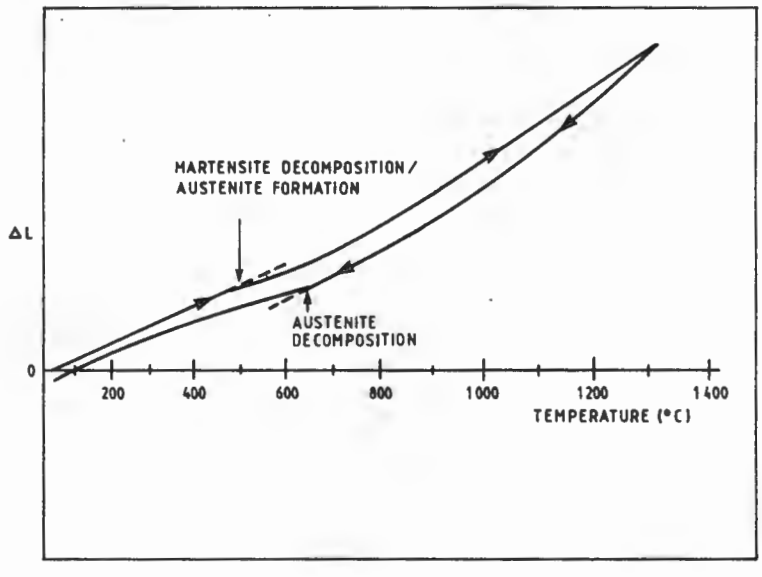

(c)

FIGURE A2 : Microstructure and transformation behaviour of alloy E1

(a) Hot rolled condition

(b) Normalised condition (1000 °C 2hours - air cool)

(c) Dilatometer trace

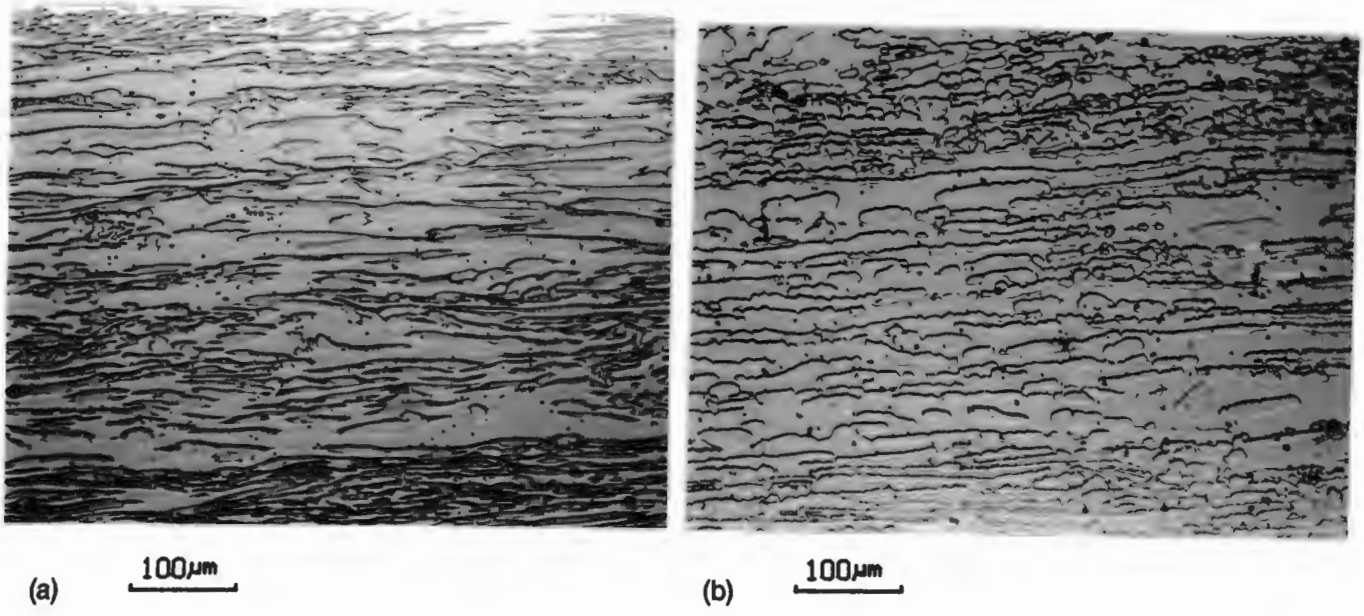

(a) (b)

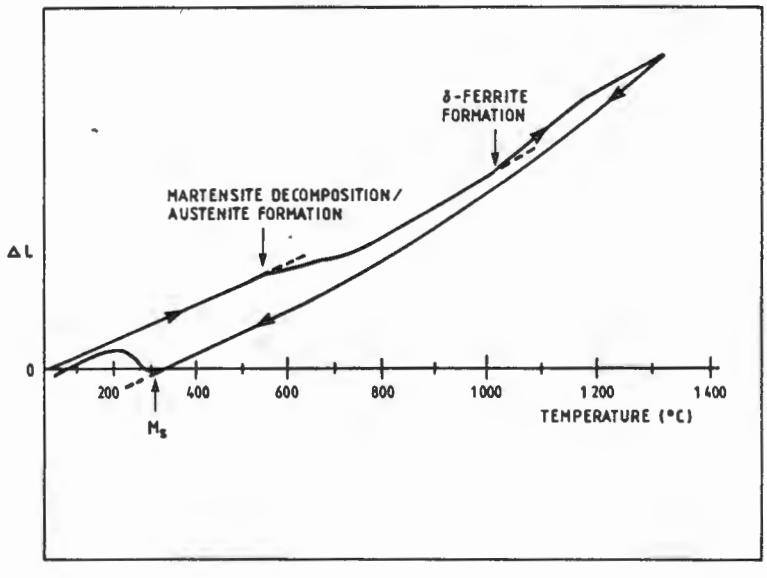

(c)

FIGURE A3 : Microstructure and transformation behaviour of alloy E2

(a) Hot rolled condition

(b) Normalised condition (1000 °C 2hours - air cool)

(c) Dilatometer trace

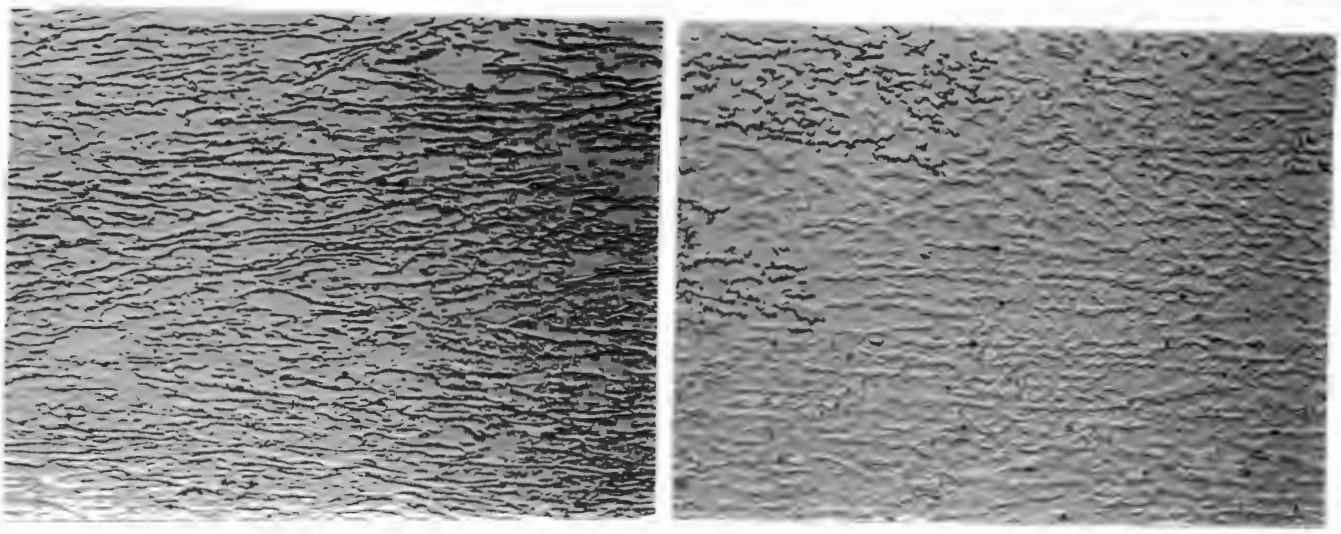

(a) (b)

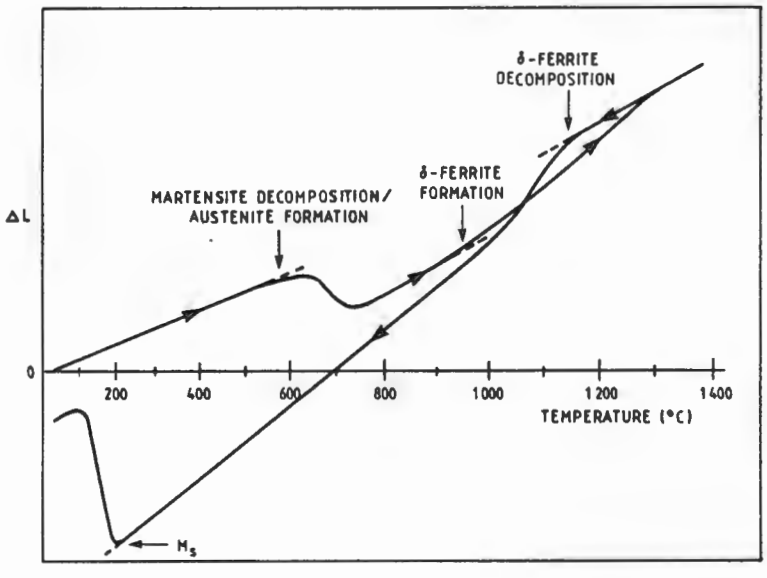

(c)

FIGURE A4 : Microstructure and transformation behaviour of alloy E3

(a) Hot rolled condition

(b) Normalised condition (1000°C 2hours - air cool)

(c) Dilatometer trace

A3 COMMENT

The microstructures of alloys E1-E3 in both the hot rolled and normalised conditions emphasize the fact that appreciable grain refinement is only achieved when extensive δ-ferrite decomposition occurs. In other words, the higher the austenite (martensite) content of the steel, the greater is the tendency for grain refinement. A comparative study of the microstructures of the three alloys indicates a much more refined microstructure in the case of alloy E3. The as-rolled structure of alloy E2 is indicative of fairly minor solid state $\delta \rightarrow \gamma$ transformation and it is apparent from the normalised structure that the austenite mainly occurred as a result of the precipitation of grain boundary allotriomorphs. In the case of alloy E3, however, a much more advanced $\delta \rightarrow \gamma$ transformation has occurred and the rolled structure is indicative of an interlath residual δ-ferrite/austenite structure that has been deformed. Consequently the original δ-ferrite grains became much more broken up and the overall grain size was considerably reduced.

The deleterious effect of the large grain size associated with alloy E2 is illustrated by comparing the Charpy V-notch impact toughness of alloys E2 and E3. Sub-size Charpy specimens (5mm) were normalised at 1000°C and tested at room temperature. The impact energies for alloys E2 and E3 were 15J and 47J respectively.

A4 COMPOSITIONAL LIMITS

The microstructural behaviour of the experimental alloys can obviously be directly related to the alloy compositions. The marked difference in the transformation behaviour of alloy E3 can be attributed to both the absence of titanium and the higher nickel content. The removal of titanium reduces the chromium equivalent and increases the effective carbon content, whilst increasing the nickel content also increases the austenitising ability of the steel. It would seem that sizable nickel additions to the titanium stablised alloys, E1 and E2, are required in order to provide advanced δ-ferrite decomposition. In view of the substantial chromium content and the low carbon levels (0.03 wt%), it is probably not necessary to stabilise these alloys. Certainly the absence of titanium would lead to a lower nickel requirement which would undoubtedly reduce cost.

Plotting the nickel and chromium equivalents for the three alloys on the 1400°C and 1000°C isothermal sections for solid phase equilibria in the Fe-Cr-Ni ternary system gives some idea of the difference in the transformation behaviour of these three alloys (fig A5). At 1400°C all three alloys are fully ferritic (δ-ferrite) whereas the 1000°C section shows varying degrees of δ-ferrite decomposition for each alloy. It is quite self evident that alloy E3 should show

the highest austenite (martensite) content, although it is clear from the normalised structure that the decomposition of δ-ferrite is far from complete. On account of the fact that the grain refinement of the δ-ferrite is initially the most important criterion in modifying ferritic steels, composition limits for experimental alloys can be defined according to the composition of alloy E3. As mentioned previously, the maintenance of low interstitial content is essential and the chromium level should fall in the range 16-17 wt%. On this basis compositional limits can be specified so as to render similar chromium and nickel equivalents to that of alloy E3 which will lead to the desired grain refinement being achieved. The proposed composition range which falls in a similar area to alloy E3 on the Fe-Cr-Ni phase diagram is listed in Table A3. Section 4.5 in chapter 4 analyses the constitution and properties of alloys conforming to the proposed compositional range.

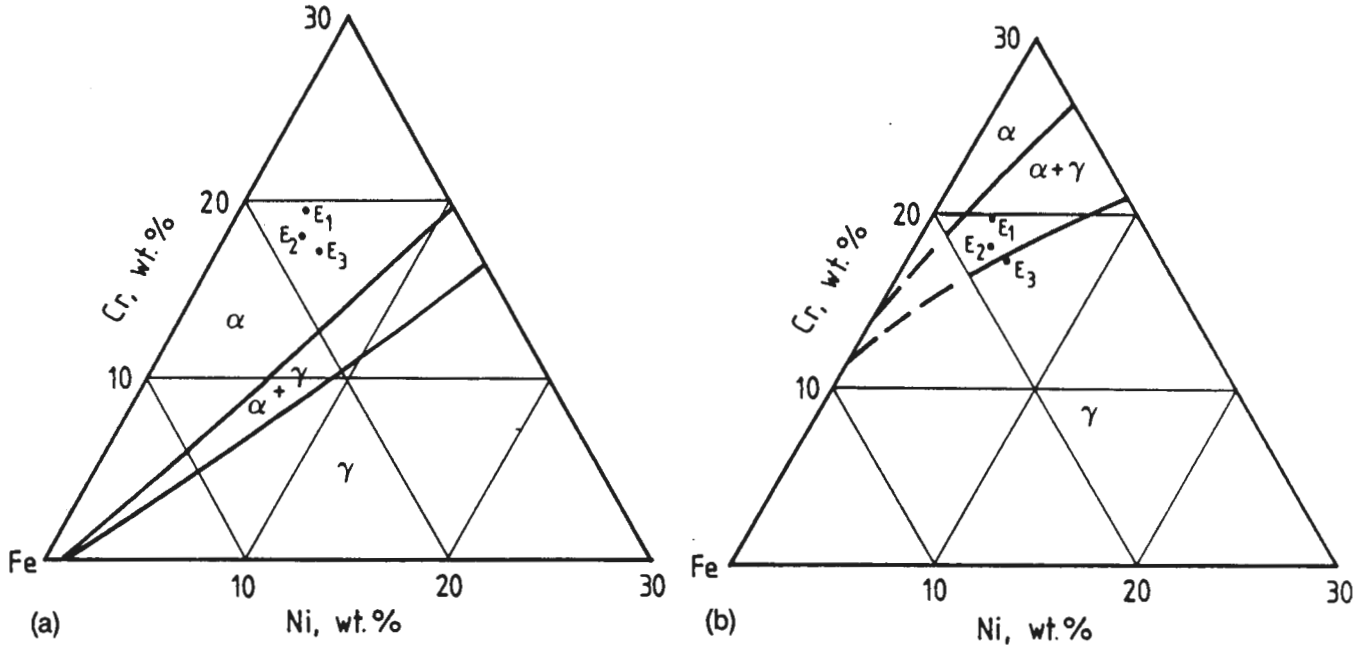

FIGURE A5 : The composition of alloys E1-E3 (Ni and Cr equivalents) in relation to phase equilibria in the Fe-Cr-Ni system.

(a) 1400°C isothermal section

(b) 1000°C isothermal section

TABLE A3 : Proposed composition for a duplex ferrite-martensite steel containing approximately 16% Cr. All figures represent wt %.

C	N	S	P	Mn	Si	Cr	Ni
.03 max	.03 max	.008 max	.008 max	1.00 max	.4-.5	16.0-16.5	2.5-2.8

APPENDIX B

DETERMINATION OF THE EFFECT OF NON-METALLIC INCLUSIONS ON THE CORROSION BEHAVIOUR OF 3CR12

B1 SYNOPSIS

The effect of non-metallic inclusions on the corrosion behaviour of 3CR12 was investigated. Potentiodynamic and potentiostatic tests were carried out on run-of-the-mill commercial 3CR12 heats in order to examine the occurrence of micropitting associated with inclusions. Variations in inclusion populations were found to give rise to notable differences in corrosion behaviour. In particular, the dissolution of manganese sulphide inclusions led to the formation of micropits, with the concomittant reduction in passive breakdown potentials, and increased the propensity for crevice formation. Negligible effect on corrosion performance was observed for titanium sulphide and titanium carbonitride inclusions.

B2 INTRODUCTION

The analysis of the non-metallic inclusion occurrence in 3CR12 steels has led to the identification of a wide range of inclusion types in these steels (Chapter 4, section 4.3). In addition, subtle variations in the overall chemistry of the steels are noted to affect the compositions of certain inclusions. The extent of the occurrence of manganese sulphide (MnS), in particular, is dependent on the sulphur and titanium levels in the steel. In view of the fact that sulphide inclusions can affect the corrosion properties of alloys, it is feasible to suspect that 3CR12 alloys may possess a range in corrosion behaviour which is somehow related to the size, shape, and composition of inclusions pertaining to each specific heat. To this end, a series of corrosion tests were performed in order to examine the effects of the dissolution of certain inclusions on the overall corrosion behaviour of the alloys.

B3 HISTORICAL REVIEW

The formation of a passive layer on a suitably alloyed chromium containing steel provides a corrosion resistance far superior to that of conventional carbon steels. Nevertheless, the successful commercial and industrial exploitation of these steels depends on the maintenance of the passive film in order to resist the many corrosive environments[1]. The breakdown of passivity, notably in the presence of chlorides and other aggressive anions, leads to various forms of localised corrosion such as pitting, crevice corrosion and intergranular attack. In considering the nucleation of pitting on a passive metal surface, it has been suggested that the following conditions must be fulfilled[1]: (a) aggressive ions such as Cl^- must be present in concentrations higher than a critical value, (b) the electro-chemical potential must be higher than the potential for pit nucleation, and (c) the induction period must be exceeded. This approach, however, does not take into account that in reality commercial metals and alloys are not "ideal" homogeneous systems. Metals contain inhomogeneities such as non-metallic inclusions and second phases which may occur either randomly dispersed throughout the matrix, or as impurity segregation at the grain boundaries. This results in the formation of a defective passive film over these regions and its structure and composition is different from that over the metal matrix. Therefore, inherent flaws in the passivating film will lead to an earlier localised breakdown of the film than that which would have been expected had the passivating film been homogeneous.

B3.1 ROLE OF NON-METALLIC INCLUSIONS IN PIT INITIATION

It is generally believed that non-metallic inclusions play a large role in the initiation of pits[2], but the extent to which pitting occurs is influenced by their composition and geometric shape. Obviously the composition of the inclusion will affect the dissolution rate of the inclusion itself. It has been found in the case of stainless steels that sulphide inclusions are the most active as regards pit initiation[2]. However, the chemical behaviour of sulphides varies according to the metal element present[3]. From Table B1, which shows the solubilities of some sulphides of importance in steel, it is clear that of the commonly occurring sulphides, sulphides containing iron and manganese are potentially the most active as regards pit initiation. On the other hand, not all soluble sulphides necessarily cause pits since in the initiation stage of pitting, the geometry of the micro-cavities left by the inclusion dissolution has a determining role.

Observations on stainless steels subjected to atmospheric exposure have shown that although many non-metallic inclusions can be lost during exposure to an industrial environment, the holes thus created do not necessarily propagate as pits[4]. Therefore, in

order for pit propagation to occur as a result of inclusion dissolution, the following requirements must be met : (a) dissolution of the active inclusions and initiation of micro-cavities, (b) agglomeration of chloride ions in those micro-cavities which are geometrically favourable (incubation stage), and (c) initiation and growth of pits.

TABLE B1 : Solubility products of some metal sulphides (after Ref 3.)

ELEMENT	SULPHIDE	SOLUBILITY PRODUCT, pKs
Cu	Cu_2S	48
Fe	FeS	17
Cr	Cr_7S_8	Sparingly soluble in acids
Mn	MnS	13
Ti	TiS	Insoluble in acids

B3.2 CHEMICAL BEHAVIOUR OF SULPHIDES

A potential-pH diagram calculated for the MnS-H_2O-Cl^- system has been useful in defining the dissolution behaviour of MnS[3]. The potential-pH relationship has indicated that even in the pH range 4.8-13.8, the highest potential at which MnS can exist is about $140mV_{SCE}$. At more noble potentials, it is found that MnS dissolves to sulphur. The corrosion potential of passive stainless steels in aqueous chloride solutions is often between 250 and $450mV_{SCE}$, and since MnS is an electronic conductor, it will be polarised to the corrosion potential of the passive stainless steel and therefore tend to dissolve. In this respect MnS inclusions are considered to be active anodic sites at a stainless steel surface in the presence of aqueous chloride solutions.

On dissolution of MnS in acid solutions, such as may be encountered in active pits or crevices, H_2S is formed. The presence of H_2S makes the formation of passive films more difficult, and in reducing acids, increasing the H_2S content can eliminate active-passive behaviour. This is shown in fig B1 where it is seen that the active-passive transition is no longer in evidence when the H_2S concentration reaches $10^{-2}\underline{M}$[3]. H_2S also appears to facilitate the breakdown of passive films on stainless steels and the depassivation pH is known to be raised to less acid values as H_2S is introduced into solution.

The addition of titanium, resulting in the formation of TiS in competition to MnS, has been shown to improve the corrosion performance of an 18Cr-2Mo ferritic stainless steel[4]. The much less soluble TiS decreases the tendency for pit initiation at sulphide

sites and has been shown to increase the pitting resistance of the steel. Nevertheless, the benefit derived by the addition of titanium in this case may not be universal. It has been noted that traditionally titanium additions to stainless steel have been regarded as detrimental to pitting resistance and there is as yet no unambiguous evidence to support the view that replacing MnS by TiS is beneficial to pitting resistance[3].

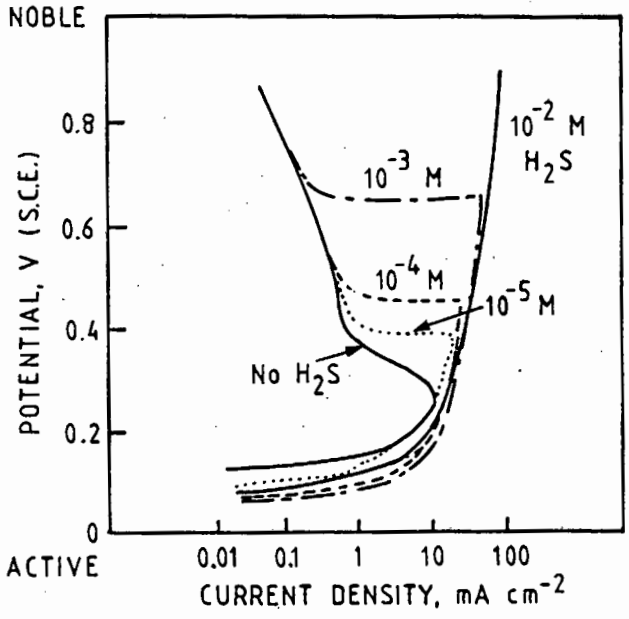

FIGURE B1 : Effect of H_2S on the anodic polarisation behaviour of austenitic stainless steel in 1.1M H_2SO_4 + 1.75M HF solution, (after Ref 3).

B3.3 INCLUSION DISSOLUTION MECHANISMS

As mentioned previously, MnS inclusions are anodic with respect to the passive steel surface in stainless steels. One of the more comprehensive pitting mechanisms suggesting how an MnS inclusion can initiate a propagating pit in a stainless steel in a chloride solution[3] is shown in fig B2. A near surface sulphide inclusion is considered which is covered by a film defective in comparison with the film covering the adjacent stainless steel matrix (fig B2(a)).

The first stage of attack is the formation of a salt (chloride) layer over the defective area. This is accomplished by the transport of metallic ions through the defective film and their reaction with the chloride (fig B2 (b & c)). The second stage involves the hydrolysis of the chloride, leading to acidification (fig B2(d)). The acid formed dissolves the defective film, and begins to attack the manganese sulphide inclusion and the stainless steel surrounding the inclusion (fig B2(e)). The pit will propagate when the acidity has reached a level at

which repassivation of the stainless steel surface cannot occur. As mentioned previously, the presence of any hydrogen sulphide formed by the dissolution of the MnS inclusion, will also hinder the repassivation process. Salt layers are reported to form at the bottom of pits in stainless steel (fig B2(f)), and are believed to control the kinetics of corrosion via the dissolution of the salt film.

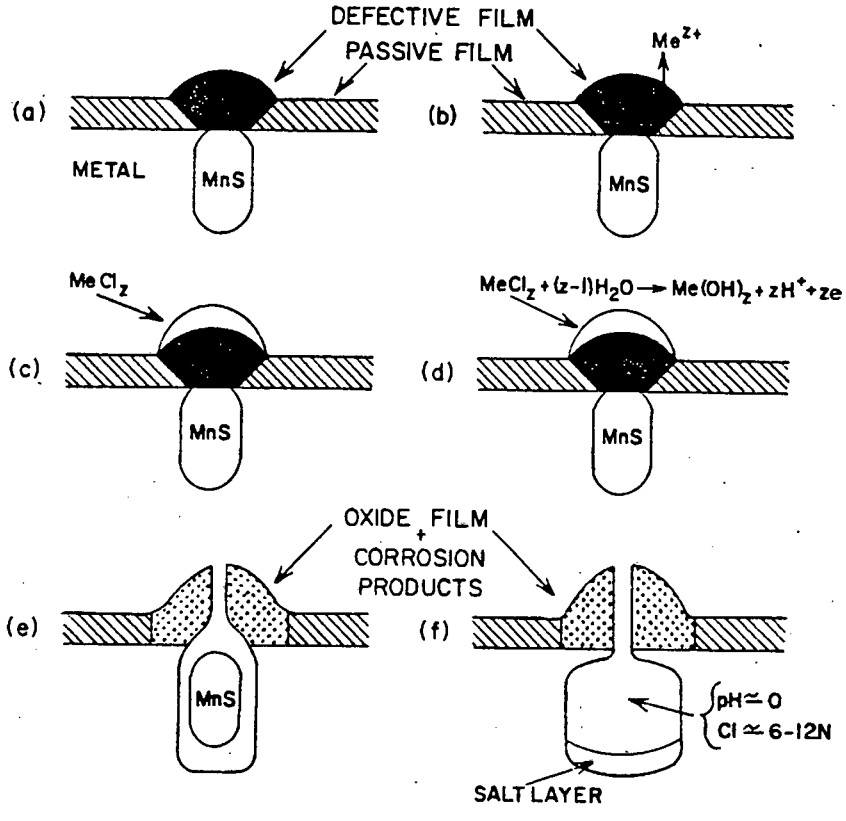

FIGURE B2 : Mechanism of dissolution for a near surface sulphide inclusion in a chloride environment. See text for explanation. (after Ref 3).

In the case of an inclusion intersected by the surface, pits are suggested to initiate by crevice corrosion at the sulphide/metal interface[5]. Chloride ions are reported to be preferentially adsorbed on the surface at the inclusion/matrix interface[6] and dissolution of the sulphide leads to attack on the exposed metal matrix. Once again the chemical dissolution of the sulphide, thereby giving rise to the formation of H_2S, coupled with the localised concentration of chloride ions, can prevent repassivation of the metal matrix.

B4 EXPERIMENTAL APPROACH

Alloys B1-B8 (Chapter 3, Table 3.2) were tested in order to compare the corrosion behaviour for a typical range of commercial 3CR12 steel compositions. Following the outcome of these investigations, more specific corrosion testing was carried out on alloys A2 and A5 (Chapter 3, Table 3.1). The latter two alloys were selected on account of their very marked differences in manganese sulphide and titanium sulphide inclusion distributions. The manganese, titanium, carbon, nitrogen and sulphur levels as well as the Ti/S ratios for these alloys are listed below in Table B2.

Corrosion tests were performed using potentiodynamic and potentiostatic techniques. The basic apparatus and test procedures are described in the next section.

TABLE B2 : Composition of alloys B1-B8, A2 and A5. Figures represent wt %.

ALLOY	Mn	Ti	C	N	S	Ti/S
B1	1.24	.52	.017	.012	.014	37.1
B2	1.09	.46	.019	.017	.011	41.8
B3	1.28	.46	.030	.014	.008	57.5
B4	1.20	.23	.026	.027	.006	38.3
B5	1.27	.48	.024	.009	.006	80.0
B6	1.13	.21	.024	.019	.023	9.1
B7	1.18	.35	.024	.011	.024	14.6
B8	1.07	.40	.024	.031	.023	17.4
A2	1.17	.26	.023	.016	.018	14.4
A5	1.19	.31	.022	.014	.008	38.8

B4.1 TEST APPARATUS

A PRINCETON potentiostat equipped with an automatic baseline advance and a logarithmic current converter was used to perform both potentiodynamic and potentiostatic testing. Specimens were supported in a polyethylene holder which exposed a test surface of exactly 1 cm^2 by sealing off the rest of the specimen area with a teflon (PTFE) gasket. The test surface always corresponded to the rolling surface. Corrosion potential values were measured with reference to a saturated calomel electrode (SCE).

B4.2 SPECIMEN PREPARATION AND TEST PROCEDURES

Specimens were tested in the hot rolled and annealed (HRA) condition and were mechanically polished using a 0.25μm diamond paste, followed by thorough cleaning in ethanol prior to testing. Test solutions were produced using distilled water and AR grade chemicals. Sodium chloride (NaCl) was used to achieve the necessary chloride ion concentrations. The electrolyte was oxygen saturated and was maintained at a temperature of 30°C.

Potentiodynamic tests were carried out by initially polarising the specimens to a potential of 200 mV more negative than the rest potential for a period of 15 minutes. Thereafter the specimens were anodically polarised either at a fast scan rate (14mV/sec), or at a very slow scan rate of 0.14mV/sec, depending on the type of test being performed. Fast scan rates were employed in order to simulate non-equilibrium conditions where the formation of a passive film would be difficult; the idea being that under these conditions the dissolution of inclusions would have a greater effect on the attainment of passivity. The slow scan rate corresponding to 0.14mV/sec was applied in order to clearly differentiate corrosion behaviour under equilibrium conditions. The polarisation scan was terminated once the breakdown of passivity had been achieved. A corrosion behaviour diagram was obtained by plotting potential as a function of the current density measured on the specimen surface.

Potentiostatic testing was performed in order to compare the corrosion behaviour of alloys A2 and A5 as a function of time at constant potential. Specimens were prepared in the same way as that for the potentiodynamic tests, but were directly polarised to set holding potentials (eg, 200, 250, or 300mV_{SCE}) after the initial holding period at 200mV less than the rest potential. Current density variations were monitored as a function of time for periods of up to 20 hours at constant potential. Each test was carried out using a freshly polished specimen.

B5 RESULTS

B5.1 POTENTIODYNAMIC TESTING OF ALLOYS B1 - B8

Results of the anodic polarisation tests performed on alloys B1-B8 in neutral solutions containing 10ppm Cl^- and at a scan rate of 14mV/sec, are illustrated in the corrosion behaviour diagram in fig B3. All the curves appear to follow the same trend up to approximately $+0.5V_{SCE}$, but as the potential is increased above this value, there is evidence for the occurrence of variations in corrosion behaviour. The curves for alloys B1, B3, B4 and B5 show a definite change in slope at approximately $+0.5V_{SCE}$, and the current density between $+0.5V_{SCE}$ and $+1.0V_{SCE}$ remains fairly constant. The curves for alloys B6 and B8, however, show virtually no change in slope at $+0.5V_{SCE}$, and the current density continues to increase with increasing potential. Alloys B2 and B7 show a somewhat intermediate behaviour and although there is a definite change in the slope of the curves above $+0.5V_{SCE}$, the current density is generally higher than that for alloys B1, B3, B4, and B5.

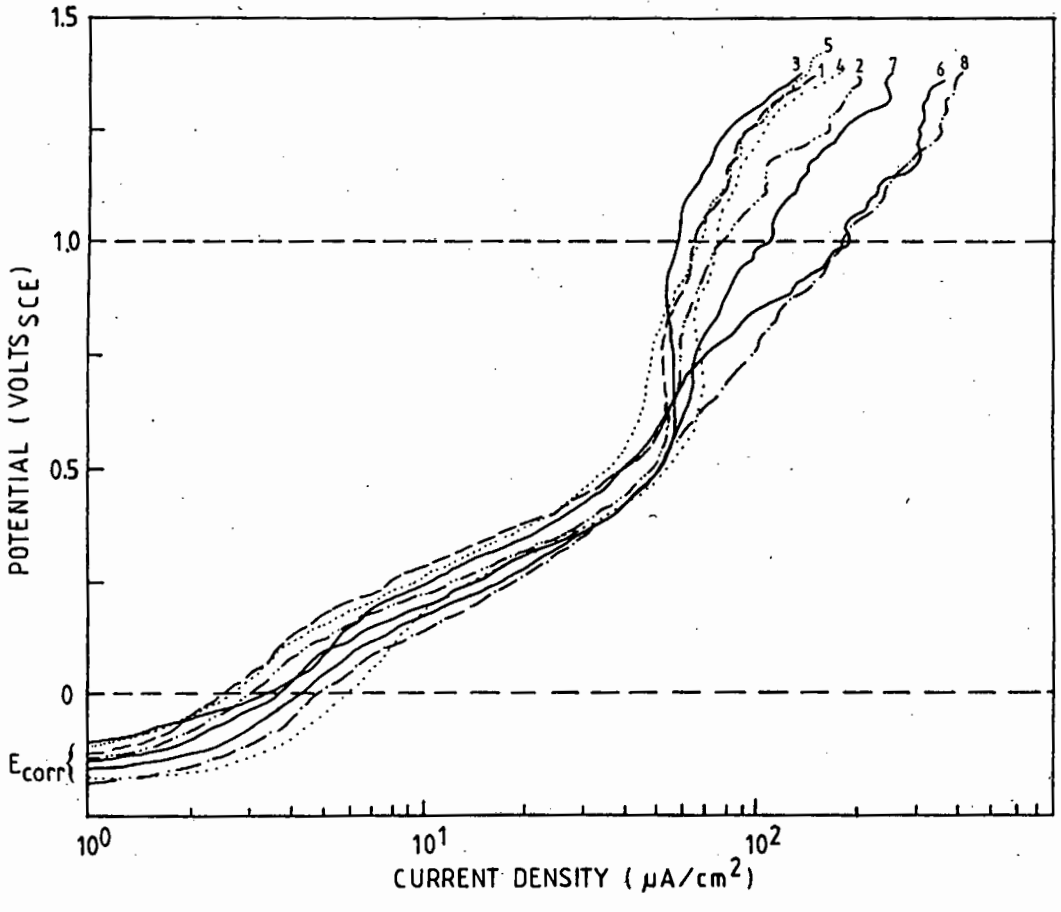

FIGURE B3 : Anodic polarisation curves for alloys B1-B8 tested in 10 ppm Cl^- solutions. Scan rate = 14mV/sec.

A semi-quantitative assessment of the corrosion behaviour of the eight alloys was attempted by examining the current density for each specimen at $+1V_{SCE}$, as indicated in fig B3. Plotting current density at this potential as a function of the Ti/S ratio (Table B2) for the various alloys yielded a general trend which is illustrated in fig B4. Current density is seen to decrease with increasing Ti/S ratio for the eight alloys.

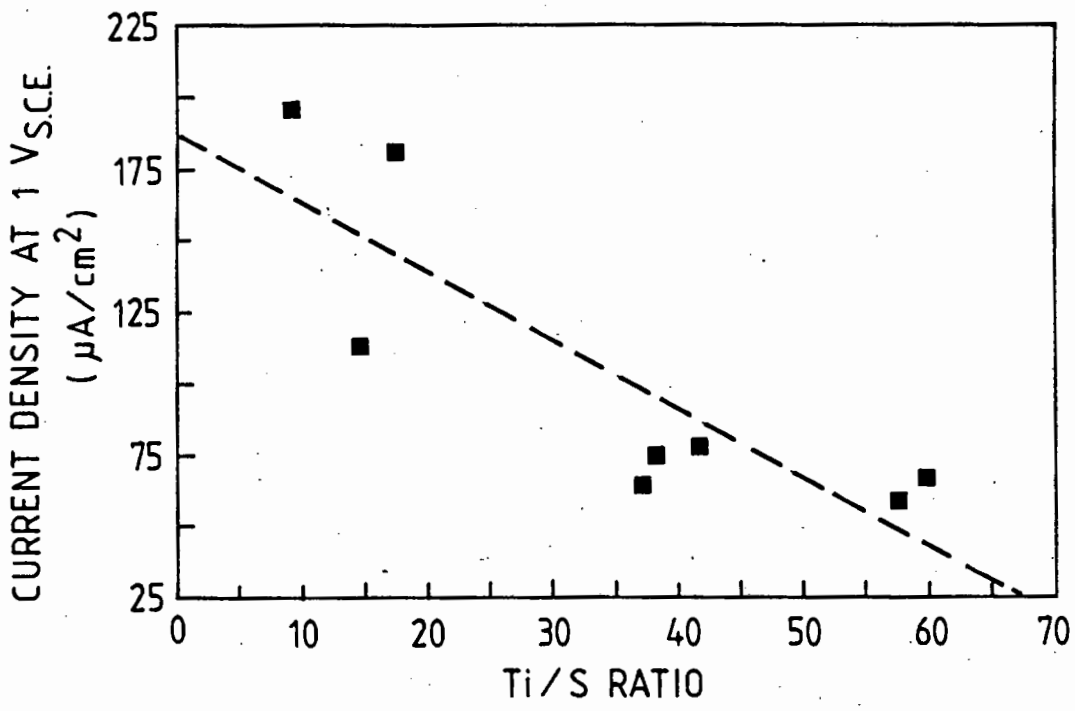

FIGURE B4 : Current density as a function of Ti/S ratio for alloys B1-B8.

Apart from the occurrence of very minor crevice corrosion at the specimen/gasket interface of all the alloys, a distinct relationship between the appearance of the specimen test surfaces and the shape of the anodic polarisation curves could be identified. Alloys B6 and B8 showed a marked occurrence of localised attack compared to alloys B1, B3, B4, and B5. Fig B5 illustrates the difference in appearance of the specimen test surfaces for alloys B3 and B6. The test surface of alloy B3 generally inidicated very minor attack (fig B5(a)), whereas fig B5(b) demonstrates pitting parallel to the rolling direction on the test surface of alloy B6. A higher magnification of the area in fig B5(b) is shown in fig B5(c) and indicates the remnants of inclusions within some pits.

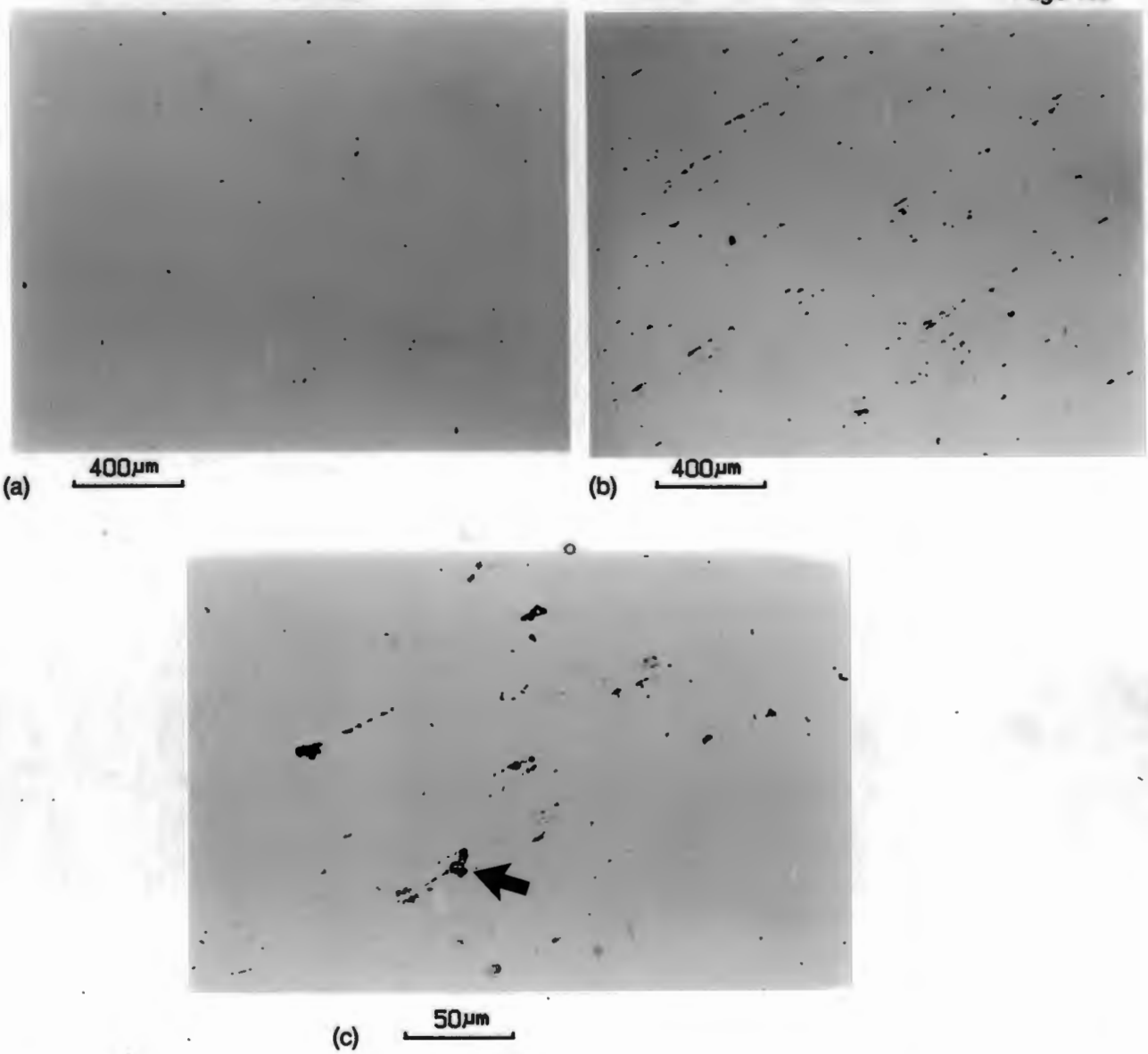

FIGURE B5 : Comparison of the test surfaces of alloys B3 and B6 after anodic polarisation in 10ppm Cl^- solutions.

(a) Very minor attack observed on the test surface of alloy B3.

(b) Alloy B6 showed localised attack orientated parallel to the rolling direction.

(c) Inclusion fragments still visible within some pits on the test surface of alloy B6.

B5.2 CORROSION BEHAVIOUR OF ALLOYS A2 AND A5

B5.2.1 Potentiodynamic Tests

The anodic polarisation curves for alloys A5 and A2, tested in solutions containing 200ppm Cl^- and at scan rates equivalent to 0.14mV/sec, are shown in figs B6(a) and (b) respectively. A comparison of the two curves shows a fairly significant difference in the

corrosion behaviour of the two alloys when anodically polarised under these conditions. On increasing the potential of alloy A5 above the corrosion potential (-190mV$_{SCE}$), the material remained passive until +490mV$_{SCE}$ whereafter a breakdown in passivity occurred, as indicated by the sudden increase in current density. The passive region was fairly stable except for a few sudden increases in current density (current spikes) at potentials above +250mV$_{SCE}$. Alloy A2, on the other hand, had a much less defined passive region. Numerous current spikes occurred between -100mV$_{SCE}$ and the breakdown potential (E_b) at +360mV$_{SCE}$. The average passive current density for alloy A2 was greater than the corresponding current for alloy A5.

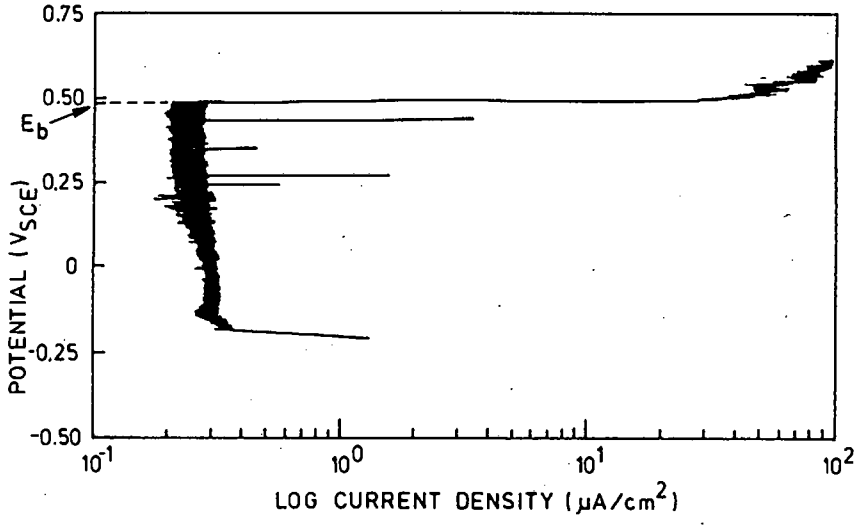

FIGURE B6(a): Anodic polarisation curve for alloy A5 in a 200ppm Cl$^-$ solution (Scan rate = 0.14mV/sec).

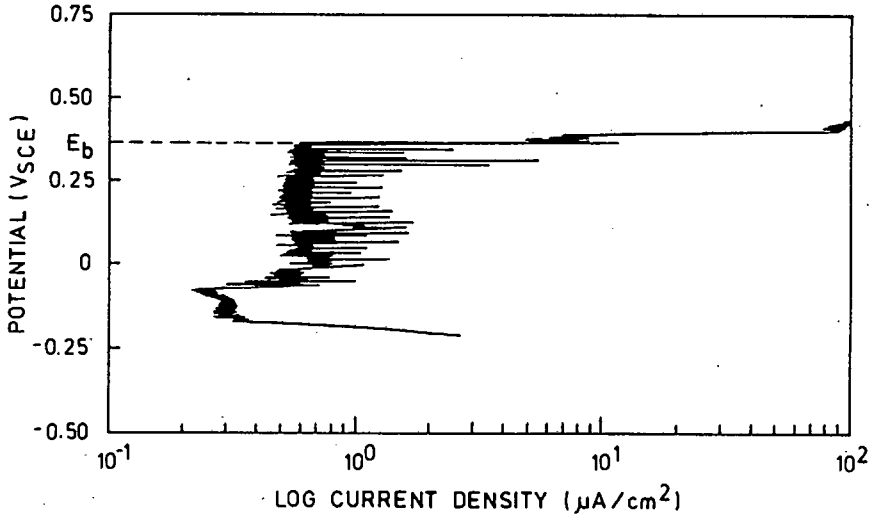

FIGURE B6(b): Anodic polarisation curve for alloy A2 in a 200 ppm Cl$^-$ solution (Scan rate = 0.14mV/sec)

Inspection of the surfaces after testing has showed similar effects to the comparison of alloys B3 and B6 illustrated in figs B5(a), (b) and (c). Alloy A5 showed little or no localised attack, whereas alloy A2 exhibited marked localised attack parallel to the rolling direction.

B5.2.2 Potentiostatic Tests

Current density was monitored as a function of time for alloys A2 and A5 in neutral solutions containing 200ppm Cl^-. The holding potentials were +200, +250 and +300 mV_{SCE}.

Potential = +200 mV_{SCE}

Both alloys A2 and A5 were seen to steadily passivate when polarised to +200mV_{SCE} (fig B7). Initially the current density increased to approximately 10$\mu A/cm^2$, but decreased fairly rapidly to less than 1$\mu A/cm^2$. Although the average current density remained low after the initial period, sudden current increases occurred for short durations, as indicated by the current spikes. In the case of alloy A2, the current spikes occurred at considerably shorter intervals than in the case of alloy A5. For alloy A5, the current spikes no longer occurred after a period of 9 hours and the passive current density remained constant. For alloy A2, however, current spikes still occurred after 18 hours, although the intervals were increased to about 25 minutes. Inspection of the surfaces after testing demonstrated a similar effect to that produced during potentiodynamic testing. The surface of alloy A5 was relatively unattacked, whereas alloy A2 showed the effects of considerable inclusion dissolution.

Potential = +250 mV_{SCE}

When polarised to +250mV_{SCE} , alloy A5 passivated to the same extent as that shown for the test conducted at +200mV_{SCE}. Initially, alloy A2 also followed a similar trend with the occurrence of the same degree of current density fluctuation as that exhibited in the +200mV_{SCE} test. However, after a period of approximately 7 hours, the current density for alloy A2 suddenly increased to a level greater than 10$\mu A/cm^2$ (fig B8). The current density remained at this level until the test was terminated after a total period of 8 hours. The surface of alloy A2 once again showed local attack at inclusion sites but was also characterised by the presence of a small crevice at the specimen/gasket interface, as indicated in fig B9.

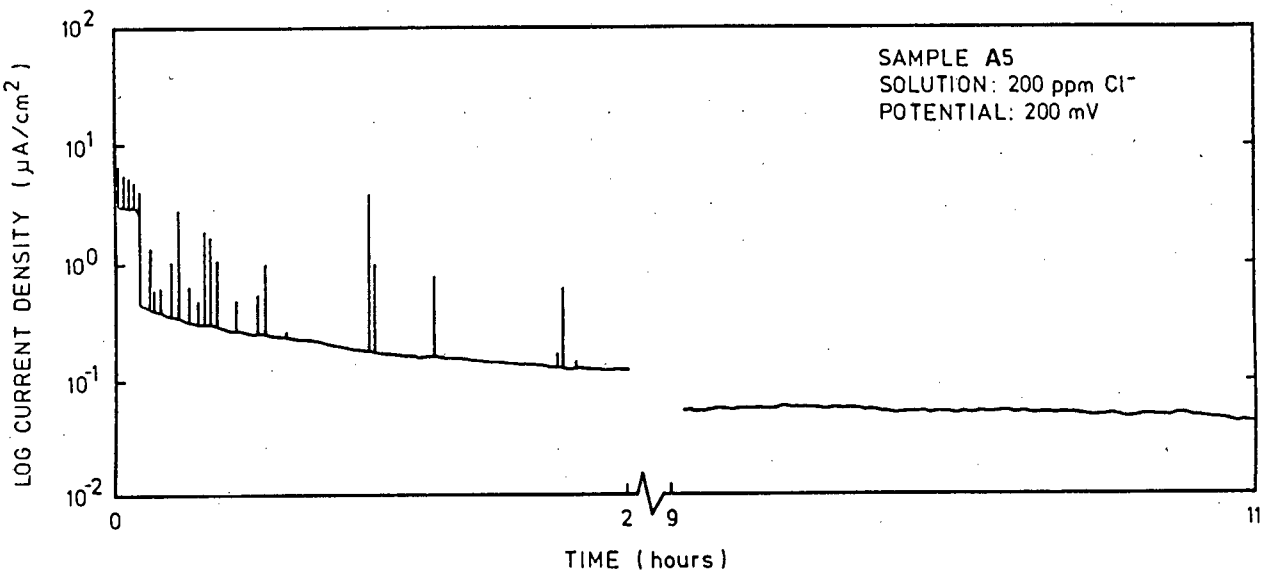

(a)

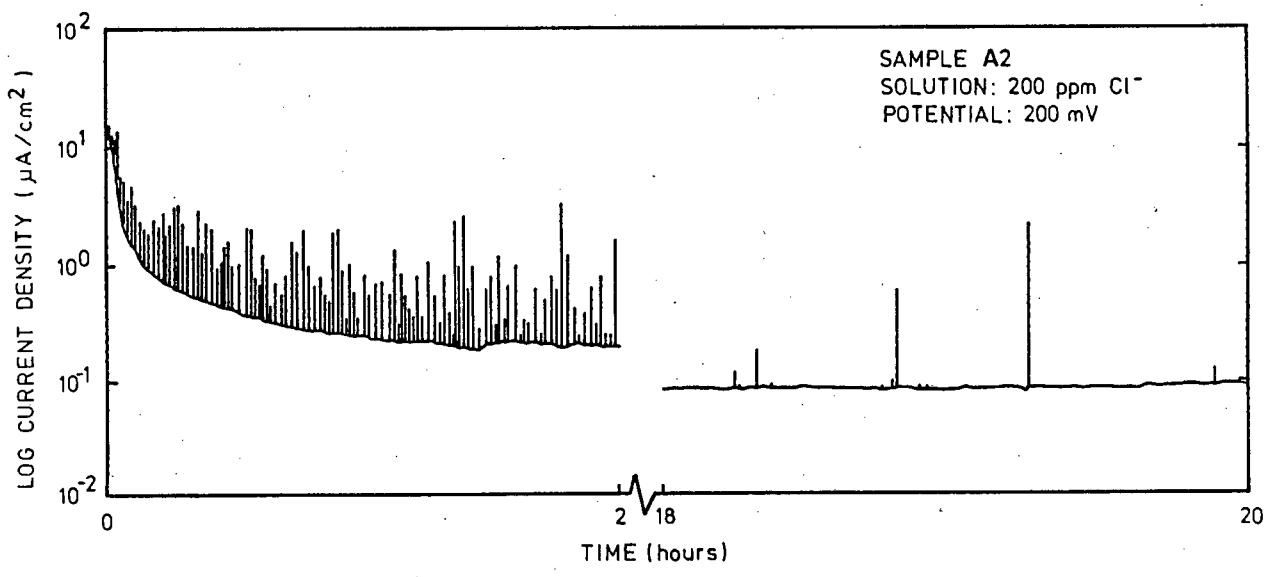

(b)

FIGURE B7: Current density - time diagrams for alloys A5 and A2 tested at $+200mV_{SCE}$.

(a) Alloy A5

(b) Alloy A2

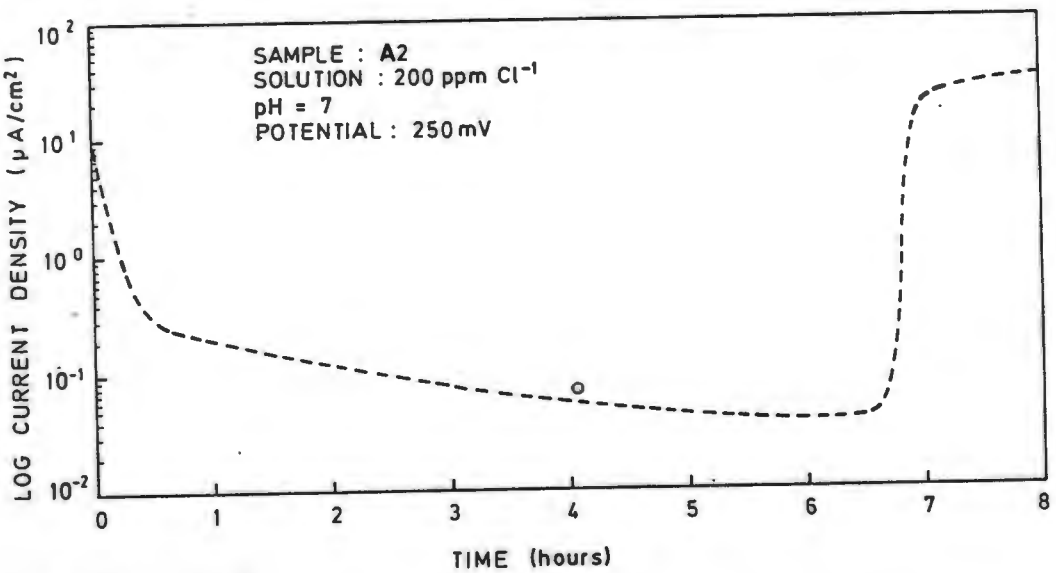

FIGURE B8 : Current density - time diagram for alloy A2 tested at $+250mV_{SCE}$. (NOTE: Although detected, the current spikes are not indicated in this diagram).

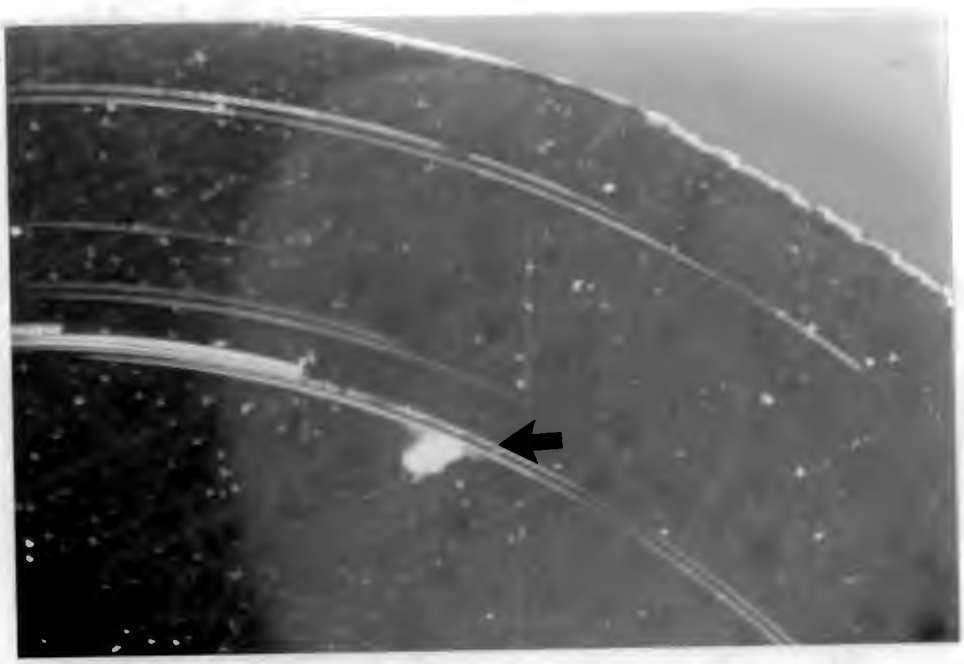

FIGURE B9 : Formation of a crevice at the specimen/gasket interface (Alloy A2 tested at $+250mV_{SCE}$).

Potential = +300 mV_{SCE}

At a polarisation potential of +300mV_{SCE}, alloy A5 passivated with little fluctuation in the current density. Alloy A2, on the other hand, did not passivate at all and the current density steadily rose to a level of about 1000$\mu A/cm^2$ (fig B10). After a test duration of 6 hours, alloys A2 and A5 were removed from the test solutions and a marked difference in the appearance of the two specimen surfaces was noted. This is indicated in fig B11. Alloy A5 showed relatively little localised attack, whereas alloy A2 exhibited a high degree of both localised attack parallel to the rolling direction and crevice corrosion at the specimen/gasket interface. The surface of alloy A2 in fig B12(a) clearly shows the pit morphology resembling that of the stringered inclusion morphology. Evidence that titanium carbonitride cuboids are not attacked is indicated in fig B12(b).

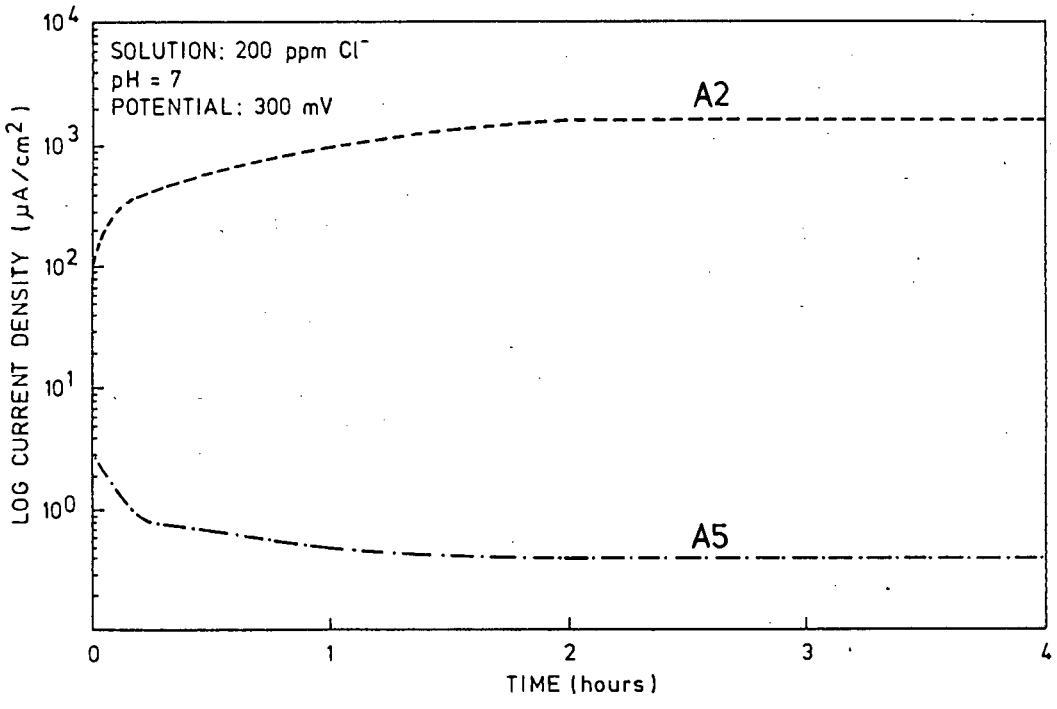

FIGURE B10: Current density - time curves for alloys A5 and A2 tested at +300mV_{SCE}.

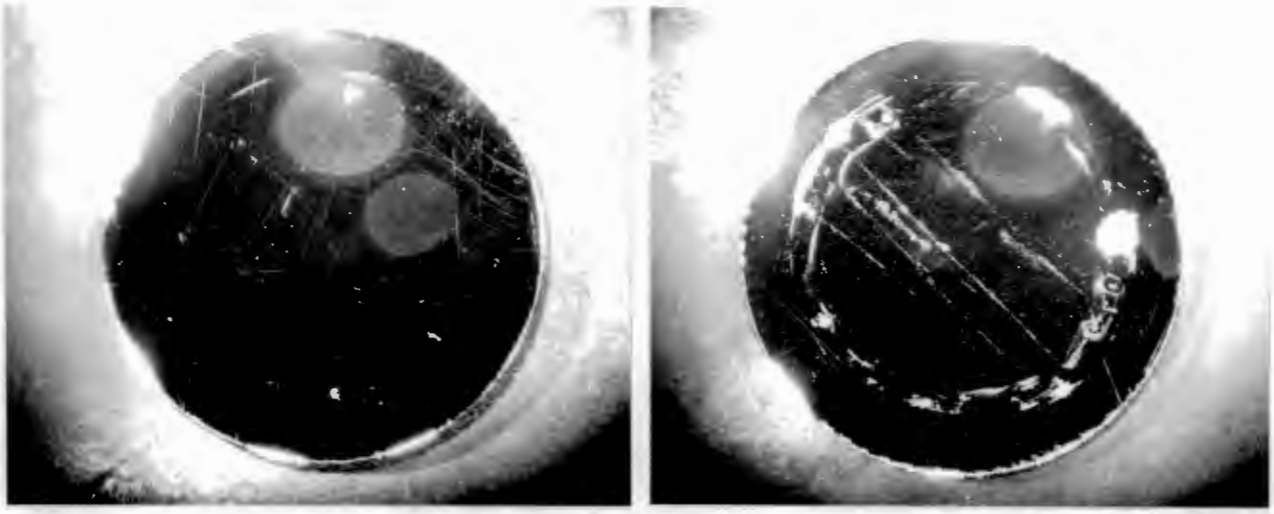

(a) (b)

FIGURE B11 : Comparison of the surfaces of Alloys A5 and A2 after 6 hours at $+300mV_{SCE}$

(a) Alloy A5

(b) Alloy A2

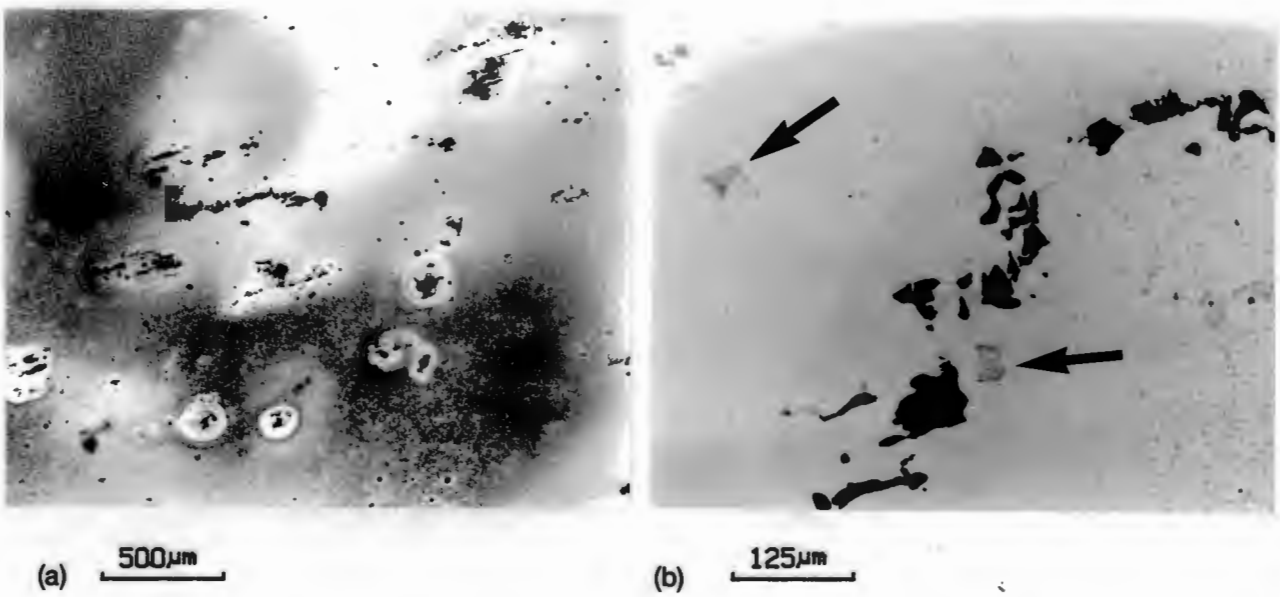

(a) (b)

FIGURE B12 : Localised attack on the surface of Alloy A2 after 6 hours at $+300mV_{SCE}$

(a) Pit geometry similar to inclusion morphology

(b) Relatively unattacked cuboid inclusions

B5.2.3 Pit Density Measurements

The pit densities were measured on the test surfaces of alloys A2 and A5 after anodically polarising (scan rate = 0.14mV/sec) the test specimens to $+1V_{SCE}$ in a solution containing 400ppm Cl^-. Pitting was observed to be much more severe in the case of alloy A2, as is shown by comparing the two test surfaces after testing (fig B13). The average pit densities for alloys A5 and A2 were measured as 50 and 260 pits/cm^2 respectively.

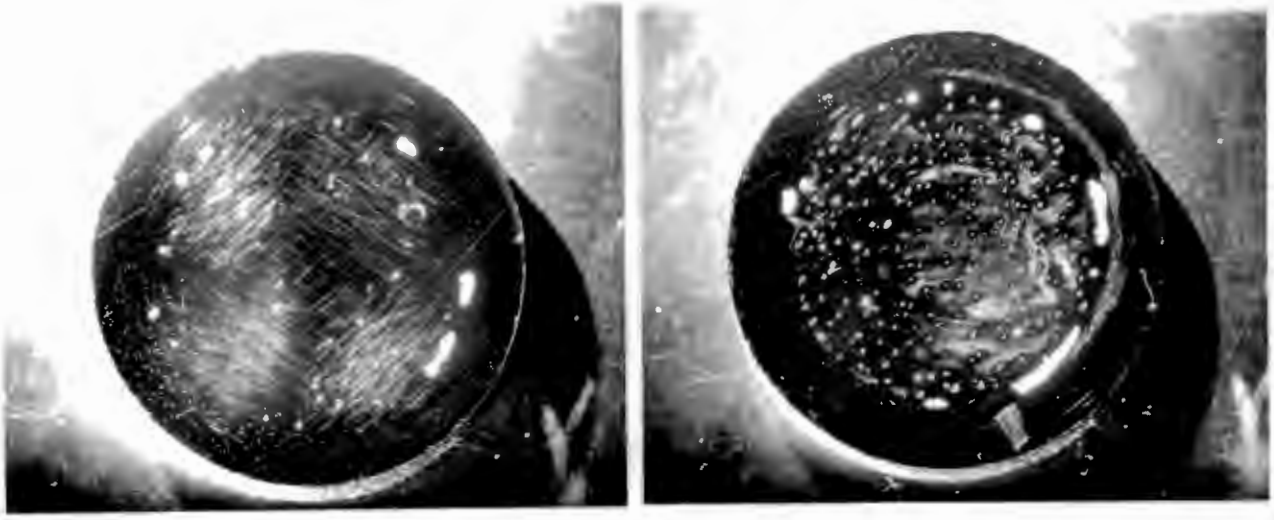

(a) (b)

FIGURE B13 : Relative pit densities exhibited by alloys A5 and A2 after anodically polarising to $+1V_{SCE}$ in a 400ppm Cl^- solution.
(a) Alloy A5
(b) Alloy A2

Although pit growth resulted in fairly extensive dissolution of the matrix, the pit geometry in many instances is reminiscent of the original inclusion morphology. This is illustrated in fig B14 which once again compares the relative pit densities of alloys A5 and A2.

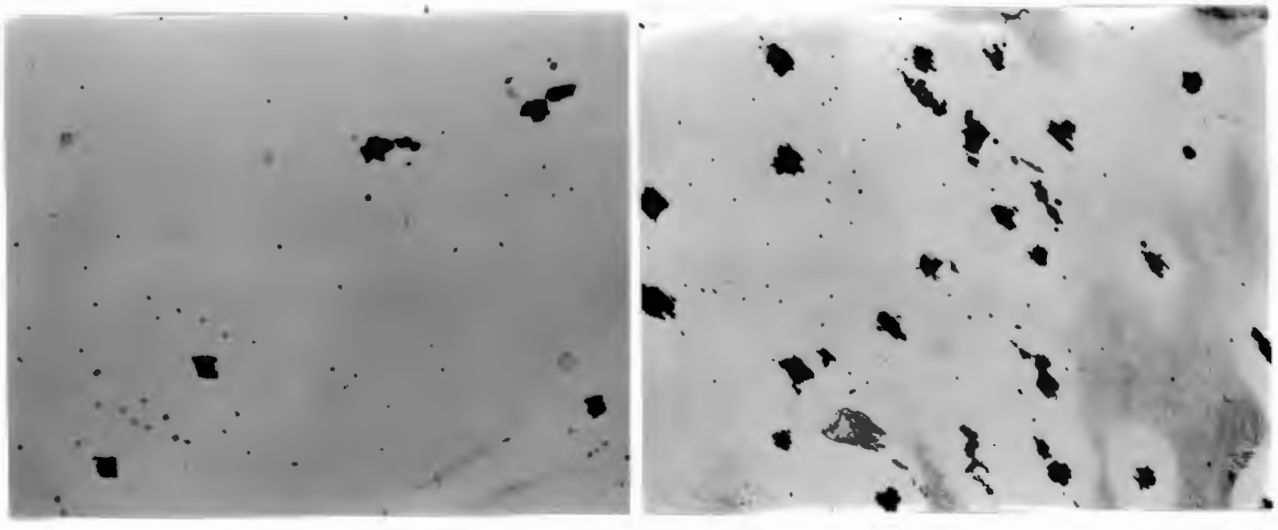

FIGURE B14 : Comparison of the pitting attack exhibited by alloys A5 and A2. Note the pit geometry in the case of alloy A2.
(a) Alloy A5
(b) Alloy A2

B5.3 PIT INITIATION STUDIES

Two alloys A2 and B6, were immersed in a 1 wt% $FeCl_3$ solution for 15 minutes in order to study the pit initiation sites more closely. Examination of the specimen surfaces after testing clearly illustrated the initiation of pitting at inclusion sites. An SEM micrograph in fig B15 shows the occurrence of an inclusion just below the metal surface. In this case, part of the metal matrix film has dissolved in the central area of the inclusion (area A) and the inclusion has been exposed. Energy dispersive X-ray spectroscopy (EDS) analysis of area A indicated the composition to be largely MnS. Analysis of area B, which still appeared to be covered by a metal film, indicated the existence of a high concentration of titanium as well as sulphur, with only a fairly minor amount of manganese evident.

Figure B16(a) illustrates corrosion attack at stringered manganese sulphide inclusions which resulted in concomittant dissolution of the surrounding steel matrix and the creation of micropits. It is clear that the extent of the dissolution is much greater than the inclusion volume itself. Figure B16(b) also shows matrix dissolution associated with cuboid inclusions. The surrounding steel matrix is attacked quite extensively but there is no obvious attack visible on the cuboid inclusions themselves.

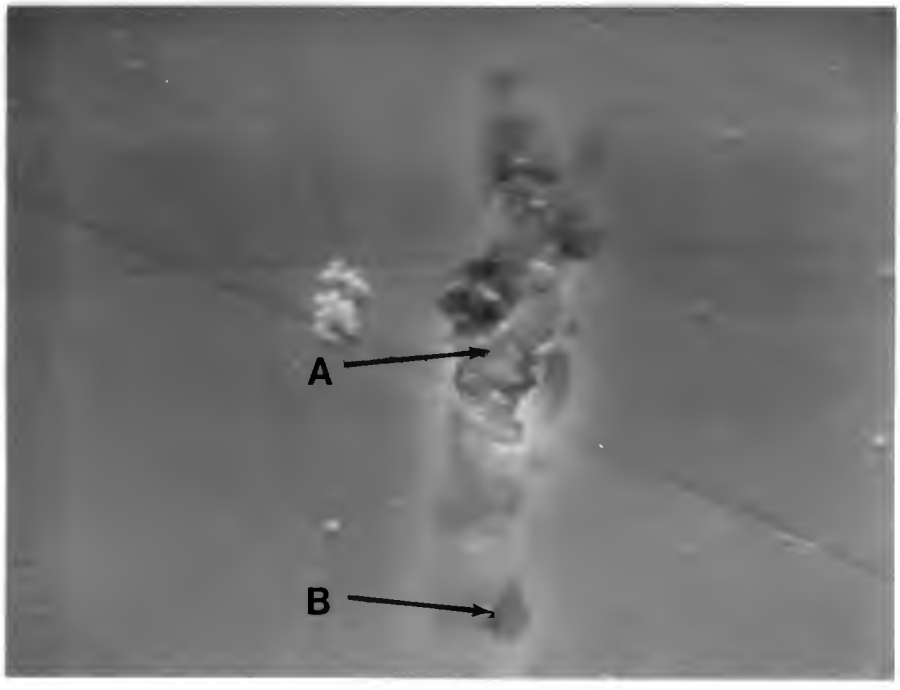

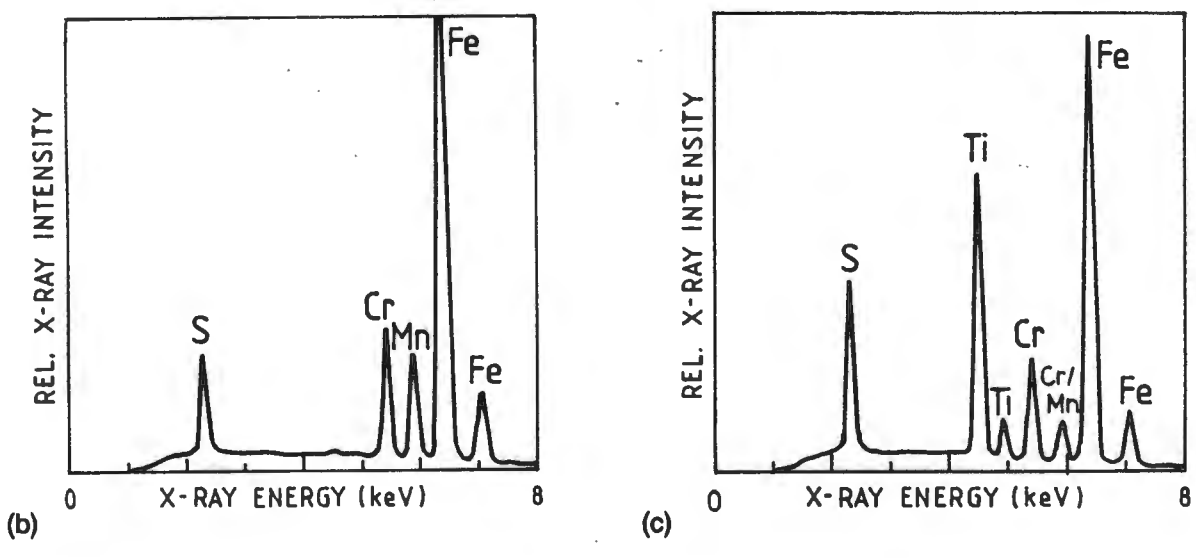

FIGURE B15 : Corrosion initiation at a sulphide inclusion (Alloy B6).

(a) Near surface sulphide inclusion

(b) EDS analysis of Area A

(c) EDS analysis of Area B

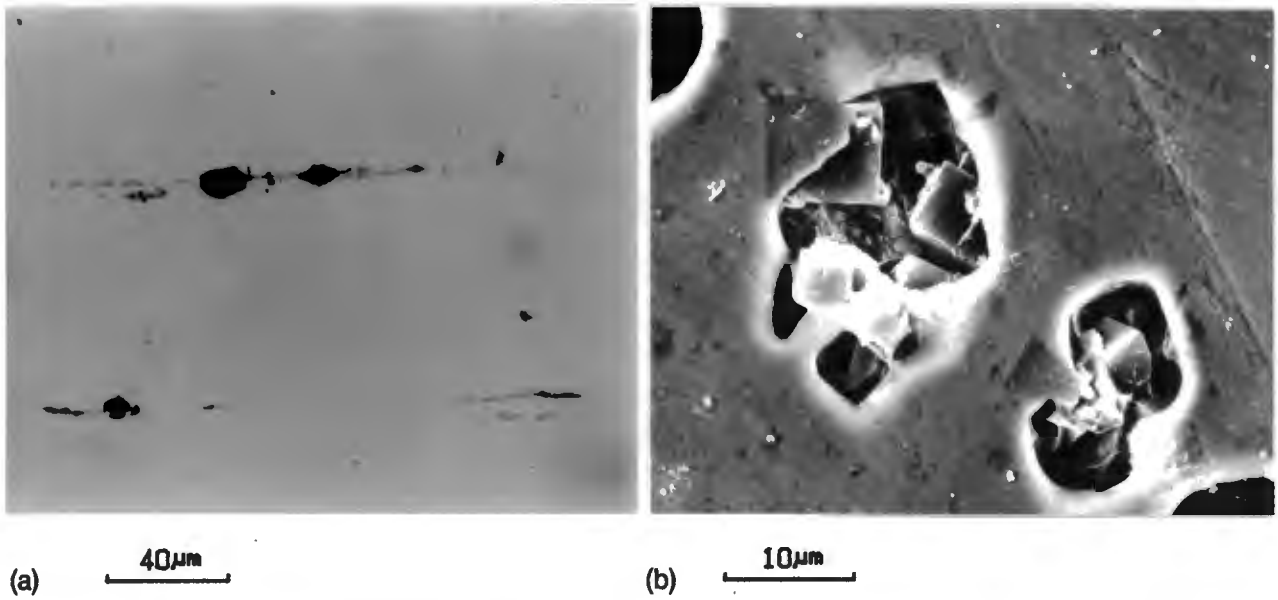

FIGURE B16 : Corrosion initiation at inclusion sites in alloy A2.
(a) Corrosion attack at stringered MnS inclusions
(b) Matrix dissolution around cuboid inclusions

B6 DISCUSSION

B6.1 ALLOYS B1-B8

The corrosion tests performed on alloys B1-B8 in very mild chloride solutions (10ppm Cl^- ions) have indicated variations in the corrosion performance of these alloys. Although the relatively fast scan rate (14mV/sec) employed during anodic polarisation is not representative of an equilibrium situation, the inconsistencies in the passive behaviour of the various alloys can be rationalised. These inconsistencies correlate well with the appearance of the test surfaces after polarisation, and with the sulphur levels and Ti/S ratios for the alloy range.

Based on a qualitative assessment of the shape of the polarisation curves, and the current densities determined at $+1V_{SCE}$, the corrosion performance of the alloys can be ranked, in decreasing order, as B1, B3, B4, B5 > B2, B7 > B6, B8. Although the nature of the test procedures carried out by no means represents a practical situation, the factor/s contributing to these variations in corrosion performance are important. Considering the general chemistries of the eight commercial alloys, there are no obvious inconsistencies identifiable in terms of the production specifications for 3CR12 steel. Certainly the most influential major alloying element, chromium, indicates negligible variation. In general, most alloying elements vary very little, except for the relative variation in titanium content

which is noteworthy. From an impurity element point of view, however, a considerable variation is noted in the sulphur and nitrogen levels. As has been shown in the study on the occurrence of non-metallic inclusions in 3CR12, these elements, titanium, sulphur, and nitrogen, are most likely to affect the sulphide inclusion populations in the steel.

The graph indicating a plot of current density (at $+1V_{SCE}$) versus Ti/S ratio for the 8 alloys (fig B4) suggests that the decrease in passivity behaviour is related to the increased propensity for the existence of manganese sulphide. Once again only a qualitative trend is represented by this graph since the decision to measure the current density at $+1V_{SCE}$ is fairly arbitrary. In addition, there is no way that the Ti/S ratio bears any precise relationship to the manganese sulphide content. Certainly, if the alloys B6, B7, and B8 are considered, then the higher sulphur contents alone can explain the decreased passivity tendencies. However, the titanium content is important when considering an alloy such as B1 which has a considerably higher sulphur content when compared to alloys such as B3, B4, and B5, although they all possess similar corrosion behaviour. The higher titanium content and relatively low nitrogen level for alloy B1 must surely allow a more favourable tendency for the formation of TiS than for MnS in this situation.

The surface condition of the alloys after testing has shown more visible signs of corrosive attack on alloys B6 and B8. Indications are that micro-pitting has occurred at sites preferentially aligned parallel to the rolling direction. The shape and orientation of these pits compares favourably with the distribution of MnS inclusions identified in these steels. In contrast, examination of the surface of alloy B3 indicated only very isolated incidences of micro-pitting and the surface generally remained unattacked. This observation is in agreement with the relatively minor occurrence of MnS inclusions in this alloy.

Corrosion initiation studies in ferric chloride solutions (1 wt %) have justified the proposed contribution of MnS to micro-pitting. It is clear from fig B16(a) that micro-pitting can result from both the dissolution of elongated MnS inclusions followed by attack on the exposed matrix, and the concomittant dissolution of the inclusion and matrix at the inclusion/matrix interface. Both these situations are depicted in fig B16(a). Corrosion can also initiate at the Ti(NC) inclusion/matrix interface and may arise as a result of the existence of a crevice (void) at the interface, or the creation of a crevice by the dissolution of MnS surrounding the cuboid. This form of attack is exhibited in fig B16(b). Although this contribution to micropitting is also noted, the general morphology of micro-pitting favours attack at MnS inclusion sites as being the predominant influence.

The difference in the corrosion behaviour of TiS and MnS is suitably illustrated in fig B15. A mixed sulphide inclusion showing different proportions of manganese and titanium

appears to indicate preferential attack at the site richer in MnS. In spite of the fact that the inclusion depth below the surface could vary, it seems more than coincidental that the area richer in MnS is attacked, whereas the area richer in TiS shows no visible signs of corrosion. Indeed behaviour such as this would be expected considering the very low solubility of TiS[3].

On the basis of the abovementioned evidence, there appears to be little doubt that the variations in the passivation tendencies of alloys B1-B8 during anodic polarisation are related to the relative occurrences of MnS inclusions in these steels. Higher current densities coincide with greater degrees of micropitting and it is obvious that the morphology of the micropits is similar to the MnS inclusion distributions. In addition, it is possible that the formation of a localised concentration of H_2S, as a result of MnS dissolution, has contributed to the absence of a notable active-passive transition in the case of alloys B6 and B8.

B6.2 ALLOYS A2 AND A5

A direct comparison of the corrosion behaviour of alloys A2 and A5 has led to a more thorough determination of the effect of MnS inclusions on the corrosion performance of 3CR12. The marked difference in the MnS populations of these two alloys has been clearly illustrated (Chapter 4, fig 4.37). In addition, the variation in the Ti/S ratios for these two steels is large (14.44 and 38.75 for A2 and A5 respectively).

The potentiodynamic tests, under slow scan rate conditions (0.14mV/sec) in solutions containing 200ppm Cl^-, have shown considerable variations in the passive range of the two alloys. The larger passive range of of alloy A5 (-190 to $+490mV_{SCE}$) and the fewer current spikes identified indicates a greater stability of the passive layer. In contrast, alloy A2 displays a smaller passive range (-200 to $+360mV_{SCE}$), a much greater frequency of current spikes, and a higher average current density. Each of these variations can be attributed to the greater population of MnS inclusions in the case of alloy A2. The fluctuations in the current density in the passive region, referred to as current spikes, suggests an increase in current density due to the dissolution of MnS inclusions and the transient exposure of the metallic matrix. It would appear that the micropit formed in this instance, however, does not propagate, since the current density returns to the average value. The latter observation is certainly more marked in the case of Alloy A5. The origin of the current spikes has been verified by conducting a simple scratch test during potentiodynamic scanning. Periodic scratching of the passive surface of a test specimen was carried out using a glass point. In response to each scratch, which presumably penetrated the oxide film, a sudden increase in current density was observed. This was

followed by almost immediate repassivation as the current density again decreased in response to the healing of the passive film.

The higher average passive current density in the case of alloy A2 can be explained by the greater instability of the oxide film as a result of the more frequent dissolution of MnS inclusions. In addition, the increased concentration of H_2S expected from this situation is possibly responsible for the lower breakdown potential recorded for this alloy. These observations in terms of dissolution of MnS inclusions and the formation of micropits are consistent with the appearance of the surfaces of the two alloys after testing.

Rapid polarisation of specimens to predetermined potentials and the subsequent monitoring of the effect of time on corrosion at these potentials has further elucidated the differences in the corrosion performance of the two alloys. At the lower potentials ($+200mV_{SCE}$), potentiostatic testing showed little difference in the average passive behaviour of the two alloys, but the greater extent of inclusion dissolution on the surface of alloy A2 was once again identified. It is clear from the low current density detected even after 20 hours that pit propagation had not occurred. Polarisation to $+250mV_{SCE}$ indicated similar low current density-passive behaviour for both alloys with the usual amount of micropitting expected. However, these conditions indicated that given sufficient time, alloy A2 is susceptible to crevice corrosion at the gasket/metal interface with accompanying rise in current density (figs B8 and B9).

The sequence of events leading to the formation of crevices due to MnS inclusion dissolution is illustrated in fig B17. Information for this model was obtained by inducing crevice corrosion in alloy A2 and observing the crevice formation at various stages. In fig B17(a) the random scatter of stringered sulphide inclusions is schematically illustrated and suggests that some inclusions must occur at the gasket/metal interface. The dissolution of these inclusions can therefore result in the formation of a micro-crevice at the interface, as shown in fig B17(b). The favourable crevice conditions initiated now facilitate further dissolution of the metal matrix under the gasket and the crevice becomes enlarged (fig B17(c)).

During the rapid polarisation from the cathodic region to $+300mV_{SCE}$, the instantaneous dissolution of MnS in alloy A2 prevented the formation of passivity entirely, and advanced pitting and crevice corrosion occurred. This suggests that the greater instability invoked at the higher potential due to the faster inclusion dissolution rate did not allow repassivation of the exposed metal. Obviously under these conditions an increased propensity also exists for the formation of crevices at the specimen/gasket interface. On the other hand,

alloy A5 passivated following polarisation and, apart from the occasional current spike, passivity was maintained for the duration of the test.

Further evidence for the lowering of corrosion resistance due to the existence of large MnS inclusion populations is provided by the greater pitting density measured for alloy A2 after potentiodynamic testing in 400ppm Cl^- solutions. Under these conditions, the increased chloride content and higher potential range has promoted pit propagation in both alloys. However, the pitting density measured for alloy A2 was approximately five times greater than that for alloy A5. This is hardly surprising in view of the greater number of potential dissolution sites evident on the surface of alloy A2.

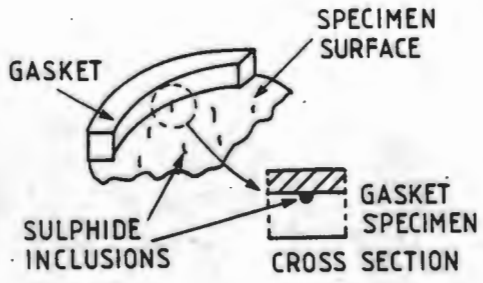

(a)

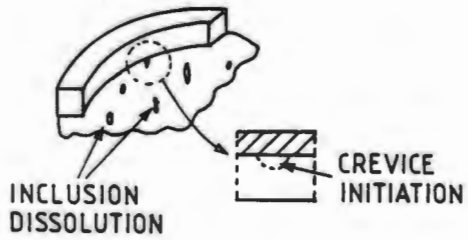

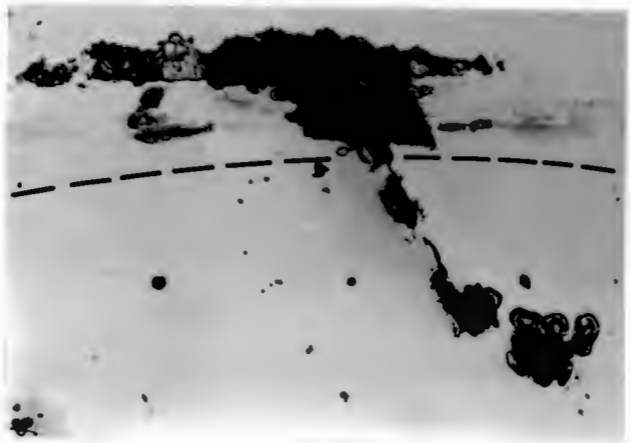

(b)

200μm

FIGURE B17 : Model for crevice corrosion initiated by inclusion dissolution.

(a) Occasional occurrence of MnS inclusions at the specimen/gasket interface.

(b) Inclusion dissolution leading to cavity formation under the gasket.

FIGURE B17/contd...

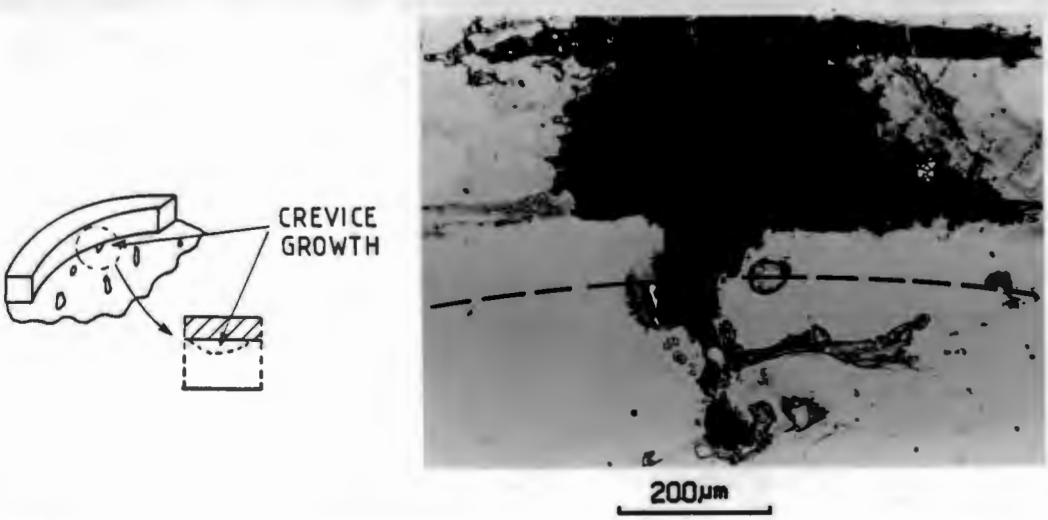

(c)

FIGURE B17 : Model for crevice corrosion initiated by inclusion dissolution.
(c) Propagation of crevice under gasket.

B7 CONCLUSIONS

The preceding discussion outlines the deleterious effects of MnS inclusions on the corrosion behaviour of 3CR12 steel. Although the dissolution of MnS inclusions does not automatically imply that pit propagation will occur, the general stability of the passive film and the susceptibility to crevice attack is affected. This means that increasing MnS inclusion density will lead to an increasing tendency for the lowering of the corrosion resistance of the steel, and as the environment becomes more harsh, the effect of the presence of MnS inclusions will become more marked. Lower sulphur levels and improved Ti/S ratios will avoid many of the deleterious effects associated with large populations of MnS. Negligible effect on corrosion performance was observed for titanium sulphide and titanium carbonitride inclusions. Only very occasional matrix dissolution was noted at titanium cuboid/matrix interfaces.

REFERENCES

1. JANIK-CZACHOR M., WOOD G.C. and THOMPSON G.E., Br. Corros. J., 1980, 15(4), pp.154-161.
2. SCOTTO V., VENTURA G. and TRAVERSO E., Corros. Sci., 1979, 19, pp.237-250.
3. SEDRIKS A. J., Intnl. Metals Rev., 1983, 28(5), pp.295-307.
4. KIESSLING R. and LANGE N., "Non-metallic Inclusions in Steel", 2nd. edn., part IV, pp.15 and 16, 1978, London, The Metals Society.
5. WRANGLEN G., Corros. Sci., 1974, 14, pp.331-349.
6. SZUMMER A. and JANIK-CZACHOR M., Br. Corros. J., 1974, 9(4), pp.216-219.

ISSN 0250-0418 - Elektronmikroskopievereniging van Suidelike Afrika PIETERMARITZBURG (1985)

EFFECT OF NON-METALLIC INCLUSIONS ON THE FRACTURE OF 3CR12 CORROSION RESISTANT STEEL

Robert D. Knutsen

Department of Materials Engineering, University of Cape Town

In view of the complex chemistry of 3CR12, careful monitoring of element additions is required. Chromium is added to provide corrosion resistance and, together with nickel, gives a controlled dual-phase ferrite/martensite microstructure. Stabilisation is achieved by titanium additions, and elements such as carbon, nitrogen and manganese complete the alloy chemistry. These additions, together with impurities present, give rise to non-metallic inclusions in the form of titanium carbo-nitrides, titanium sulphides and manganese sulphides. The exact composition, morphology, distribution and volume fraction, however, will depend on the relative amounts of Ti, Mn, S, C and N present in the steel. In most instances, titanium carbo-nitrides are cuboid in shape and have been shown to contain a surrounding thin layer of iron - and/or iron-manganese sulphides[1].

The present work involves a detailed analysis of inclusion types and distributions, and their effects on the impact toughness of the steel. Inclusion analyses on polished surfaces using energy dispersive spectroscopy (EDS) have shown a variety of compound inclusions to be present. Ti(CN), for example, has also been seen to contain titanium sulphide in the surrounding layer. Stringered MnS inclusions can also occur, in which case titanium may or may not be present.

In order to determine the effect of inclusions on the impact toughness of 3CR12, Charpy V-notch impact tests were conducted on several 3CR12 samples having varying amounts of titanium, sulphur and nitrogen. Specimens were prepared in the T-L orientation[2] and were given a standard heat treatment prior to testing. Results show that the impact energy decreases with increasing sulphur content, but increases with increasing Ti/S ratio. The macroscopic appearance of all the fracture surfaces is similar and a typical example is shown in Fig. 1. Both cleavage and ductile-dimple fracture modes can be identified, giving rise to a highly contoured surface which appears jagged in profile. The occurrence of these alternating bands of cleavage and ductile fracture can be explained by the combined effect of plastic constraint during fracture and the presence of elongated inclusion populations parallel to the rolling direction. The plastic constraint causes a secondary tensile stress perpendicular to the applied stress, i.e. a tensile stress in the through-thickness direction, and results in cleavage being initiated by matrix/inclusion decohesion. Fig. 2a shows the occurrence of fragmented inclusions in the area where cleavage is presumed to have initiated. Analysis of the inclusions using EDS indicates the presence of both titanium and sulphur (Fig. 2b). A further example of matrix/inclusion decohesion in Fig. 3 clearly shows the separation of the matrix from the

inclusions which leads to a low energy fracture. In this case sulphur was not detected and it is assumed that the inclusions are Ti(CN).

A quantitative assessment of the relative contributions of the various inclusions is not feasible due to the complex nature of the fracture surface. However, inclusion analyses using EDS on polished surfaces have shown that stringered manganese sulphide inclusions occur more abundantly in samples having low impact values. This is in agreement with the fact that impact energy decreases with increasing sulphur content. The higher the sulphur content, the greater the tendency for MnS formation. On the other hand, increasing Ti/S ratio results in the formation of titanium sulphide in preference to stringered manganese sulphide. Titanium sulphide appears to have a less detrimental effect on the impact toughness.

References

1. Blum, F., Stander, C.M. and Comins, N.R. (1984) Proc. Electron Microsc. Soc. South. Afr., 14, 9.
2. Metals Handbook 9th edition, vol. 1 (1978) Metals Park, ASM, 700.

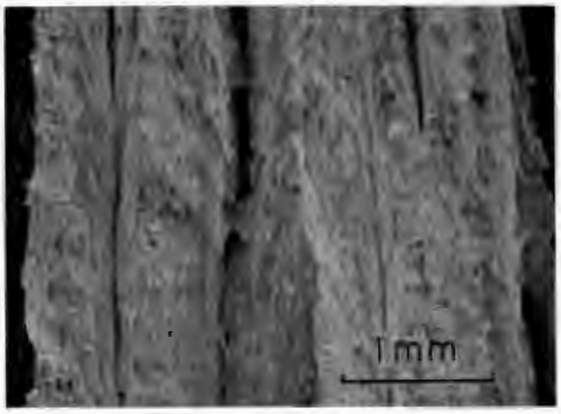

Fig. 1: Typical Charpy Impact fracture surface

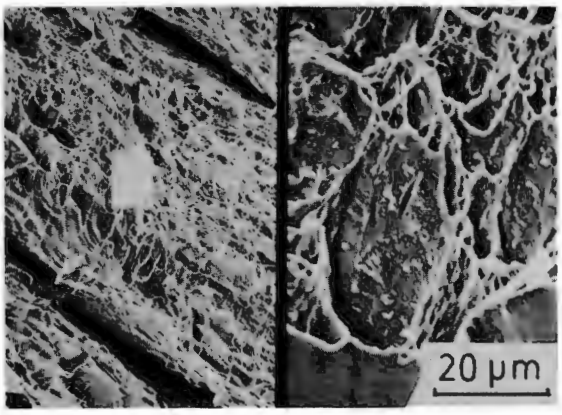

Fig. 2a: Fragmented inclusions associated with cleavage

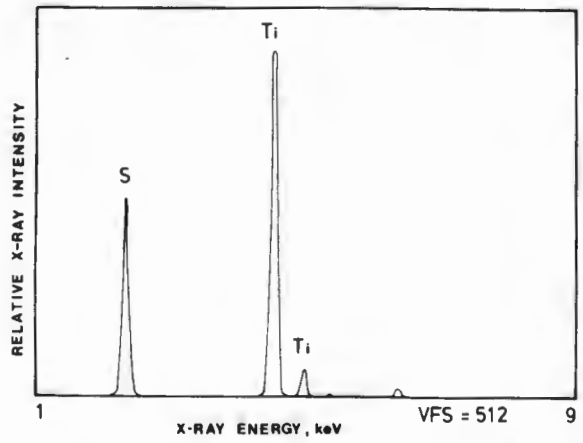

Fig. 2b: EDS analysis of inclusions in Fig. 2a

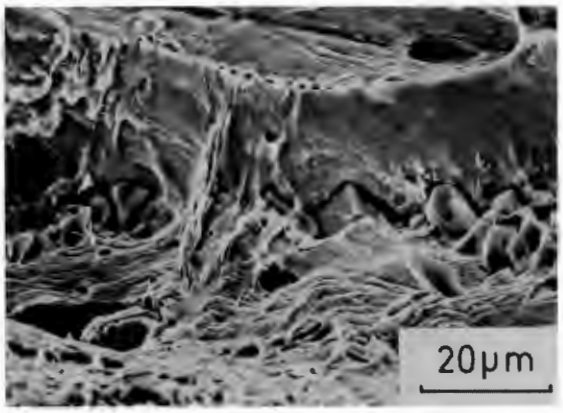

Fig. 3: Splitting of matrix caused by Ti(CN) inclusions

THE USE OF EDS IN IDENTIFYING THE INCOMPLETE δ-FERRITE TO AUSTENITE TRANSFORMATION IN 3CR12

R.D. Knutsen

Department of Materials Engineering, University of Cape Town

The achievement of a tough, fine grained microstructure in dual-phase ferrite/martensite alloys is largely dependent on the existence of a fully austenitic structure at some intermediate temperature. Cooling below this austenitic region will result in the nucleation and growth of α-ferrite as the material passes through the dual-phase α-ferrite + austenite region. However, if the high temperature transformation from δ-ferrite to austenite is not complete, then it is possible that residual δ-ferrite will be present at room temperature. Since the presence of residual δ-ferrite will interfere with the grain refining transformation from austenite to α-ferrite, the mechanical properties of the alloy are likely to be affected.

The phase diagram for 3CR12, as determined from isothermal sections for solid-phase equilibria in the Fe-Cr-Ni system[1], indicates that the alloy is fully austenitic in the region extending from approximately 1150°C to 900°C. However, heat treatments performed on the alloy indicate that the transformation from δ-ferrite to austenite is not complete and residual δ-ferrite is identified at room temperature. Energy dispersive spectroscopy (EDS) analysis of the two phases present (residual δ-ferrite and transformed δ-ferrite), after cooling from 1400°C, indicates substitutional element partitioning between the two phases. The compositions of the residual δ-ferrite and the transformed phase are shown in Table 1. From these results it is clear that the main ferritiser, chromium, has partitioned to the δ-ferrite phase, whereas nickel has partitioned to the austenite phase. In view of the fact that the transformation from δ-ferrite to austenite is diffusion controlled, it appears as if the reaction reaches a certain point after which the driving force is no longer strong enough for further transformation to occur. This is possibly due to a combination of the partitioning effect in the two phases and the decrease in diffusivity. It is also evident from the SEM micrograph in Fig. 1 that impurities have segregated to the δ-ferrite phase. EDS analysis has shown these inclusions to contain predominantly titanium and phosphorous.

The commercial production of alloys such as 3CR12 involves the continuous casting of ingots which are subsequently hot-rolled. During the hot-rolling procedure, the residual δ-ferrite becomes elongated parallel to the rolling direction and forms pancake-shaped stringers[2]. As a result of the segregation of impurities to the δ-ferrite boundaries, the inclusions also become elongated parallel to the rolling direction. The SEM micrograph shown in Fig. 2 illustrates the banded effect of the δ-ferrite stringers and the segregated impurities after hot-rolling. Although this sample has been hot-rolled and annealed (HRA), the

partitioning effect caused by the incomplete transformation can still be identified. The respective phase compositions are listed in Table 2.

The presence of ferrite stringers, and also the numerous impurity particles on the grain boundaries, restricts the formation of an equiaxed microstructure, thereby giving rise to a degree of anisotropy in the properties of the material. This elongated microstructure is mostly responsible for the delamination which occurs during the testing of transverse Charpy impact specimens[3].

References

1. Rivlin, V.G. and Raynor, G.V. (1980) Int. Metals Review 1, 21.
2. Knutsen, R.D. (1987) Current research for PhD thesis.
3. Knutsen, R.D. and Hutchings, R. (1987) paper submitted to Materials Science and Technology.

Table 1: EDS (20kV) analysis after cooling from 1400°C (wt-%)

Element	Residual δ-ferrite	Transformed phase
Ti	0.20	0.15
V	0.20	0.10
Cr	11.08	9.07
Mn	0.74	0.89
Ni	0.34	0.76

Table 2: EDS (20kV) analysis of HRA micro-structure (wt-%)

Element	Residual δ-ferrite	Transformed phase
Ti	0.24	0.28
V	0.16	0.13
Cr	12.19	10.96
Mn	1.37	1.47
Ni	0.46	0.66

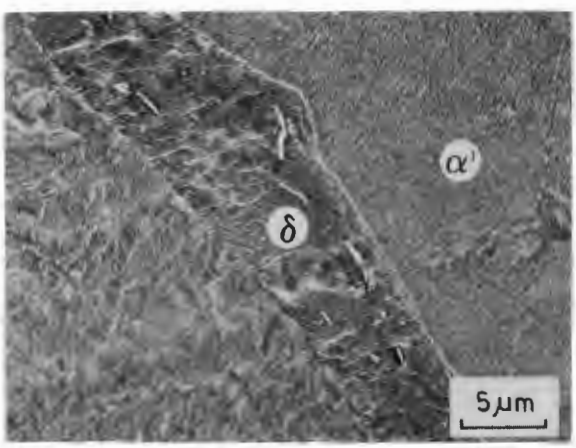

Fig. 1: Segregation of impurities to the δ-ferrite phase.

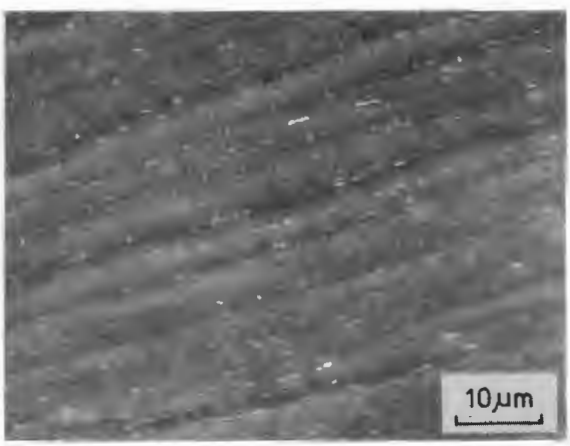

Fig. 2: Banded microstructure evident after hot-rolling.

Both micrographs are secondary electron images obtained using a LaB_6 emitter at an acceleration voltage of 30 kV.

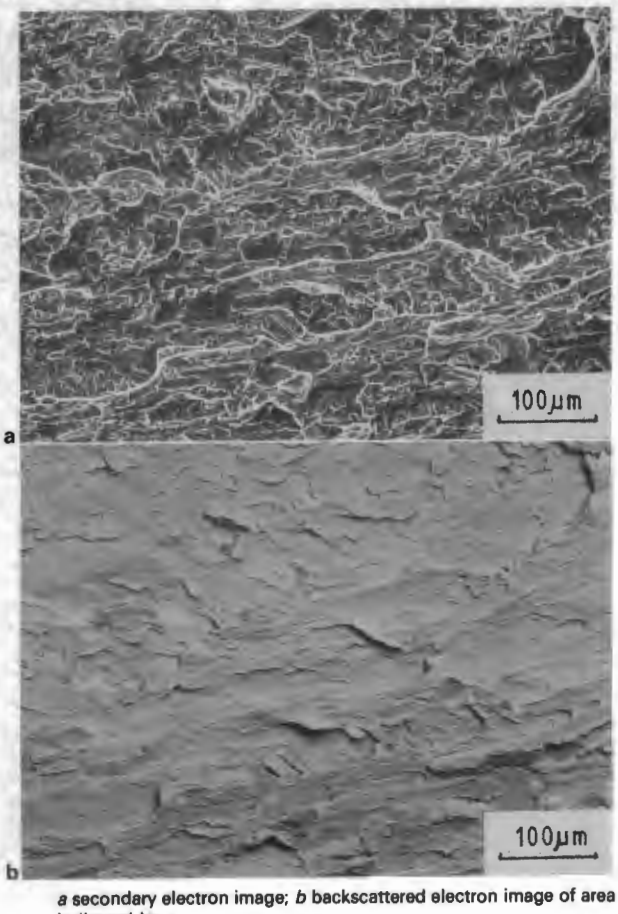

a secondary electron image; *b* backscattered electron image of area indicated by *a*

21 Grain boundary separation revealed by backscattered electron imaging of surface of split

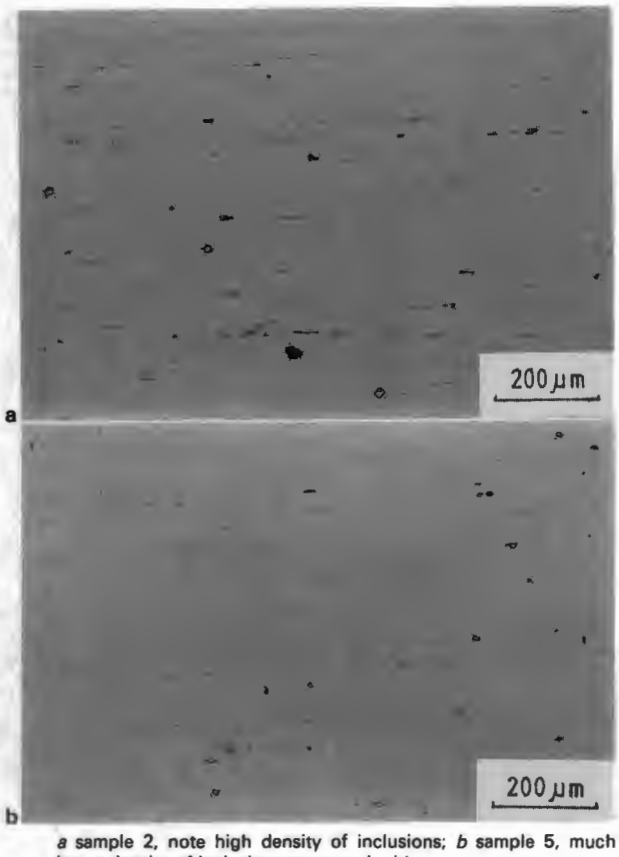

a sample 2, note high density of inclusions; *b* sample 5, much lower density of inclusions compared with *a*

22 Stringered sulphide inclusions in samples 2 and 5

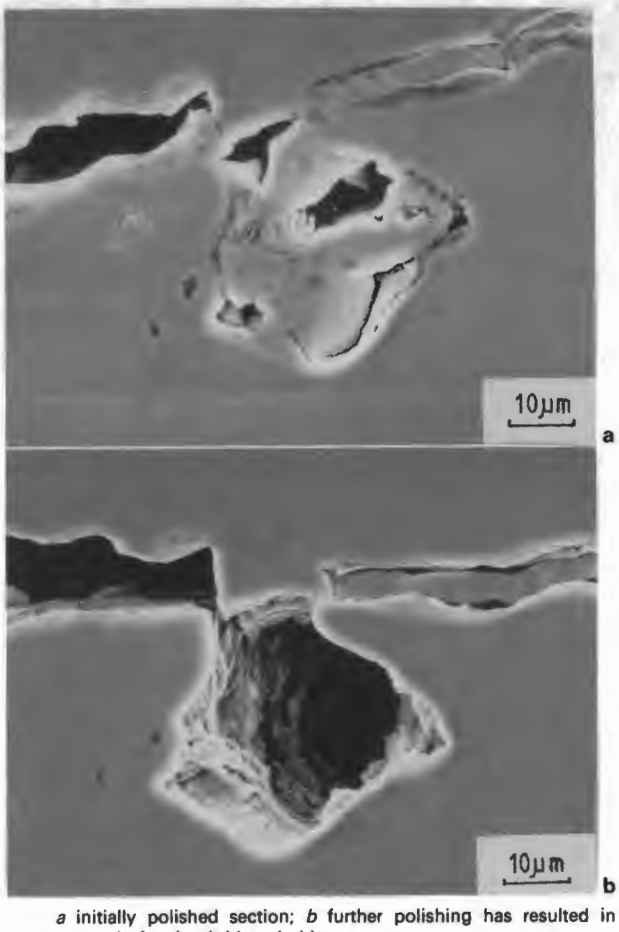

a initially polished section; *b* further polishing has resulted in removal of carbonitride cuboid

23 Cross-section of split surface showing cuboid associated with splitting phenomena (sample 5)

Conclusions

The fracture of 3CR12 in the annealed condition gives rise to a series of complex fracture modes. These fracture modes can be attributed to a combination of the elongated nature of the ferrite grains and the presence of non-metallic inclusions. The following relationships between bulk chemistry and impact energy have been observed.

1. Impact energy decreases as the sulphur content of the steel increases.
2. Impact energy increases with increasing Ti/S ratio.
3. Good impact energies are consistent with high Ti/S ratios and low nitrogen contents.

Although all inclusions would be expected to play some role in fracture initiation, the trends outlined above indicate that manganese sulphide had the most deleterious effect. The tendency for manganese sulphide formation is enhanced with high sulphur contents and low Ti/S ratios. Stringered manganese sulphide inclusions appear to be very effective in causing inclusion/matrix decohesion because of their pancake-shape and differences in thermal expansion coefficients.

It has been shown that by the correct control of impurities, the toughness of 3CR12 can be optimised. To achieve such optimisation, it is necessary to meet the following requirements.

1. Sulphur contents of less than 0·008%, to reduce the tendency for MnS formation.
2. Moderate titanium levels (0·30–0·40%), to ensure formation of TiS instead of MnS.
3. A low nitrogen content (0·010%), to reduce the volume fraction of titanium carbonitrides and therefore

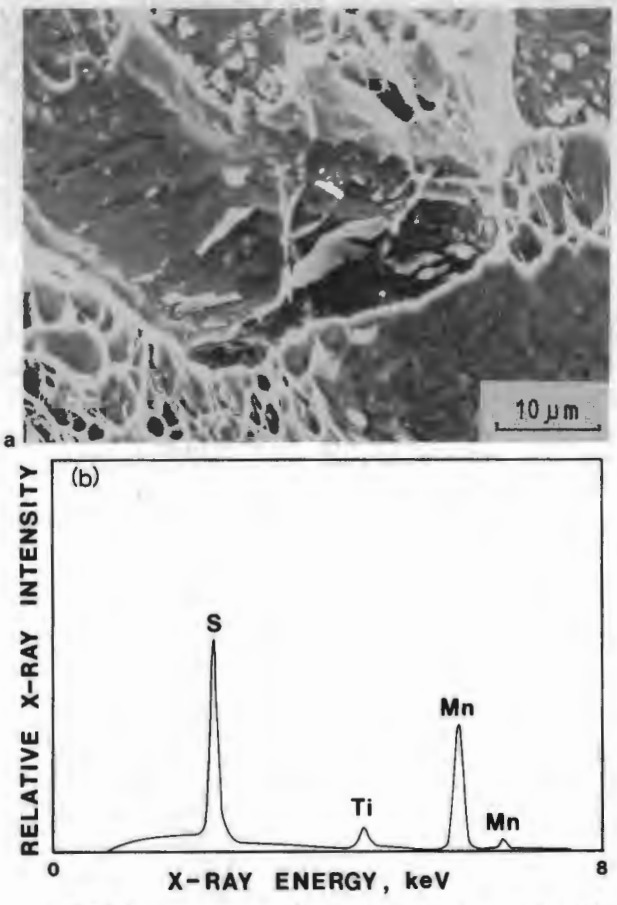

a SEM; *b* X-ray spectrum of inclusion (vertical full scale = 4096 counts)

17 Fragmented manganese sulphide inclusion exposed on split surface (sample 2)

cracks propagating between pancake-shaped ferrite grains parallel to the rolling plane of the as-rolled plate. A similar effect is shown in Fig. 19 which indicates the separation of ferrite grains along the split. As the split propagates, crack opening occurs at points of weakness ahead of the main crack. The main subsidiary cracks then join up to give the split a fairly irregular appearance in profile. The tearing associated with the joining up of the cracks gives rise to the so-called quasicleavage as indicated in Fig. 20. The split surface itself also reveals individual grain boundaries as shown in Fig. 21*b*. However, the steels tested by Bramfitt and Marder[12] did not contain any second phases, and it was found that splitting disappeared after the ferrite

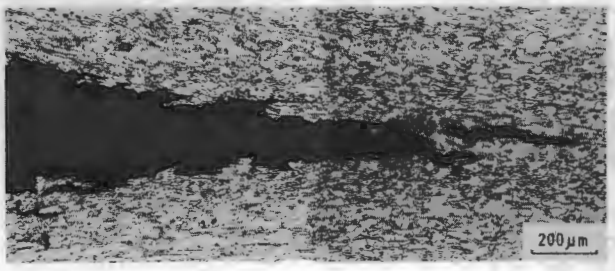

19 Cross-sectional view of splitting occurring between ferrite grains (sample 2)

recrystallised due to annealing. Steel 3CR12, on the other hand, does not show much of a tendency to form equiaxed grains upon annealing (Fig. 2) and splitting persists. There appears to be a suppression of the formation of equiaxed grains which can possibly be explained in terms of the presence of stringered sulphide inclusions. The stringered pancake-shaped manganese sulphide inclusions do not change shape during annealing and would tend to inhibit ferrite growth in the through-thickness direction. In this way a steel having a high concentration of manganese sulphides has a greater tendency to maintain elongated ferrite grains. Elongated sulphides also allow for easier matrix/inclusion decohesion because of their larger surface area in contact with the matrix. The difference in thermal expansion coefficients between iron and MnS facilitates the formation of voids at the matrix/inclusion interface.

The stringered sulphide distributions in samples 2 and 5 are shown in Figs. 22*a* and *b*, respectively. The sample having a lower Ti/S ratio (sample 2) has a much greater volume fraction of manganese sulphide and subsequently has a lower impact energy (Table 3). As mentioned above, Ti(CN) inclusions also have an effect on fracture and in a polished section (Fig. 23*a*) the edge of a cuboid within a split can be seen. On further polishing (Fig. 23*b*), the cuboid has been pulled out and the extent of the cavity can be seen. This indicates the degree of decohesion which occurs at the inclusion/matrix interface.

There is no apparent influence of ferrite factor on the impact energy, as shown in Fig. 9. Since the ferrite factor is an indication of the ferrite/martensite ratio, it was thought that a phase influence might be reflected in the variation in impact toughness. The differences in ferrite/martensite ratios over the ferrite factor range 9·28–11·29, however, are not significant. This confirms the findings of Grobler and van Rooyen[6] which show that for the three alloys studied, there is no direct relationship between ferrite factor (in the range 9·7–11·26) and splitting in 3CR12 transverse Charpy specimens.

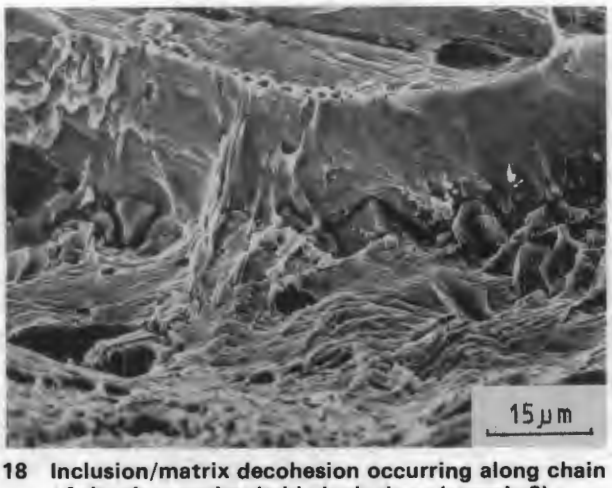

18 Inclusion/matrix decohesion occurring along chain of titanium carbonitride inclusions (sample 3)

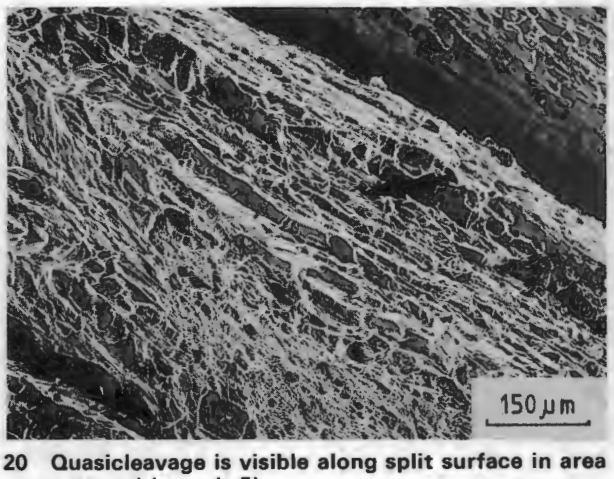

20 Quasicleavage is visible along split surface in area arrowed (sample 5)

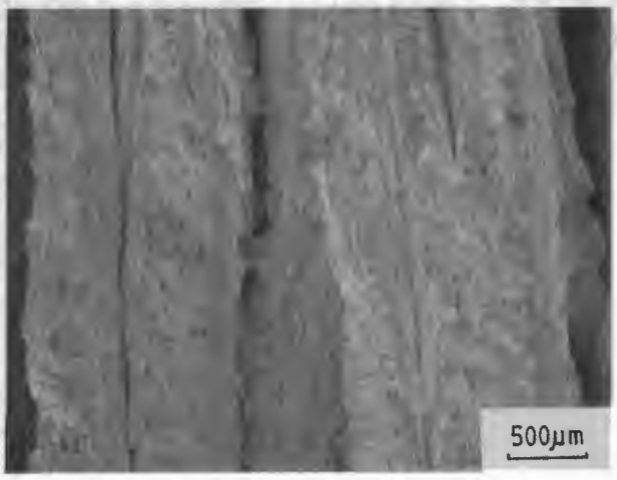

13 General view of fracture surface displaying characteristic features associated with splitting (sample 1)

which represent limited plastic deformation separating cleavage facets. Unlike pure cleavage, energy is absorbed as a result of the limited plastic deformation.

All these fracture modes can be identified on almost every one of the fracture surfaces. The inclusions associated with the various fracture modes have been monitored using EDS. Inclusions are seen to occur within the ductile dimples as well as in areas where splitting is assumed to have initiated. A typical association of inclusion fragments with ductile failure on the ridge areas is shown in Fig. 14. Particles are clearly visible within the cuplike features. The presence of inclusions along a split surface is clearly indicated in Fig. 15 which displays a characteristic inclusion/matrix decohesion mode of fracture. The EDS analysis has shown all types of inclusion to be associated with splitting and in Fig. 16 even titanium sulphide fragments are identified along the edge of a split. The fact that the inclusions are commonly exposed at the top of the split surface seems to indicate that splitting is often initiated at the inclusion sites. Large numbers of manganese sulphide inclusions are also often associated with splitting, as shown in Fig. 17. A chainlike formation of titanium carbonitrides seen in Fig. 18 clearly shows the separation of the matrix from the cuboid inclusions, although a considerable amount of ductile tearing of the material is also evident.

A quantitative assessment of the relative contributions of the various inclusion types is not feasible because of the

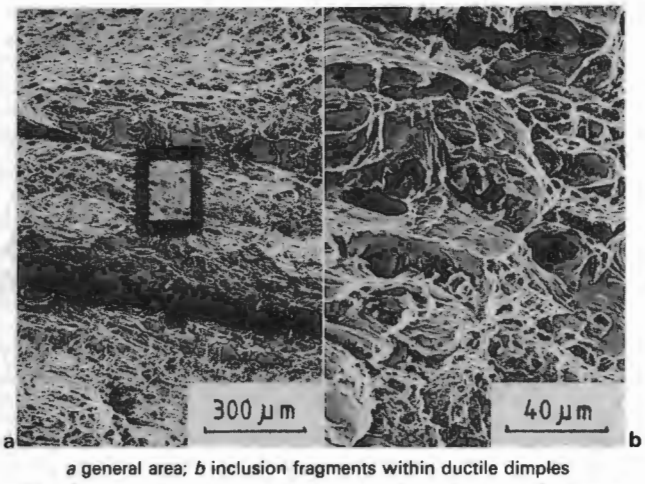

a general area; *b* inclusion fragments within ductile dimples

14 Association of inclusions with ductile fracture (sample 2)

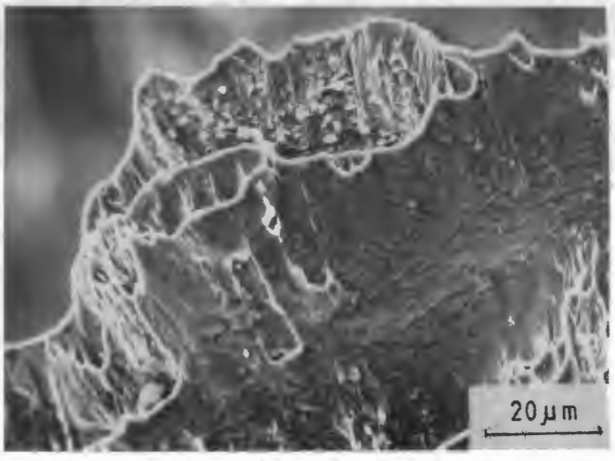

15 Typical example of inclusions on fracture surface at top of split (sample 2)

complex nature of the fracture surface. However, inclusion analyses using EDS on polished surfaces have shown that those alloys in which stringered manganese sulphide inclusions occur more abundantly have lower impact values. The fact that these inclusions are pancake-shaped as a result of hot rolling probably allows splitting in the rolling plane to occur more easily.

Discussion

Bramfitt and Marder[12] have found the splitting behaviour in Charpy specimens of low carbon steel to be caused by

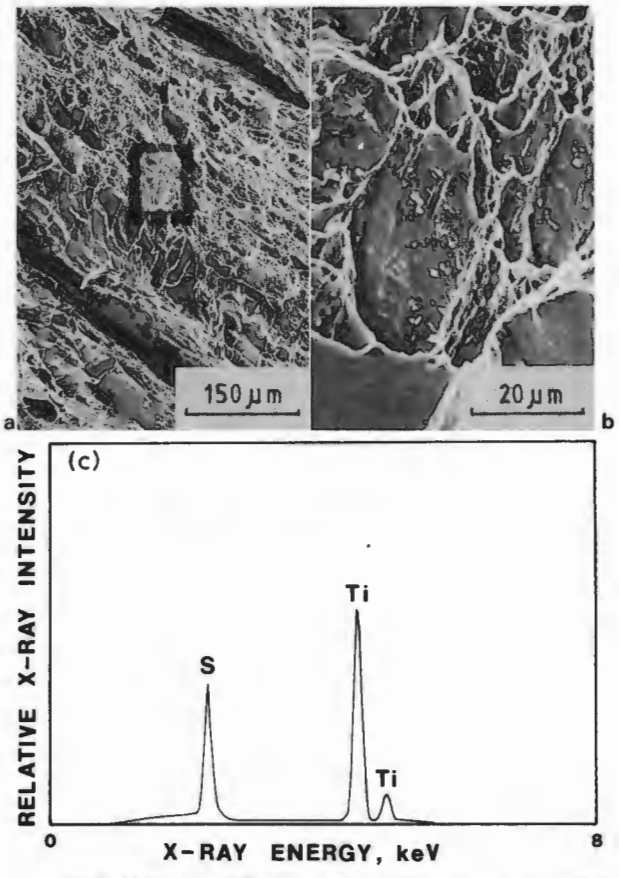

a SEM; *b* higher magnification of boxed area in *a*; *c* X-ray spectrum of inclusions (vertical full scale = 8192 counts)

16 Titanium sulphide inclusions along edge of split (sample 5)

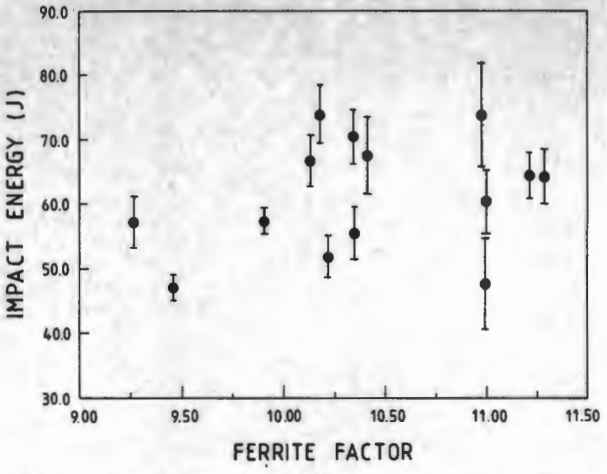

9 Impact energy as function of ferrite factor (values from Tables 2 and 3)

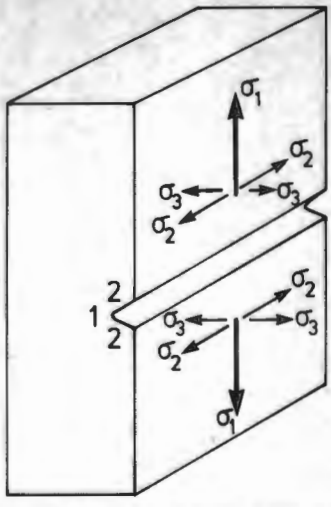

11 Development of triaxial stress system at root of V-notch

model of the splitting events shown in Fig. 12 indicates the initial maximum σ_2 stress concentration to be in the centre of the test specimen. Therefore, the first split is expected to occur in this region and subsequently two necking systems are produced. A new maximum in the σ_2 stress concentration is now set up in the centre of each secondary necking system and results in further splitting at regular spacings. The development of triaxial stresses in a ductile material is inherent in the Charpy V-notch test. However, the factors which determine whether splitting will occur or not are chiefly microstructural, as is discussed in the subsequent sections.

As mentioned above, a recent paper by Grobler and van Rooyen[5] has examined the effect splitting has on the ductile to brittle transition temperature of 3CR12 transverse Charpy specimens. They have shown that the reduction of the stress state in the notch as a result of splitting will reduce the temperature at which cleavage fracture can be expected, and splitting can therefore be expected to reduce the ductile to brittle transition temperature. However, it is also mentioned that the reduction in the stress state will cause a reduction in the upper shelf impact energy. This further validates the necessity to determine the factors which influence the extent to which splitting occurs in the upper shelf energy regime.

FRACTOGRAPHY: MICROSCOPICAL FEATURES

Examination of the fracture surfaces in the SEM reveals a variety of fracture modes. If the topography produced by splitting is considered to consist of a number of ridges and valleys (Fig. 13), the ridges are typically associated with ductile-dimple fracture, whereas the valleys show a relatively smooth surface, indicative of failure by a low energy mode. From a closer inspection of the fracture surface at higher magnifications, it is clear that inclusions play a large role in both splitting and in microvoid nucleation. McDonald and Ludwigson[13] have described four modes of fracture associated with inclusions in steel which can be briefly summarised as follows.

1. Ductile rupture. Dimples, resulting from microvoid formation and coalescence, are characteristic of ductile rupture. Microvoids are generally initiated at inclusions which can sometimes be observed within the dimples.

2. Decohesion. Fields of inclusions, interrupted by little, if any, ductile rupture, are characteristic of decohesion at the inclusion/matrix boundaries.

3. Cleavage. Stepped facets are caused by fracture through regions of different crystallographic orientation. Cleavage occurs by rapid propagation of a crack along crystallographic planes, and may be initiated by inclusion/matrix decohesion. This is a very low energy type of fracture.

4. Quasicleavage. A less well defined fracture mode, known as quasicleavage, is associated with tear ridges

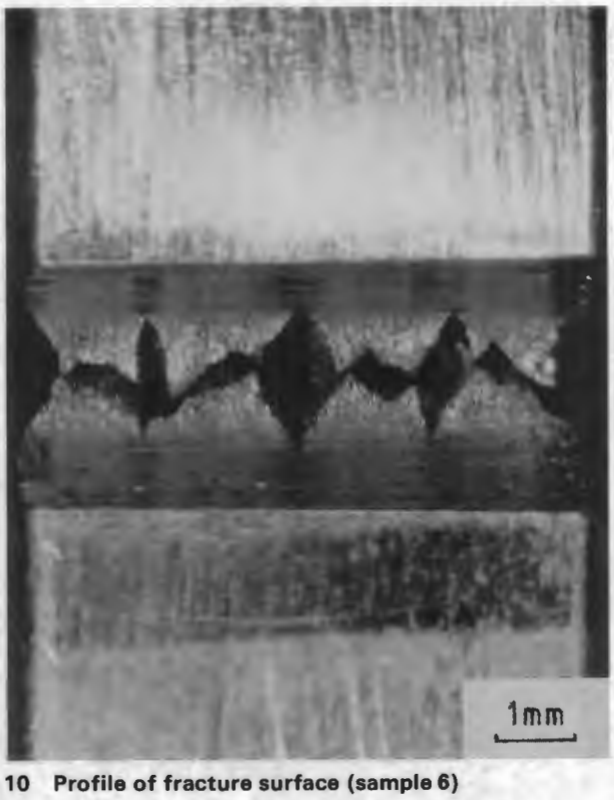

10 Profile of fracture surface (sample 6)

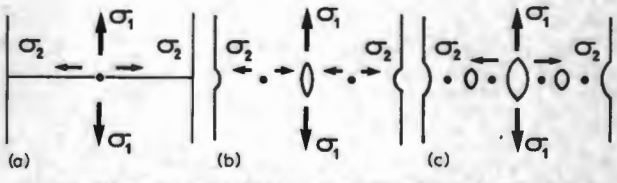

a initial maximum σ_2 stress concentration; *b* two necking systems produced by first split; *c* new maximum σ_2 produces further splitting

12 Simple model of splitting events (*see* text)

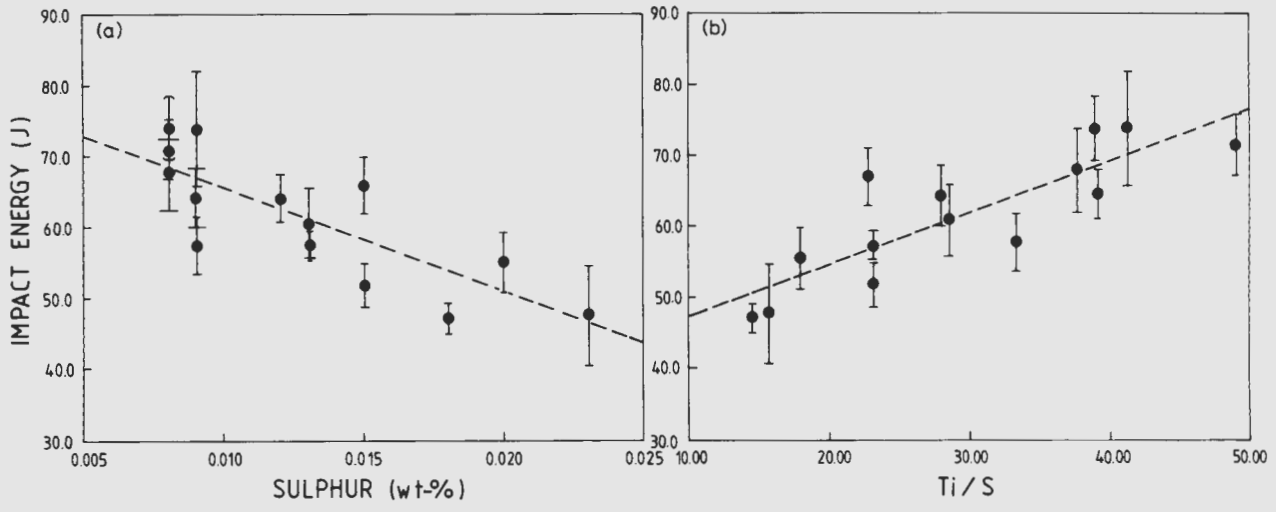

a sulphur content; *b* Ti/S ratio

7 Dependence of impact energy on titanium and sulphur contents

changes the morphology of the inclusions, it appears that the presence of titanium sulphide is less deleterious to the impact energy than stringered manganese sulphide inclusions. However, Ti(CN) cuboids may also contribute towards impact energy losses, although variations are not as evident. In view of the increased activity of titanium as the nitrogen content is decreased, and the effective increase in titanium available to associate with sulphur, it follows that a steel with a reasonably low nitrogen level and a high Ti/S ratio should show optimum impact values. Plotting impact energy as a function of both nitrogen content and Ti/S ratio (Fig. 8) shows an area to the right hand side of the dashed curve which has impact energy values > 60 J. A graph of impact energy as a function of ferrite factor (from values given in Tables 2 and 3) is shown in Fig. 9. No obvious trend is indicated owing to the wide scatter of points.

FRACTOGRAPHY: MACROSCOPIC OBSERVATIONS

The impact fracture surfaces are all characterised by a number of splits which occur at regular spacings perpendicular to the parting surface. Splitting occurs parallel to the rolling plane and gives rise to a highly contoured surface which appears jagged in profile (Fig. 10). Rematching of the Charpy specimens after fracture shows a series of secondary necking systems produced by the splitting. Dabkowski *et al.*,[11] as referenced by Bramfitt and Marder,[12] have proposed a model for the splitting in terms of the reduction of the energy absorbed during fracture. When splitting occurs, the area of the main fracture behaves like a cluster of small specimens. Since the width of the plastic zone in front of an advancing shear fracture is proportional to the thickness of the material, the width of the plastic zone in each of the volumes between the splits is smaller than in a homogeneously deforming specimen. Thus, the total volume of material plastically deformed is reduced and the level of energy for fracture consequently decreases with the onset of splitting. However, such an argument is not sufficient. In a homogeneous material the extra energy absorbed in producing the large degree of crack extension in the direction of the splits would be considerable. Obviously such a model requires a low energy fracture mode in the plane of the splits, and an applied stress which can open up these cracks.

The stress causing the splitting can be explained in terms of the triaxial stress system set up at the root of the V-notch. With reference to Fig. 11, the applied stress, σ_1, causes the material to yield at the root of the notch (area 1), while the material above and below the notch (area 2) is still constrained. This results in secondary stresses being imposed in the σ_2 and σ_3 directions. It is these secondary stresses (σ_2) which occur perpendicular to the rolling plane that are responsible for the splitting. A

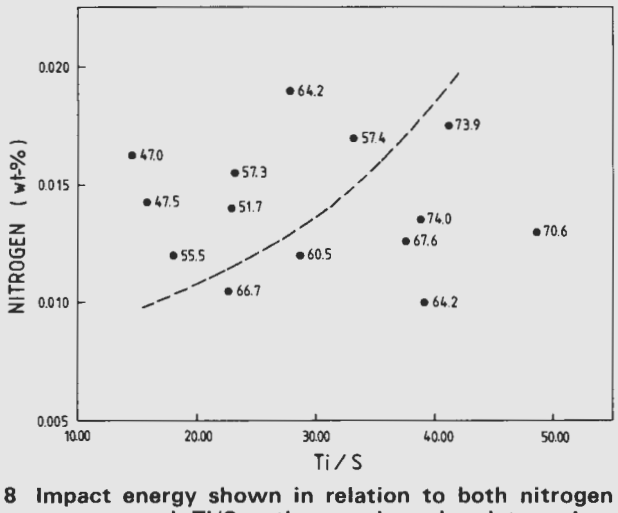

8 Impact energy shown in relation to both nitrogen content and Ti/S ratio; numbers by data points indicate impact energies (J)

Table 3 Charpy impact test results

Sample no.	Ti/S ratio	Impact energy, J	
		Mean	SD*
1	27·78	64·2	4·3
2	14·44	47·0	2·1
3	23·07	57·3	1·9
4	37·50	67·6	5·9
5	38·75	74·0	4·4
6	23·33	51·7	3·1
7	18·00	55·5	4·1
8	22·67	66·7	3·9
9	39·17	64·2	3·4
10	48·75	70·6	4·2
11	33·33	57·4	4·1
12	41·11	73·9	8·6
13	28·46	60·5	5·0
14	15·65	47·5	7·4

*SD standard deviation.

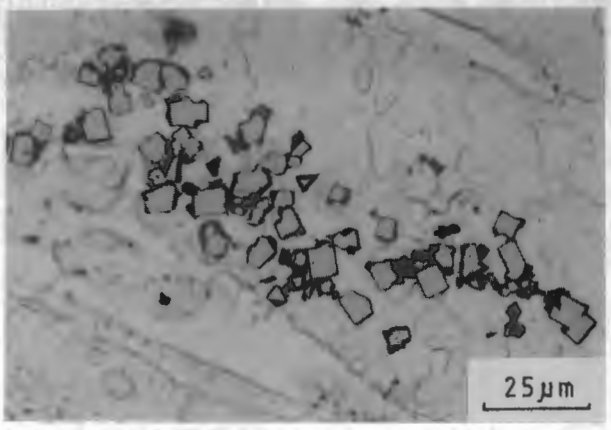

3 Localised cluster of titanium carbonitride inclusions; etched electrolytically in 10% oxalic acid solution (sample 7)

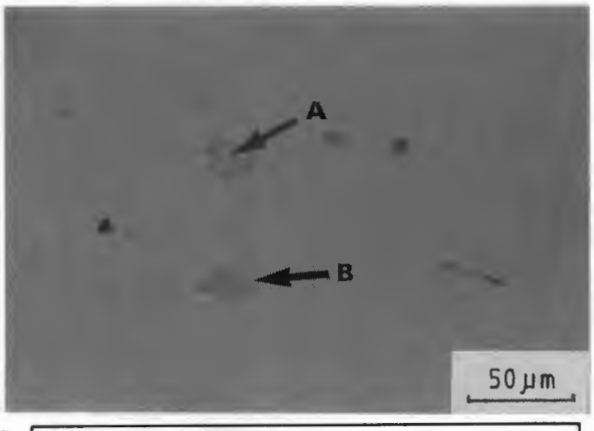

a two isolated cuboids A, B show presence of second phases at their boundaries; *b* X-ray spectrum from centre of particle A indicates titanium only (vertical full scale = 4096 counts); *c* sulphur is seen to be present in addition to titanium in boundary phase associated with particle B (vertical full scale = 4096 counts)

4 Analysis of cuboid precipitates (sample 2)

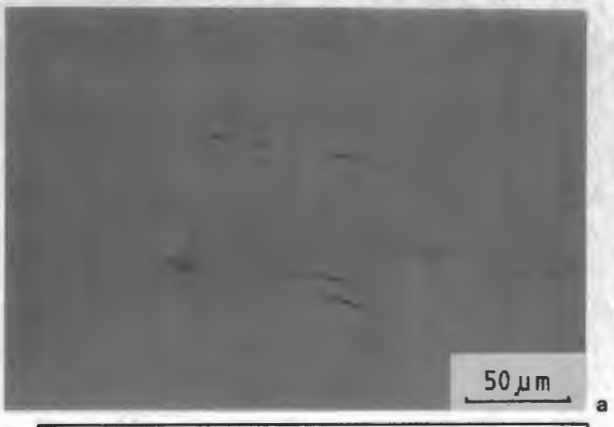

a stringered manganese sulphide inclusions; *b* titanium is seen to be associated with manganese sulphide inclusions (vertical full scale = 8192 counts)

5 Analysis of stringered sulphides (sample 2)

tion are fairly consistent (Table 3). An attempt at correlating impact energies with elemental compositions and ratios of the various elements yields two reasonable trends as shown in Fig. 7. In Fig. 7*a*, a general decrease in impact energy with increasing sulphur content is indicated. This result is in agreement with Spitzig and Sober[10] who showed a definite decrease in upper shelf energy with increasing sulphur content for 0·10 and 0·20%C steels. The effect is particularly marked for through thickness specimens and can be attributed to the increase in volume fraction of stringered manganese sulphide inclusions with increase in sulphur content. In Fig. 7*b*, however, the impact energy is shown to increase with increasing Ti/S ratio. Since increasing the titanium content decreases the probability of manganese sulphide formation and also

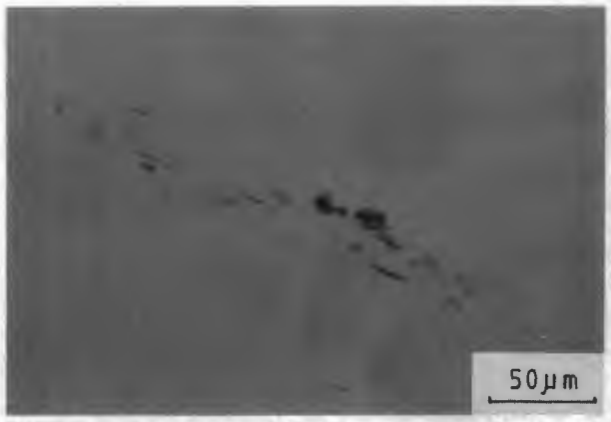

6 Increased amounts of titanium are associated with globular inclusions (sample 6)

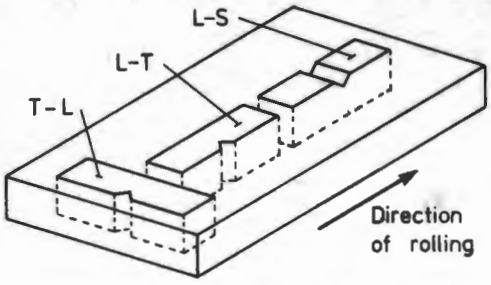

TL transverse–longitudinal; LT longitudinal–transverse; LS longitudinal–short transverse

1 Orientation of Charpy specimens with respect to direction of rolling; all specimens were tested in TL orientation

bifluoride + 1·0 g potassium metabisulphite), or electrolytically etched in a 10% oxalic acid solution. Non-metallic inclusion compositions were determined using energy dispersive spectroscopy (EDS) on a semiquantitative basis. Individual inclusions were identified on polished surfaces by using microhardness indentations as markers. Analysis was performed in a scanning electron microscope (SEM) equipped with an EDS facility.

For each sample, X-ray spectra were obtained for individual inclusions as well as for the bulk matrix. The inclusion spectra were processed by subtracting the matrix spectrum from the inclusion spectrum after normalisation with respect to the Fe$K\alpha$ peaks. This enabled an approximate allowance to be made for the matrix contribution.

Fractography was conducted using a low power optical microscope and the SEM. An assessment of the type and frequency of inclusions associated with the various modes of fracture was carried out using the EDS system in conjunction with the SEM.

Results

MICROSTRUCTURAL FEATURES AND ANALYSIS OF INCLUSIONS

As a result of the annealing heat treatments, the microstructures of the steels consisted predominantly of ferrite with small amounts of tempered martensite. The ferrite grains were elongated parallel to the rolling direction (Fig. 2) and appeared pancake-shaped in the rolling plane. The tempering of the martensite, however, had resulted in pockets of fine recrystallised grains. Although the ferrite factors for the 14 samples were not identical, there was no significant difference in their microstructures.

Table 2 Titanium, sulphur, and nitrogen contents of test samples, wt-%

Sample no.	Titanium	Sulphur	Nitrogen	FF*
1	0·25	0·009	0·0190	11·29
2	0·26	0·018	0·0162	9·51
3	0·30	0·013	0·0155	9·91
4	0·30	0·008	0·0126	10·42
5	0·31	0·008	0·0135	10·18
6	0·35	0·015	0·0139	10·22
7	0·36	0·020	0·0120	10·35
8	0·34	0·015	0·0105	10·14
9	0·47	0·012	0·0100	11·22
10	0·39	0·008	0·0127	10·34
11	0·30	0·009	0·0166	9·28
12	0·37	0·009	0·0165	10·95
13	0·37	0·013	0·0120	10·97
14	0·36	0·023	0·0142	11·03

* FF ferrite factor

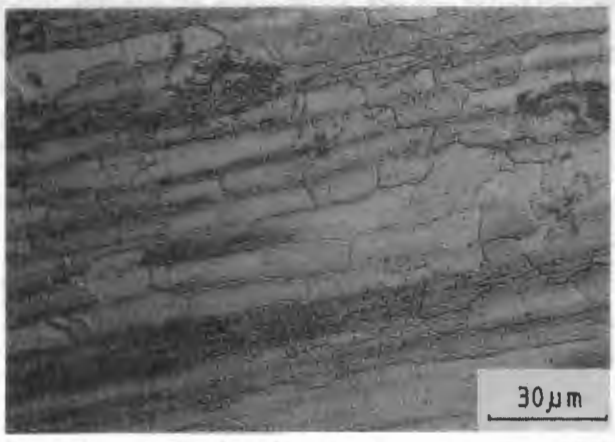

2 Predominantly ferritic microstructure of 3CR12 after annealing at 800°C for 1 h (sample 1)

Cuboid titanium containing inclusions were by far the most commonly occurring non-metallic inclusions in 3CR12. Individual inclusions ranged up to 10 μm in size and occurred in chainlike formations, random dispersions, or as distinct clusters (Fig. 3). They were yellow in colour and often had a pink/grey second phase around their boundaries.

Two isolated cuboids are shown in Fig. 4*a*. A typical X-ray spectrum of the centre of a cuboid can be seen in Fig. 4*b*. Because of the limitations of EDS, only titanium was detected, but carbon and nitrogen have been identified by means of scanning Auger microscopy.[7] It is generally accepted that these are titanium carbonitride inclusions, and such inclusions have been identified in the melt before pouring.[8] The extent to which these inclusions occur, however, depends on the nitrogen content of the steel. Volume fractions determined by point counting have shown that the Ti(CN) particle content increases proportionally with the nitrogen content. In a spectrum of the boundary area, the surrounding phase is shown to consist of titanium and sulphur (Fig. 4*c*). In some cases, minor amounts of manganese have also been detected at the boundaries.

Manganese sulphide (MnS) inclusions generally occur as stringers, but their presence is very much dependent on the bulk chemistry of the steel. These inclusions were elongated parallel to the rolling direction and ranged from 1 to 20 μm in length. Although isolated homogeneous sulphide inclusions were common in some of the steels tested (Fig. 5*a*), varying amounts of titanium were often associated with such inclusions (Fig. 5*b*). After considering relative peak intensities from numerous X-ray spectra, it was generally found that the titanium content in the inclusions increases as the Ti/S ratio in the steel increases. This is hardly surprising, since TiS is thermodynamically more stable than MnS,[9] and hence forms in preference to MnS. Further, it confirms that free titanium was available, not all of it being tied up in the carbonitrides. This situation could easily be different in steels containing more carbon and/or nitrogen.

The morphology of the sulphides changed with increasing titanium content, becoming more globular and less continuous (Fig. 6). Steels having Ti/S ratios > 40 generally had few or no stringered inclusions present and the sulphide occurred mostly at the boundaries of the carbonitride inclusions.

CHARPY IMPACT RESULTS

A considerable range of impact energy was obtained for the 14 compositions tested, although results for each composi-

Occurrence of non-metallic inclusions in 3CR12 steel and their effect on impact toughness

The impact toughness and microstructure of a dual phase 12 wt-% Cr steel (3CR12) have been investigated. In particular, the occurrence of non-metallic inclusions has been studied in relationship to the detailed chemistry of the steel. The effect of these inclusions on the modes and morphology of fracture has also been determined. It is shown that splits form parallel to the rolling plane when Charpy specimens are subjected to impact testing. Non-metallic inclusions, particularly manganese sulphides, facilitate low energy modes of fracture associated with the splitting phenomenon. Stringered and pancake-shaped inclusions also prevent the formation of equiaxed ferrite on annealing, thus retaining the directional microstructure. Careful control of the chemistry of the steel permits the most deleterious inclusions to be restricted to levels at which acceptable impact properties are maintained. *MST/637*

 Manuscript received 18 December 1986; in final form 15 July 1987. *At the time the work was carried out the authors were in the Department of Materials Engineering, University of Cape Town, Rondesbosch, Republic of South Africa. Dr Hutchings is now with Beta Research and Development Ltd, Advanced Battery Research, Derby.*

R. D. Knutsen
R. Hutchings

Introduction

A 12%Cr, titanium stabilised corrosion resisting steel, designated 3CR12, has been developed to replace mild steel on the basis of improved corrosion resistance and superior mechanical properties. It is not a stainless steel, but has been designed to fill the gap between stainless steels, at the one end of the market, and the rust prone carbon steels at the other end.[1] Successful applications have been found in areas involving abrasive wear in conjunction with corrosive environments, such as those encountered in the mining and minerals industry. The strength, ductility, toughness, formability, and weldability are comparable to mild steel in most respects.[2]

The steel was developed from AISI 409 by carefully balancing the ferrite formers (chromium, silicon, titanium) with the austenite formers (carbon, nitrogen, nickel, manganese) using the Kaltenhauser relationship

$$\text{ferrite factor (FF)} = [\%Cr + 6(\%Si) + 8(\%Ti) + 4(\%Mo) + 2(\%Al) + 4(\%Nb)] - [2(\%Mn) + 4(\%Ni) + 40(\%C + \%N)]$$

The typical composition of 3CR12 is shown in Table 1. Typical ferrite factors fall in the range 8–12. This balanced composition produces a steel with a banded two phase structure in the hot rolled condition which, on tempering at subcritical temperatures, results in a fine grained duplex structure of ferrite and tempered martensite.[2]

Because of the complex chemistry of 3CR12, numerous inclusions of various shapes, sizes, and degrees of coherency are found to occur both within grains and along grain boundaries. Commonly occurring non-metallic inclusions are titanium carbonitrides, titanium sulphides, and manganese sulphides. The exact composition, morphology, distribution, and volume fraction of these inclusions, however, will depend on the relative amounts of titanium, manganese, sulphur, carbon, and nitrogen present in the steel. Since it is well known that inclusions affect fracture mechanisms to some degree,[3,4] it is probable that variations in inclusion type and morphology in a particular steel type may give rise to differences in mechanical properties.

In recent studies by Grobler and van Rooyen,[5,6] the impact fracture in relation to the microstructure of 3CR12 was examined for a fairly limited compositional range, the findings of which are discussed below. These tests were conducted on transverse Charpy specimens over a wide temperature range in order to determine the effect that the mechanism of fracture has on the ductile to brittle transition temperature. In their work, the influence of titanium carbonitride inclusions was considered, but no specific mention of stringered manganese sulphide inclusions was made.

The present work involves a detailed analysis of inclusion types and distributions, and their effects on the impact toughness of 3CR12, with a view to understanding the relationship between chemistry and impact strength, in such a way that compositional limits may be stipulated for consistent and acceptable mechanical properties. A more extensive compositional range is covered, thus giving rise to a greater variation in inclusion types likely to affect fracture mechanisms in the upper shelf energy regime.

Experimental procedure

Fourteen samples with various titanium, sulphur, and nitrogen contents (Table 2) were supplied in plate form, ranging from 9 to 12 mm in thickness by Middelburg Steel and Alloys. Samples were received in the hot rolled annealed condition (750–780°C for 40–80 min per 25 mm of thickness). However, all material was subjected to a final laboratory anneal at 800°C for 1 h, followed by furnace cooling before testing. This was performed in order to standardise the specimens in a fully annealed condition.

Toughness measurements were conducted on each composition using Charpy V-notch impact specimens. Four subsidiary test specimens (7·5 × 10 mm) were machined from each composition in the TL orientation (Fig. 1) and tested at room temperature.

After impact testing, longitudinal and transverse specimens were examined using conventional metallographic techniques. Samples were either chemically etched (in a solution of 100 ml 1:5 vol/vol HCl + 2·0 g ammonium

Table 1 Typical composition of 3CR12 steel, wt-%

C	Si	Mn	P	S	Cr	Mo	Ni	Al	Cu	N_2	Ti
0·026	0·440	1·160	0·023	0·015	11·26	0·02	0·68	0·008	0·060	0·014	0·35

allow more free titanium to be available for sulphide formation.

The mode of splitting in the rolling plane occurs predominantly by the separation of elongated ferrite grains. The exposure of inclusions on the split surfaces indicates that this is aided considerably by inclusion/matrix decohesion. The extent to which splitting occurs after annealing is thought to be controlled by the presence of stringered inclusions. Annealing is not effective in producing equiaxed ferrite grains by recrystallisation. This may be because of the pinning of the grain boundaries by the stringered manganese sulphide inclusions. Therefore, splitting persists in annealed material.

Acknowledgments

The authors would like to thank Middelburg Steel and Alloys, Transvaal, Republic of South Africa, and the Council for Scientific and Industrial Research (CSIR), Pretoria, for supporting this work, with special thanks to Mr J. Hewitt and Mr J. P. Hoffman, of Middelburg Steel and Alloys, for their interest and encouragement. Professor A. Ball, University of Cape Town, is gratefully acknowledged for his generous advice and numerous valuable discussions. The authors would also like to express their gratitude to the technical and secretarial staff of the Department of Materials Engineering, University of Cape Town, for their assistance in completing this work. Finally, thanks are due to Dr C. Grobler and Professor G. T. van Rooyen for making available preprints of Refs. 5 and 6 before their publication.

References

1. J. P. HOFFMAN: in Proc. 'Inaugural international 3CR12 conference', Johannesburg, Mar. 1984, Middelburg Steel and Alloys, L1–L23.
2. A. BALL and J. P. HOFFMAN: *Met. Technol.*, 1981, **8**, 329–338.
3. V. P. RAGHUPATHY, V. SRINIVASAN, H. KRISHNAN, and M. N. CHANDRASEKHARAIAH: *J. Mater. Sci.*, 1982, **17**, 2112–2126.
4. M. TANAKA and H. IIZUKA: *J. Mater. Sci.*, 1985, **20**, 3750–3762.
5. C. GROBLER and G. T. van ROOYEN: in Proc. '25th annual conference of metallurgists', Toronto, Ont., Aug. 1986, paper 34.2 (in press).
6. C. GROBLER and G. T. van ROOYEN: in Proc. '25th annual conference of metallurgists', Toronto, Ont., Aug. 1986, paper 34.1 (in press).
7. F. BLUM, C. M. STANDER, and N. R. COMINS: *Proc. Electron Microsc. Soc. South Afr.*, 1984, vol. 14, 9–10.
8. J. HEWITT: personal communication, Middelburg Steel and Alloys, Middelburg, Republic of South Africa, 1985.
9. R. KIESSLING and N. LANGE: in 'Non-metallic inclusions in steel', 2 edn, Part II, 97–99; 1978, London, The Metals Society.
10. W. A. SPITZIG and R. J. SOBER: *Metall. Trans.*, 1981, **12A**, 281–291.
11. D. S. DABKOWSKI, P. J. KONKOL, and M. F. BALDY: paper presented at Canadian Metallurgical Society Symposium on 'Arctic line pine', Toronto, Ontario, Aug. 1974.
12. B. L. BRAMFITT and A. R. MARDER: *Metall. Trans.*, 1977, **8A**, 1263–1273.
13. M. M. McDONALD and D. C. LUDWIGSON: *J. Test. Eval.*, 1983, **11**, 165–173.

High nitrogen stainless steel wire

The effect of nitrogen as a solid solution strengthening element in steel is well known, but is also generally associated with embrittlement. The present work describes the nitrogenation of nitrogen alloy stainless steel wire to produce material of high nitrogen content, which is shown to have beneficial effects on strength and corrosion resistance. Heat treatment of the alloys to induce precipitation of chromium nitride causes embrittlement, but when nitrogen is retained in solid solution excellent ductility is obtained. Pilot plant wire drawing trials show that suitable combinations of wire drawing and heat treatment can be devised to produce high strength stainless steel wire; development of manufacturing technology to give higher nitrogen concentrations will lead to still greater improvements in properties. *MST/706*

© *1988 The Institute of Metals. Manuscript received 9 April 1987; in final form 24 August 1987.* *At the time the work was carried out, the authors were in the Crystallography Laboratory, University of Newcastle upon Tyne. Dr Rayaprolu is now in the Division of Mechanical Engineering and Engineering Materials, University of Bristol and Dr Hendry is in the Department of Metallurgy, University of Strathclyde, Glasgow.*

D. B. Rayaprolu
A. Hendry

Introduction

Austenitic stainless steels find applications in a wide range of uses, mainly because of their excellent corrosion resistance and formability. These steels are more expensive than, and have mechanical properties inferior to, ferritic and martensitic alloys, but these mechanical properties can be improved by the introduction of interstitial elements either in solid solution or as precipitation strengthening additions when used in combination with other strong carbide- and nitride-forming alloy elements. Carbon has the disadvantage that severe grain boundary sensitisation can occur, with consequent loss of corrosion resistance. Therefore, the benefits of nitrogen alloying of austenitic stainless steels have received wide attention recently[1–8] and may be summarised as

(i) increased stability of the γ phase
(ii) increased strength
(iii) improved corrosion resistance.

Nitrogen is a strong austenite stabilising element and may be used effectively in combination with manganese, which increases the nitrogen solubility in austenite, to decrease the amount of (expensive) nickel required to maintain a fully austenitic structure. Strengthening by nitrogen has been discussed in a number of papers[3,7–11] and significant increases in mechanical properties have been obtained. Molybdenum is frequently added to austenitic stainless steels to improve resistance to pitting corrosion in marine environments, but since it is a ferrite stabiliser it must be balanced by corresponding nickel equivalent elements. Nitrogen fulfils this requirement with the additional benefit that it has been shown to increase resistance to pitting still further.[12]

Commercial high nitrogen stainless steel wire is already in limited use for marine cables, but there is insufficient knowledge about effects on properties resulting from variations in nitrogen content and from transformations during production, heat treatment, and aging. In the present work, the range of nitrogen concentrations which can be obtained in a commercial nitrogen alloy steel is investigated and the results show the effects which these changes produce in the microstructure and on the properties of the steel. The results of laboratory experiments provided information on which a series of wire drawing trials were based and led to the development of a suggested scheme of heat treatment and deformation which produces significant improvements in tensile, fatigue, and corrosion properties of nitrogen alloy wires. It is obvious that development of suitable manufacturing technology will lead to greater increases in properties of nitrogen alloy stainless steel and widen the range of application of these new alloys.

Experimental

The present study was carried out on a commercial nitrogen alloy steel Nitronic 50, the composition of which is given in Table 1. Wire samples were provided by British Ropes, Doncaster. The nitrogen content was varied by equilibration of solid samples of this steel in $N_2:H_2$ gas mixtures at 1200°C, followed by a suitable cooling cycle: slow cooling to induce nitride precipitation or quenching to retain nitrogen in solid solution. Heat treatment of samples was also carried out in nitrogen or $N_2:H_2$ gas mixtures. Samples for wire drawing trials were too long for treatment in $N_2:H_2$ atmospheres in laboratory furnaces; therefore coils of wire were sealed in silica containers under a suitable pressure of nitrogen before heat treatment. The nitrogen concentration in steel samples was measured by X-ray determination of unit cell dimensions or by vacuum fusion analysis (Leco Corporation, St Joseph, MI, USA).

For corrosion studies, wires of 1·42 mm dia. and 100 mm^2 surface area were heat treated and welded to copper leads. The welded joints were placed in glass capillary tubes and these then sealed with araldite resin, thus exposing only the sample steel to the electrolyte and not the welded area. Potentiodynamic polarisation curves were determined in 3·5%NaCl solution against a saturated calomel reference electrode. The samples were electropolished before immersion in the salt solution at a potential of −1·0 V; the potential was then scanned up to +1·0 V at a rate of 20 mV min^{-1}. At 1·0 V the sweep was reversed and the test continued to 0 V.

The wire drawing tests of heat treated samples and tensile tests of the wires produced were carried out by British Ropes, Doncaster.

Conventional optical microscopy, together with scanning and transmission electron microscopy, were carried out to characterise the microstructures produced in all of the experiments. When X-ray powder diffraction

Table 1 Composition of Nitronic 50, wt-%

C	Mn	Cr	Mo	Ni	N	Nb	V
0·03	4·92	21·6	2·19	12·5	0·24	0·18	0·18

Nitronic 50 is a registered trademark of Armco Steel Corporation, Middleton, OH, USA.